Gamma-ray Spectroscopy Measurements for Nuclear Reactions in Novae

Gavin James Lotay

School of Physics and Astronomy

The University of Edinburgh

Thesis submitted for the degree of
Doctor of Philosophy in the subject of *Physics*

September 2008

For
My Family

Abstract

The ^{23}Mg$(p,\gamma)^{24}$Al and ^{26}Al$(p,\gamma)^{27}$Si astrophysical reactions are expected to be of considerable importance in the nucleosynthesis of $A\geq$20 nuclei in classical novae. Previous studies have indicated that both reactions are dominated by resonant capture to excited states, above the proton-emission thresholds, in the proton-rich nuclei ^{24}Al and ^{27}Si, respectively. Consequently, by determining the nuclear properties of such resonant states it is possible to estimate the ^{23}Mg$(p,\gamma)^{24}$Al and ^{26}Al$(p,\gamma)^{27}$Si stellar reaction rates.

In this thesis work, excited states in ^{24}Al and ^{27}Si were populated via the ^{10}B$(^{16}$O$,2n)$ and ^{12}C$(^{16}$O$,n)$ heavy-ion fusion-evaporation reactions, respectively. The beams of ^{16}O ions were produced by the Argonne Tandem Linear Accelerator System and prompt electromagnetic radiation was detected using the GAMMASPHERE detector array, which, in the case of the ^{24}Al experiment, was used in coincidence with recoil selection provided by the Argonne Fragment Mass Analyzer. The two γ-ray spectroscopy studies performed in this work allowed level structure determinations below the respective proton-emission thresholds of ^{24}Al and ^{27}Si nuclei, with improved precision on previous work. In addition to this, these studies also allowed a determination of the nuclear properties of proton-unbound astrophysically important γ-decaying states, which, in turn, were used to re-evaluate the ^{23}Mg$(p,\gamma)^{24}$Al and ^{26}Al$(p,\gamma)^{27}$Si stellar reaction rates. The improved precision of the level energies and unambiguous assignments of resonant states has reduced the relative uncertainties in both the ^{23}Mg$(p,\gamma)^{24}$Al and ^{26}Al$(p,\gamma)^{27}$Si stellar reaction rates, constraining the production of $A\geq$20 nuclei in classical novae.

Acknowledgements

Firstly, I would like to thank my supervisor, Prof. Philip J. Woods, for all his support and words of wisdom throughout my PhD research. His continual confidence in my ability as a scientist has pushed me to achieve my very best and I will be forever grateful for all his guidance and encouragement over the past three years.

Secondly, I would like to thank Darek Seweryniak for all the time he has given up to aid my education in experimental nuclear astrophysics. I have learnt a great deal from working with him and am very appreciative of the significant difference his guidance has made to the quality of work I have been able to produce.

Thirdly, I would like to thank Alex Murphy, Tom Davinson, Dan Watts, Derek Glazier, Zhong Liu, Marialuisa Aliotta and Derek Branford, who have always been available to answer any questions I may have had throughout my time at Edinburgh.

Additional thanks go to members of the Edinburgh Nuclear Physics Group; Alexis Josephides, Chamkaur Ghag, Steven Plank, Claire Tarbert, Paul Scovell, Emma Barnes and Tom Jude whose friendship has been a constant supply of reassurance and confidence throughout my studies.

Special thanks go to my dearest Rosamund for the belief she has shown in me during my PhD. I am truly grateful for all her support and, although she has frequently thought herself to be a distraction from my work, I hope she realises how important she is to me in all aspects of my life.

Last but by no means least, my deepest thanks go to my family. They have always supported me in every venture I have undertaken and are the reason I have been able to achieve all that I have to date.

I owe all of my successes to the opportunities provided to me by my family and as such, I dedicate to them this thesis.

Declaration

The two experiments described in this thesis were performed by myself, fellow members of the Edinburgh University Nuclear Physics Group, and our collaborators at Argonne National Laboratory. The data analysis and interpretation of results are my own work, and this thesis has been written by myself. No portion of the work referred to in this thesis has been submitted in support of an application for another degree qualification at this university or any other academic institution.

Gavin Lotay

Contents

List of Figures

List of Tables

Chapter 1

Introduction to Nuclear Astrophysics

The field of nuclear astrophysics links the microscopic world of nuclear physics to the macroscopic realm of astronomy and astrophysics, by studying the nuclear processes that occur within stars. These nuclear reactions are responsible for the synthesis of almost all of the chemical elements and generate the energy that makes stars shine. When stars eject part or all of their matter via stellar outbursts and energetic explosions, they enrich the interstellar medium and thereby provide the building blocks for the birth of new stars, of planets and of life itself. The theory of this building of elements is called nucleosynthesis and signatures of its processes, past and present, can be found in the isotopic abundances observed on the earth, in the solar system, in meteoritic remains and in cosmic γ-ray emissions.

Over the years, astrophysicists have endeavoured to explain the observed isotopic abundances by constructing theoretical models of nucleosynthesis within various stellar environments. The predictions of these models, although indicating possible astrophysical production sites for observed isotopes, are often limited by considerable uncertainties in the input data. Consequently, one of the main aspects of nuclear astrophysics is the integration of astrophysical models with information provided by nuclear physics, to allow such models to be tested and used to further aid understanding of the chemical evolution of the Galaxy.

In this thesis work, the $^{23}\mathrm{Mg}(p,\gamma)^{24}\mathrm{Al}$ and $^{26}\mathrm{Al}(p,\gamma)^{27}\mathrm{Si}$ radiative proton capture reactions in novae environments were investigated by studying the nuclear structures of the proton-rich nuclei ^{24}Al and ^{27}Si, respectively. Classical

novae are among the most frequent and violent stellar explosions, to be observed by astronomers, that contribute to the chemical composition of the Galaxy. Distinctive isotopic abundance spectra have been determined for such environments and astrophysical models indicate that uncertainties in both the $^{23}\mathrm{Mg}(p,\gamma)^{24}\mathrm{Al}$ and $^{26}\mathrm{Al}(p,\gamma)^{27}\mathrm{Si}$ reaction rates may influence the observed galactic abundances of a number of isotopes. Thus, the work presented in this thesis encompasses one of the main aspects of nuclear astrophysics, in which nuclear physics information is used to test and constrain theoretical models of stellar nucleosynthesis.

The following sections give a general background to nuclear astrophysics, describing stellar evolution and the nuclear reactions involved in the life-cycles of stars.

1.1 Astronomical Observables

Since the late 1930s it has been known that the fusion of light nuclides into heavier species serves as the source of energy generation in stars [1; 2; 3]. However, it was not until several years later that it was established that the same nuclear processes are responsible for the synthesis of the metal elements [4; 5; 6] (by which we mean any element heavier than hydrogen and helium). The theory of this building of elements is called nucleosynthesis and represents the basis of nuclear astrophysics.

1.1.1 Solar System Abundances

A necessary prerequisite for the testing and development of a theory is observational data. The observational data of most significance for nucleosynthesis are the abundances of the nuclear species and, at present, by far and away the best abundance data in existence are those for the solar system. It is commonly accepted that the solar system formed from the collapse of a gaseous nebula that had an almost uniform chemical and isotopic abundance distribution and consequently, data from solar system objects are regarded as a measure of the abundances in our region of the Galaxy at the time of formation. The Sun contains most of the mass in the solar system and, therefore, derived elemental abundances from observed solar spectra are representative of the overall composition. However, a further source of solar system elemental abundances are found from the analysis of a specific class of meteorites, called CI carbonaceous

chondrites, and although they contain a minuscule amount of matter, they are believed to be among the most primitive objects in the solar system, retaining most of the elements present in the original matter of the solar nebula. The first study using a detailed compilation of both meteoritic and solar spectra abundance data was presented by Suess and Urey in 1956 [7]. This influential work and subsequent such tables of solar system abundances have had an enormous effect on the investigations of the origin of the elements and for the field of nuclear astrophysics as a whole.

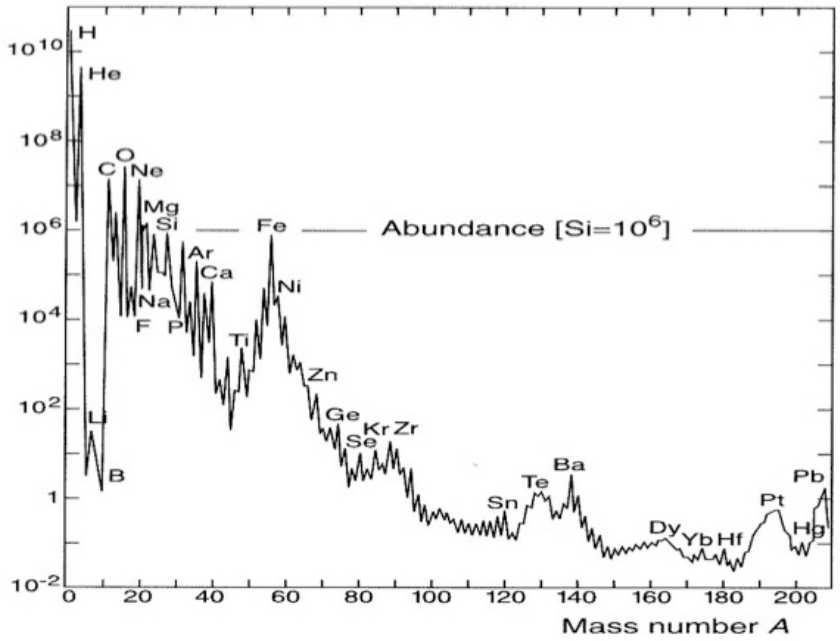

Figure 1.1: Abundances of nuclides in the solar system at its birth [8].

The solar system abundances of nuclides versus mass number are shown in Fig. 1.1 [8]. The abundances have been normalised to the number of silicon atoms. In Fig. 1.1, it can be seen that the abundances do not scatter randomly, but instead exhibit a certain regularity and systematics in the form of abundance maxima and minima. It is reasonable to assume, therefore, that the abundances within any group or subgroup of nuclides can be attributed primarily to a specific mechanism of nucleosynthesis. All nuclei with few exceptions are synthesized in stars and as such, from the observed solar system abundances, not only is it possible to identify and study various processes of nucleosynthesis that leave distinctive signatures in the abundance distribution, but a connection can also

be made to the stellar environments in which these sources of nucleosynthesis operate. In addition, stellar nucleosynthesis plays a decisive role for explaining the chemical composition of the interstellar medium and is thus intertwined with γ-ray astronomy, the study of primitive meteorites, and the nature of cosmic rays.

1.1.2 Stellar Populations

Over the years, significant unambiguous direct evidence for the nucleosynthesis in stars has been accumulated [9; 10; 11; 12]. Of particular note, however, was the astronomical discovery of two distinct stellar populations, which are referred to as population I and population II stars. Population I stars, which include the Sun, are found in the spiral arms of the Galaxy and are metal-rich, by which astronomers mean any other element other than hydrogen or helium. Population II stars, however, are found in the halo and bulge of the Galaxy and have a metallitic content relative to hydrogen smaller by a factor of 100 or more compared to that of population I stars. If one assumes that the initial composition of the Galaxy was uniform and there exists no mechanism capable of concentrating the metals in the disk of the Galaxy, then the Galaxy must have synthesized an overwhelming fraction of its own metals. Therefore, the differences in metallicity between the two stellar populations suggest that population I stars, which make up the bulk of presently observed stars, formed significantly later on in the history of the Galaxy than population II stars.

1.1.3 Hertzsprung-Russell Diagram

A further striking observational fact about stars is their enormous range in both stellar surface temperature and luminosity. A comparison between these two quantities was first made by Hertzsprung and Russell [13], in which the luminosities of stars, observed within several clusters, were plotted against their effective surface temperatures. It was found that the stars did not scatter randomly across the diagram but instead cluster into several distinct groups. This correlation, known as the Hertzsprung-Russell diagram, is shown in Fig. 1.2.

Most stars are aligned along a narrow band running from the upper left-hand part of the diagram to the lower right-hand part, which is called the “main sequence”. A substantial number of stars lie above the main sequence in the

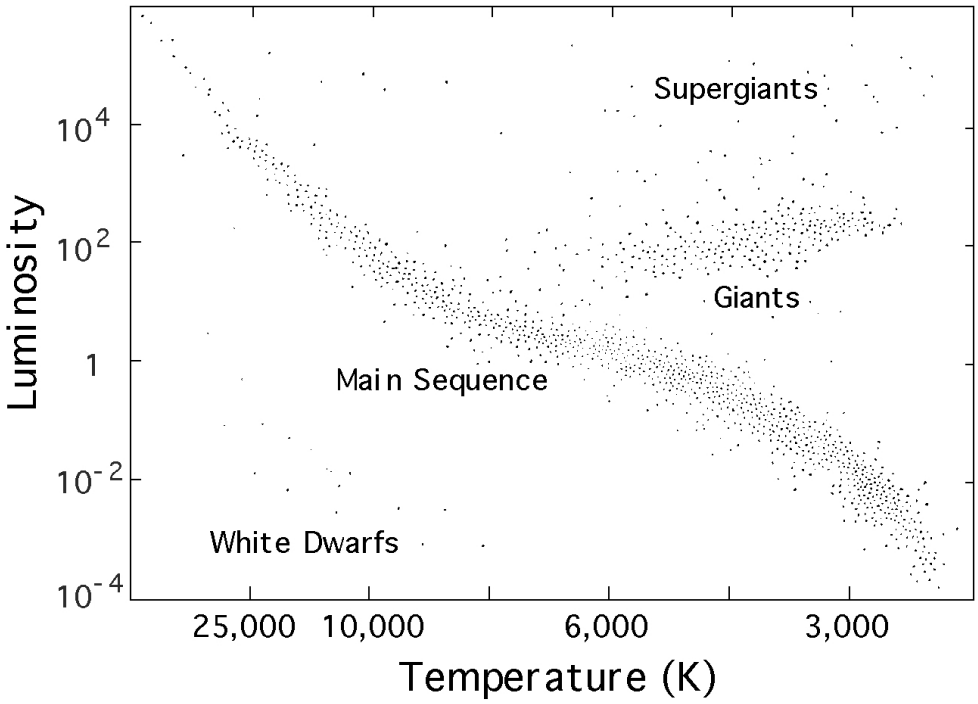

Figure 1.2: The Hertzsprung-Russell diagram for a sample of stars in the solar neighbourhood. The diagram represents a snapshot in the history of the stars' lives.

upper right-hand region of the diagram and are called “red giants”. At the top of the diagram are stars of even higher luminosity, called “red super-giants” and finally, there are stars in the lower left-hand corner, known as “white-dwarfs”.

1.2 The Evolution of Single Stars

One of the most important goals of the theory of stellar structure and evolution is to understand why certain stars appear only in specific regions of the Hertzsprung-Russell diagram and how they evolve from one region to another. In the following subsections we shall cover the main aspects of the stellar life cycle and the thermonuclear reactions involved at each evolutionary stage.

1.2.1 The Birth of Stars

A star may form when a cool cloud of gas in the interstellar medium collapses to a high density. At first, the internal heat resulting from the contraction [14] is readily radiated away because of the relatively high transparency of the gas, which is essentially in gravitational free fall. Eventually the cloud becomes dense enough that it becomes opaque to radiation and the cloud undergoes a rapid heating process forming a protostar [15]. Once the core temperature is in excess of 10^6 K, nuclear fusion reactions are possible, contraction is ceased and the star begins its main sequence. Some protostars, however, do not have sufficient mass to ignite the self-sustaining hydrogen burning and evolve directly into “brown” or “black” dwarfs.

Smaller gas clouds, such as solar nebulae, prevent spontaneous gravitational collapse through a repulsive thermal pressure. However, it is widely thought that star formation is possible if a violent external source, such as the shock wave from a supernova, is incident on such a gas cloud [16]. The additional pressure provided by the shock wave will initiate the cloud’s contraction, eventually causing a gravitational collapse and a star is born.

1.2.1.1 Physical State of the Stellar Interior

It is important to mention at this point that there are two key inferences that can be made about the state of the stellar interior if the star is to be a stable body over long time periods. The first arises from the fact that at any given

spatial point within a star's interior, the internal pressure must be high enough to support the weight of the outer layers. The mass needed to be supported changes as a decreasing function of the distance r from the centre and therefore, so too must the internal pressure.

$$\frac{dP(r)}{dr} = -\frac{GM(r)\rho(r)}{r^2} \tag{1.1}$$

Here, $P(r)$ is the total gas pressure at the radial distance r, G is the gravitational constant, $\rho(r)$ is the density at the distance r and $M(r)$ is the mass contained inside the sphere of radius r. The condition given above is known as hydrostatic equilibrium and must be satisfied in order to support the star against further gravitational collapse. However, a further condition, known as thermal equilibrium, must also be satisfied. Thermal equilibrium in this case is not that all parts of the star are the same temperature but instead that the energy lost at the surface must be replaced by energy released in nuclear reactions occurring throughout the stellar interior. Consequently, it follows that the energy balance must also be satisfied everywhere within the star, as energy gradients in the stellar interior would cause instability leading to gravitational collapse. This condition can be expressed as

$$\frac{dL(r)}{dr} = \epsilon(r)\rho(r)4\pi r^2, \tag{1.2}$$

where $L(r)$ is the energy flux through a sphere with radius r and $\epsilon(r)$ is the energy released per gram of stellar matter per second.

These two conditions ensure the star's stability over long time periods and allow it to continue along its evolutionary path of nuclear burning, which is known as the main sequence and makes up most of the star's lifespan.

1.2.2 The Main Sequence

The life of the star starts on the main sequence when hydrostatic hydrogen burning is achieved in the core. The basic concept of the hydrogen-burning process involves the fusion of four ^{1}H nuclei to form the tightly bound ^{4}He nucleus, producing a net energy release of 26.731 MeV. It was clear, however, that the probability for the simultaneous interaction of four protons in the stellar plasma is far too small to account for the observed luminosity of stars. Consequently, it was suggested that two principal sequences of nuclear reactions, involving

two particle entrance channels, are responsible for the conversion of hydrogen to helium in stars [1; 2; 3].

In stars with masses below $\sim 2\ M_{\odot}$, hydrogen fusion proceeds predominantly via a sequence of nuclear reactions known as the *pp* chains, while more massive stars predominantly burn hydrogen via a further set of reactions called the CNO cycles. These processes, originally suggested in the late 1930s, will continue as the main source of energy within the star until nearly all of its hydrogen fuel is expended.

1.2.2.1 The *pp* Chains

The three sequences of nuclear reactions involved in the proton-proton (*pp*) chains and are shown in Fig. 1.3. It can be seen that the result of the first two

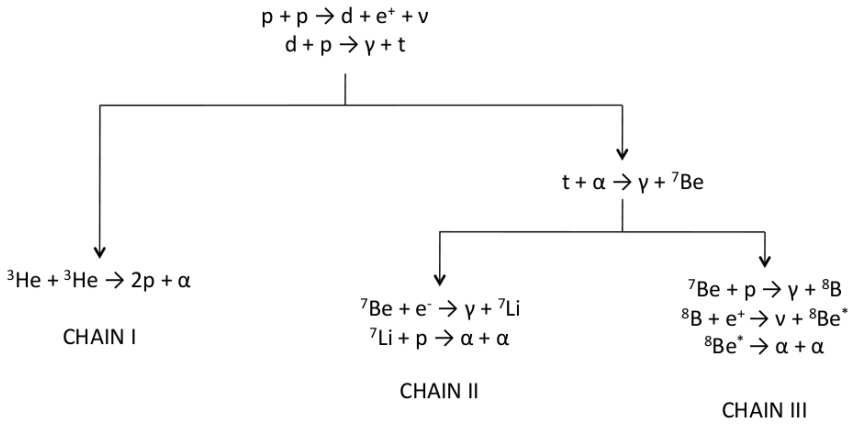

Figure 1.3: Schematic representation of the three possible chains of reactions through the *pp* process.

reactions, common to all chains, is the production of ^{3}He nuclei. The destruction of ^{3}He and the completion of four protons to one ^{4}He nucleus is then achieved via the ^{3}He(^{3}He, $2p$)^{4}He reaction in the *pp*-I chain. However, if the star contains significant ^{4}He derived from the ashes of previous stars, or synthesized through the operation of the *pp*-I chain, then the ^{3}He nuclei may also be burned through the ^{3}He(^{4}He, γ)^{7}Be capture reaction. This opens the *pp*-II and *pp*-III chain reaction paths and in this case, all three *pp* chains will operate simultaneously. The energy produced in each chain is identical but the amount of energy carried

away by the escaping neutrinos differs for each. Furthermore, the contribution of the each chain to the overall energy production and nucleosynthesis will depend upon the stellar temperature, density and composition.

1.2.2.2 The CNO Cycles

If a star is composed exclusively of hydrogen and helium, then energy production will proceed solely through the operation of the *pp* chains. Most stars, however, consist of gas that contains heavier elements, mainly in the C, N and O mass regions. These nuclides can participate in the hydrostatic burning of hydrogen

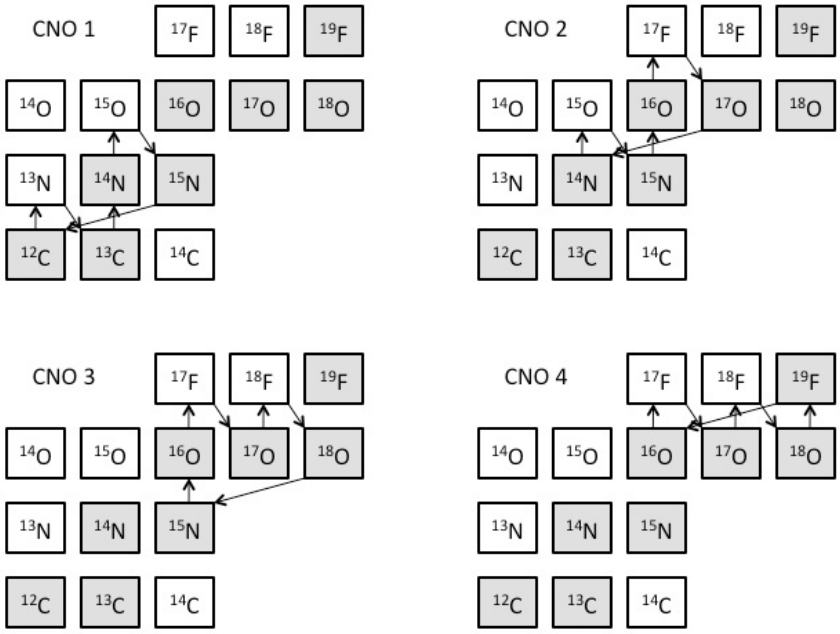

Figure 1.4: Representation of the four CNO cycles in the chart of nuclides. Stable nuclides are shown as shaded squares.

and consequently, the resulting four sets of reactions through which hydrogen can be converted to helium are referred to as the CNO cycles, shown in Fig. 1.4 [17].

The overall outcome of the CNO cycles is identical to that of the *pp* chains, with the conversion of four protons into one ^{4}He nucleus. In each cycle, the heavier nuclei involved can simply be thought of as catalysts, with their relative abundances remaining unchanged. Therefore, a substantial amount of energy

can be generated even if the total abundance of the heavy nuclei is relatively low.

1.2.2.3 Other Cycles

In massive population I stars, which obtain a sufficiently high core temperature and contain pre-existing seed nuclei with masses $A \geq 20$, hydrostatic hydrogen burning will not only involve nuclei in the CNO mass range, but these heavier nuclei as well. In this situation the conversion of hydrogen to helium most

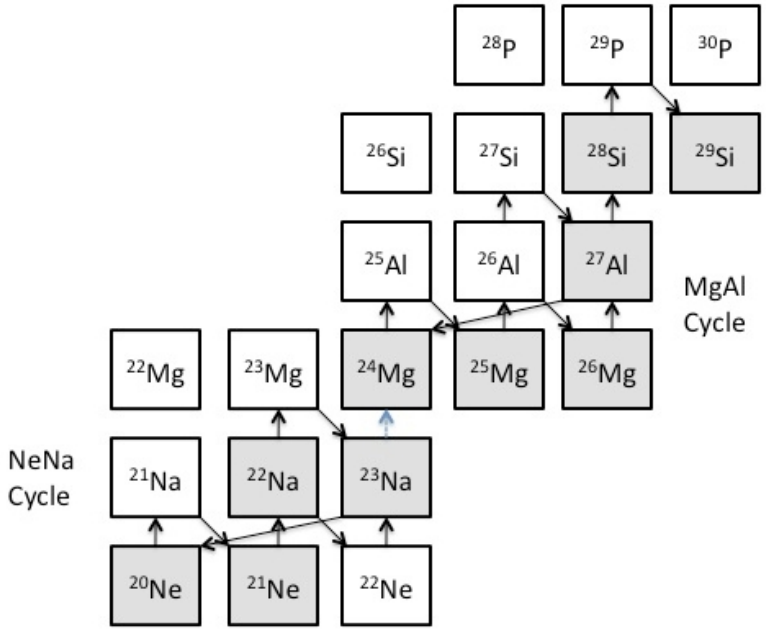

Figure 1.5: Nuclear reactions in the mass $A \geq 20$ region during hydrostatic hydrogen burning, Stable nuclides are shown as shaded squares.

likely proceeds through the NeNa and MgAl cycles, which are shown in Fig. 1.5 [17]. It should be noted that although these nuclear reaction sequences play an important role for the nucleosynthesis of elements between ^{20}Ne and ^{27}Al, the higher Coulomb barriers involved make both cycles relatively unimportant as sources of additional energy in stars.

1.2.3 The Fate of the Stars

Once nearly all of a star's hydrogen fuel has been exhausted, the star will be located at the bluest and hottest point on the main sequence, known as the "turn-off point". The subsequent fate of the star from this point will depend strongly on its initial mass.

1.2.3.1 Initial Mass 0.4 $M_\odot \lesssim M \lesssim 2\ M_\odot$

With, now, a predominantly helium core and a vastly depleted supply of hydrogen, the star resumes its gravitational contraction to generate the energy no longer provided by nuclear processes. The temperature of the star increases until nuclear reactions are re-established in a thin shell of hydrogen surrounding core, at which point contraction is ceased. In this state the core produces too much energy to be radiated away through this layer of nuclear burning and thus, the layers surrounding the core expand and cool and a "red giant" star is formed. As the star ascends the red giant branch (RGB), the luminosity increases continuously. Maximum luminosity is achieved at the tip of the RGB ∼0.6 Gy after the star left the main sequence. During the red giant phase of evolution the star experiences significant mass loss and the subsequent contraction of the core increases the central temperature and density by factors of 10 and 10^4, respectively. This eventually results in an electron degenerate core composed predominantly of helium.

When the core temperature reaches ∼ 0.1 GK, helium starts to fuse to carbon via the triple α-reaction. This reaction is a two-step process [18] and in the first step, two α-particles interact to form ^{8}Be in its ground state. Although the nucleus ^{8}Be is unstable and decays back into two α-particles with a half-life of 6.7 x 10^{-17}s [19], over time, a small concentration of ^{8}Be will build up until the rate of ^{8}Be formation becomes equal to its decay rate,

$$^4He +^4 He \longleftrightarrow^8 Be \tag{1.3}$$

In the second step, a third α-particle interacts with the ^{8}Be nucleus to form ^{12}C via the resonant reaction [5],

$$^8Be +^4 He \longrightarrow^{12} C^* + \gamma \tag{1.4}$$

Once the stable ^{12}C nucleus is formed, further ^{4}He capture reactions can occur to form heavier elements such as; ^{16}O, ^{20}Ne, ^{24}Mg, ^{28}Si, and so on. However,

since the α-capture reaction $^{16}O(\alpha,\gamma)^{20}Ne$ is a very slow process, the helium is mainly converted into ^{12}C and ^{16}O. This sequence of nuclear reactions is referred to as helium burning and, at this stage of nuclear burning, small increases in temperature result in very large increases in the energy generation rate of the star. This increase in energy would normally be compensated for by an expansion, however, in a degenerate gas the increase in temperature does not affect the pressure, no expansion occurs, the gas becomes highly explosive and the star experiences detonations, often referred to as "helium flashes".

Eventually the star becomes a "horizontal branch" star, quietly burning helium in the core. The nuclear energy release in helium fusion is considerably less compared to hydrogen fusion. Therefore, the duration of the core helium burning stage is much shorter than that of the core hydrogen burning stage and the star remains on the horizontal branch for about 0.1 Gy.

When the helium in the core is exhausted, the core contracts again, heats up and ignites the helium in a surrounding shell. The star now burns helium in a shell surrounding the carbon-oxygen core and hydrogen in a shell surrounding the helium burning region. This stage of stellar evolution is known as the "asymptotic giant branch" (AGB) and while the star ascends the asymptotic giant branch, the energy is not generated at a steady rate, but the hydrogen and helium burning shell alternate as the major contributor to the overall luminosity. Hydrogen burning adds continuously to the mass of the helium zone so that the temperature and density near this zone rise until the rate of energy generation of helium burning is larger than the rate at which it can be radiated away by diffusion. As a result, a thermonuclear runaway occurs. The sudden release of energy pushes out and cools the hydrogen burning shell until it ceases to burn, at which point the helium burning shell is now the major source of energy. Eventually, the expansion quenches the helium shell flash (or thermal pulse) and the star contracts again. The hydrogen burning shell reignites and ultimately takes over as the dominant nuclear energy source, until the next thermal pulse occurs about 10^5 y later. It should be noted that the cycle may repeat many times but the total amount of time the star spends on the AGB amounts to only about 20 My.

At some point on the AGB, the star suffers an episode of significant mass loss via a strong stellar wind. With only a fraction of its initial mass left and the other part returned to the interstellar medium, thermal pulses cease and

the star becomes a post-asymptotic giant branch star (P-AGB). As more of the hydrogen envelope is ejected into space, hotter layers are uncovered and the surface temperature of the star increases. When the surface of the star becomes hot enough, the intense ultraviolet radiation ionizes the expanding ejecta, which, in turn, begin to fluoresce brightly as a "planetary nebula". Once there is no hydrogen envelope left and the hydrogen burning shell extinguishes, a core remnant is left, composed mainly of carbon and oxygen, in which all thermonuclear reactions have ceased, and is known as a "white dwarf". An extremely slow cooling process is then undertaken ($\sim$ 500 Gy) until the star finally dies as a "black dwarf".

1.2.3.2 Initial Mass 2 $M_\odot \lesssim M \lesssim$ 11 $M_\odot$

The fate of stars with initial masses of $M \gtrsim 2\ M_\odot$, although somewhat accelerated, occurs through very much the same evolutionary process described above. A major difference, however, arises from the fact that for stars with $M \gtrsim 2\ M_\odot$ the helium core during the RGB phase does not become electron degenerate. Therefore, a helium flash does not occur but instead helium ignites quiescently in the centre.

1.2.3.3 Initial Mass $\gtrsim$ 11 $M_\odot$

The total nuclear burning lifetime of stars with initial masses $\gtrsim 11\ M_\odot$ is relatively short, in comparison to those previously discussed ($\sim$ 7 My). In these cases, once the hydrogen in the core is exhausted and the core contracts igniting helium, the outer layers of the star are greatly expanded and a "super giant" star is formed. The temperatures reached in super giant stars allow helium burning to occur under non-degenerate conditions and eventually the core becomes hot enough for the fusion of carbon nuclei (carbon burning). In fact, such massive stars are capable of igniting successive burning stages in their cores using the ashes of the previous core burning stage as fuel (neon burning, oxygen burning and silicon burning). The endpoint of elemental synthesis from nuclear burning within massive stars is represented by the iron peak nuclei, owing to the fact further fusion reactions are not energetically favourable. However, some of the heavy nuclides with masses $A \geq 60$ may be synthesized, during the super giant phase of evolution, through a series of neutron captures known as the *s* (for

slow) process [6]. A detailed discussion of this process will not be presented here.

The approximate structure of the star after silicon has been exhausted in the core is shown in Fig. 1.6 [20]. It should also be noted that the luminosity

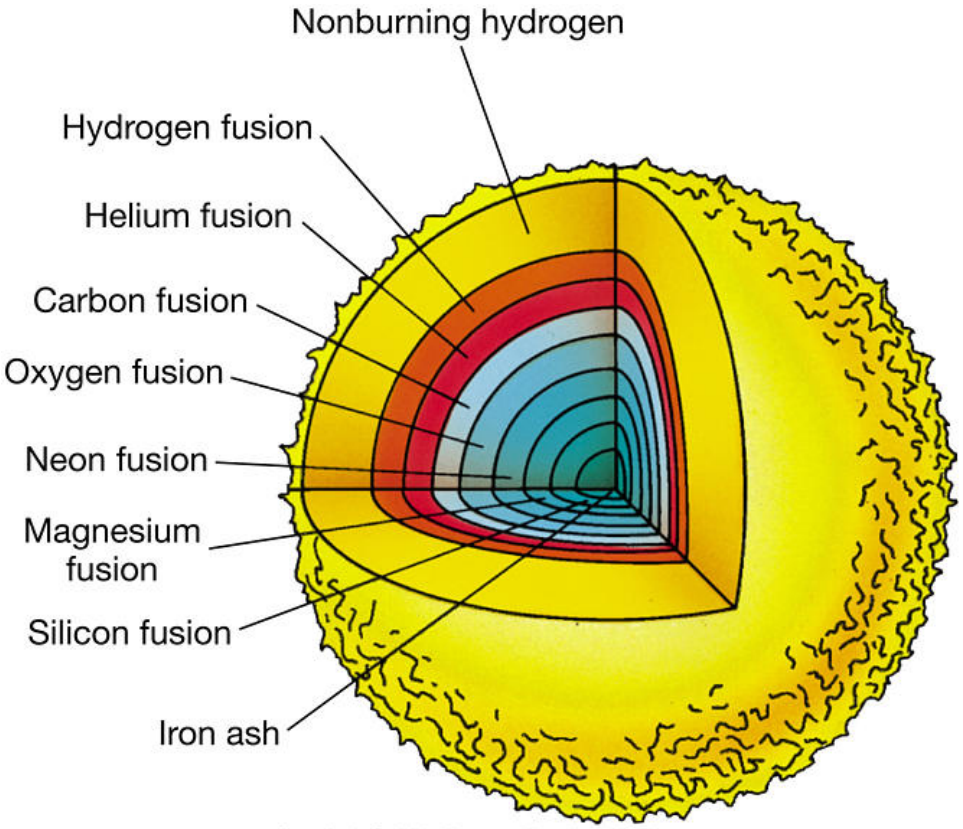

Figure 1.6: Cross section of a star in its super giant phase of stellar evolution [20].

during the red giant phase is so large that the star undergoes a significant mass loss. The effect is more pronounced for stars with M $\gtrsim$ 30–35 $M_\odot$ that lose eventually most of their hydrogen envelope. The observational counterparts of such stars are the hot and massive "Wolf-Rayet" stars, shown in Fig. 1.7 [21], which have been observed to lose mass at a rate of $\sim 10^{-5}$ $M_\odot$ per year at stellar wind speeds of $\sim$ 2000 kms^{-1}.

With no further sources of nuclear energy and the contributions of nuclear ashes from the overlying nuclear burning shells, the electron degenerate core begins to grow in mass. Once the mass of the core exceeds the Chandrasekhar limit

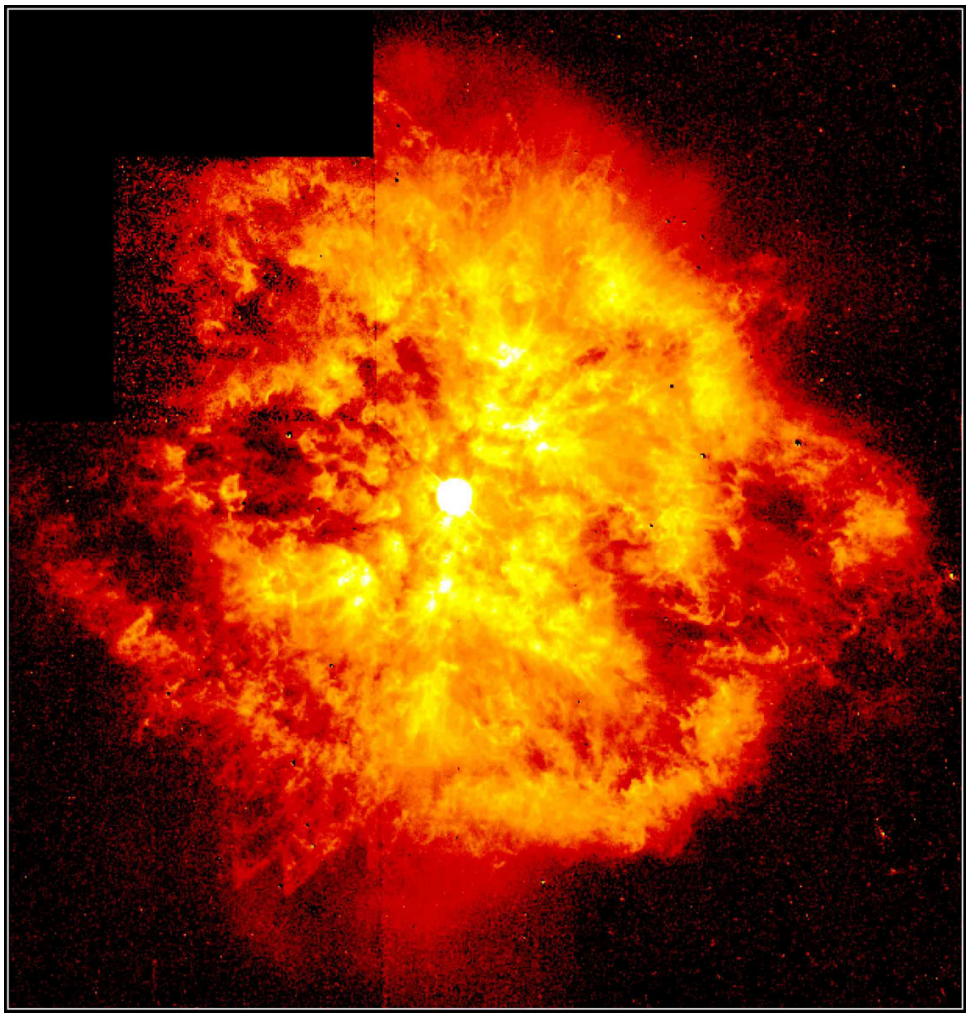

Figure 1.7: The nebula M1-67 surrounding the Wolf-Rayet star WR 124, located in the constellation Sagittarius [21].

($\sim 1.4\ M_\odot$), the electron degeneracy pressure is unable to counteract gravity, and the core collapses. As the core of a massive star collapses, photo-disintegration of iron nuclei and electron capture occur, removing electrons from the gas and consuming energy. Both effects speed up the collapse, and vasts amounts of energy are lost to the star by escaping neutrinos. These energy losses can only be compensated for by an extremely rapid gravitational collapse of the iron core, leading to a violent stellar explosion, known as a supernova, in which the star is essentially destroyed except for a possible high-density central core remnant in the form of a neutron star, or a black hole if the star is suitably massive. It is important to mention at this point that the deepest regions of the star ejected into the interstellar medium during such an explosion are characterized by a large abundance of free neutrons. It is expected, therefore, that such events give rise to the nucleosynthesis of many heavy nuclei in the $A > 60$ mass range via another set of neutron capture reactions known as the r (for rapid) process [6]. Again the details of which shall not be discussed here.

The above scenario for the core collapse of a massive star is responsible for supernovae of types II, Ib and Ic and ends the present discussion on the evolution of single stars. The different supernova types are classified observationally according to their spectra, in which type II supernovae exhibit strong hydrogen lines while those of type I do not.

1.3 Explosive Hydrogen Burning

Under astrophysical conditions of extreme temperature (≥ 0.06 GK) and density ($\sim 10^3$ g/cm^3), it is possible for the nuclear reactions involved in the CNO cycles to occur on timescales of a few seconds. In such explosive burning scenarios β-unstable nuclei will live long enough to be burned by nuclear reactions before they β-decay and thus, a new cycle of reactions are possible, known as the hot CNO cycles [22]. These hot (or β-limited) CNO cycles are shown in Fig. 1.8 [17].

As with hydrostatic hydrogen burning, the nucleosynthesis of $A \geq 20$ nuclei occurs in explosive hydrogen burning scenarios if pre-existing seed nuclei with masses of $A \geq 20$ are present in the stellar environment. The character of the burning, however, changes drastically since proton-induced reactions on short-lived nuclei may successfully compete with their corresponding β^+-decays.

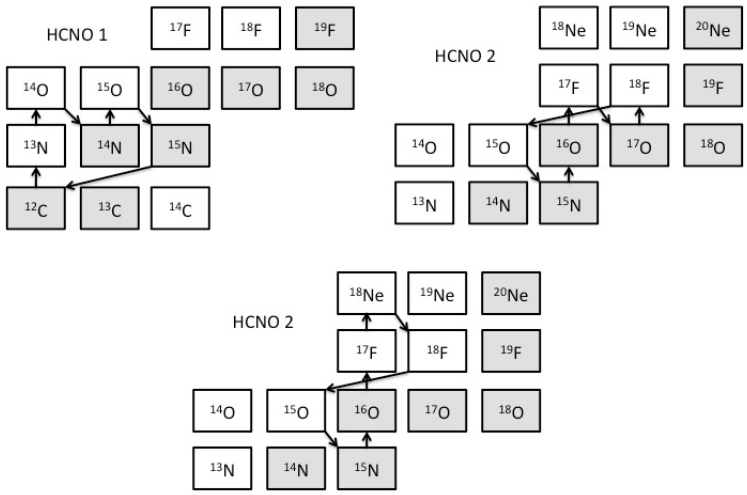

Figure 1.8: Representation of the three hot CNO cycles in the chart of nuclides. Stable nuclides are shown as shaded squares.

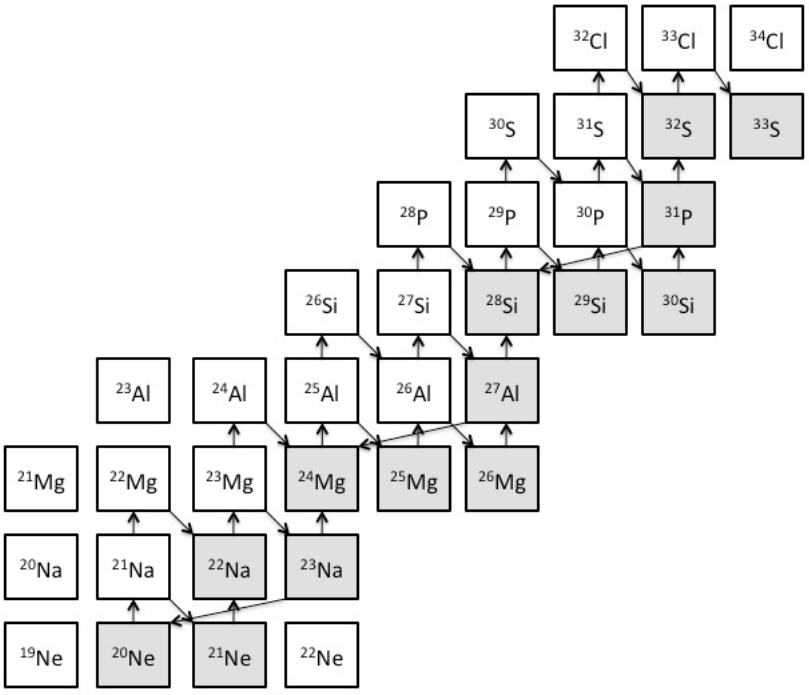

Figure 1.9: Nuclear interactions in the mass region A $\geq$ 20 during explosive hydrogen burning. Stable nuclides are shown as shaded squares.

Therefore, at such elevated temperature stellar environments, these reactions must be taken into account in determining the resulting nucleosynthetic path, which is shown in Fig. 1.9 [17].

Explosive hydrogen burning can take place in a number of astrophysical sites, the most notable of which are cataclysmic stellar binary systems.

1.4 Binary Systems

According to recent estimates nearly half of all stars in the Galaxy are members of binary systems. In considering a binary system, we must first define the Roche surface, a figure eight equipotential surface situated around a point between the two stars where the gravitational potentials are equal. When one of the stars evolves off the main sequence and becomes a red giant, the entire star may fill its Roche lobe and transfer material to its binary companion. Many different kinds of stars may be members of binary systems and the transfer of mass from one star to another leads to astrophysically interesting phenomena.

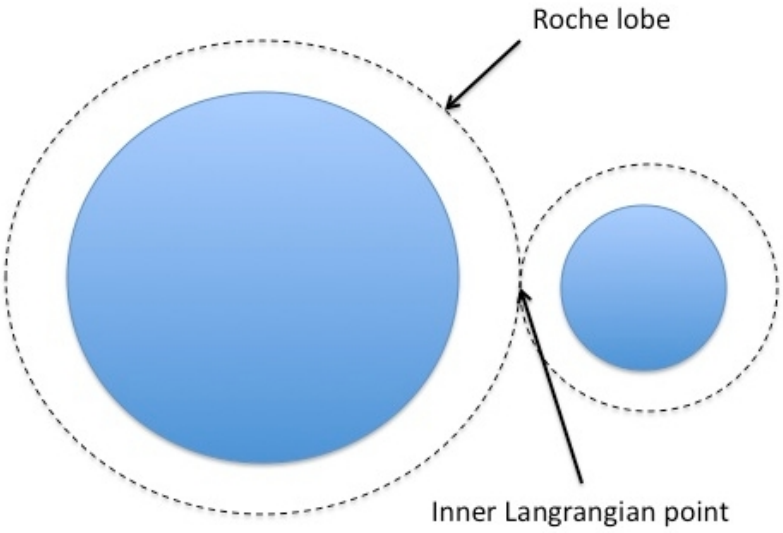

Figure 1.10: Diagrammatical representation of a binary star system. Each star is surrounded by a hypothetical surface that marks its gravitational domain, called the Roche lobe. The location where the two Roche lobes touch is called the inner Lagrangian point.

1.4.1 Classical Novae

A classical nova event is understood to occur in a close stellar binary system, comprising of a low-mass red dwarf star and a companion white dwarf star [23]. Hydrogen-rich material from the red dwarf star exits through the inner Lagrange point, where it initially forms an accretion disk surrounding the white dwarf. A proportion of matter from the base of the accretion layer spirals inward and accumulates on the white dwarf surface, where it is heated and compressed by the strong surface gravity. This fraction of matter has, at some point, become electron degenerate during its fall to the white dwarf surface and thus, as the accretion process continues, the white dwarf is prevented from cooling through expansion and an extremely high surface temperature is reached. At such high temperatures, the addition of hydrogen to the heavier elements already present on the white dwarf, allows explosive hydrogen burning thermonuclear reactions to take place. This thermonuclear runaway takes place below the surface of the white dwarf where the abundances of both carbon and hydrogen are large, and the convective zone that is then formed mixes heavy elements to the surface. Once a sufficient amount of energy has been released, a sudden lift in the degeneracy leads to an explosive mass ejection into the interstellar medium, which is expected to recur with periods of $\sim 10^4$–10^5 years. An artistic impression of

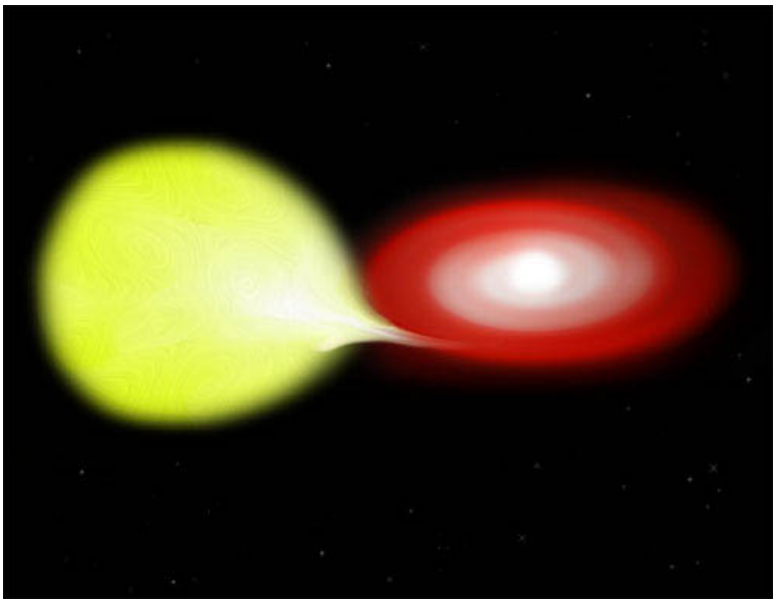

Figure 1.11: An artist's depiction of a classical novae event [24].

a classical nova event is shown in Fig. 1.11 [24].

Data from the optical, ultraviolet and infrared spectra of classical novae ejecta have been used to determine the elemental abundances present in the expanding nova shells. The enhancement with respect to solar abundances in carbon and oxygen elements found in the majority of nova ejecta demonstrates that at some time during the evolution of the outburst the accreted material must have mixed to a certain degree with matter from a white dwarf, composed predominantly of carbon and oxygen. These particular events are known as carbon-oxygen (CO) novae and a typically observed abundance spectrum is shown in Fig. 1.12 [25]. In addition to the most common CO novae described

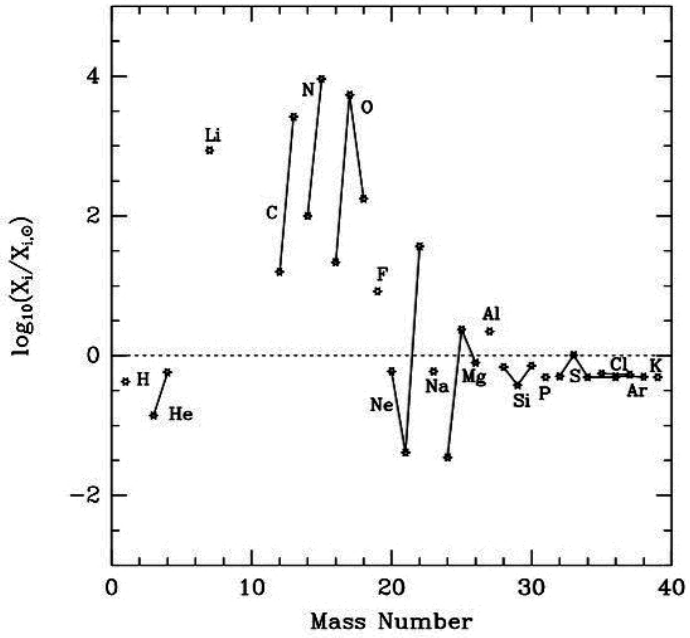

Figure 1.12: Mean overproduction factors, relative to solar, in the ejecta of a 1.15 $M_\odot$ CO novae.

above, around 1/4 of novae events, show ejecta strongly enriched in neon. These stellar events are known as oxygen-neon (ONe) novae and are expected to involve a more massive companion white dwarf star composed predominantly of oxygen and neon (the end result of a progenitor star with initial mass of 9–11 $M_\odot$). Typical abundance spectra for ONe novae events, displayed in Fig. 1.13 [25], show that a larger nuclear activity than CO novae occurs, extending up to

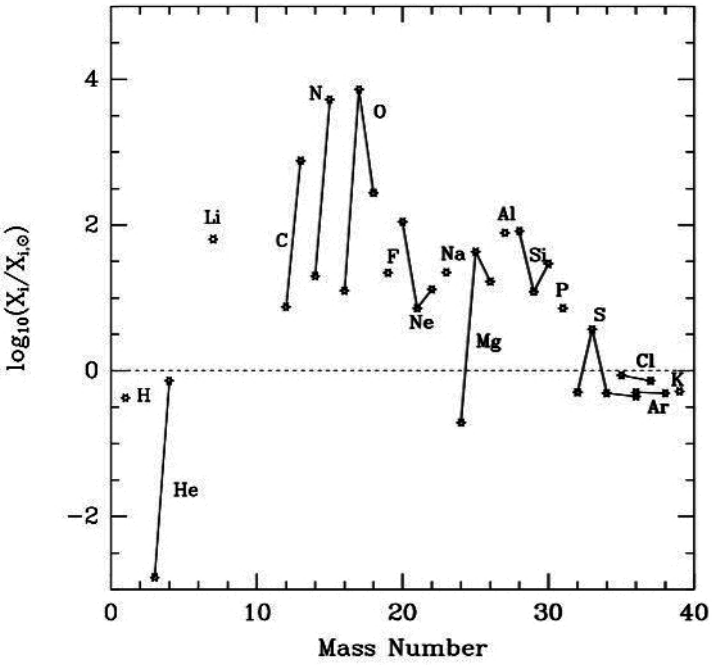

Figure 1.13: Mean overproduction factors, relative to solar, in the ejecta of a 1.15 $M_\odot$ ONe novae.

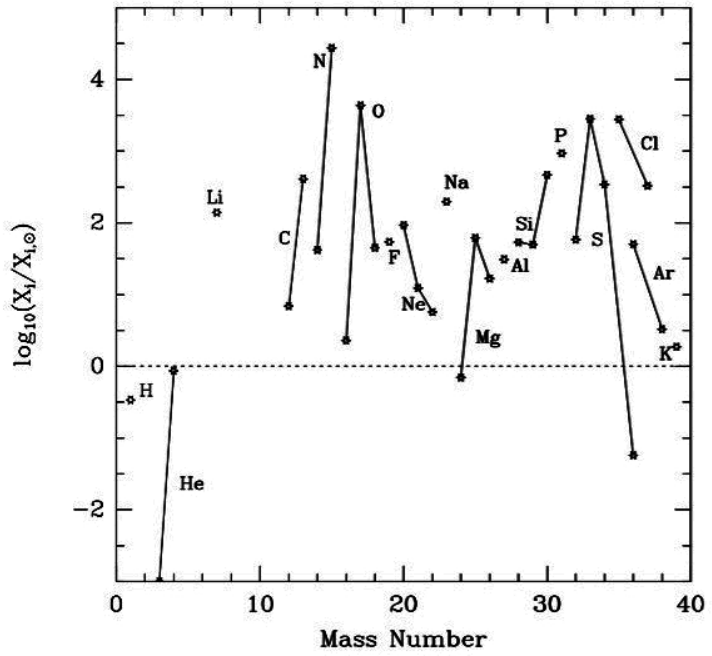

Figure 1.14: Mean overproduction factors, relative to solar, in the ejecta of a 1.35 $M_\odot$ ONe novae.

silicon or argon. Such observations support the presence of heavier element seed nuclei (*e.g.* Ne and Mg) and suggest that higher peak temperatures are reached in ONe novae (T_{peak}∼0.4 GK) compared to those of CO novae (T_{peak}∼0.2 GK).

1.4.2 X-ray Bursts

Although classical novae are of the most importance in the present thesis work, for completeness, an additional special case for explosive stellar nucleosynthesis will be discussed here, in which the close binary system involves a neutron star as the compact companion star [26]. Again, as with novae, a degenerate accretion scenario is formed but due to the much greater gravitational potential, in which the material falls through, nuclear burning starts at comparatively greater density (ρ∼10^6–10^8 g/cm^3) and the layer in which thermonuclear reactions occur in the neutron star can achieve much higher temperatures (T∼0.7–1.5 GK) before degeneracy is lifted. The mass ejection explosions in this case are characterized by strong x-ray activity and are hence known as x-ray bursters.

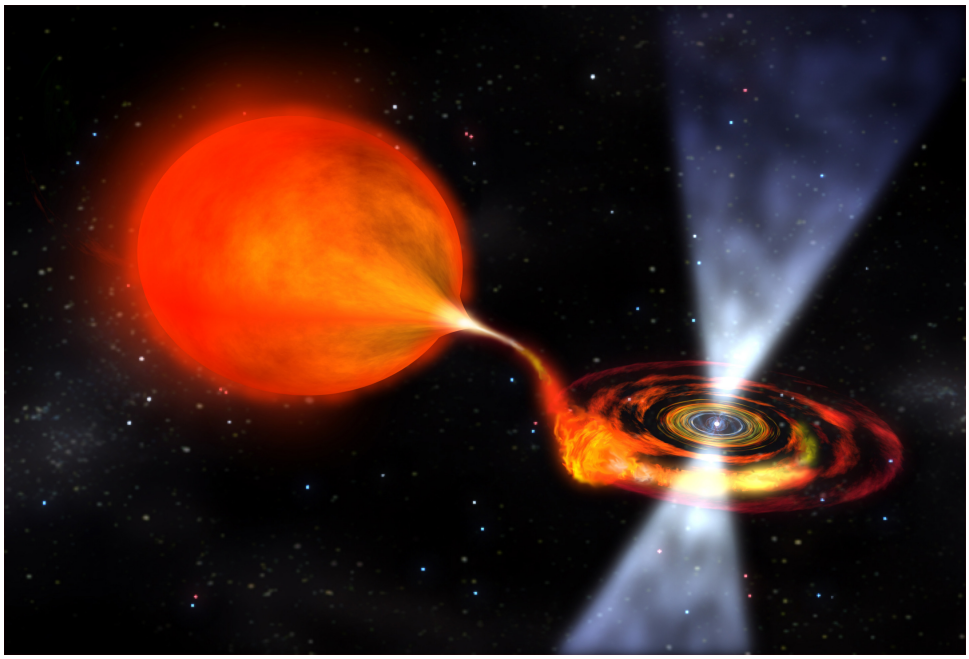

Figure 1.15: An artist's depiction of an x-ray burster scenario [24].

At the very high temperatures ≥ 0.5 GK, readily obtained in x-ray burster scenarios, it is expected that alpha-capture reactions on ^{15}O and ^{18}Ne isotopes

can proceed favourably. These reactions provide a means of "breakout" of the hot CNO cycles to the *rp* (for rapid proton) process, in which heavier radioisotopes between the line of stability and the proton drip line are synthesized by a rapid succession of proton capture reactions. This process is capable of synthesizing elements beyond the iron peak and only occurs in the most extreme high-temperature astrophysical environments.

However, it should be noted that it is unlikely that any significant amount of accreted and processed matter to escapes the large gravitational potential of the neutron star. Therefore, X-ray bursts are not expected to be important contributors to the chemical evolution of the Galaxy.

1.5 Nuclear Reactions of Interest in Novae

In order to improve our understanding of the observed galactic elemental abundances, it is important to identify the astrophysical production sites from which they originate. Classical novae are among the most frequent and violent stellar events to contribute to the chemical evolution of the Galaxy and thus, are expected to influence a number of the observed elemental abundances. Furthermore, it is also believed that radioactive isotopes are also synthesized in nova outbursts, the decays of which may be the source of γ-ray radiation signatures observed throughout the interstellar medium and the specific excess elemental masses observed in meteorites. Therefore, a detailed knowledge of the nucleosynthetic path followed, and hence the rates of the specific reactions involved, in novae scenarios is required. In the present work we have investigated the astrophysical ^{23}Mg$(p,\gamma)^{24}$Al and ^{26}Al$(p,\gamma)^{27}$Si reactions, both of which are expected to proceed favourably in classical novae environments, influencing the overall abundances of a number of isotopes in novae ejecta.

1.5.1 The ^{23}Mg$(p,\gamma)^{24}$Al Reaction

At low stellar temperatures the nuclear reaction path of $A \geq 20$ nuclei initially proceeds through the NeNa cycle: ^{20}Ne$(p,\gamma)^{21}$Na$(p,\gamma)^{22}$Mg$(\beta^+\nu)^{22}$Na$(p,\gamma)^{23}$Mg $(\beta^+\nu)^{23}$Na$(p,\alpha)^{20}$Ne. In the low temperature limit this reaction sequence is closed due to the β^+ decay of ^{23}Mg to ^{23}Na, followed by the ^{23}Na$(p,\alpha)^{20}$Ne reaction. However, at higher stellar temperatures $\geq$ 0.1 GK, such as those found in explosive environments, the proton capture reaction on ^{23}Mg becomes

faster than the competing β decay and thus provides a nucleosynthetic path to a whole range of heavier nuclei (Fig. 1.5). This "breakout" of the NeNa cycle into the MgAl cycle, via the ^{23}Mg$(p,\gamma)^{24}$Al reaction, is expected to predominantly occur in classical novae scenarios as at the very high temperatures, above 1 GK, attained in X-ray bursts, the production of the isotope ^{23}Mg is bypassed via the reaction sequence ^{21}Na$(p,\gamma)^{22}$Mg$(p,\gamma)^{23}$Al$(p,\gamma)^{24}$Si$(\beta^+\,\nu)^{24}$Al, rendering the ^{23}Mg$(p,\gamma)^{24}$Al reaction superfluous.

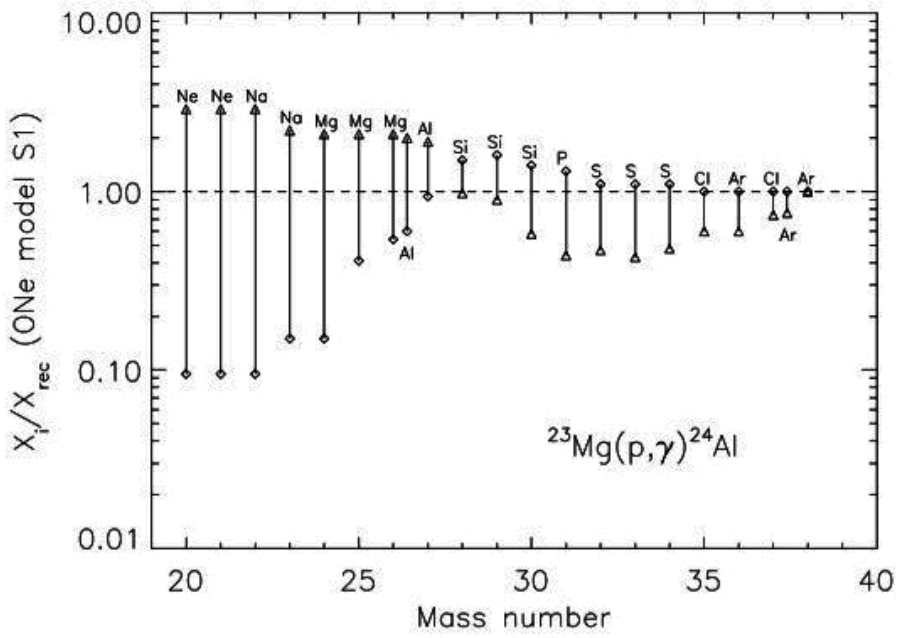

Figure 1.16: Factor change $X_i/X_{i,rec}$, in final isotopic abundance as a result of varying the ^{23}Mg$(p,\ \gamma)^{24}$Al reaction rate within its associated errors vs. mass number [27].

In recent years, theoretical models of nucleosynthesis in classical novae have been used to estimate the impact of nuclear reaction rate uncertainties on final nova yields [25; 27]. The most detailed approach of this kind was performed by Iliadis *et al.* [27] covering peak temperatures in the range $T = 0.2$–0.4 GK. This analysis varied 175 different reactions within their associated errors and yet only a restricted number of reactions were highlighted as having a significant influence on the final isotopic abundances. The ^{23}Mg$(p,\gamma)^{24}$Al reaction was one such highlighted reaction and it was noted that the significant uncertainty still

present in the stellar reaction rate will influence the final isotopic abundances of ^{20}Ne, ^{21}Ne, ^{22}Na, ^{23}Na and ^{24}Mg in ONe novae ejecta, as shown in Fig. 1.16 [27]. Consequently, an accurate determination of the rate is needed in order to better model nucleosynthesis of $A > 20$ nuclei in ONe novae.

1.5.2 The ^{26}Al$(p,\gamma)^{27}$Si Reaction

The nucleus ^{26}Al may be produced in a number of nucleosynthetic environments and has been previously observed in two very different cosmological studies.

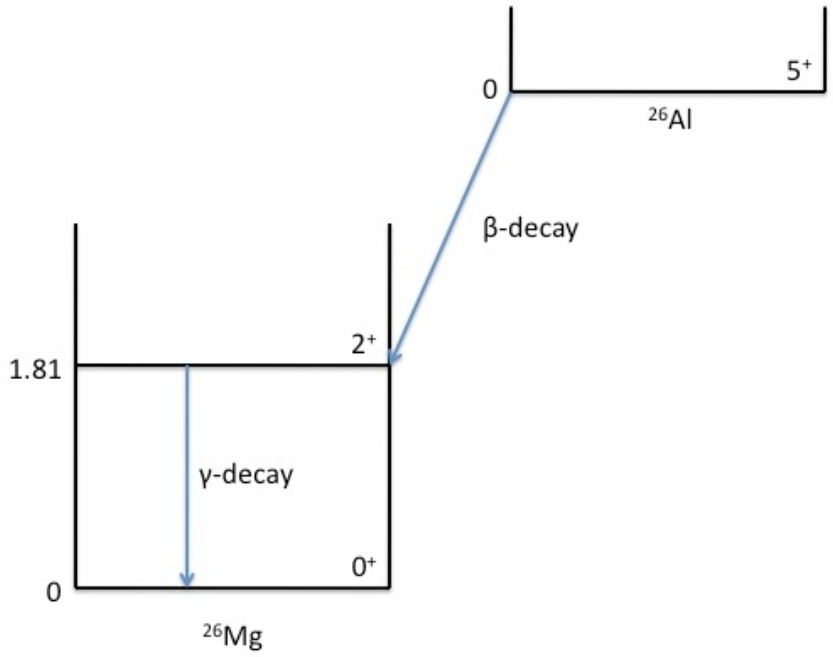

Figure 1.17: β decay of ^{26}Al and γ decay of ^{26}Mg.

The first strong evidence for the stellar nucleosynthesis of ^{26}Al came from the study of the inclusions in meteorites produced at the formation of the solar system [28]. Given its relatively short lifetime ($t_{1/2}$ = 7.2x10^5 y), if ^{26}Al was part of a particular meteoritic inclusion, when it was formed billions of years ago, it will have long ago decayed away. However, the nucleus ^{26}Al β decays to the stable nucleus ^{26}Mg and consequently, its presence within the meteoritic inclusion may be deduced from an increase in the relative ^{26}Mg abundance. In 1976 Lee *et al.* [28] used sensitive mass spectrometry techniques to determine

the excess elemental masses of meteoritic inclusions and observed a significant overabundance of ^{26}Mg. This discovery indicated that the meteorite itself must have, at some point, contained a notable fraction of ^{26}Al.

The second, even more striking evidence for the stellar nucleosynthesis of ^{26}Al came in 1983, when the HEAO-3 satellite detected its characteristic γ-ray signature at 1.809 MeV [29]. This was the first γ-ray line ever observed in the interstellar medium and provided clear evidence of continuing nucleosynthesis in the Milky Way Galaxy [30]. Since this discovery, state-of-the-art space-based γ-ray observatories have been employed to ascertain the galactic origin of ^{26}Al. The COMPTEL all-sky map of the 1.809 MeV γ-ray line, shown in Fig. 1.18, reported irregular emission along the galactic plane, suggesting a galaxy-wide origin dominated by high-mass progenitors, such as core collapse supernovae and Wolf-Rayet stars [31]. Recent observations by the RHESSI and INTEGRAL

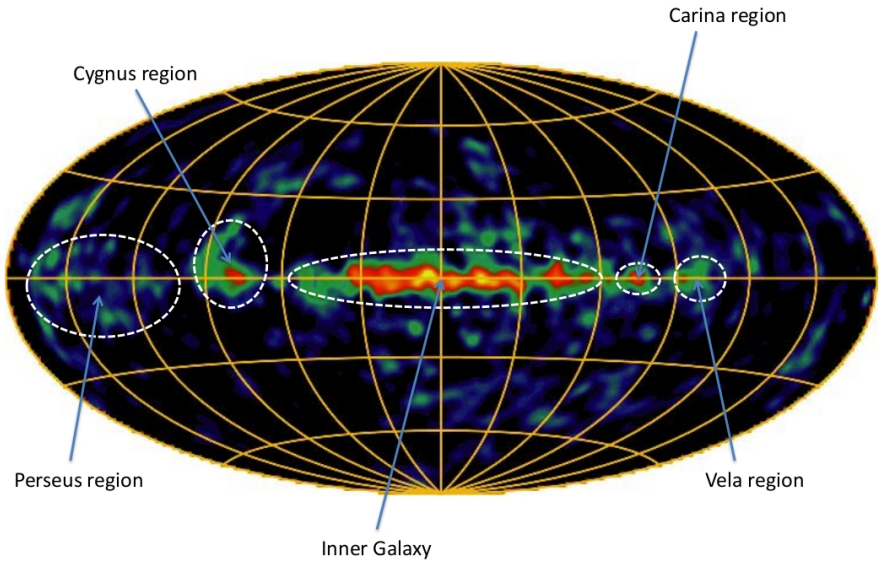

Figure 1.18: COMPTEL all-sky map of the 1.809 MeV γ-ray line.

satellites indicate that core collapse supernovae may have a much less dominant component than initially expected [32] and suggest that Wolf-Rayet stars are the likely dominant astrophysical source of ^{26}Al [33; 34]. However, classical novae are also one potential source of ^{26}Al and it has been shown that these stellar environments may contribute to up to 0.4 $M_{\odot}$ of the observed galactic abundance

(presently measured at 2.8(8) M$\odot$) [35]. Under such astrophysical conditions, the ^{26}Al$(p,\gamma)^{27}$Si reaction is expected to govern the destruction of ^{26}Al and as a result it has been the subject of considerable study over the past two decades [35; 36; 37; 38; 39; 40; 41; 42; 43]. The ^{26}Al$(p,\gamma)^{27}$Si reaction rate still remains uncertain at low stellar temperatures [37; 41] and it has been suggested that large variations in the rate in this temperature region may significantly reduce the amount of ^{26}Al synthesized in novae scenarios [39]. Thus, a reevaluation of the resonant rate in the low temperature region is needed in order to better determine the amount of ^{26}Al synthesized in novae scenarios.

Chapter 2

Thermonuclear Reaction Rates

An in depth knowledge of thermonuclear reactions, and in particular thermonuclear reaction rates, plays a key role in our understanding of the energy production and nucleosynthesis of elements in stars. As discussed in the previous chapter, nuclear reactions are responsible for the liberation of kinetic energy, at the expense of mass, in stars. These same nuclear reactions slowly change the chemical composition of the stellar interior and allow the structure of the star to evolve. If, after a finite lifetime, a star ejects all or part of its mass into space, the chemical composition of the interstellar medium will have been altered by the thermonuclear debris. Consequently, as almost all of the elements found in our Galaxy have been synthesized in stars, it follows that determinations of thermonuclear reaction rates lie at the focal point in the study of stellar nucleosynthesis. In this chapter, we discuss the general properties of thermonuclear reactions and present an analytical formalism for the determination of stellar reaction rates [17; 44].

2.1 Kinematics and Energetics

The simplest type of nuclear reaction, where a particle "a" strikes a nucleus "X" producing a nucleus "Y" and a new particle "b", may be expressed as

$$a + X \rightarrow Y + b \tag{2.1}$$

or

$$X(a, b)Y. \tag{2.2}$$

If the entrance channel reactants "a" and "X" have ground state atomic masses M_a and M_X, and the exit channel products "b" and "Y" have ground state atomic masses M_b and M_Y, then by conservation of energy we may define the energy released in a nuclear reaction, Q, as,

$$Q = (M_a + M_X - M_b - M_Y)c^2. \tag{2.3}$$

This is known as the reaction Q-value. If the Q-value is positive, there is a net production of energy in the reaction and the reaction is said to be exothermic. Conversely, if the Q-value is negative, a minimum energy equal to Q has to be provided to make the process go and the reaction is said to be endothermic. It should also be noted, here, that if the reaction in question reaches excited states of Y, the Q-value equation should include the mass energy of the excited state,

$$Q_{ex} = (M_a + M_X - M_b - M_Y^*)c^2 = Q - E_{ex}, \tag{2.4}$$

where Q is the Q-value corresponding to the ground state of Y and E_{ex}=$M_Y^*c^2$-M_Yc^2 is the excitation energy of the nucleus Y above the ground state. A large collection of nuclear reaction Q-values are known and tabulated in the 2003 atomic mass tables [19].

Additional useful properties, that are often tabulated, are the neutron and proton separation energies of atomic nuclei. The "neutron separation energy" S_n is the amount of energy that is needed to remove a single neutron from a given nucleus,

$$S_n = (M_A + M_n - M_Y)c^2, \tag{2.5}$$

where M_n is the mass of the neutron. Similarly, the "proton separation energy" S_p is the amount of energy that is needed to remove a single proton from a given nucleus,

$$S_p = (M_A + M_p - M_Y)c^2, \tag{2.6}$$

where M_p is the mass of the proton.

In this thesis work we have focused on radiative proton capture reactions, $X(p,\gamma)Y$, in which the projectile proton is absorbed by the target nucleus "X", emitting γ-ray radiation and forming the nucleus "Y". These reactions are among the most important types of reactions occurring in explosive stellar environments and in such cases, the proton separation energy is equal to the excitation energy above which proton-decay is energetically favourable in the nucleus

Y. This is also known as the proton threshold energy and is useful in determining which excited states are likely to be of astrophysical interest in proton radiative capture reactions.

2.2 Cross Sections and Stellar Reaction Rates

Although the reaction Q-value yields the energy liberated by each nuclear reaction, of importance in stellar environments is the total nuclear energy liberated in a stellar plasma per unit volume. In order to determine the total nuclear energy liberated in a stellar plasma per unit volume, a measure of the probability that a given nuclear reaction will take place is required. A quantitative measure of this probability is called the nuclear reaction cross section σ and in general, nuclear cross sections depend on the relative velocity of the target-plus-projectile system, that is, σ=$\sigma(v)$.

If we consider the reaction $X(a,b)Y$, occurring in a gas consisting of N_X particles per cm^3 of type X and N_a particles per cm^3 of type a, where both "a" and "X" have rest mass and move with a relative velocity v, we obtain an expression for the reaction rate given by,

$$r_{aX}(v) = N_a N_X v\sigma(v). \tag{2.7}$$

In a stellar plasma, as in other gases, the interacting nuclei exhibit a spread of relative velocities, which are described by the probability function $P(v)$,

$$\int_0^\infty P(v)dv = 1. \tag{2.8}$$

In this case we may generalize the reaction rate for a distribution of relative velocities as

$$r_{aX} = N_a N_X \int_0^\infty vP(v)\sigma(v)dv \equiv N_a N_X < \sigma v >_{aX}, \tag{2.9}$$

where $<\sigma v>_{aX}$ is the reaction rate per particle pair and $N_a N_X$ is the total number density of pairs of nonidentical nuclei "a" and "X". It should be noted that in practice, the reaction rate adopts the form

$$r_{aX} \equiv N_A < \sigma v >_{aX}, \tag{2.10}$$

where N_A denotes the Avogadro constant, and r_{aX} is expressed in units of cm^{3}mol^{-1}s^{-1}.

In normal stellar matter the nuclei move non-relativistically and are non-degenerate. Thus, the relative velocities of interacting nuclei in stellar plasmas can be described by a Maxwell-Boltzmann distribution,

$$P(v) = 4\pi v^2 \left(\frac{\mu}{2\pi kT}\right)^{3/2} exp\left(-\frac{\mu v^2}{2kT}\right), \tag{2.11}$$

where T refers to the temperature of the plasma and μ is the reduced mass. Since the numerator in the exponential term represents twice the kinetic energy of the interacting nuclei, it is also possible to express the function $P(v)$ in terms of energy,

$$P(E) \propto Eexp\left(-\frac{E}{kT}\right) \tag{2.12}$$

Incorporating the Maxwellian velocity and energy distributions into equation (2.9) we now obtain for the reaction rate per particle pair,

$$< \sigma v >= \int P(v)\sigma(v)vdv = \int P(E)\sigma(E)vdE \tag{2.13}$$

$$= \left(\frac{8}{\pi\mu}\right)^{1/2} \frac{1}{(kT)^{3/2}} \int_0^\infty \sigma(E)Eexp\left(-\frac{E}{kT}\right) dE. \tag{2.14}$$

From the discussion above, it can be clearly seen that the reaction rate depends critically on the energy dependent cross section $\sigma(E)$, which reflects the reaction mechanism involved and is necessarily different for each nuclear reaction.

2.3 Non-resonant and Resonant Thermonuclear Reactions

Once the cross section $\sigma(E)$ has either been measured or estimated theoretically, the reaction rate $<\sigma v>$ can always be found by solving equation (2.14) numerically. In fact, if the energy dependence of the cross section is complicated then there is usually no alternative to this procedure. On the other hand, if the energy dependence of the cross section is relatively simple, then the reaction rate can be calculated analytically [45; 46; 47]. Analytical expressions can have several benefits over numerical descriptions, providing additional insight into stellar fusion reactions; firstly, in certain situations, such as for narrow resonances, the cross-section curve is not known explicitly, and hence the rate

cannot be integrated numerically, secondly, in cases where the reaction rate has to be extrapolated to the region of interest, an analytical description allows for an improved estimate of the rate.

2.3.1 Charged-Particle-Induced Non-resonant Reactions

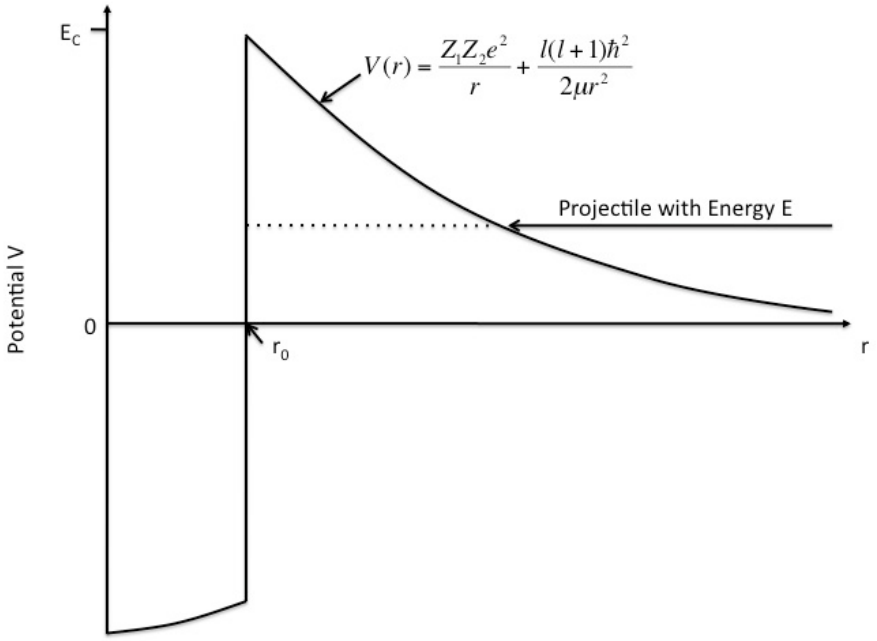

Figure 2.1: Schematic representation of the combined nuclear, centrifugal and Coulomb potentials. A projectile incident with $E<E_C$ has to penetrate the combined Coulomb and centrifugal barrier in order to reach the nuclear domain.

As discussed in the previous chapter, the chief source of energy generation in stars comes from the fusion of hydrogen nuclei into helium. In order for particles to reach the nuclear interaction radius, r_0, in which such nuclear fusion reactions can occur, a stellar temperature of $\sim 10^7$ K is required. This high temperature is necessary because nuclei must overcome an effective potential barrier $V(r)$ caused by both the positive charge of nuclei (Coulomb potential),

$$V_C(r) = \frac{Z_1 Z_2 e^2}{r}, \tag{2.15}$$

and the relative orbital angular momentum of the particles (centrifugal potential)

$$V_{cf}(r) = \frac{l(l+1)\hbar^2}{2\mu r^2} \tag{2.16}$$

This barrier is shown in Fig. 2.1 and, in the case of the $p + p$ reaction, has an effective height E_C of 550 keV.

From a classical perspective, the $p + p$ reaction can only occur when the energy of the interacting proton exceeds 550 keV, which corresponds to a stellar temperature of 6.4 GK. If this were the case, however, then once a temperature of 6.4 GK was reached in the stellar interior, all pairs of nuclear particles would react instantaneously and stars would experience catastrophic explosions rather than burn nuclear fuel for billions of years.

The situation was resolved in 1928, when Gamow showed that if quantum mechanical effects are taken into account there is a probability that a particle, with $E<E_C$, can penetrate the potential wall and reach the nuclear force at $r=r_0$ [48]. At energies $E \ll E_C$, such as those typically found in stellar interiors, the probability of barrier penetration can be simplified to the so-called "Gamow factor",

$$P = exp(-2\pi\eta), \tag{2.17}$$

where η represents the "Sommerfeld parameter" and

$$2\pi\eta = 31.29 Z_1 Z_2 \left(\frac{\mu}{E}\right)^{1/2}, \tag{2.18}$$

where the centre-of-mass energy E is given in units of keV and μ is in amu.

This probability is directly proportional to the energy-dependent nuclear reaction cross section $\sigma(E)$ and as such, the cross section for charged-particle-induced nuclear reactions drops rapidly for energies below the height of the potential barrier E_C. This point is of particular relevance when performing direct experimental measurements of nuclear reaction cross sections over the range of effective stellar energies. In such experiments, stellar reactions are reproduced in the laboratory by the bombardment of a target by a beam of particles of varying energy. Below a certain beam energy, which could indeed be greater than the stellar energy range of interest, the cross section becomes too small to be measured using present techniques and extrapolation is needed, as shown in Fig. 2.2(a). However, because the cross section varies so rapidly with

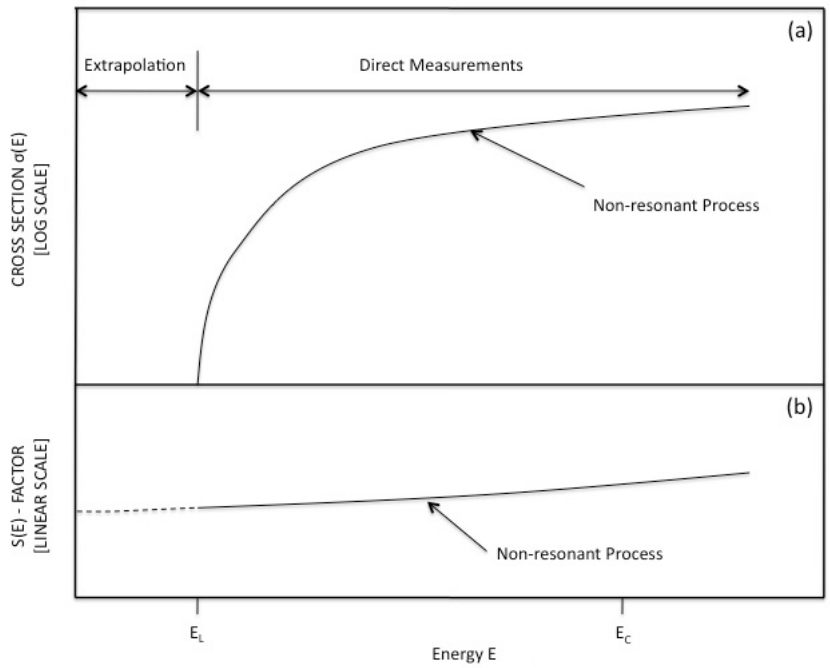

Figure 2.2: (a) Cross section $\sigma(E)$ as a function of beam energy. (b) Astrophysical $S(E)$-factor as a function of beam energy. E_L represents the lowest beam energy at which direct cross sectional measurements can be made and E_C represents the height of the potential barrier.

beam energy, extrapolation using just the cross section from such measurements is difficult.

At this point it is customary to introduce the astrophysical S-factor $S(E)$, which contains all strictly nuclear parts of the probability and is defined by

$$\sigma(E) = \frac{1}{E} exp(-2\pi\eta) S(E) \tag{2.19}$$

The advantage of writing the cross section in this way is that two strongly energy-dependent factors appearing in the nuclear cross sections are factored explicitly, leaving a residual function of energy, $S(E)$, which may, in favourable circumstances, be extremely simple itself. For non-resonant reactions the factor $S(E)$ is a smoothly varying function of energy, varying much less rapidly with beam energy than the cross section, and consequently, provides a much more useful means in extrapolating cross sections to astrophysical energies, as shown in Fig. 2.2(b).

Inserting the definition for the S-factor into equation (2.14) we obtain for the non-resonant reaction rate per particle pair,

$$< \sigma v >= \left(\frac{8}{\pi\mu}\right)^{1/2} \frac{1}{(kT)^{3/2}} \int_0^\infty S(E) exp\left(-\frac{E}{kT} - \frac{b}{E^{1/2}}\right) dE, \tag{2.20}$$

where the quantity b, which arises from the barrier penetrability, is given by

$$b = (2\mu)^{1/2} \pi e^2 \frac{Z_1 Z_2}{\hbar} \tag{2.21}$$

The quantity b^2 is also called the Gamow energy, E_G, and the reaction rate per particle pair can be rewritten as,

$$< \sigma v >= \left(\frac{8}{\pi\mu}\right)^{1/2} \frac{1}{(kT)^{3/2}} \int_0^\infty S(E) exp\left[-\frac{E}{kT} - \left(\frac{E_G}{E}\right)^{1/2}\right] dE. \tag{2.22}$$

As stated previously, for non-resonant reactions, $S(E)$ varies smoothly with energy. Thus, the energy dependence of the integrand in equation (2.22) is governed primarily by the two exponential terms. The product of these two terms leads to a peak of the integrand near an energy E_0, which is usually much larger than kT. This peak is known as the Gamow peak, shown in Fig. 2.3, and for a given temperature T, the width of the Gamow peak ΔE_0 represents the narrow energy window in which nuclear reactions are likely to take place.

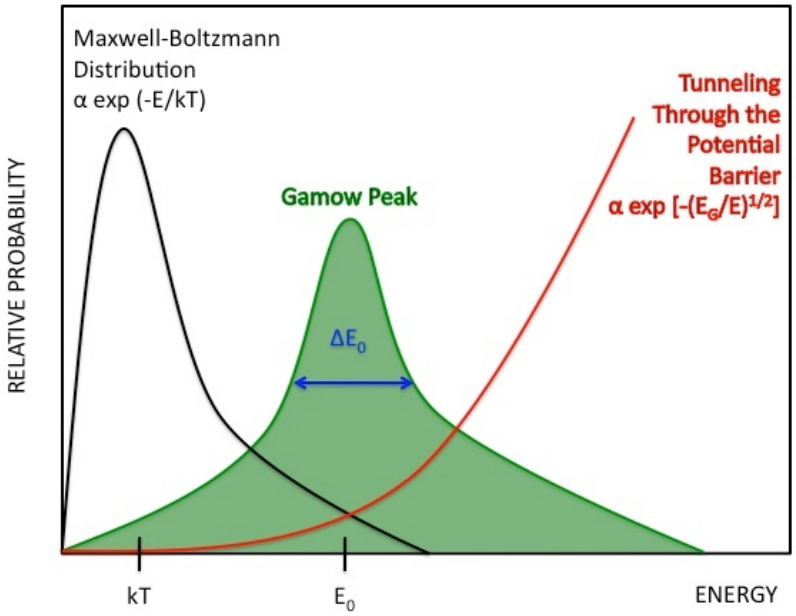

Figure 2.3: Diagram showing the dominant energy-dependent functions for nuclear reactions between charged particles.

Over the energy window ΔE_0, the factor $S(E)$ is frequently constant and the reaction rate reduces to

$$< \sigma v >= \left(\frac{8}{\pi\mu}\right)^{1/2} \frac{1}{(kT)^{3/2}} S(E_0) \int_0^\infty exp\left[-\frac{E}{kT} - \left(\frac{E_G}{E}\right)^{1/2}\right] dE. \quad (2.23)$$

By taking the first derivative of the integrand in equation (2.23), one can find the the energy E_0,

$$E_0 = \left(\frac{bkT}{2}\right)^{2/3}, \quad (2.24)$$

and furthermore, in approximating the integrand as a Gaussian function, the effective width of the Gamow energy window ΔE_0, in which most of the nuclear reactions take place, may be expressed as,

$$\Delta E_0 = \frac{4}{3^{1/2}} (E_0 kT)^{1/2}. \quad (2.25)$$

This completes our discussion of an analytical formalism for non-resonant stellar reaction rates and if all reactions occurring in stellar interiors proceeded completely via non-resonant components, in which the $S(E)$-factor varies smoothly,

no further discussion would be necessary. However, for many nuclear reactions there exist resonances in the range of effective stellar energies. These cause strong variations in the astrophysical S-factor, and consequently, an entirely different analytical approach must be adopted.

2.3.2 Narrow-Resonance Reaction Rates

In the following section we shall discuss a particular branch of reactions, in which the astrophysical S-factor varies strongly, involving isolated and narrow resonances, where the corresponding particle partial widths are approximately constant over the total resonance energy width, Γ.

Let us consider the reaction $a + X$, in which a compound nucleus W is initially formed in an excited state, before decaying to the exit channel products $Y + b$,

$$a + X \rightarrow W^* \rightarrow Y + b \tag{2.26}$$

Resonances can occur in such a nuclear reaction if the centre-of-mass kinetic energy of "a" and "X" coincides with the energy of one of the quasi-stationary excited states of the compound nucleus, which is illustrated in Fig. 2.4.

Furthermore, if J_n is the angular momentum of the excited state E_n in the compound nucleus W, J_a and J_X are the spins of the particles "a" and "X", and L is the orbital angular momentum of "a" relative to "X", then conservation of angular momentum demands that in order for a resonance to occur,

$$\mathbf{J}_n = \mathbf{J}_a + \mathbf{J}_X + \mathbf{L}, \tag{2.27}$$

where the standard rules of vector addition apply.

Quasi-stationary states having positive energy, such as the one labelled E_n can exist because the high potential barriers of the nucleus give the state a relatively long lifetime against breakup. However, it is apparent from Fig. 2.4 that all resonant states by which incoming particles can interact are particle "unbound" states, since they can both be formed by, and decay to, "a" and "X" with positive kinetic energy. Therefore, although such positive energy quasi-stationary states can have relatively long lifetimes, due to the large potential barrier $V(r)$, as the excitation energy increases, particle decay becomes more favourable and the lifetimes shorten.

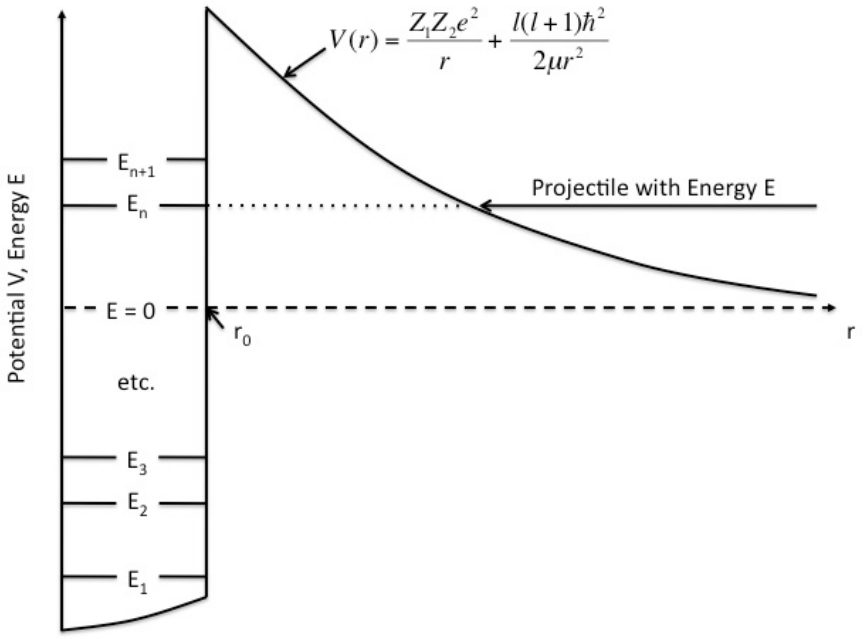

Figure 2.4: Diagrammatic representation of resonant formation in the compound nucleus W. The quasi-stationary nuclear states in the compound nucleus W are denoted by E_1, E_2, etc.

The energy-dependent reaction cross section for an isolated resonance may be described by the Breit-Wigner formula and, for the reaction above, this can be written as

$$\sigma_{BW}(E) = \frac{\lambda^2}{4\pi}\frac{(2J+1)(1+\delta_{Xa})}{(2j_X+1)(2j_a+1)}\frac{\Gamma_a\Gamma_b}{(E_r-E)^2+\Gamma^2/4} \tag{2.28}$$

Here, $\lambda = 2\pi\hbar/\sqrt{2\mu E}$, j_X and j_a are the spins of target and projectile, J and E_r are the resonance spin and resonance energy, E is the centre-of-mass energy, Γ_a and Γ_b are the particle partial widths of "a" and "b" (the decay/formation probability of a particular channel), and Γ is the total resonance width. The Kronecker symbol has also been included for the case of identical entrance channel nuclei, which increases the cross section by a factor of 2. The effect on the reaction cross section $\sigma(E)$ by both resonant and non-resonant reaction processes is shown in Fig. 2.5. From Fig. 2.5, it is clear that the reaction cross

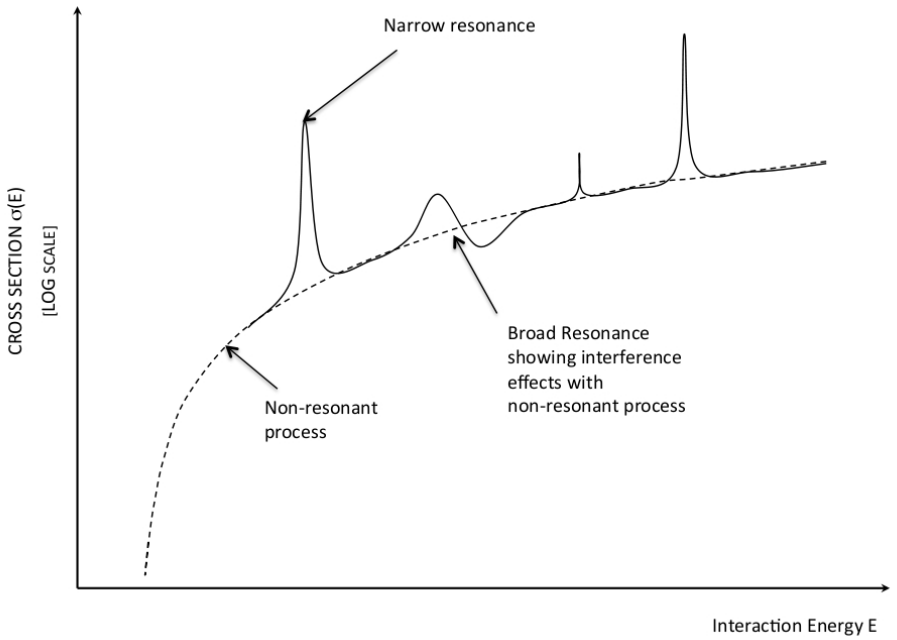

Figure 2.5: Schematic diagram showing the reaction cross section $\sigma(E)$ as a function of interaction energy for both non-resonant and resonant reaction processes.

section for a given interaction energy can increase dramatically if a resonance is present.

In this thesis work we have investigated radiative proton capture reactions, in which the incident proton is absorbed by the target nucleus and γ radiation is then emitted. In the studied (p,γ) reactions there are only two open channels, the proton channel (Γ_p) and the γ-ray channel (Γ_γ), and the total width of the resonant state is given by $\Gamma = \Gamma_p + \Gamma_\gamma$. Thus, we shall now limit the further discussion of resonant reaction rates to these types of reactions.

For a narrow resonance ($\Gamma \ll E_r$) in a given proton capture reaction, the reaction rate may be expressed as

$$< \sigma v >= \left(\frac{8}{\pi\mu}\right)^{1/2} \frac{1}{(kT)^{3/2}} \int_0^\infty \sigma_{BW}(E) E exp\left(-\frac{E}{kT}\right) dE \tag{2.29}$$

$$= \frac{\sqrt{2\pi}\hbar^2}{(\mu kT)^{3/2}} \omega \int_0^\infty \frac{\Gamma_p \Gamma_\gamma}{(E_r - E)^2 + \Gamma^2/4} exp\left(-\frac{E}{kT}\right) dE, \tag{2.30}$$

where $\omega \equiv (2J+1)/[(2j_X+1)(2j_p+1)]$. Furthermore, for a sufficiently narrow resonance, the Maxwell-Boltzmann factor and partial widths Γ_p and Γ_γ are approximately constant over the total width of the resonance, allowing their values at $E=E_r$ to be taken outside the integral:

$$< \sigma v >= \frac{\sqrt{2\pi}\hbar^2}{(\mu kT)^{3/2}} exp\left(-\frac{E_r}{kT}\right) \omega \frac{\Gamma_p \Gamma_\gamma}{\Gamma} 2 \int_0^\infty \frac{\Gamma/2}{(E_r - E)^2 + \Gamma^2/4} dE \tag{2.31}$$

$$= \frac{\sqrt{2\pi}\hbar^2}{(\mu kT)^{3/2}} exp\left(-\frac{E_r}{kT}\right) \omega \frac{\Gamma_p \Gamma_\gamma}{\Gamma} 2\pi \tag{2.32}$$

$$= \left(\frac{2\pi}{\mu kT}\right)^{3/2} \hbar^2 exp\left(-\frac{E_r}{kT}\right) \omega\gamma, \tag{2.33}$$

where $\omega\gamma \equiv \omega\Gamma_p\Gamma_\gamma/\Gamma$ and is known as the resonance strength. At this point it should be noted that if a nuclear reaction has several narrow and isolated resonances, as is often the case, then their contributions to the reaction rate will simply be summed,

$$< \sigma v >= \left(\frac{2\pi}{\mu kT}\right)^{3/2} \hbar^2 \sum exp\left(-\frac{E_i}{kT}\right) (\omega\gamma)_i. \tag{2.34}$$

2.3.3 Experimental Considerations

From equation (2.34), it is clear that in order to determine the overall resonant contribution to the stellar reaction rate:

1. The energy of all resonant states, that may contribute to rate, must be measured precisely.

2. The spins and parities of all resonant states, that may contribute to the rate, must be determined.

3. The resonance strengths of all resonant states, that may contribute to the rate, must be determined.

The methods used to measure and determine these quantities will be discussed in the following sections.

2.3.3.1 Light-ion Transfer Reaction Measurements for the Determination of Stellar Reaction Rates

Traditionally, a measure of the resonance energy and a deduction of the resonance spin-parity assignment are accomplished by performing light-ion transfer reaction experiments. Such studies populate near-threshold resonances in a given nucleus, that dominate the astrophysical reaction of interest, using a nuclear reaction other than the one of direct astrophysical interest. For example, the stellar reaction ^{26}Al$(p,\gamma)^{27}$Si has been investigated by populating near threshold resonances in the nucleus ^{27}Si using the $(^3\mathrm{He},d)$ [42], $(^3\mathrm{He},\alpha)$ [39] and $(^3\mathrm{He},t)$ [40] transfer reactions. These studies allowed a measure of the outgoing particle momentum (i.e. d, α and t in the reactions listed above) and the differential cross section, $d\sigma/d\Omega$, as a function of angle. The momentum of the outgoing particle was used to determine the energy of the excited states in the nucleus under investigation while its angular distribution, although only sensitive to the orbital angular momentum transfer, Δl, was used to infer the spin. Let us consider the ^{26}Al$(^3\mathrm{He},d)^{27}$Si experiment performed by Vogelaar *et al.* [42] to investigate the astrophysical ^{26}Al$(p,\gamma)^{27}$Si reaction rate. In this study a radioactive ^{26}Al target was fabricated and bombarded with ^{3}He nuclei in order to populate near proton-threshold states in ^{27}Si. The energy of the outgoing deuteron identified the residual ^{27}Si state formed, as shown in Fig. 2.6.

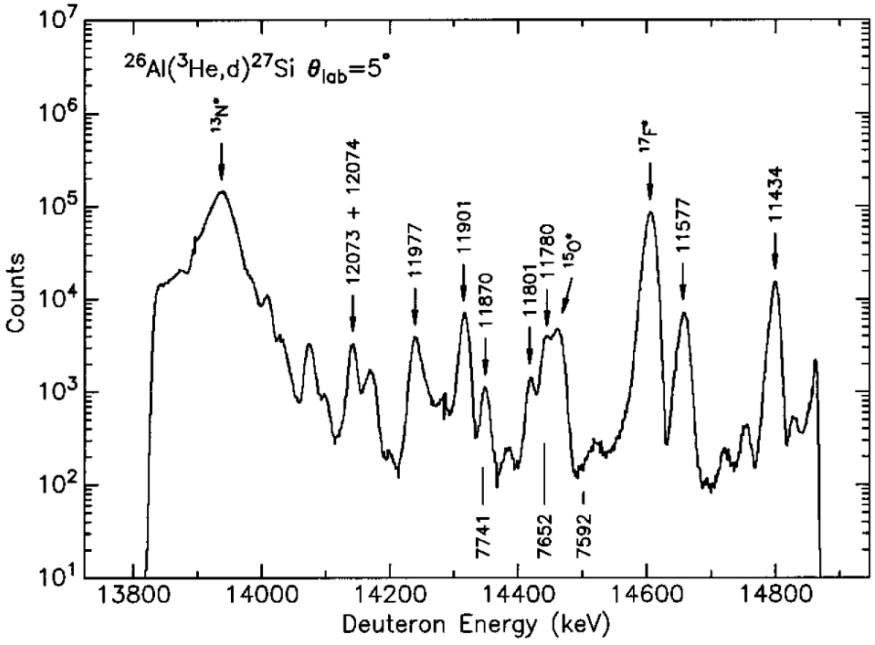

Figure 2.6: Deuteron groups identified by the excited state of the residual nucleus. Those from ^{28}Si are labelled above the curve, while those from ^{27}Si states are labeled below.

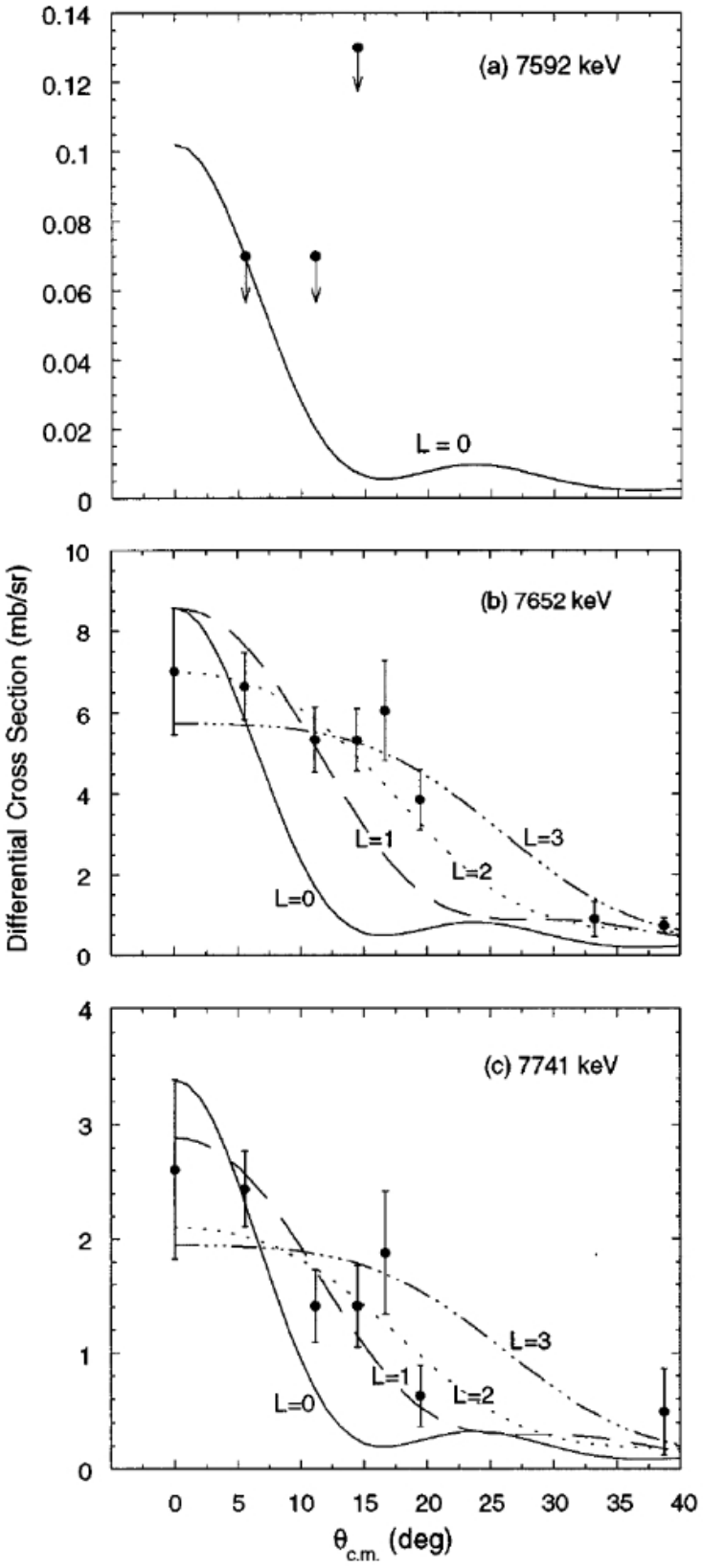

Figure 2.7: Angular distributions and DWBA fits for the ^{27}Si states of interest.

The level energies obtained for the observed excited states showed good agreement with the previous studies of Refs. [38][39][40]. The measured differential cross section, as a function of angle, for the three ^{27}Si states, labelled above, was compared with those calculated for pure $l = 0$, 1, 2 and 3 transfers using a Distorted-Wave Born-Approximation (DWBA) computer code. This comparison, shown in Fig. 2.7, was used to determine the proton's l-transfer in the $^{26}\mathrm{Al}(p,\gamma)^{27}\mathrm{Si}$ reaction for each of the observed states. However, as can be seen from the fits, the angular distributions are not particularly distinctive and in this case it was not possible to deduce unique l assignments.

From the example given above, it is clear that transfer reaction studies offer a great deal of information regarding the nuclear properties of excited states of astrophysical interest. However, as is also shown in the example above, such studies can suffer from poor energy resolution and ambiguous angular distributions. In fact, only Δl may be determined from transfer reaction studies and DWBA analyses are insensitive to the J assignment of the state. Consequently, in this thesis work we have chosen to use γ-ray spectroscopy techniques to determine the nuclear properties of resonant states, populated through heavy-ion fusion evaporation reactions involving stable nuclei, in astrophysically important proton-rich nuclei. The results are more precise energies and less ambiguous assignments compared to light-ion transfer reactions, the details of which shall be discussed at the end of this chapter.

2.3.3.2 Direct Measurements of Resonance Strengths

Returning to equation (2.34), in order to determine the resonance strength directly, a measurement of the cross section for the astrophysical reaction of interest is needed. Such direct measurement studies reproduce astrophysical reactions of interest (*e.g.* $^{26}\mathrm{Al}(p,\gamma)^{27}\mathrm{Si}$) in the range of effective stellar energies by the bombardment of a target by a beam of particles of given energy. This allows a determination of the total number of nuclear reactions that occurred during the experiment, N_R, and the total number of incident beam particles, N_b. The ratio of these two quantities,

$$Y \equiv \frac{N_R}{N_b}, \tag{2.35}$$

is called the "yield" per incident particle of the reaction and is directly related to the reaction cross section. It is customary to plot the yield as a function of

bombarding energy, which, in turn, is referred to as a "yield curve" or "excitation function". The resonance strengths for specific resonance energies, E_r, are then calculated through the relation,

$$\omega\gamma = \frac{2\epsilon Y}{\lambda^2}\frac{M_T}{M_P + M_t}, \tag{2.36}$$

where λ is the de-Broglie wavelength in the CM system, ϵ is the effective stopping power of the target and M_T and M_P are the masses of the target and projectile, respectively.

At the elevated temperatures found in explosive astrophysical environments, proton-induced reactions do not only involve stable nuclides but unstable proton-rich nuclides also participate in the nucleosynthesis. The direct measurement of astrophysical reactions, in which one of the interacting nuclei is unstable, represents a significant challenge to the experimenter. However, several methods have been devised in which such measurements may be performed. Firstly, if the half-life of the radioactive nuclide of interest exceeds several days, then it may be possible to fabricate a radioactive target and measure the reaction directly by bombarding the target with a stable beam of protons. As an example, the study performed by Buchmann *et al.* [38] investigated the proton capture reaction ^{26}Al$(p,\gamma)^{27}$Si by bombarding a fabricated radioactive ^{26}Al target with a stable beam of protons in the energy range E_p = 0.17–1.58 MeV. A Ge(Li) detector was placed at 0° in close geometry with respect to the target, in order to obtain excitation functions for the ^{26}Al$(p,\gamma)^{27}$Si reaction via $\gamma\gamma$ cascades through low-lying states in ^{27}Si. The resulting excitation function for the ^{26}Al$(p,\gamma)^{27}$Si reaction as obtained for the 2164 keV secondary γ-ray transition, is shown in Fig. 2.8 [38]. The investigated energy range E_p = 0.17–1.58 MeV corresponds to a stellar temperature range of 0.2–1 GK and resonances were observed at E_R = 286.6(3), 376(3), 719(2), 727(2), 790(2), 856(2) and 927(2) keV with resonance strengths of 3.8(10), 65(18), 51(27), 16(6), 35(13), 41(16) and 67(28) meV, respectively. Thus, from this study, uncertainties in the resonant contribution to the ^{26}Al$(p,\gamma)^{27}$Si reaction rate were constrained for $T \geq 0.2$ GK.

A later direct measurement of the proton capture ^{26}Al$(p,\gamma)^{27}$Si reaction using a radioactive aluminium target, performed by Vogelaar [41], also observed resonances at E_R = 286.6(6), 360.5(6), 720.3(4), 729.1(1), 792.6(4), 856.9(4) and 927.6(2) keV with comparable resonance strengths to Ref. [38] of 2.9(3), 69(7),

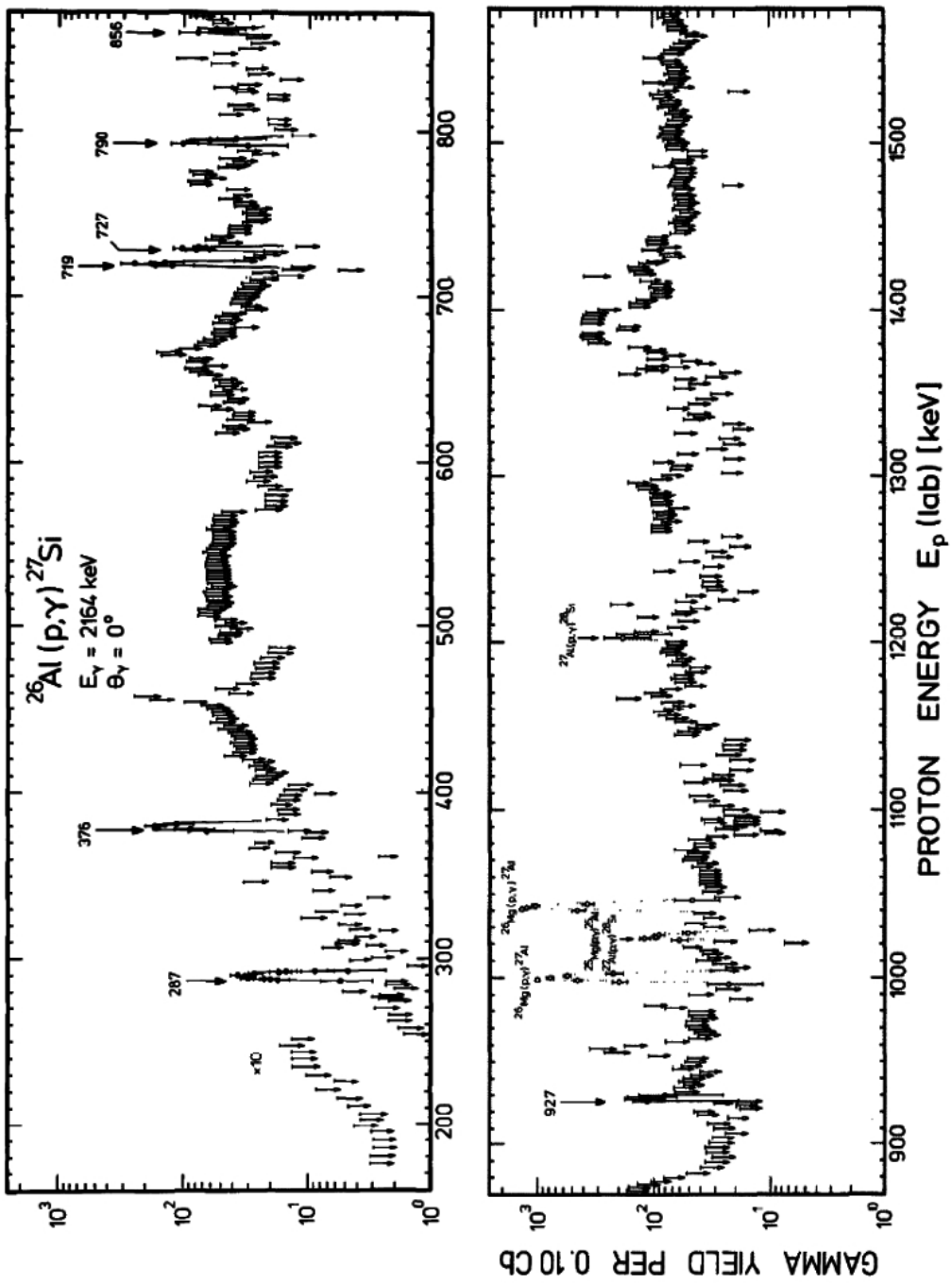

Figure 2.8: Excitation function of $^{26}\mathrm{Al}(p,\gamma)^{27}\mathrm{Si}$ as obtained for the 2164 keV secondary γ-ray transition.

67(9), 33(6), 46(7), 52(7) and 38(8) meV, respectively. However, additional low-lying resonances were observed at E_R = 195.6(11), 235(3) and 246.5(10) keV with resonance strengths of 0.055(9), $\leq$0.010 and 0.010(5) meV, respectively, and although the measured resonance strengths of these resonances were significantly smaller than those previously observed, the resonance at E_R = 195.6(11) was suggested to have a significant contribution to the stellar reaction rate at temperatures <0.2 GK.

These observations again confirm the need to identify all resonances that may contribute to the reaction rate and highlight that the radioactive target technique presents two major problems. The first problem arises from the large background produced by the radioactive decay of the target nuclei (β- and γ-radiation). In the case of ^{26}Al, target activity background manifests itself in the form of Compton events from the 1809 keV γ ray from ^{26}Al decay summing with annihilation quanta from the emitted β^+, which has been suggested to dominate the background in such experiments [41]. The second problem arises from chemical contaminants in the radioactive target (decay products of radioactive nuclei and impurities in the target and target backing), which can significantly reduce the signal-to-noise ratio. Buchmann *et al.* [38] highlighted the fact that the presence of contaminant light elements ^{12}C, ^{19}F, ^{23}Na and ^{27}Al gave rise to a significant background and hampered measurements of the reaction yield. This problem is highlighted by the fact that the resonances at E_R = 195.6(11), 235(3) and 246.5(10) keV were not observed by Buchmann *et al.* [38] even though they fall well within the investigated energy range.

Consequently, in order to achieve better sensitivity in measuring resonance strengths, a method resolving these issues has been developed, in which the role of the projectile and target are interchanged. These studies, known as inverse kinematic studies, involve the bombardment of light particle targets, which can be manufactured with high purities, with beams of heavier radioactive nuclei, significantly reducing the problems with background radiation. It is also important to mention at this point that, although reactions on ^{26}Al may be studied using both radioactive beams and targets, if the half-life of the radioactive nuclei of interest amounts to a few minutes or less, as is the case for ^{23}Mg, then the fabrication of a radioactive target is not feasible and there is no alternative but to use a radioactive ion beam for a direct measurement of the corresponding resonance strengths.

The production, transport and acceleration of radioactive ion beams suitable for nuclear astrophysics measurements requires substantial resources and efforts as even under the most extreme astrophysical conditions, the most effective energies for stellar nuclear reactions are well below the Coulomb barrier. Thus, in order to obtain a direct measurement of the reaction cross section beams of low energy and high intensity are required. Significant success in this area has been achieved through the use of the isotope separator online (ISOL) technique [49; 50]. In the ISOL technique, an accelerated beam of stable nuclei are used to bombard a thick target and produce radioactive ions. These atoms diffuse out of the target material and through a transfer tube into an ion source, where they are ionized and extracted. The radioactive ions are then mass separated from other isotopes and their energies are increased by a second accelerator. The accelerated radioactive ion beam may then be used to bombard a hydrogen or helium target in order to measure the radiative capture reaction of interest. The ISOL method has been successfully used to produce radioactive beams at the Louvain-la-Neuve, Oak Ridge, CERN, GANIL and TRIUMF facilities. Unfortunately, there is no single combination of production beam, thick target, and ion source that can produce all radioactive species of astrophysical interest and more typically, each radioactive ion beam experiment requires an extensive and time-consuming effort of beam development. In fact, to date there have only been four (p,γ) astrophysical reactions studied through the use of radioactive ion beams; the ^{13}N$(p,\gamma)^{14}$O reaction [51], the ^{21}Na$(p,\gamma)^{22}$Mg reaction [52], the ^{26}Al$(p,\gamma)^{27}$Si reaction [43] and the ^{7}Be$(p,\gamma)^{8}$B reaction [53]. The pioneering work in this field was the study of the astrophysical ^{13}N$(p,\gamma)^{14}$O reaction by Decrock *et al.* [51] in 1991. At temperatures $\geq 10^8$K the ^{13}N$(p,\gamma)^{14}$O reaction cross section is determined by a single strong l_p=0 resonance at $E_R = 545$ keV, which corresponds to the first 1^- excited state in ^{14}O at 5173 keV. As a result, in the study by Decrock *et al.* [51], no recoil separation was needed and the reaction cross section was determined through the detection of 5173 keV ^{14}O γ rays using a single large volume Ge diode. A complementary approach by Motobayashi *et al.* [54] studied the ^{13}N$(p,\gamma)^{14}$O reaction via the Coulomb dissociation of an ^{14}O radioactive beam. The results of these measurements [54] were consistent with the direct measurements of Decrock *et al.*, further indicating that the ^{13}N$(p,\gamma)^{14}$O reaction is dominated by a single resonance.

In more recent years, the study of astrophysical reactions in which a number of resonances contribute to the stellar reaction rate has required the employment of recoil detection equipment to select out reaction products from the radioactive beam. An example of such a device is shown schematically in Fig. 2.9 [55]. The DRAGON (Detector of Recoils And Gammas Of Nuclear reactions) separa-

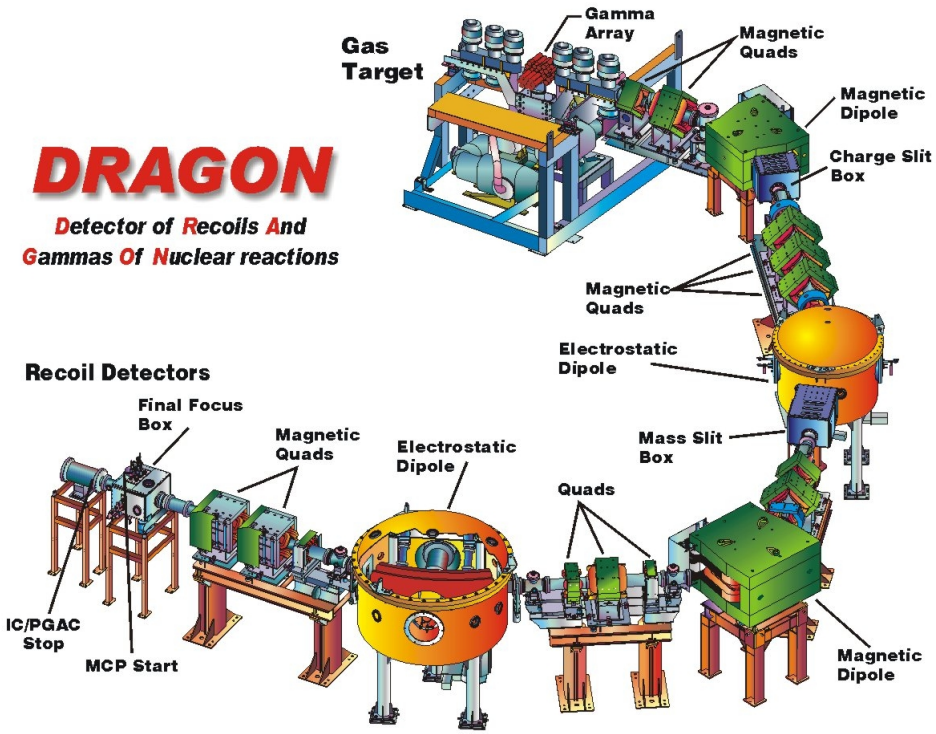

Figure 2.9: A schematic diagram of the DRAGON recoil separator at the ISAC facility at TRIUMF [55].

tor at the TRIUMF-ISAC radioactive beams laboratory in Vancouver, Canada, shown in Fig. 2.9, was designed to accept recoils and separate them from beam particles for relevant astrophysical reactions. The clean identification of recoils allows for a precise measurement of the energy and strength of a given resonance, with a significantly reduced background compared to radioactive target experiments. However, it is important to note that, in using the DRAGON separator at the ISAC facility at TRIUMF, only a single resonance strength can be measured for any given radioactive beam energy. A recent study by Ruiz *et al.* [43] measured the strength of the 184 keV resonance, previously observed at 196 keV [41], in the $^{26}\mathrm{Al}(p,\gamma)^{27}\mathrm{Si}$ reaction using the DRAGON recoil separator

in inverse kinematics at TRIUMF's ISAC facility. The radioactive ^{26}Al beam was directed onto a windowless hydrogen gas target and prompt γ rays were detected in an array of 30 BGO scintillator detectors, tightly packed around the gas target, with an almost 4π coverage. The ^{27}Si nuclei were separated from the intense beam by using the DRAGON recoil separator [56] and then detected in the focal plane by a double-sided silicon strip detector in coincidence with the γ rays measured near the target by the BGO array. This allowed a sensitive resonance strength measurement of the 184 keV resonance and a value of 35(7) μeV was obtained, with slightly improved precision over the previous measurement of 55(9) μeV by Vogelaar [41]. It is important to mention at this point that in order to obtain resonance strength measurements using the DRAGON facility at TRIUMF, the energy of the resonance of astrophysical interest must be known. This is so that a beam energy determination may be performed to place the resonance at the centre of the gas target for subsequent detection. Therefore, it is essential to identify all excited states that may proceed as resonances in the nuclei of astrophysical interest before undertaking the associated direct measurement experiment using radioactive ion beams.

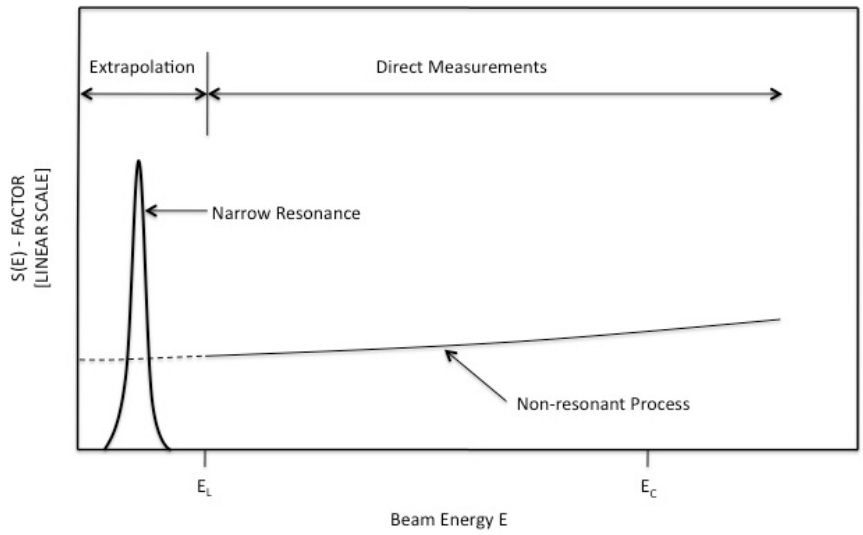

Figure 2.10: Schematic diagram showing the presence of a low energy resonance outside the region of direct experimental measurements

In both cases of direct measurements, using a radioactive target or radioactive ion beam, below a certain beam energy the cross section becomes so small

that it cannot be directly measured using present techniques. When considering only non-resonant components it is possible to extrapolate the cross section down to the particle emission threshold of interest. However, if resonances are present close to the threshold, such an extrapolation is dangerous, as shown in Fig. 2.10. A low energy resonance, such as the one shown in Fig. 2.10, can have a significant affect on the rate at low stellar temperatures. Thus, reinforcing the necessity to identify all resonances above the threshold that can affect the reaction rate. In the case of low energy resonances and resonances in reactions of astrophysical interest, which have not been measured directly (which is most astrophysical reactions involving radioactive nuclei), an indirect determination of the resonance strength is required. Such studies populate the astrophysically important levels in the compound nucleus by using reactions other than the one of direct astrophysical interest.

2.3.3.3 Indirect Measurements of Resonance Strengths

From the definition of the resonance strength for a proton radiative capture reaction $X(p,\gamma)Y$,

$$\omega\gamma = \frac{(2J+1)}{(2J_X+1)(2J_p+1)}\frac{\Gamma_p\Gamma_\gamma}{\Gamma}, \tag{2.37}$$

where J_p is the spin of the proton, it is clear that the resonance strength relies critically on both the spin of the resonant state and the relative partial widths Γ_p and Γ_γ. Therefore, if the quantities J, J_x, J_p, Γ_p and Γ_γ are known, a direct measurement of $\omega\gamma$ is not necessary. In fact, provided J, J_x and J_p are known, in many cases approximations can be made so that only one of the particle widths, Γ_p or Γ_γ, need be measured in order to determine the resonance strength. However, for states of astrophysical interest, this is normally the weaker decay branch and by definition is harder to measure.

Let us assume first that the resonant state of interest predominantly γ decays, $\Gamma_p \ll \Gamma_\gamma$, and consequently, the corresponding resonance strength is governed by the proton partial-width, Γ_p.

$$\omega\gamma = \omega\frac{\Gamma_p\Gamma_\gamma}{\Gamma_p+\Gamma_\gamma} \approx \frac{\Gamma_p\Gamma_\gamma}{\Gamma_\gamma} = \omega\Gamma_p \tag{2.38}$$

The proton partial width can be estimated through the expression,

$$\Gamma_p = C^2 S\Gamma_{sp}, \tag{2.39}$$

where Γ_{sp} is the single-particle partial width, C is the isospin Clebsch-Gordan coefficient and S is the single particle spectroscopic factor. The single-particle partial width is given by,

$$\Gamma_{sp} = 2\frac{\hbar^2}{mR^2}P_c\theta_{pc}^2, \tag{2.40}$$

where m is the mass of the particle, R=1.25$A^{1/3}$fm, P_C is the penetration factor (the probability that the particle will penetrate the Coulomb and centrifugal barriers) and θ_{pc}^2 is the dimensionless single-particle reduced width of the protons [57]. The collective term C^2S is known as the "spectroscopic factor" and is defined in terms of the overlap integral between the final state wave function of Y and the initial state wave function $X + p$. This quantity may be obtained from transfer reaction studies through the expression,

$$\frac{d\sigma}{d\Omega}(exp) = NC^2S\left(\frac{2J+1}{2J_t+1}\right)\frac{d\sigma}{d\Omega}(DWBA), \tag{2.41}$$

where J is spin of the excited state, N is a normalisation factor and J_t is the transferred spin. In considering the transfer reaction discussed previously, ^{26}Al(^{3}He, d)^{27}Si, spectroscopic factors of pure proton l-transfers of 0, 1, 2 and 3 were obtained for the 7652 and 7741 keV excited states, respectively. In fact, once the spin of the resonant state is known, such measurements of associated spectroscopic factors are essential to indirectly determine the resonance strength of states, which have not yet been or cannot be directly measured. It should also be noted that spectroscopic factors may be calculated using the shell model.

Suppose now that the γ-ray partial width is much smaller than the particle width, $\Gamma_a \gg \Gamma_\gamma$, and consequently, the resonance strength is governed by the γ-ray partial width,

$$\omega\gamma = \omega\frac{\Gamma_a\Gamma_\gamma}{\Gamma_a+\Gamma_\gamma} \approx \frac{\Gamma_a\Gamma_\gamma}{\Gamma_a} = \omega\Gamma_\gamma. \tag{2.42}$$

The values of the γ-ray partial widths are typically of the order of 1eV or less and thus, are determined from the lifetimes of the resonant states. However, the resonant states of astrophysical interest in (p,γ) reactions, lying above the particle-emission threshold, predominantly proton decay and therefore, lifetime measurements of these unbound states in proton-rich nuclei, such as those studied in this thesis, are, in general, difficult. Consequently, in most cases, the Γ_γ partial widths of astrophysically important resonant states are estimated by a

comparison to the energy lifetimes of bound states in the mirror nucleus, incorporating a correction for the energy difference between isobaric analogue states. In fact, the nuclear properties of mirror nuclei are nearly identical in this region and thus, if the properties of the neutron-rich nucleus of a mirror pair are well known, which is often the case as these nuclei are relatively easy to study using a variety of nuclear reactions, they can be used to predict many of the nuclear properties of astrophysically important states in the proton-rich mirror nucleus. Such mirror comparisons are of particular importance in astrophysical studies, such as those carried out in the present work, since many of the nuclear properties of astrophysically important excited states, located above the threshold in the proton-rich nuclei investigated in this work, are still unknown. Thus, by studying the structure of mirror nuclei, the unknown nuclear properties of astrophysically important states may be deduced.

2.3.3.4 Mirror Nuclei

The isospin formalism, which stems from the assumption that the strong nuclear force is charge-independent, describes the neutron and the proton as identical particles with isospin T=1/2 and projections T_z(n)=+1/2 and T_z(p)=-1/2, respectively [58; 59]. This leads to the concept that the structures of nuclei with the same mass number, A, and isospin, T, are nearly identical. Consequently, determining the nuclear properties of a nucleus can give insight into the nuclear properties of its isobaric analogues. Isobaric nuclei with the same isospin T belong to a $2T$+1 multiplet with the projections T_z=(N-Z)/2, where N is the number of neutrons and Z is the number of protons in the nucleus.

A classic example of such an isobaric multiplet is a pair of "mirror" nuclei, in which the neutron and proton numbers are exchanged. In mirror nuclei, as with all isobaric multiplets, the isospin symmetry is broken by the Coulomb interaction, resulting in the lowering of the total binding energy of nuclear states in one member of the multiplet relative to the other. A connection between the change in binding energy due to the charge state difference in an isobaric multiplet and the isospin quantum number, T, was first established in a study by Wigner in 1957 [60]. The result of this study was the formulation of the well known Isobaric Multiplet Mass Equation (IMME) [60],

$$\Delta BE(T, T_z) = a + bT_z + cT_z^2 \tag{2.43}$$

where, the coefficients a, b and c represent the isoscaler, isovector and isotensor Coulomb energies, respectively. It should be noted that although the expression given above only represents the binding energy difference between the ground states of a multiplet of isobaric nuclei, it has been shown that the IMME coefficients can also be used to determine the energy difference between the excited states of isobaric nuclei [61]. In such calculations, the absolute binding energies of the ground states are effectively normalised and thus, the Coulomb energy difference between excited states is determined as a function of excitation energy and angular momentum. For mirror nuclei the energy difference between excited states (MED) is given by,

$$MED_{J,T} = E^*_{J,T_z=-T} - E(Z<N)^*_{J,T_z=T} = -\Delta b_J, \tag{2.44}$$

where J is the total angular momentum of the excited state and Δb_J represents the change in the coefficient b as a function of spin in relation to the ground state. In a study by Champagne *et al.* [37], mirror energy differences calculated from the IMME were used to pair well-established excited states in ^{27}Al to analogue states in ^{27}Si, for which many of the nuclear properties were unknown. From such calculations Champagne *et al.* attempted to constrain the spin-parity assignments of excited states above the proton threshold in ^{27}Si, important for the astrophysical ^{26}Al$(p,\gamma)^{27}$Si reaction. In Ref. [37], analogue pairs were directly matched up to an excitation energy of 4510 keV. However, at higher excitation energies the level density of states became too high for a unique matching of analogue states and instead, from a predicted global energy shift between mirror states of around $\pm$200 keV, for each state in ^{27}Al several states in ^{27}Si were suggested as possible analogues.

For the case of isospin triplets, the triplet energy displacement (TED) is given by,

$$TED_{J,T} = E^*_{J,T_z=-T} + E^*_{J,T_z=T} - 2E^*_{J,T_z=0} = 2\Delta c_J. \tag{2.45}$$

This particular prescription was used in a study by Herndl *et al.* [62], in which experimental energies of ^{24}Na and and ^{24}Mg excited states, with known spins and parities, were used to calculate the energies of ^{24}Al analogue states. In this study good agreement was found between the IMME calculations and previously reported energies of ^{24}Al excited states [63]. In fact, as will be shown in Chapter 4, good agreement is found between the present results of this thesis work and

the IMME calculations previously reported in Ref. [62]. However, as with the work of Champagne *et al.*, such IMME calculations were limited to low excitation energies.

2.3.3.5 Gamma-ray Spectroscopy Measurements of T=1 Nuclei

The advent of powerful multi-detector γ-ray spectrometers coupled with the development of efficient reaction-channel selection devices to identify nuclei produced in reactions with low production cross-sections, has allowed the detailed study of isobaric nuclei similarities and the Coulomb energy shifts between analogue excited states even at high excitation energies. These studies have been shown to be extremely powerful tools in determining the structure of proton-rich nuclei and consequently, offer an excellent means to determine the nuclear properties of astrophysically important resonant states, which may then be used to constrain uncertainties in the stellar reaction rate of interest. As an example, Seweryniak *et al.* [64] performed such a study and obtained a complete level structure determination of the T=1 nucleus, ^{20}Na, below the proton threshold (2193(7) keV) [19]. The original objective of this study was to observe excited states above the proton threshold in ^{20}Na, of importance for the astrophysical ^{19}Ne$(p,\gamma)^{20}$Na reaction. No such states were observed and instead the work was used to test the general validity of the nuclear shell model in regions where the proton is relatively loosely bound. The γ-ray spectra obtained for the mirror nuclei ^{20}Na and ^{20}F, by Seweryniak *et al.* [64], are shown in Fig. 2.11, and it is clear that similar γ-ray transitions are present in both nuclei. However, a more striking similarity can be found by comparing the level schemes of the two nuclei, which include the relative intensities of the γ-ray transitions, shown in Fig. 2.12. Figure 2.12 shows that the structures of the mirror nuclei are nearly identical and thus, reconfirms that the nuclear properties of one member of the mirror pair can be extremely helpful in deducing the nuclear properties of the other[1].

A further study by Seweryniak *et al.* [66] determined the level structure of the T=1 nucleus, ^{26}Si, in order to reduce uncertainties in the nucleosynthesis of the important β-decaying cosmic γ-ray emitter, ^{26}Al, that are associated with

[1] In general, the isospin symmetry in nuclei holds fairly well but in previous work by Ekman *et al.* [65], different γ-decay paths were observed for several mirror analogue states in A=35 nuclei. However, this effect has not been observed in medium sd-shell nuclei.

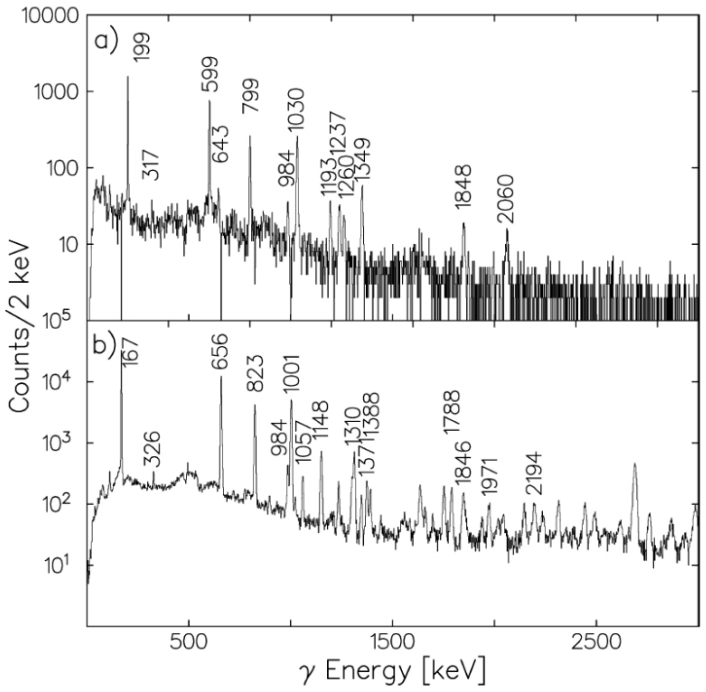

Figure 2.11: γ-ray spectra obtained for (a) ^{20}Na and (b) ^{20}F nuclei. It is clear that a far greater number of γ-ray transitions are observed in ^{20}F than ^{20}Na. This is due to several factors; (1) ^{20}F is more heavily populated than ^{20}Na and (2) States in ^{20}Na particle decay at a lower excitation energy than states in ^{20}F because of the much lower proton-emission threshold energy.

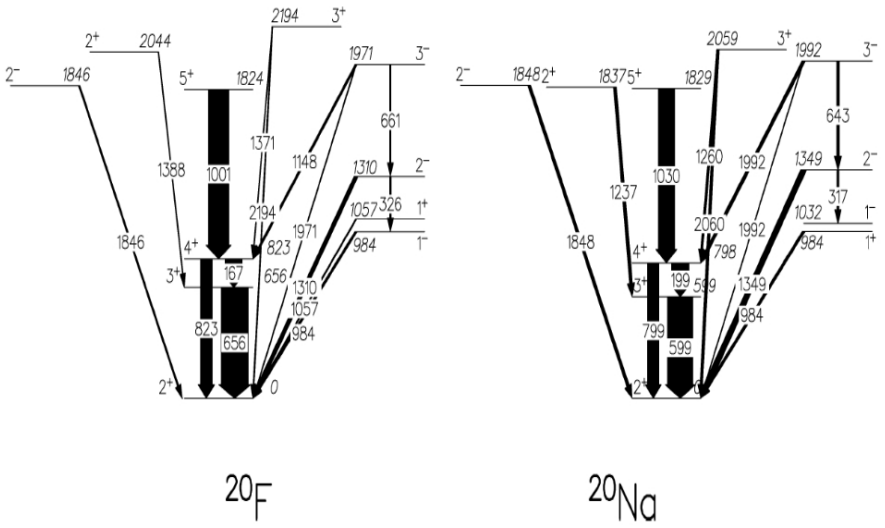

Figure 2.12: The γ-decay schemes for the mirror nuclei ^{20}F and ^{20}Na. Only the portion of the ^{20}F level scheme overlapping with the ^{20}Na level scheme is shown.

the ^{25}Al$(p,\gamma)^{26}$Si reaction rate at novae temperatures [36]. In this work, one to one correspondence was found between excited states observed in ^{26}Si and all known levels in the mirror nucleus ^{26}Mg, with the results suggesting that the complete structure of ^{26}Si below, and in the region of the proton threshold, can also be well reproduced by comparisons with the shell model calculations [67], as shown in Fig. 2.13. As a result, Seweryniak *et al.* [66] were able to identify the key 1^+ 159.2(35) keV astrophysical resonance, located above the proton-emission threshold (5517(3) keV) [19], which is expected to dominate the ^{25}Al$(p,\gamma)^{26}$Si reaction rate at novae temperatures. Compared to earlier estimates of the rate [68], the improved precision of the resonance energy, had the effect of increasing the ^{25}Al$(p,\gamma)^{26}$Si reaction rate at $T{\sim}0.1$ GK by a factor of $\sim$2, with the net result being a slight increase in the predicted yield of the cosmic γ-ray emitter ^{26}Al in novae modeling calculations [36]. This reduced uncertainty in the production of ^{26}Al in novae environments is of particular importance in the present thesis work as previously unidentified low-energy resonances, above the proton threshold, in the nucleus ^{27}Si may contribute significantly to the destruction of ^{26}Al, via the astrophysical ^{26}Al$(p,\gamma)^{27}$Si reaction at $T{\sim}0.1$ GK. Thus, further constraining the overall expected nucleosynthesis of ^{26}Al in classical novae environments.

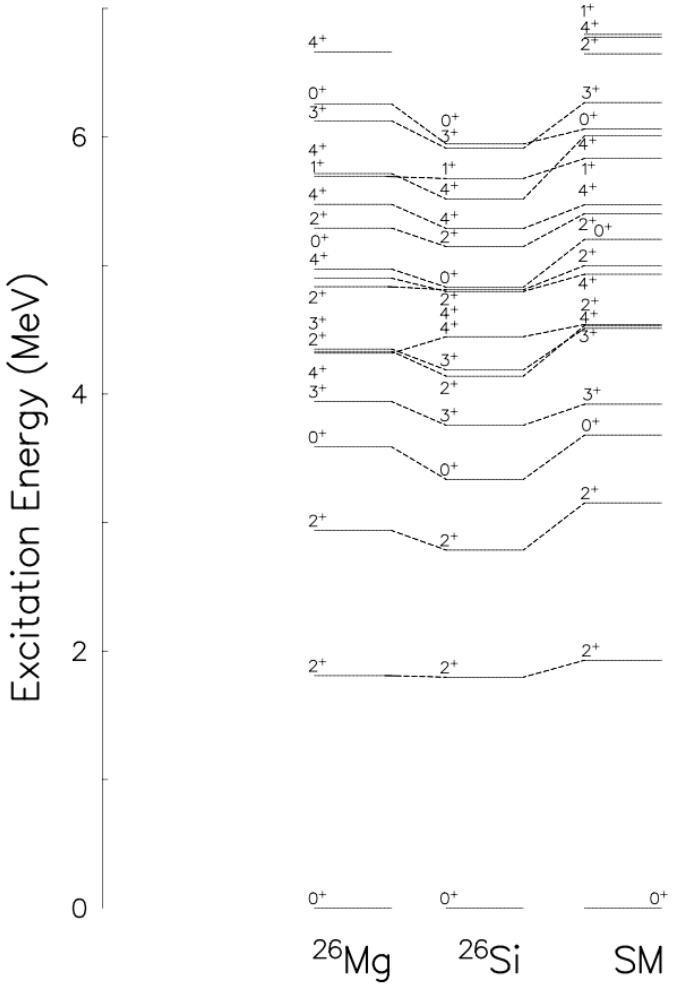

Figure 2.13: Comparison between the excited states in ^{26}Si levels, the states in ^{26}Mg, and the results of shell model calculations.

2.4 Basic Techniques of γ-ray Spectroscopy

From the above examples of Refs. [64] and [66], it is clear that modern γ-ray spectroscopy techniques provide a key alternative to light-ion transfer studies in studying the structure of astrophysically important proton-rich nuclei. Such studies of nuclei do not suffer from problems associated with difficult to produce ion beams or difficult to manufacture reaction targets, and the excited states of the nuclei of astrophysical interest can be populated through heavy-ion collisions with stable nuclei. This approach allows level structure determinations below the particle threshold of interest and the observation of γ-decaying states of astrophysical interest just above this threshold. The determination of the nuclear properties of astrophysically important excited states, in a given nucleus, can then be used to estimate indirectly the stellar reaction rate of interest. Consequently, in the present thesis work γ-ray spectroscopy techniques were used to investigate the structure of the astrophysically important proton-rich nuclei ^{24}Al and ^{27}Si and their implications for the astrophysical $^{23}\mathrm{Mg}(p,\gamma)^{24}\mathrm{Al}$ and $^{26}\mathrm{Al}(p,\gamma)^{27}\mathrm{Si}$ reaction rates, respectively. In the remainder of this section we shall focus on the principles of γ-ray spectroscopy and how they may be used to obtain structural information about the nuclei from which the radiation originates.

2.4.1 Energetics of γ Decay

From the conservation of energy, electromagnetic transitions between nuclear states must be accompanied by the emission or absorption of energy given by

$$\Delta E = E_\gamma + \frac{E_\gamma^2}{2Mc^2}, \tag{2.46}$$

where the term ${E_\gamma}^2/2Mc^2$ represents the energy taken away by the associated recoiling nucleus. At γ-ray energies ≥ 1 MeV, this recoil becomes comparable to the statistical errors associated with measuring γ-ray energies and consequently, must be taken into account when assigning transitions between states.

Gamma ray energies may be measured to precisions of $\sim$0.01 keV and thus, by measuring the energies of γ-ray transitions between states in a given nucleus, it is possible to determine, very precisely, the relative locations of the excited states.

2.4.2 Angular Momentum and Parity Selection Rules in γ Decay

A further condition that must be satisfied by a γ-ray transition between two states, is the conservation of angular momentum. Every photon carries a total angular momentum, often referred to as the multipole order, given by

$$\mathbf{L} = \mathbf{l} + \mathbf{s}, \tag{2.47}$$

where l represents the orbital angular momentum carried and s the intrinsic spin of the photon. For real photons s=1, with a component along the direction of propagation, s_z=$\pm$1, in units of $\hbar$.

Let us now consider a γ-ray transition from an initial excited state of angular momentum J_i and parity π_i to a final state J_f and π_f. Conservation of angular momentum requires that the total initial angular momentum be equal to the total final angular momentum.

$$\mathbf{J}_i = \mathbf{L} + \mathbf{J}_f \tag{2.48}$$

Since J_i, J_f and L form a closed vector triangle, L can only have non-zero integer values in the range $|J_i$ - $J_f| \leq L \leq J_i + J_f$, leading to the first selection rule for a given transition.

Whether the emitted radiation is of electric or magnetic type is then determined by the relative parity of the initial and final levels. This comes from the condition that the parities differ for electric and magnetic multipoles, given by,

$$\pi(ML) = (-1)^{L+1} \tag{2.49}$$

$$\pi(EL) = (-1)^{L} \tag{2.50}$$

From the expressions above, it is clear that electric transitions have even parity if L = even, while magnetic transitions have even parity if L = odd. Therefore, a transition consists of even electric multipoles and odd magnetic multipoles when there is no change in parity and odd electric multipoles and even magnetic multipoles when there is a change in parity between the initial and final states.

It should be noted that the spins J_i and J_f usually have values for which the selection rules permit a number of multipoles to be emitted in a given decay.

However, single-particle Weisskopf estimates indicate that the lowest-order permitted multipoles dominate and in general, only multipole orders of L=1 and L=2 need to be considered.

2.4.3 Angular Distributions

One method of deducing the multipolarity of transitions is to measure the angular distribution of γ-rays. This process requires the distribution of emitted γ-rays to be measured with respect to a fixed axis, which in fusion evaporation reactions is taken as the beam direction.

The angular dependence of the γ-ray yield may then be expressed by the directional angular distribution function,

$$W(\theta) = \sum_{k=even}^{2L_{max}} a_k P_k(cos\theta), \tag{2.51}$$

where a_0=1, P_k(cosθ) are Legendre polynomials and L_{max} denotes the largest multipolarity which actually contributes to the decay. As most states decay predominantly by L=1 or L=2 radiation, usually only terms with $k \leq 4$ have to be considered. Of particular importance are the coefficients a_2 and a_4, which may be approximated for transitions in which a change in spin between initial and final states equal ± 2, ± 1 and 0, respectively [69]. The results of such approximations reveal a relationship between the coefficients a_2 and a_4, which is shown in Fig. 2.14 [69].

If the angular distribution of a given transition is measured experimentally, it is possible to fit Legendre polynomials to the data. This procedure is achieved through the use of computer programs, for example LEGFT [70], which was used in the current work. The parameters of such fits are equal to the a_k coefficients of the angular distribution function $W(\theta)$ for a given γ-ray transition and, as can be seen in fig. 2.14, the absolute values of a_2 and a_4 can then be used to determine whether the transition changes the spin, between the initial and final states, by ± 2, ± 1 or 0.

From the discussions above, it is clear that the results of using γ-ray spectroscopy techniques to study the structure of nuclei are more precise energies and relatively unambiguous J assignments for all observed excited states compared to those obtained from reaction studies.

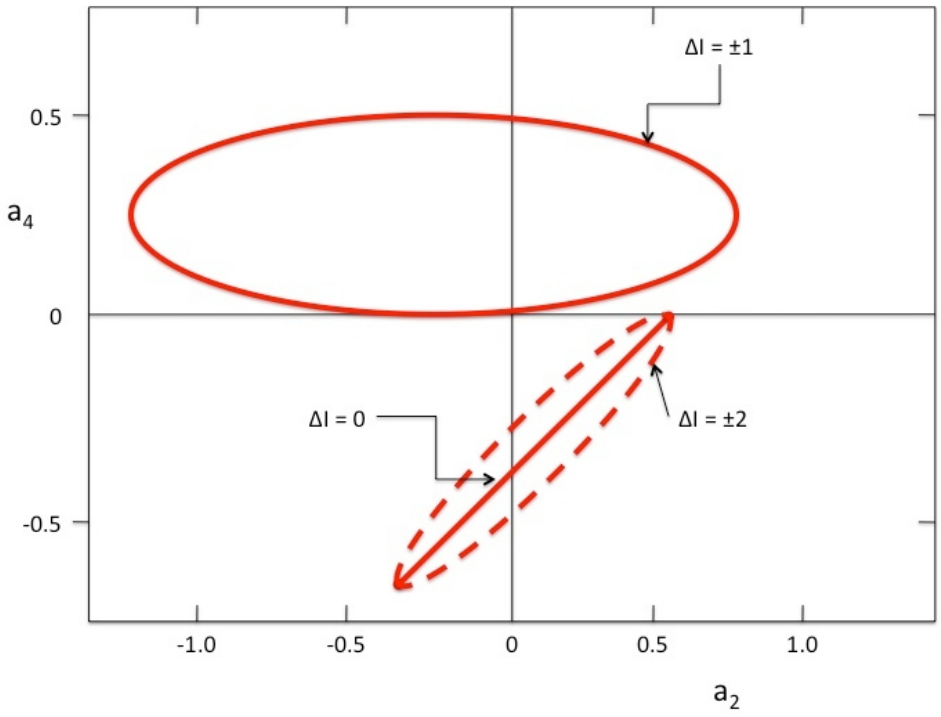

Figure 2.14: Plot of the a_4 versus a_2 coefficients of the angular distribution function $W(\theta)$.

Chapter 3

Experimental Method

In this thesis work, ^{12}C(^{16}O, n)^{27}Si and ^{10}B(^{16}O, $2n$)^{24}Al heavy-ion fusion-evaporation reaction experiments were performed to investigate the astrophysical ^{26}Al(p, γ)^{27}Si and ^{23}Mg(p, γ)^{24}Al reactions, respectively. The results of these ^{12}C(^{16}O, n)^{27}Si and ^{10}B(^{16}O, $2n$)^{24}Al experiments, which shall be referred to as Experiment I and Experiment II for the remainder of this chapter, are presented in Chapters 4 and 5. Both experiments were performed at Argonne National Laboratory using the ATLAS accelerator facility and the GAMMASPHERE germanium array. In Experiment I, there were only three open evaporation reaction channels, $1p$, $1n$ and 1α, and the GAMMASPHERE detector array was used in stand-alone mode. As a result, the channel selection in Experiment I was performed using γ-γ and γ-γ-γ coincidence techniques alone. In Experiment II, however, the Argonne Fragment Mass Analyzer was used as a channel selection device in addition to the GAMMASPHERE array as the nucleus under study, ^{24}Al, was relatively weakly produced in comparison to other reaction channels.

The following sections give an overview of the nuclear reaction mechanism and experimental equipment used in the current studies.

3.1 Heavy-ion Fusion Reactions

In this work, it was necessary to produce proton-rich nuclei and study their excited states with high precision. These particular characteristics are best achieved through the use of fusion-evaporation reactions with heavy ions. In such reactions, sufficiently high beam energies are used to overcome Coulomb repulsion and fuse two nuclei together. This process results in the formation of

a compound nucleus in a highly excited state and due to the curvature of the line of stability towards $N>Z$, the fusion of two stable nuclei normally results in a final nucleus of proton-rich character.

The decay of the compound nucleus will initially proceed through the emission of particles, as shown in Fig. 3.1 [71], in which charged-particle emission is hindered by the Coulomb-barrier and neutron evaporation usually dominates. For simplicity, as both nuclei studied in the present work were formed through the evaporation of neutrons from the compound system, this section will mainly focus on heavy-ion fusion-evaporation reactions involving neutrons. Each step of neutron emission removes a certain amount of excitation energy from the compound nucleus, equal to the sum of the neutron separation energy and the kinetic energy of the emitted neutron. The associated change in angular momentum, however, is relatively small due to the small mass and average energy of the evaporated neutrons (i.e. most of the evaporated neutrons are in l=0 or 1 quantum states). Hence, through the process of neutron evaporation, the nucleus loses a large amount of excitation energy, but only a little angular momentum.

Once the excitation energy above the y-rast line (the limit of nuclear stability with respect to angular momentum at a given excitation energy) is approximately equal to or less than the neutron separation energy, neutron emission is strongly inhibited and the nucleus continues to de-excite by the emission of γ rays. These electromagnetic transitions may be detected with high-precision γ-ray detectors and used to determine structural information for nuclei within the decay path.

In order to obtain the particular final nucleus of interest in a (HI, xn) reaction, and to populate the desired excited states, several factors must be considered; (1) a suitable beam and target combination must be chosen and (2) a suitable beam energy must be chosen. In this work, ^{12}C(^{16}O, n) and ^{10}B(^{16}O, $2n$) heavy-ion fusion-evaporation reactions were chosen to produce the proton-rich nuclei ^{27}Si and ^{24}Al, respectively. It is important to mention at this point that the formation of ^{27}Si and ^{24}Al nuclei through either $1p$ or $2p$ evaporation channels was not feasible using stable beams and targets. Consequently, such evaporation channels were not favoured as suitable reaction mechanisms for the production of ^{27}Si and ^{24}Al nuclei in this work. Furthermore, a single α evaporation channel was not favoured in Experiment II as it would have compromised the recoil detection efficiency and Z separation. Stable beams of ^{16}O ions were readily

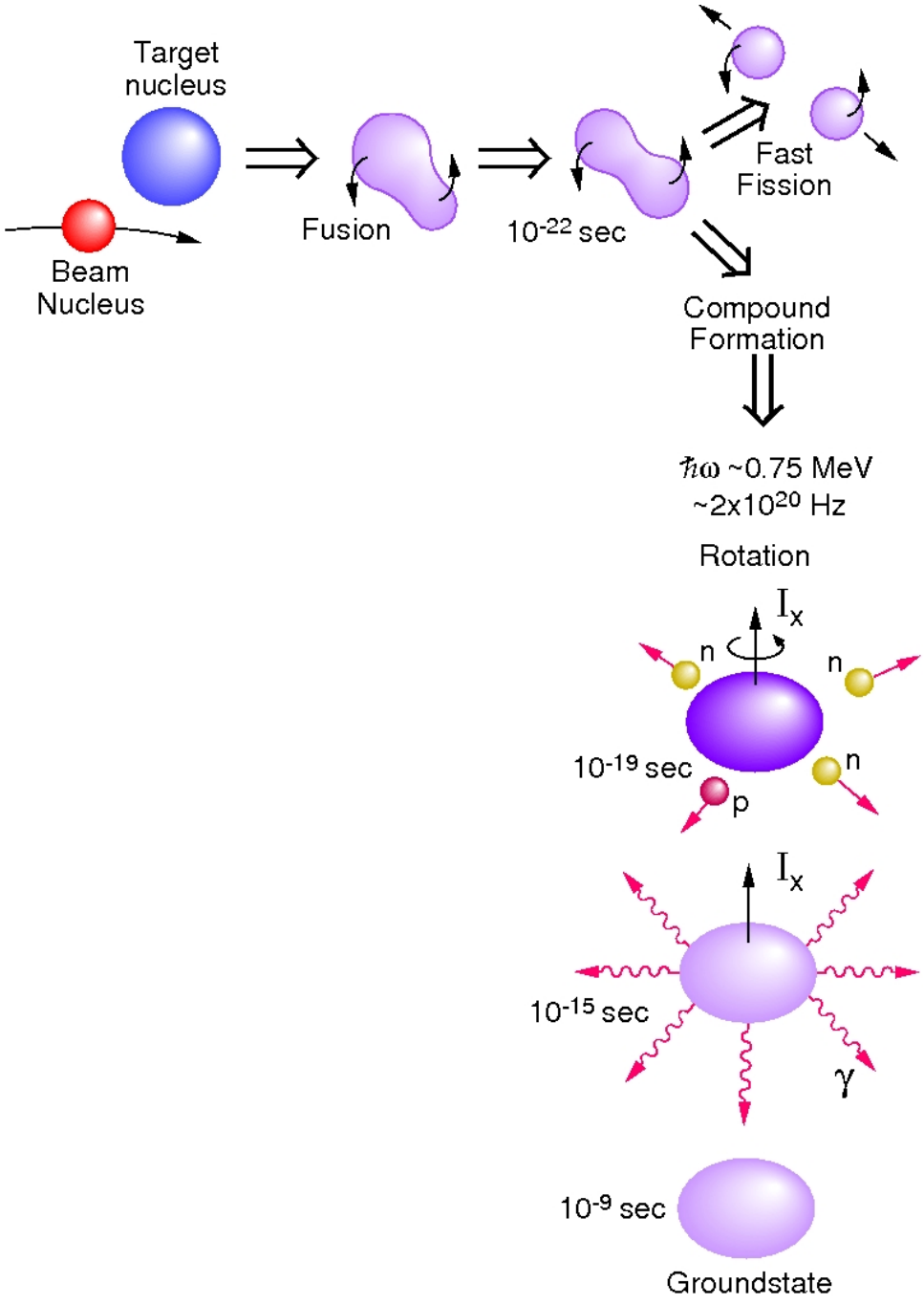

Figure 3.1: The various stages during and following a heavy-ion fusion reaction [71].

available, as were stable ^{12}C and ^{10}B targets, and previous studies of astrophysical reactions, similar to those investigated in this thesis work, used $1n$ and $2n$ evaporation channels to produce the proton-rich nuclei of interest with great success [64; 66; 72; 73]. Hence, in the current studies $1n$ and $2n$ evaporation channels were also used to produce the proton-rich nuclei ^{27}Si and ^{24}Al.

The present investigation of the astrophysical ^{26}Al$(p,\gamma)^{27}$Si and ^{23}Mg$(p,\gamma)^{24}$Al reactions required the population of excited states above the proton threshold in the nuclei ^{27}Si and ^{24}Al, respectively. These states, above the proton thresholds, are not expected to be fed by γ-ray transitions from higher-lying excited states as all high energy excited states above the respective proton-emission thresholds are expected to exhibit 100% proton decay branches. Therefore, in the heavy-ion fusion-evaporation reactions performed in the present work, γ-decaying proton-unbound excited states in ^{27}Si and ^{24}Al are expected to be populated directly by the $1n$ and $2n$ evaporation of ^{28}Si and ^{26}Al compound nuclei, respectively. As a result, the beam energy for each experiment was chosen to optimize the direct population of astrophysically important excited states above the respective proton thresholds of ^{27}Si and ^{24}Al. The estimates of required beam energy took into account the desired excitation energy of the residual nucleus, the ground state mass of the residual nucleus, the mass of the evaporated neutrons, the average kinetic energy carried away by the emitted neutrons (typically ∼8–10 MeV per neutron) and the masses of the beam and target used. In both Experiment I and Experiment II, beams of ^{16}O ions were used to bombard stable targets and the ^{16}O beams were accelerated and delivered to the target area by the Argonne Tandem Linear Accelerator System (ATLAS). In Experiment I, a beam energy of 26 MeV was chosen to maximize the population of proton-unbound states in ^{27}Si, whereas in Experiment II, a beam energy of 60 MeV was chosen to maximize the population of proton-unbound states in ^{24}Al.

3.2 ATLAS

ATLAS is a superconducting linear accelerator of heavy ions at energies in the vicinity of the Coulomb barrier. The overall system consists of a sequence of machines where each accelerates charged ions and then feeds the beam into the next section for additional energy gain. Figure 3.2 shows a schematic floor plan of the ATLAS facility and as can be seen, there are two 'injector' accelerators

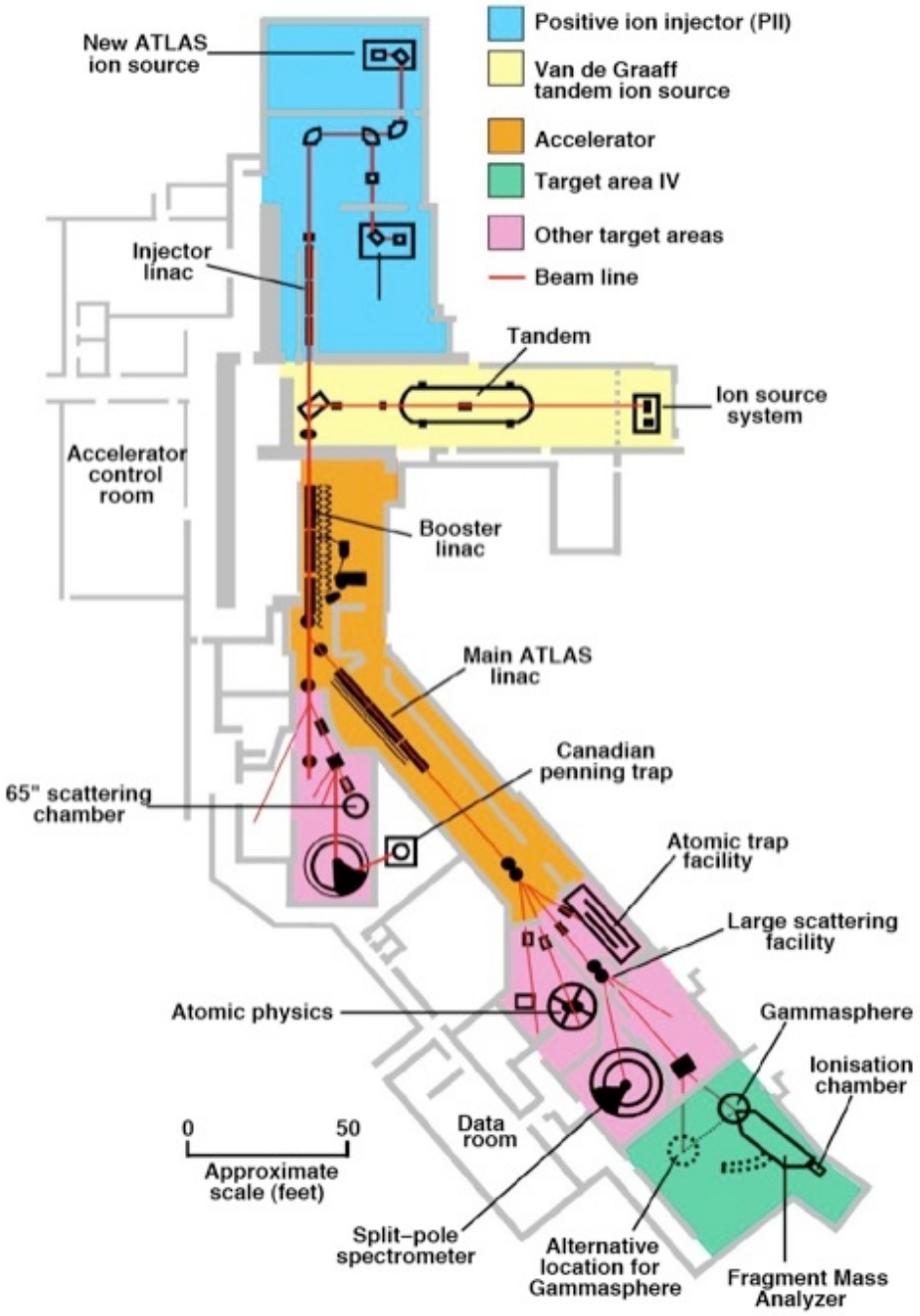

Figure 3.2: Schematic floor plan of the ATLAS facility.

available for the initial production of the ion beams; a 9 MV electrostatic tandem Van de Graaff, or a 12 MV low-velocity linac and electron cyclotron resonance (ECR) ion source called the Positive Ion Injector (PII). For the experiments performed in the present work, the PII was used to produce the desired ion beams for further acceleration.

In this section of the ATLAS system, ion species are produced by an ECR ion source, which confines a plasma in a magnetic trap. Microwave radiation is injected into the plasma chamber with a frequency equal to the electron gyro-frequency in the magnetic field. This creates a resonance zone for the electrons, accelerating them as they pass through and consequently, neutral atoms of the isotope required for acceleration are also ionised by successive collisions with these accelerated electrons. The ions are then extracted with an electrode system through a hole in the positively-biased plasma chamber and injected into the PII linear accelerator.

Following this initial production and acceleration in the PII, the ion beam is directed into the main body of the ATLAS accelerator system, consisting of a 20 MV 'booster' linac and the 20 MV ATLAS linac. In this section of acceleration, 62 superconducting split-ring resonators are used to create an accelerating field through the linac. Each resonator is individually controlled and as such, by adjusting their relative RF phases, the resonators can be tuned to a wide range of effective velocities, allowing any ion, regardless of mass, to be accelerated. Furthermore, magnetic fields are provided by superconducting solenoids between the resonators, which allow for the steering and focusing of the beam.

In Experiment I and Experiment II, the accelerated beams of ^{16}O ions were directed onto ^{12}C and ^{10}B targets, respectively, located in target area IV, as shown in Fig. 3.2.

3.3 Target Preparation

The ^{12}C and ^{10}B targets used were produced through electron beam bombardment evaporation at Argonne National Laboratories, Chicago. In this method, the enriched carbon or boron, initially in the form of a powder, is placed in a vacuum sealed crucible and subjected to electron bombardment from an electron-beam gun. This causes the evaporation of a thin film of powder material, which is deposited on a glass slide. These thin films are then transferred to a target

frame, using the surface tension of water to lift the film from the glass and position it across the frame. It should be noted that this method of target preparation, shown in Fig. 3.3, sets an upper limit of ∼100–200 μg/cm^2 for the target thicknesses.

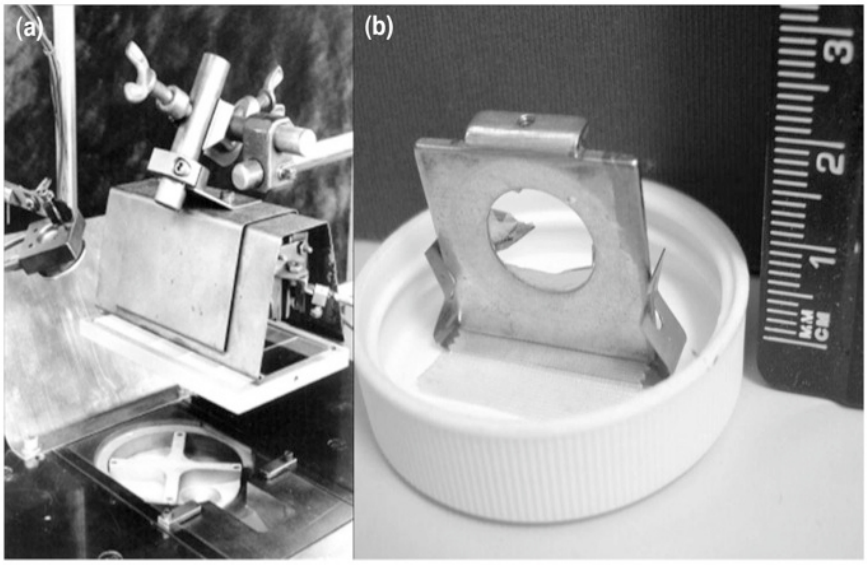

Figure 3.3: (a) A photograph of the electron-beam evaporation apparatus used for target preparation at Argonne National Laboratory. (b) A target frame used for mounting a thin carbon or boron target.

For each experiment, the respective ^{12}C and ^{10}B target was placed inside a spherical aluminium vacuum sealed target chamber situated at the centre of the GAMMASPHERE detector array.

3.4 GAMMASPHERE

In this thesis work, the GAMMASPHERE detector array [74] was used to detect the prompt electromagnetic radiation resulting from heavy-ion interactions in the target, in the energy range 50 keV – 8 MeV. The underlying structure of the array is that of a 122-element polyhedron consisting of 110 hexagons and 12 pentagons, as shown in Fig. 3.4 [75]. Each of the hexagons can house a single detector module, while the pentagons are used for the support structure and entrance and exit beam lines. The 110 GAMMASPHERE detector modules are arranged in 17 different rings of constant angle θ with respect to the beam line,

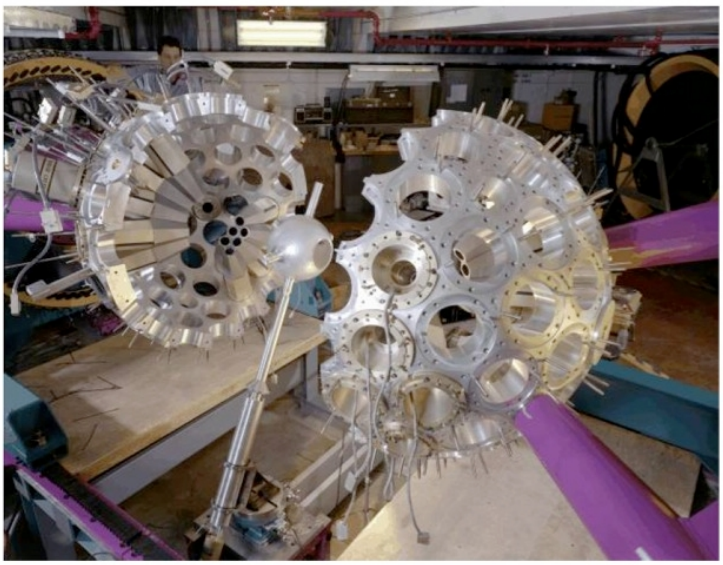

Figure 3.4: Polyhedral support structure of the GAMMASPHERE detector array, showing the target chamber situated at the centre [73].

the details of which are displayed in Table 3.1. This particular arrangement allows both the energy and the angular distribution of γ-ray radiation with respect to the beam axis, following nuclear reactions in the target chamber, to be measured.

The individual γ-ray detector modules, shown in Fig. 3.10, consist of a number of components including; an n-type high-purity germanium detector (HPGe), a Compton-suppression shield, electronics and cryogenics. Each detector module has a Ge solid angle of 0.053 sr and an opening angle of 7.4°. When all 110 detector modules are in place there is nearly a 4π geometric coverage of a γ-ray source within the target chamber. The two types of γ-ray detector used in this work were made from relatively high-Z material, resulting in high probabilities for γ rays to interact via the photoelectric effect within the detector volume. The Ge crystals, 71 mm in diameter and 84 mm long, were used to measure the energy of the emitted γ-ray radiations due to the excellent energy resolution achieved with such detectors. Compton suppression, however, was enabled by bismuth germanate (BGO) shields, which, although having a relatively poor energy resolution $\geq$6%, allow for the detection of a large number of γ rays due to the relatively high density of such detectors. Further details of the specific γ-ray detectors used in the present study are presented in Appendix A. Finally,

Table 3.1: Details of the specific rings of GAMMASPHERE, including the maximum number of detectors in each ring and their angles, θ, relative to the beam axis. The values of $\cos^2\theta$ have been included to highlight the symmetry of the array.

Ring	No. of detectors	θ(degrees)	$\cos^2\theta$
1	5	17.27	0.911
2	5	31.72	0.724
3	5	37.38	0.631
4	10	50.07	0.412
5	5	58.28	0.276
6	10	69.82	0.119
7	5	79.19	0.035
8	5	80.71	0.026
9	10	90.00	0.000
10	5	99.29	0.026
11	5	100.81	0.035
12	10	110.18	0.119
13	5	121.72	0.276
14	10	129.93	0.412
15	5	142.62	0.631
16	5	148.28	0.724
17	5	162.73	0.911

Figure 3.5: Schematic diagram of four detector modules [71].

a liquid nitrogen (LN_2) coolant system was required for every detector module to reduce the thermal excitation of valence electrons across the band gap in the Ge crystals.

As can be seen in Fig. 3.5, there are several possible outcomes for a γ-ray photon incident on a GAMMASPHERE detector module; (1) the photon can deposit all its energy in the Ge crystal via the photoelectric effect, (2) the photon can Compton scatter out of the Ge crystal and deposit its energy in the BGO shields and (3) the photon can miss the Ge crystal completely and deposit all its energy in the Hevimet shield. Of course, the only desirable outcome for data collection is the case in which the photon deposits all of its energy in the Ge crystal and thus, only these events are ultimately processed as "good events". For cases (2) and (3), the resulting signals are processed in coincidence with that of the Ge crystal and these events are subsequently vetoed.

It is important to mention at this point that, for many GAMMASPHERE experiments the γ-ray energy resolution is dominated by the Doppler broadening, caused by the motion of the recoiling nucleus. The Doppler broadening is predominantly dependent on the opening angle, θ, of the Ge detector and as

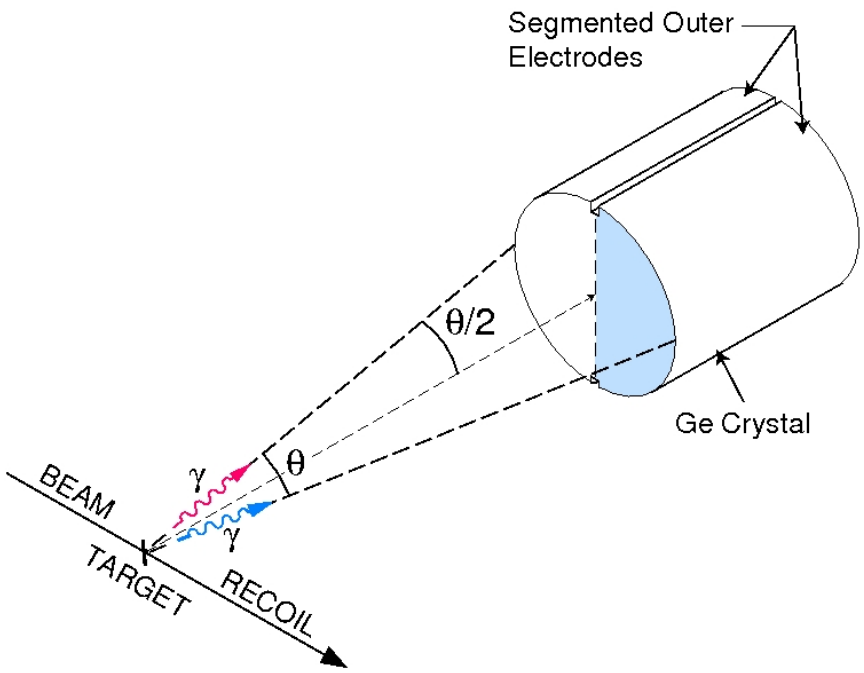

Figure 3.6: Schematic diagram of an electrically segmented Ge detector [71].

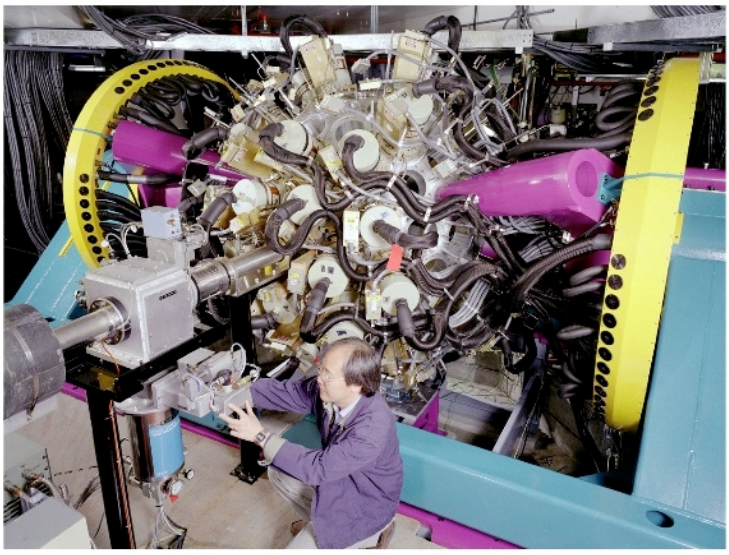

Figure 3.7: Photograph of the closed GAMMASPHERE detector array [71].

such, in order to improve the granularity of the array ∼70 of the GAMMASPHERE detectors have been electrically segmented into two D-shaped halves, as shown in Fig. 3.6. The high-resolution, total-energy signal is still read from a common electrode at the centre of the Ge detector while lower resolution signals can be read separately from each half, indicating which side of the crystal was hit first. Thus, the effective angular size of the Ge detector is reduced by a factor of two and the total resolving power of the GAMMASPHERE array is improved by a factor of two.

The GAMMASPHERE detector efficiencies are quoted as ∼78%[1] for each Ge crystal [76], with the full array of 110 detectors estimated to have a total photopeak efficiency of 9.4% for 1.3 MeV γ rays. Furthermore, the energy resolution of the GAMMASPHERE array is quoted as <2.4 keV for 1.3 MeV γ rays.

3.5 Recoil Selection

The selection of events corresponding to the strongest evaporation channels, such as the 1n channel used to produce ^{27}Si nuclei in Experiment I, may be achieved by using γ-ray coincidence techniques with the GAMMASPHERE detector array in stand alone mode. In Experiment II, however, ^{24}Al nuclei were produced via the ^{10}B(^{16}O, $2n$) fusion-evaporation channel, which represents a weakly populated reaction channel. Therefore, in Experiment II, it was necessary to employ additional equipment to be used in conjunction with the GAMMASPHERE array to select the particular reaction channel of interest; (1) the Argonne Fragment Mass Analyzer (FMA), (2) a microchannel plate and (3) an ionisation chamber.

3.5.1 The Fragment Mass Analyzer (FMA)

The Fragment Mass Analyzer is a recoil mass spectrometer consisting of electrical and magnetic dipoles and quadrupoles, as shown in Fig. 3.8 [77], which when used as a recoil selection device is situated directly behind the GAMMASPHERE array, as shown in Fig. 3.9.

[1] being the percentage of the efficiency for a 3" x 3" cylindrical NaI(TI) scintillation crystal, with a source-detector spacing of 25 cm.

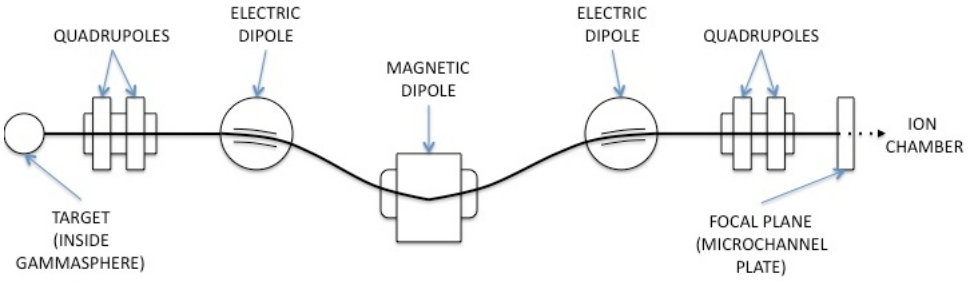

Figure 3.8: A schematic diagram of the FMA.

The force on a charged particle as a result of electric and magnetic fields, E and B is given by the Lorentz force,

$$\mathbf{F} = q(\mathbf{E} + v \times \mathbf{B}), \tag{3.1}$$

where q is the charge on the particle and v is its velocity. Furthermore, from Newton's second law of motion, the acceleration of a charged particle with mass m is given by,

$$a = \frac{q}{m}(\mathbf{E} + v \times \mathbf{B}). \tag{3.2}$$

Thus, by defining the energy of the particles entering the FMA and adjusting both the relative field strengths of the electric and magnetic dipoles and distances between them, the FMA can be used to spatially separate recoils by their mass-to-charge ratios, A/q. The quadrupole lenses are set to focus the charged particles at the focal plane and widen the solid angle acceptance of the FMA to 8 msr. The total length of the FMA is 8.2 m and the energy acceptance of the device is $\pm$20%, which translates to an A/q acceptance of $\pm$4%. The spatially separated recoils are transmitted at the focal plane of the FMA into a further detector, known as the focal-plane detector. In Experiment II, the FMA was set to transmit A=24 recoils and setup calculations indicated a 9^+ charge state as the optimum charge state for the transmission of ^{24}Al recoils, via a $2n$ evaporation channel. Furthermore, the overall transport efficiency of the FMA for A=24, charge state 9^+, recoils was calculated to be 9.8%.

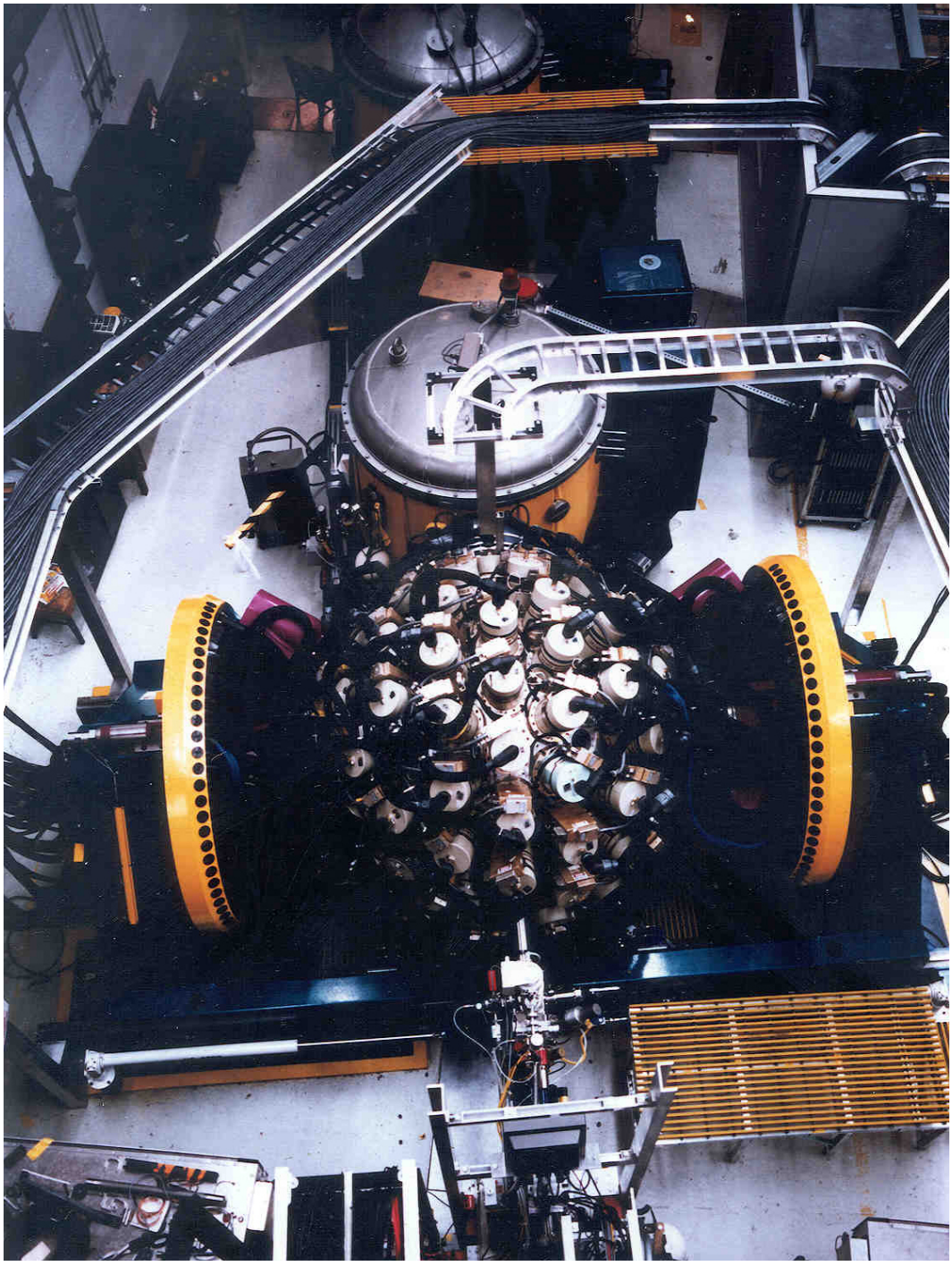

Figure 3.9: Photograph of the combined GAMMASPHERE and FMA system.

3.5.2 Microchannel Plate Detector System

A microchannel plate was used as the focal-plane detector in this work and determined both position information on the recoils passing through the FMA and signals for time-of-flight measurements between GAMMASPHERE and the focal plane of the FMA. A schematic representation of this detector system is shown in Fig. 3.10 [78].

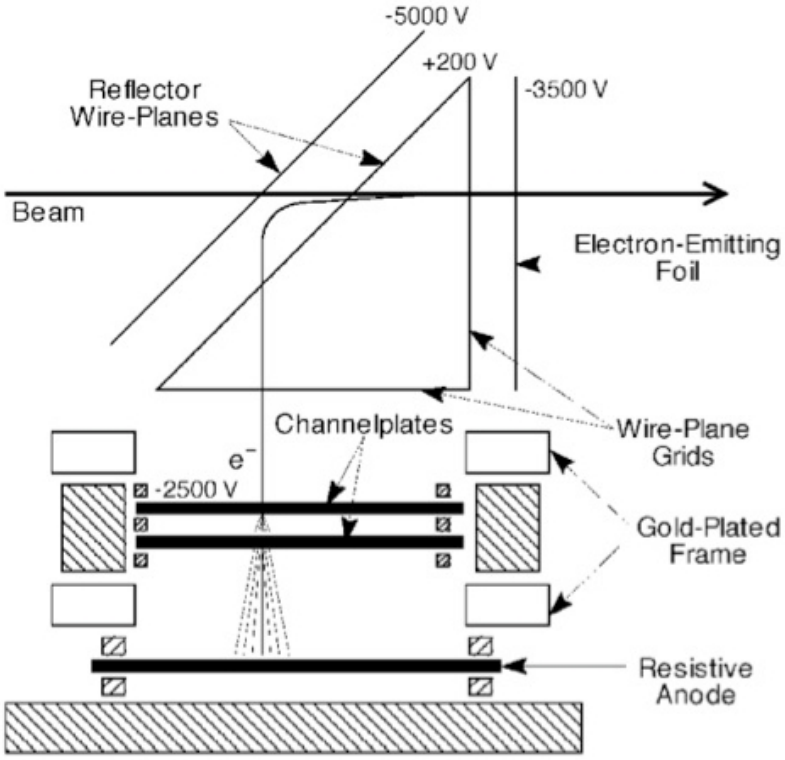

Figure 3.10: Schematic representation of the micro-channel plate detector system.

The beams of recoils transmitted by the FMA are directed onto an electron production foil. Electrons emitted from the foil, biased at -3500V, are accelerated toward a wire plane held at +200V. These electrons are then reflected through 90° using an electrostatic mirror at -5000V and subsequently decelerated onto the channel plates. The channel plates produce an avalanche of secondary electrons, which are collected at the resistive anode and result in a large output pulse. X and Y coordinate information is directly related to the

charge collected at the channel plates and in the present detector, ∼2.5 mm position resolution is achieved. The anode signal is also used to start a fast logic signal for time-of-flight measurements, in which a resolution of ∼1 ns may be achieved.

3.5.3 Ionisation Chamber

In order to determine the atomic number, Z, of the recoiling nuclei exiting the FMA and focal-plane detector, a further piece of detection apparatus is required. In the present work a segmented-anode ionisation chamber filled with isobutane gas, at a pressure of 17 Torr, was employed for this operation. Figure 3.11 shows a photograph and a schematic diagram of this device.

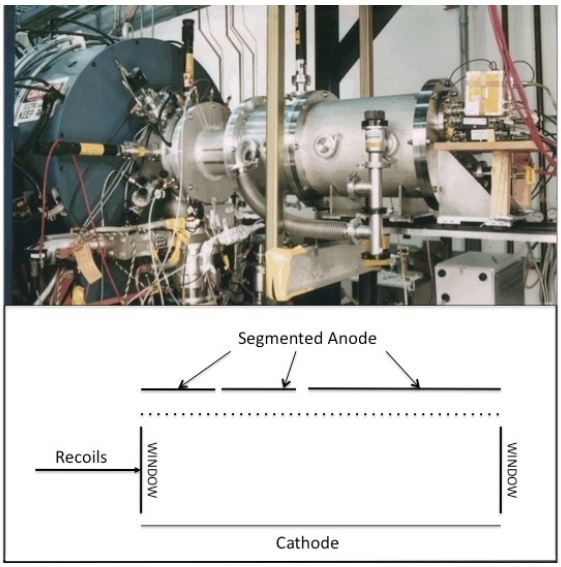

Figure 3.11: (top) a photograph of the ionisation chamber at the back of the FMA (bottom) a schematic diagram of the ionisation chamber, in which the anode and cathode electrodes are held at +ve and -ve voltages, respectively.

As recoiling ions enter the chamber, the gas molecules of isobutane begin to ionise. Under the influence of the electric field, the resulting electrons and positive ions drift toward the anode and cathode, respectively. The collection of charge at the anode then provides an electrical signal, which is proportional to the energy loss $-dE/dx$ of the recoiling particle passing through the chamber.

The energy loss of particles passing through a specific material is given by the Bethe-Bloch formula [79],

$$-\frac{dE}{dx} = \frac{4\pi Z^2 n_e}{m_e c^2 \beta^2}\left(\frac{e^2}{4\pi\epsilon_0}\right)^2\left[ln\left(\frac{2m_e c^2\beta^2}{I}\right) - ln(1-\beta^2) - \beta^2\right], \qquad (3.3)$$

where $m_e c^2$ is the electron rest mass (0.511 MeV), n_e is the electron density of the gas within the chamber, Z is the atomic number of the recoil, $\beta{=}v/c$ is the recoil velocity and I is the mean excitation potential of the gas. By plotting the total energy loss over all three anode segments in the chamber, E, against the energy loss in the first two segments, ΔE, the events corresponding to different Z can be distinguished. The ionisation chamber plot produced in Experiment II is shown in Fig. 3.12.

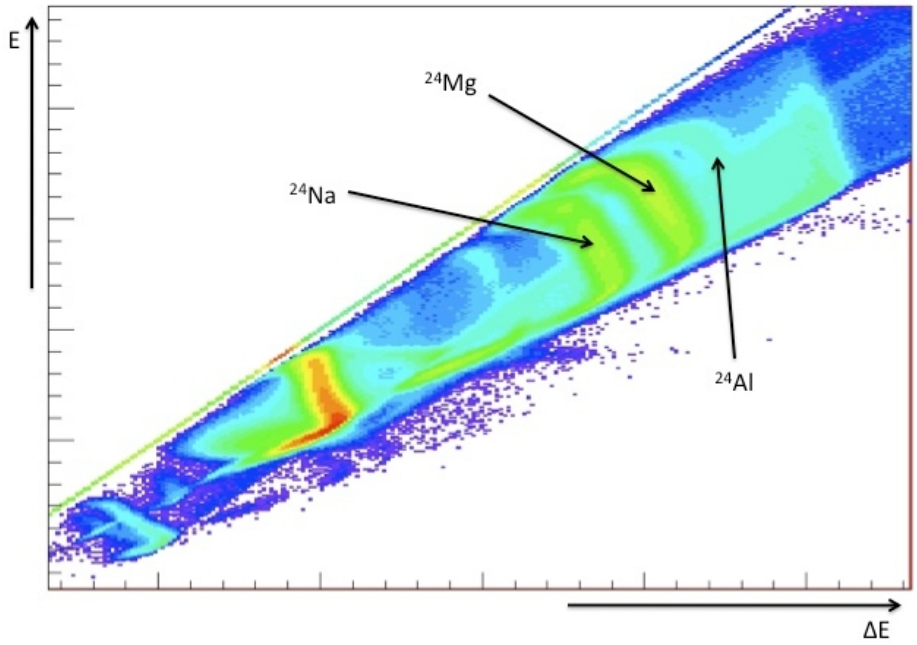

Figure 3.12: Two-dimensional spectrum of E vs. ΔE for $A{=}24$ recoils passing through the ionisation chamber.

3.6 Electronics and Data Acquisition

Both electronics and data acquisition systems are required to extract and record all data of interest from the experimental detection equipment.

3.6.1 Gammasphere Triggers

The energy and timing signals from the GAMMASPHERE Ge detector modules are processed by custom-built VXI crates. The electronic circuitry for each Ge detector module in GAMMASPHERE contains an individual amplifier and discriminator for each Ge detector (1) and BGO detector (7) in the module. These circuits are used to create logic signals associated with the firing of individual detectors, which are then used to determine whether the detected γ-ray event satisfies the minimum multiplicity conditions (trigger conditions). If these conditions are satisfied, the various signals produced by the event are recorded for off-line processing.

For the process of creating event triggers, each time a Ge detector discriminator fires, 50 mV is added to an electric sumbus for 2μs, as shown in Fig. 3.13(a). However, if a coincident signal is received from one of the BGO shields then the 50 mV addition is cut short, as shown in Fig. 3.13(b). In GAMMASPHERE, there are three triggers which can be set to determine which events are recorded. The first level of triggering is called the pre-trigger (PT), of which the value is often set to be "3". This means that once three or more Ge detectors of GAMMASPHERE have fired simultaneously (by which we mean at least three Ge detectors detect a γ ray within a time window of 200-800 ns), the PT is satisfied and blocks any further acquisition, as shown in Figs. 3.13(c) and (d). The next level of triggering is called the main trigger (MT), which is applied 1 μs after the PT and is again often set to be "3". If the pre-trigger is satisfied, but the main trigger is not, at least one of the signals that contributed to the initial magnitude of the sumbus must have been Compton suppressed such that the sumbus has fallen below the threshold for satisfying the main trigger within a 1 μs gap, as shown in Fig. 3.13(d). Finally, a late trigger will generally spend 6 μs to inspect the pile-up status in order to inspect the possibility that more than one γ ray was absorbed by a single Ge detector in the event. If all these conditions are fulfilled, the event is classed as a "GOOD EVENT" and is recorded and processed by the GAMMASPHERE acquisition system. If in any one of the above steps, the minimum multiplicity requirement is not met, the acquisition is reset within $\sim$1 μs to be available for incoming signals. For Experiment I the PT and MT were both set to "3" and the LT was set to 6μs.

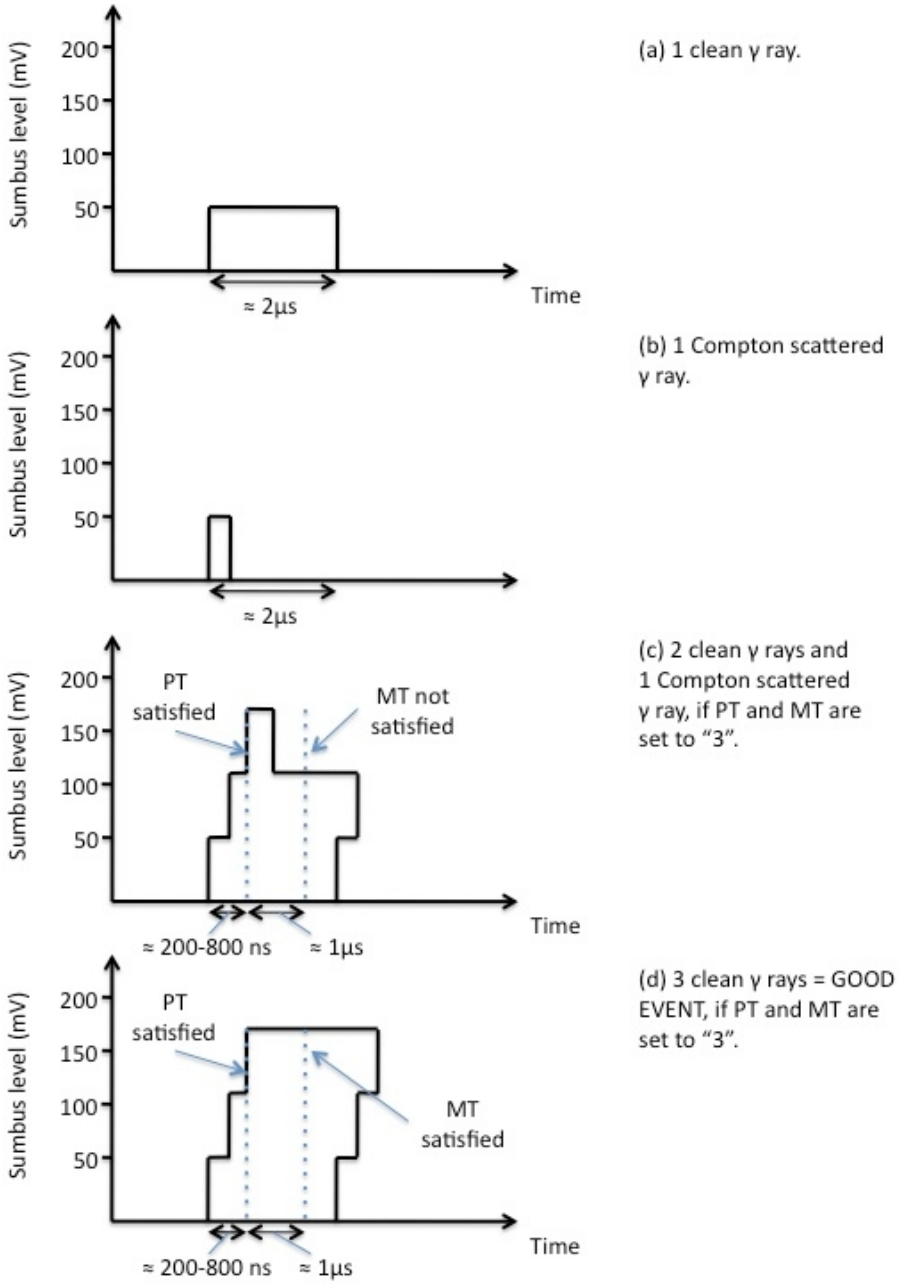

Figure 3.13: An example of how sumbus signals look for various γ-ray events in GAMMASPHERE. In (c) and (d) the pre-trigger (PT) is set to "3" (150 mV) and the main trigger (MT) is applied $\sim 1\mu$s after three coincident γ rays (detected within 200–800 ns of each other) are first detected. The final event shown in (d) is the only one classed as a 'good' event, which is then recorded and processed, if the main trigger is also set to "3".

For Experiment II, the PT was also set to “3”, the MT was set to “2” and the LT was set to 6μs.

3.6.2 Recoil Triggers

To perform recoil selection in combination with the GAMMASPHERE detector array, it is essential to ascertain when γ-ray signals are associated with a recoil which has progressed through the FMA and into the ionisation chamber. This is done by generating a recoil-γ logic signal, which represents the overlap of a single-γ 1 μs Ge signal with the 1 ns microchannel plate signal, as shown in Fig. 3.14 (duplicated from Ref. [80]). This logic signal is supplied to the

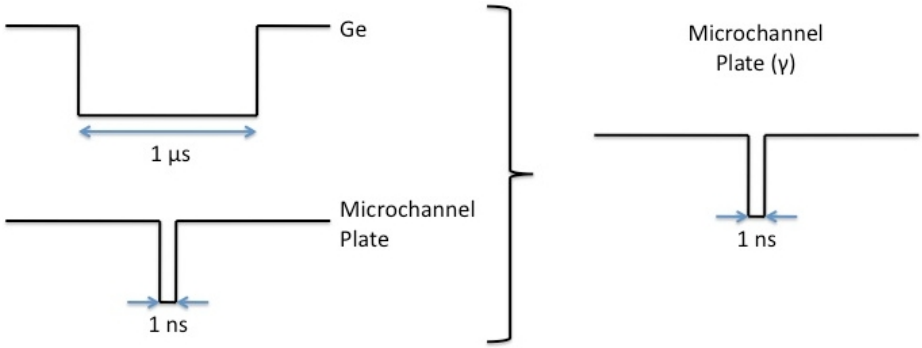

Figure 3.14: The overlap of a wide Ge signal with a narrow microchannel plate signal, resulting in a recoil-γ signal, microchannel plate(γ).

GAMMASPHERE Master Trigger Module (MTM), which can be used to apply a wide variety of trigger conditions involving γ rays and external triggers.

3.6.3 Timing Signals

A further condition essential in the acquisition of data from GAMMASPHERE experiments is the rejection of random events. This is achieved by determining the time taken, relative to the reaction, for each detector participating in a given event to generate a signal.

Timing signals for individual γ rays are measured using a TAC between the MT and the individual detector logic signals within the VXI crates. However, in order to generate timing signals for individual γ rays relative to the RF, which

is better timed than the MT, it is necessary to subtract an additional time parameter called "$TAC2$", which gives the time of the MT conditions relative to the accelerator RF. The resulting Ge time spectrum (tge), representing the time between the Ge signal and the beam RF, is shown in Fig. 3.15.

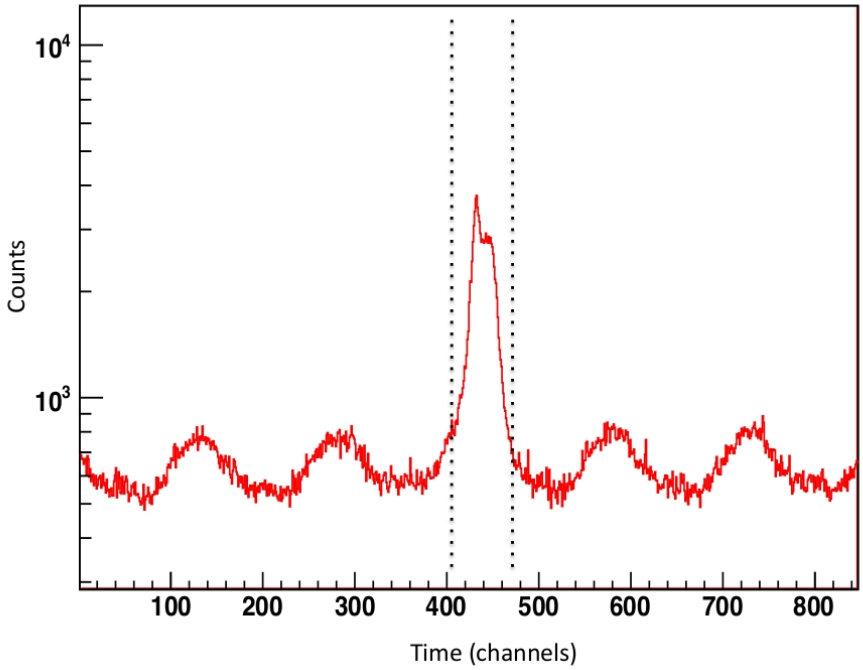

Figure 3.15: Ge time spectrum indicating the gate set to select only those events in the central peak and thus, reject random events.

From Fig. 3.15, it can be seen that most events fall into a central peak, while smaller peaks appear either side. The central peak represents the "real" events and the smaller peaks represent random coincidences between the event and the beam bursts by which the event was not generated. Consequently, a gate is set so as to analyse only those events falling within the central peak, as shown in Fig. 3.15.

In Experiment II there was also a timing parameter between the microchannel plate and Ge signals (tgcp), similarly gated upon to reject random coincidences, as shown in Fig. 3.16.

All the trigger levels described above are set for the specific experiment undertaken and determine which of the events collected are permanently recorded onto an external hard disk for analysis.

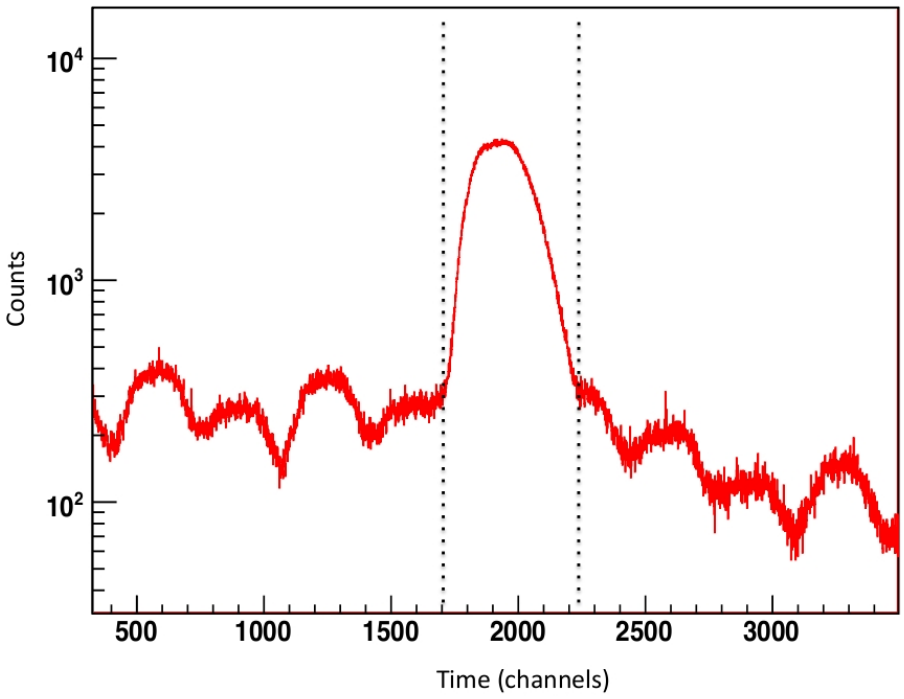

Figure 3.16: Spectrum of time between Ge and microchannel plate signals.

3.7 Preliminary Data Analysis

Once all the experimental data have been recorded onto a hard drive, the off-line analysis procedure begins. The data collected during the experiment are stored in binary form. These data are converted into spectra in "ROOT" [81] format by the use of a computing sort code called "GSSort" [82].

3.7.1 Gamma-ray Calibration

As a first step, before tackling any actual experimental data, it is important that the γ-ray calibration data be analyzed. Calibration data were obtained by placing γ-ray sources (nuclei with γ rays of well-known energy and intensity) at the target position of GAMMASPHERE. The purpose of such calibrations is to determine the relationship between the detector channel number and the actual energy value, and to establish the detection efficiency of the GAMMASPHERE detector array. The ^{24}Al experiment used both ^{152}Eu and ^{182}Ta sources [70], whereas the ^{27}Si experiment used ^{152}Eu and ^{56}Co sources [70] with an addi-

tional high energy 6128.63(4) keV γ-ray line taken from an ^{16}O source [83]. The calibration spectra obtained for the ^{24}Al experiment and ^{27}Si experiment are presented in Appendix B, together with further details of the γ-ray calibration.

3.7.2 Doppler Correction

When performing inverse kinematic experiments, such as those performed in the present work, the velocity of the recoiling nuclei produces a sizable Doppler shift on the energy of emitted γ rays. If a γ ray is produced from a source moving at a velocity, v, and is detected at an angle, θ, with respect to that velocity, the measured energy $E_{\gamma'}$ is related to the true energy $E_{\gamma 0}$ by the relativistic Doppler equation,

$$E_{\gamma'} = E_{\gamma 0}\frac{(1-\beta^2)^{1/2}}{1-\beta cos\theta}, \tag{3.4}$$

where β=v/c. However, in the experiments performed here, the recoils move non-relativistically and thus, the non-relativistic approximation,

$$E_{\gamma'} = E_{\gamma 0}(1+\beta cos\theta), \tag{3.5}$$

may be adopted. An example of Doppler uncorrected spectra for different rings of GAMMASPHERE is shown in Fig. 3.17.

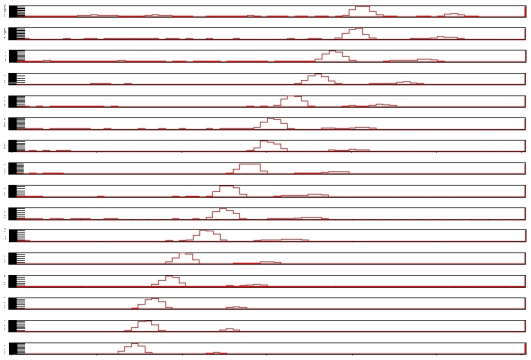

Figure 3.17: Example of γ-ray singles spectra observed for different rings of GAMMASPHERE with no Doppler correction.

In general, it is reasonable to assume a narrow distribution of recoil velocities for recoils of the same isotope and therefore, a mean value of β, calculated from classical considerations, can be used in the data sorts. An example of the corresponding Doppler corrected spectra of Fig. 3.17 is shown in Fig. 3.18.

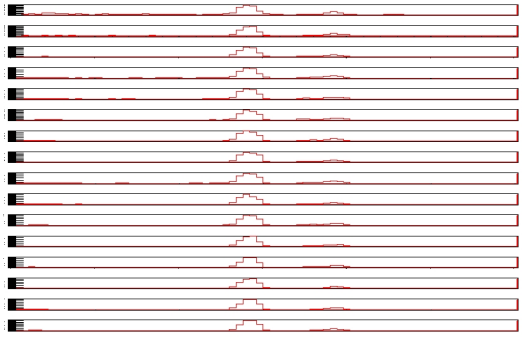

Figure 3.18: Example of γ-ray singles spectra observed for different rings of GAMMASPHERE with Doppler correction.

3.7.3 Level Scheme Construction

The level schemes presented in this thesis were deduced by analyzing γ-ray singles spectra, γ-γ coincidence matrices and γ-γ-γ coincidence cubes, using the computer programs "gf3", "ESCL8R" and "LEVIT8R" [70], respectively. The γ-ray singles spectra produced were used to fit direct γ-ray transitions to the ground state and to determine transition intensities. However, the singles spectra give no indication of the ordering of levels within a decay scheme and as such γ-γ coincidence matrices and γ-γ-γ coincidence cubes are required to examine γ-decay cascades, involving the emission of two or more photons to the ground state. For the ^{24}Al experiment a γ-ray singles spectrum and γ-γ coincidence matrix was used to construct a level scheme, whereas in the ^{27}Si experiment a γ-ray singles spectrum and γ-γ-γ coincidence cube was used.

In a two-dimensional coincidence matrix, the contents at a particular location are incremented for every event that consists of the detection of two simultaneous γ rays of energies E_1 and E_2, respectively, with the matrix symmetric about x=y. Similarly, in a three-dimensional coincidence cube, the contents at a particular location are incremented for every event that consists of the detection of three simultaneous γ rays of energies E_1, E_2 and E_3, respectively, with the matrix symmetric about x=y=z.

The analysis of coincidence matrices and coincidence cubes is done by setting "gates", in which the energies of all but one of the γ-ray transitions are specified and the projection onto the remaining axis is inspected. This resultant one-dimensional γ-ray spectrum, in principle, contains only transitions that are in

coincidence with the gated energies. Consequently, a level scheme may be built up by determining the coincidence relationships between the various transitions in either the matrix or the cube.

In determining whether a particular assignment is correct in the level scheme, several rules must be obeyed; (1) The total energies of parallel paths connecting two different levels must be equal (E_1+E_2+E_3 = E_3+E_4 = E_5), as illustrated in Fig. 3.19, and (2) the spins of the initial and final levels must reflect the

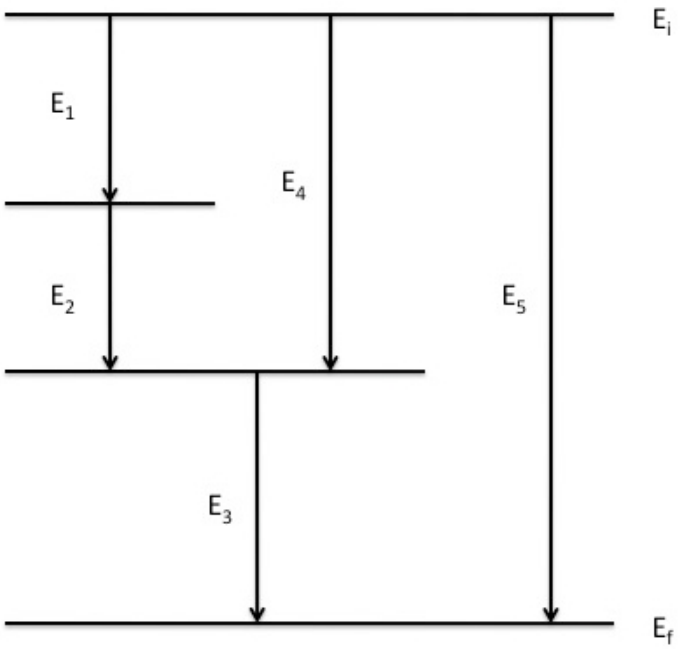

Figure 3.19: Energy sum rule for nuclear decay.

angular momentum carried away by the γ-ray transition. In order to determine the angular momentum carried by the γ-ray transitions, angular distribution measurements must be performed.

3.7.4 Angular Distribution Measurements

The symmetric arrangement of the GAMMASPHERE detectors into 17 different rings of constant angle, θ, with respect to the beam line, offers the ability to obtain extremely good angular distribution measurements.

In using this method it is important to first determine the relative efficiencies of each individual ring, owing to the fact that each ring consists of a different number of detectors. Once the relative efficiencies of each ring have been determined and individual ring spectra of experimental data have been generated, it is possible to compare the intensity of a given γ-ray transition as a function of $\cos^2\theta$. Furthermore, as the angular distributions are expected to be functions of $\cos^2\theta$, the spectra from pairs of rings at opposite angles, about 90°, may be combined for greater statistics (e.g. ring 1 and ring 17, ring 2 and ring 16, etc.).

In the present work, peak areas were measured for a given transition in each of the 17 ring spectra produced. These areas were then divided by the efficiency of each respective ring and the relative intensities obtained fitted with the function,

$$W(\theta) = 1 + a_2 P_2 cos^2\theta + a_4 P_4 cos^2\theta, \tag{3.6}$$

using the RadWare computer software "LEGFT" [70]. Here $P_{2,4}$ are Legendre polynomials and $a_{2,4}$ are the a_k coefficients, which may be used to determine the angular momentum carried away by the given γ-ray transition, as discussed in section 2.4.3. Examples of the angular distribution fits obtained in this thesis work are shown in Figs. 3.20(a) and 3.20(b), respectively.

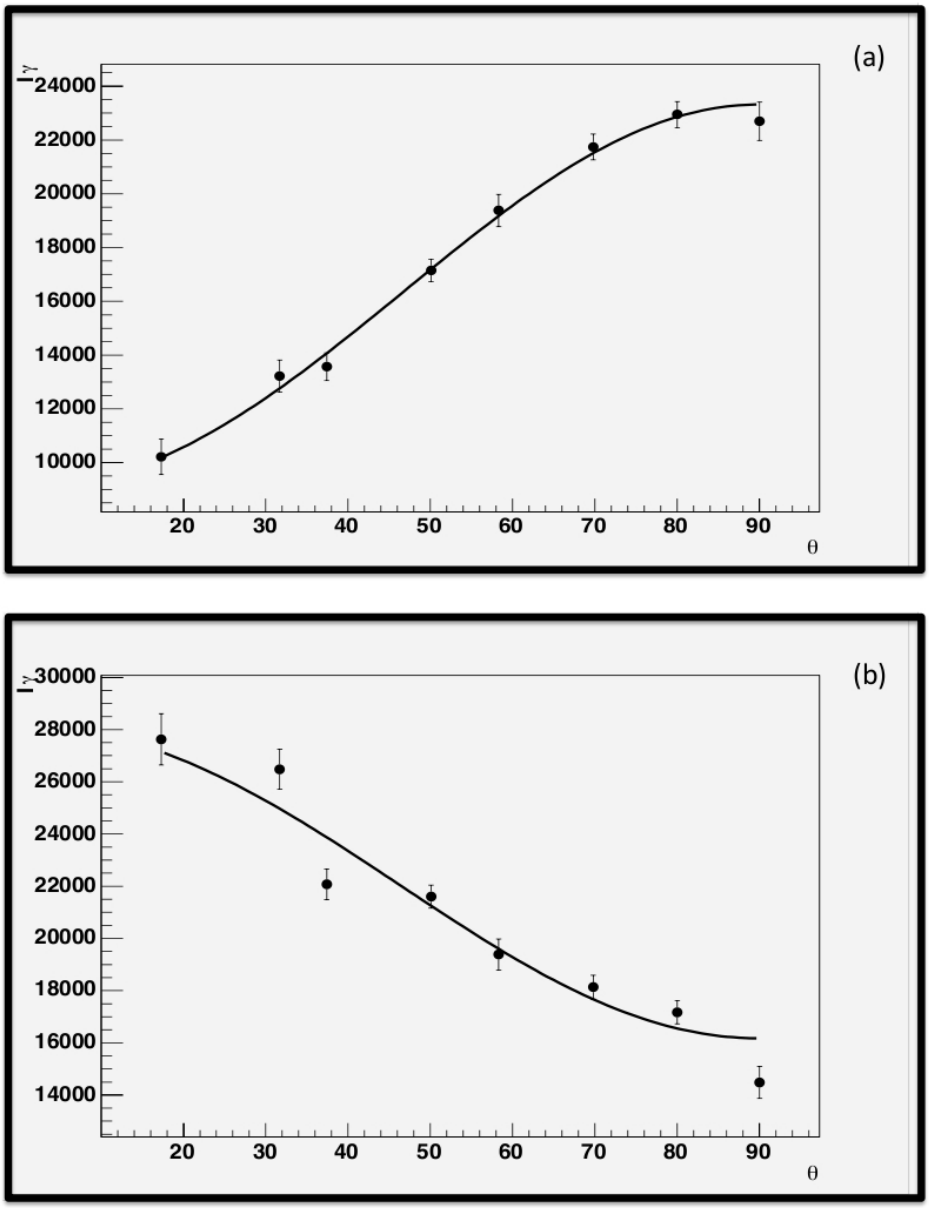

Figure 3.20: Examples of angular distribution fits obtained in this study. (a) Angular distribution fit for the 5426 keV, $\Delta I{=}\pm 1$, γ-ray transition from the 7590 keV level in ^{27}Si. (b) Angular distribution fit for the 3204 keV, $\Delta I{=}0$, γ-ray transition from the 7652 keV level in ^{27}Si.

Chapter 4

Level Structure of ^{24}Al and the ^{23}Mg$(p,\gamma)^{24}$Al Reaction Rate

In novae environments, the rate of the astrophysical ^{23}Mg$(p,\gamma)^{24}$Al reaction is expected to be dominated by resonant capture to excited states above the proton-emission threshold (1872(3) keV) [19] in the nucleus ^{24}Al. The previous work by Iliadis *et al.* [27] indicated that sizable uncertainties in the rate could significantly influence the final isotopic abundances of ^{20}Ne, ^{21}Ne, ^{22}Na, ^{23}Na and ^{24}Mg in ONe novae ejecta. Consequently, an accurate determination of the nuclear properties of proton-unbound states in ^{24}Al is required.

The most detailed structural information on the nucleus ^{24}Al, to date, comes from four ^{24}Mg$(^3$He$,t)^{24}$Al transfer reaction studies, which were performed at beam energies of 60 MeV, 81 MeV, 30 MeV and 420 MeV, respectively [84; 85; 86; 87]. These studies display significant inconsistencies in the excitation energies of all states in ^{24}Al, and several states below the proton-emission threshold, predicted by shell model calculations and expected from a comparison with the mirror nucleus, ^{24}Na, have yet to be firmly identified. In addition to this, the spin-parity assignments of several excited states in ^{24}Al and, in particular, for the key astrophysical resonance, remain ambiguous.

The proton-rich nucleus ^{24}Al lies fairly close to the proton drip line, having a relatively low proton threshold energy of 1872 keV, and as such exhibits a relatively low density of states. Consequently, in this work a 4 pnA 60 MeV ^{16}O beam was used to bombard a 200 μg/cm^2 thick ^{10}B target for 67 h, producing ^{26}Al compound nuclei with an excitation energy of $\sim$42.6 MeV. The ^{24}Al nuclei were subsequently produced via the ^{10}B$(^{16}$O$,2n)$ heavy-ion fusion-evaporation reaction, which was chosen because the $2n$ channel had previously been used

by our collaboration to study similar mass T_z=-1 nuclei; ^{20}Na [64], ^{26}Si [66] and ^{22}Mg [72]. Gamma rays were detected using the GAMMASPHERE array in coincidence with A=24 and charge state 9^+ recoils, transmitted to the focal plane of the FMA. An ionization chamber, situated behind the FMA, was used to cleanly resolve ^{24}Al, ^{24}Na and ^{24}Mg nuclei from ΔE-E information, as shown in Fig. 3.12. Such an approach allows for the observation of a γ-ray singles spectrum for the nucleus under investigation, which, in turn, may be used to obtain energies, relative intensities and angular distributions for electromagnetic transitions between excited states and directly to the ground state.

This thesis work represents the first in-beam γ-ray spectroscopy study of the nucleus ^{24}Al, the results of which led to a publication earlier this year in Physical Review C Rapid Communications [88]. Prior to the current work, Honkanen *et al.* [89] studied the β decay of ^{24}Al^m and measured a 1^+ isomeric transition having an energy of 425.8(1) keV with a lifetime of 131.3 ms, which was assigned as the lowest-lying excited state in ^{24}Al. Consequently, the 1^+_1 426 keV state was accepted as the first excited state in ^{24}Al and provided a basis for the construction of a level scheme for the nucleus ^{24}Al. This transition was not observed in the present data due to its relatively long lifetime, as the decay occurs outside the GAMMASPHERE array.

Table 4.1 presents a summary of the level energies, spins, γ ray energies, γ-ray intensities, angular distribution coefficients and γ branching ratios determined for all observed ^{24}Al excited states in the present work. Table 4.2, however, presents a comparison between the present results with the previously obtained information on the excited states in ^{24}Al from (^{3}He, t) reaction studies [84; 85; 86; 87]. The γ-ray singles spectrum detected in coincidence with ^{24}Al recoils is displayed in Fig. 4.1, while Fig. 4.2 provides a level scheme for ^{24}Al.

Table 4.1: Properties of observed excited states in ^{24}Al in the present data. A level energy correction has been included, which accounts for the energy taken away from the recoil by the associated γ ray.

E_x(keV) present	J^π	E_γ(keV)	γ branch	γ intensity	a2/a4
500.1(1)	2_1^+	74.3(1)	96(2)	45(1)	-0.23(10)/0.30(15)
		500.0(5)	4(2)	2.0(4)	
1088.2(2)	1_2^+	662.5(2)	100	15(1)	
1107.9(1)	2_2^+	682.1(2)	100	24(1)	-0.14(20)/0.17(25)
1261.2(3)	3_1^+	760.9(2)	45(8)	19(2)	
		1261.4(5)	55(8)	23(3)	
1538.5(2)	5_1^+	1538.5(2)	100	100(3)	-0.37(16)/0.16(14)
1548.4(5)	2_3^+	459.8(3)	61(14)	6.3(11)	
		1048.5(9)	39(14)	4.0(8)	
1617.0(8)	3_2^+	1116.9(5)	75(10)	38(3)	-0.63(21)/0.09(26)
		1617.0(12)	25(10)	13(4)	
2345.1(14)	3_3^+	1844.9(14)	100	1.5(8)	
3875.4(10)	(6^+)	2336.7(10)	100	13(2)	

Table 4.2: Comparison between the present data and previous results.

E_x(keV) present	J^π present	E_x(keV) Kubono [84]	J^π [84]	E_x(keV) Greenfield [85]	J^π [85]	E_x(keV) Visser [86]	E_x(keV) Zegers [87]
500.1(1)	2_1^+	506(10)	2^+	511(4)	2^+		492(10)
1088.2(2)	1_2^+	1101(10)	1^+				1090(10)
1107.9(1)	2_2^+			1111(3)	$(1,2)^+$		
1261.2(3)	3_1^+	1260(10)	3^+	1275(5)	3^+		
1538.5(2)	5_1^+	1535(10)	5^+			1543(6)	
1548.4(5)	2_3^+			1563(7)	$(2,5)^+$		1555(10)
1617.0(8)	3_2^+	1614(10)	(3^+)	1638(8)	3^+	1619(6)	1619(10)
2345.1(14)	3_3^+	2328(10)	(3^+)	2369(4)	$(4,5)^+$	2346(6)	2349(10)
	4_2^+	2521(10)	(4^+)	2546(7)	$(4,5)^+$	2523(3)	
3875.4(10)	(6^+)	3860(10)					3888(10)

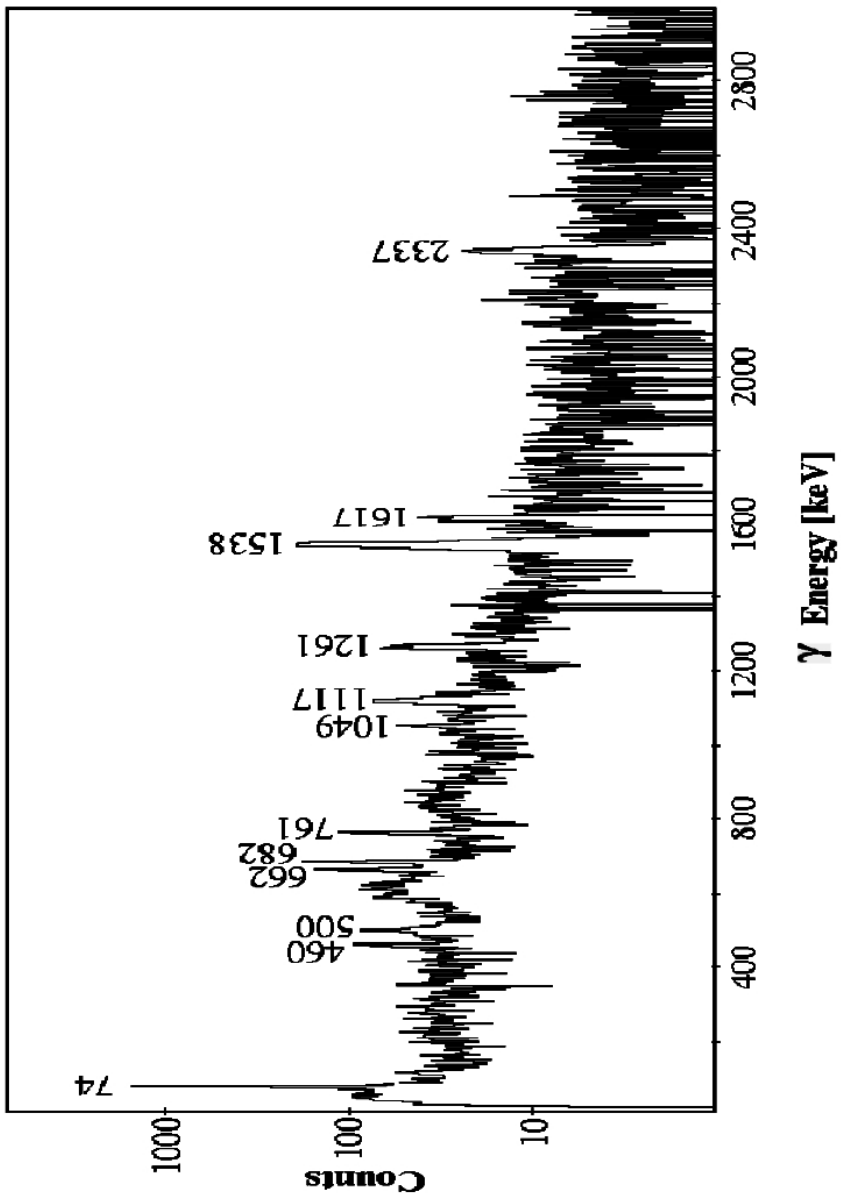

Figure 4.1: Gamma ray singles spectrum measured in coincidence with ^{24}Al residues.

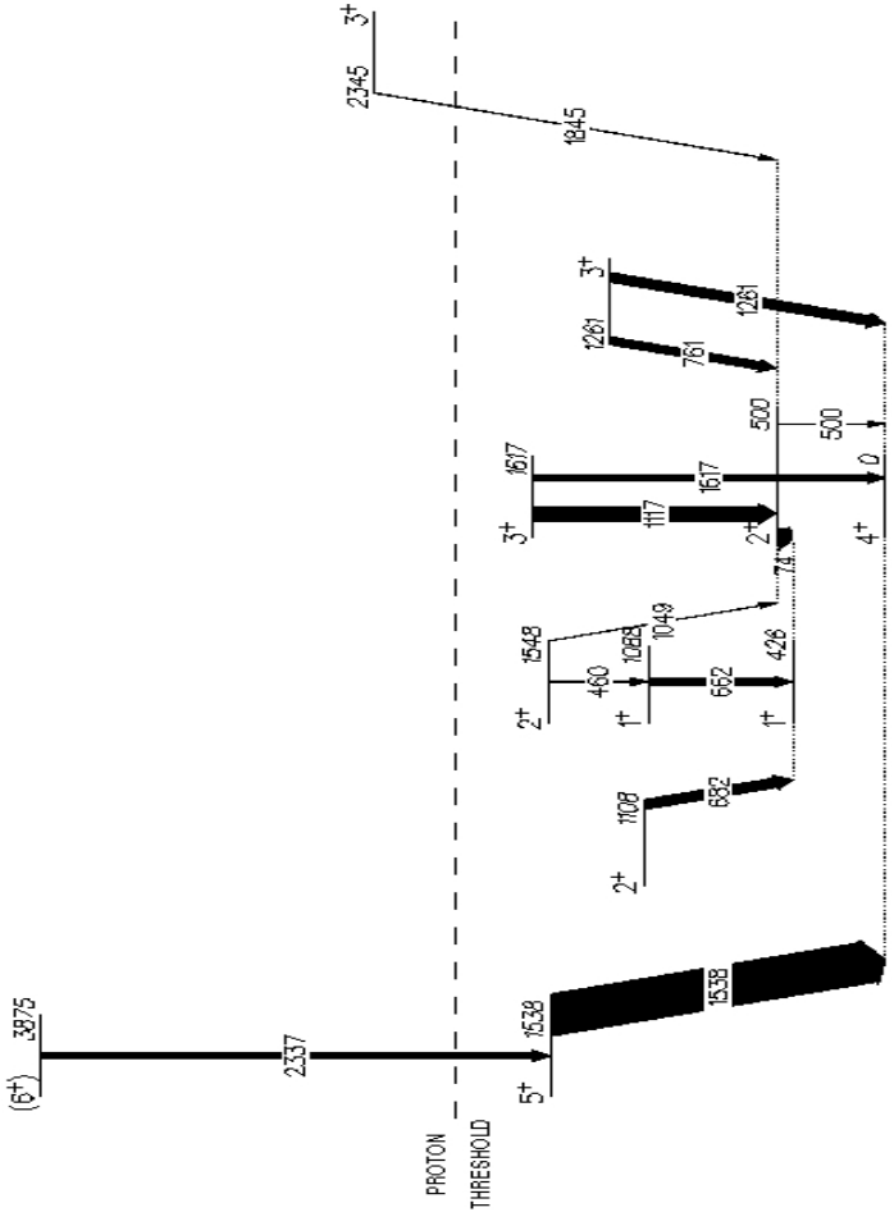

Figure 4.2: Level scheme of observed excited states in ^{24}Al.

4.1 Subthreshold Level Structure of ^{24}Al

As can be seen in Fig. 4.1, the lowest energy γ-ray appears at 74 keV. An angular distribution analysis of this transition revealed a_k coefficients of $a_2 = -0.23(10)$ and $a_4 = 0.30(15)$, respectively, indicating an angular momentum change of $\Delta I = \pm 1$ between the states in which the γ ray acts. By a comparison between the two mirror nuclei level schemes, shown in Fig. 4.3, it is clear that a similar low energy transition is found at 91 keV, which is known to be a 97% γ-decay branch from a 2^+_1 excited state to the corresponding 1^+_1 level in ^{24}Na [90].

There are no further low-energy transitions in this region in either nucleus and thus, by adding to the previously established 1^+_1 level energy in ^{24}Al [89], a 74 keV γ-ray transition from a 2^+_1 500.1(1) keV level to the 1^+_1 excited state in ^{24}Al was assigned. The present assignment agrees well with the previous structure study of ^{24}Al performed by Kubono *et al.* [84], in which an excited state in ^{24}Al was observed at 506(10) keV and was given a 2^+_1 spin-parity assignment. A recent study by Zegers *et al.* [87] also observed an excited state in ^{24}Al at 492(10) keV, which again is consistent with the presently observed level energy. In addition, the mirror analog $2^+{}_1$ excited state in ^{24}Na [90] exhibits a 3% γ-decay branch directly to the ground state. A similar low intensity transition is observed in the present data at 500.0(5) keV, as shown in Fig. 4.1, consistent with the present level energy and expected decay branch.

A subsequent γ-γ coincidence analysis, using the program 'ESCL8R' [70], was performed with a gate set upon the 74 keV γ ray transition, as shown in Fig. 4.4. A coincidence was observed at 761 keV, indicating a decay to the 2^+_1 level from an excited state at 1261 keV. The level energy obtained agrees well with the 1260(10) keV level energy observed for a 3^+_1 excited state in the study by Kubono *et al.* [84]. The mirror analog 3^+_1 excited state in ^{24}Na exhibits a 45% γ-decay branch to the 2^+_1 level and a 55% branch directly to the ground state. Thus, a γ-ray transition, directly to the ground state, is expected from the 3^+_1 excited state in ^{24}Al. This is indeed the case and a γ-ray transition is observed at 1261 keV, as seen in Fig. 4.1, with no associated coincidences. The 45% and 56% decay branches observed for the 761 and 1261 keV transitions are consistent with those expected for a 3^+_1 state from the mirror system and, together with the agreement of the present level energy with Ref. [84], 761 and 1261 keV transitions from a 3^+_1 1261.2(3) keV level in ^{24}Al were assigned.

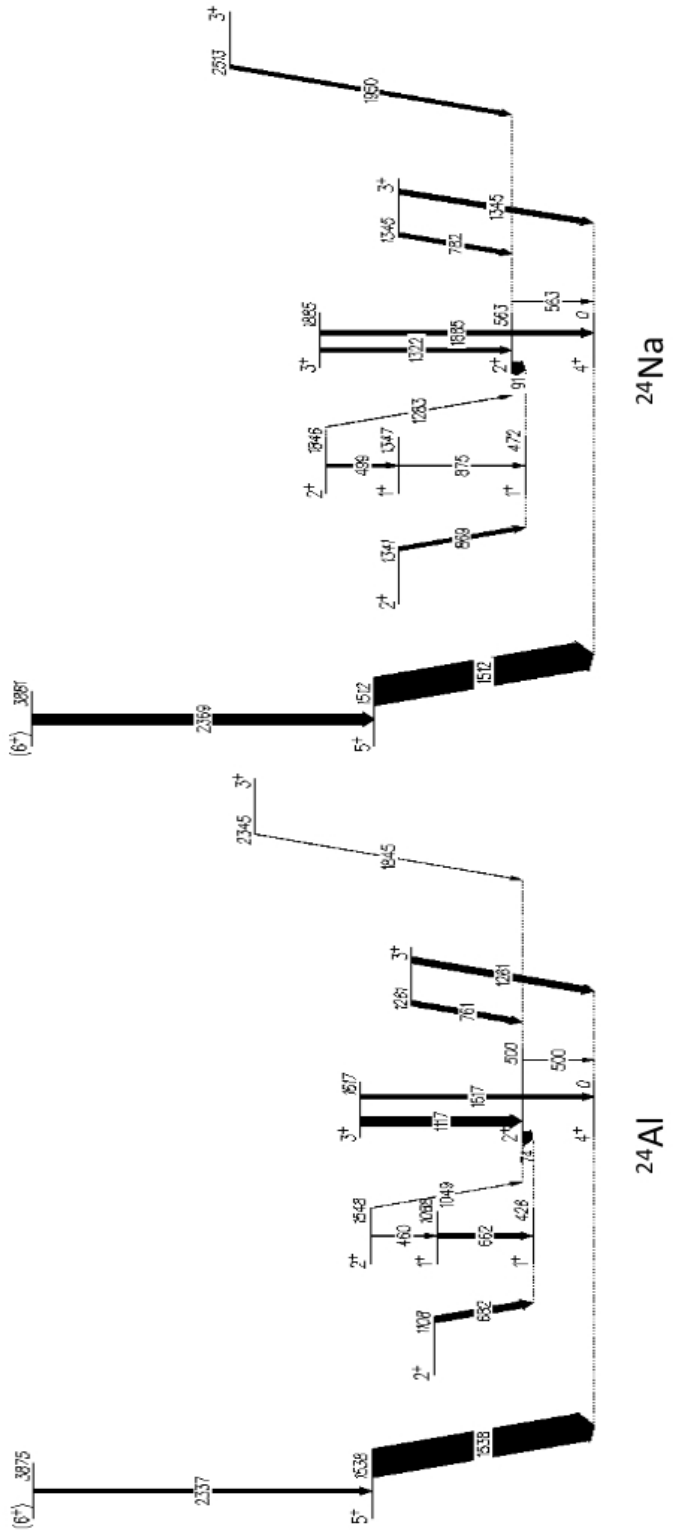

Figure 4.3: The γ-decay schemes of the mirror nuclei ^{24}Al and ^{24}Na.

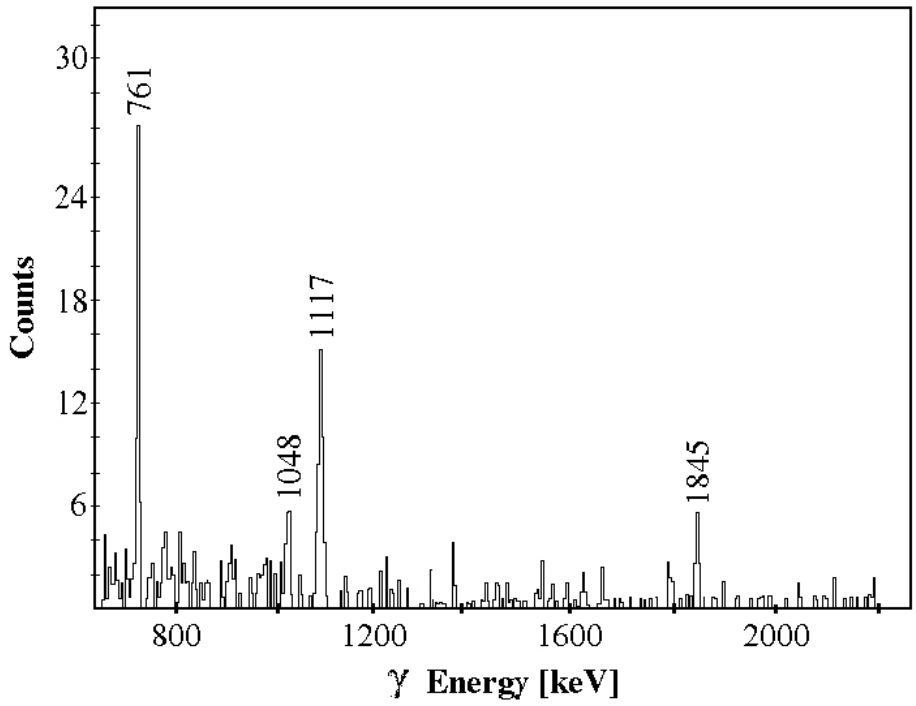

Figure 4.4: Gamma coincidence spectrum with a gate placed on the 74 keV γ-ray transition in ^{24}Al.

The most intense transition observed in the present data appears at 1538 keV. The energy of this transition is in excellent agreement with the 1543(6) keV and 1535(10) keV respective level energies observed for a 5^+_1 excited state in the previous studies by Kubono *et al.* [84] and Visser *et al.* [86]. No coincidence relationships, except for the 2337 keV transition-feeding from a higher energy excited state which shall be discussed later, were observed with the 1538 keV transition in the present data set. The measured angular distribution coefficients for this transition, $a_2 = -0.37(16)$ and $a_4 = 0.16(14)$, indicate an angular momentum change of $\Delta I{=}\pm1$, which is consistent with a decay from a 5^+ excited state to the 4^+ ground state of ^{24}Al. The mirror analog 5^+_1 excited state in ^{24}Na displays a single 100% γ-decay branch directly to the ground state, which is also consistent with what is observed in the present data. Thus, a 1538 keV transition to the ground state from a 5^+_1 1538.5(2) keV level was assigned in ^{24}Al.

In considering Fig. 4.1, a γ-ray transition with no coincidences is observed at 1617 keV. This transition indicates the presence of an excited state at 1617 keV, which is consistent with the previously observed 1619(6) keV [86], 1624(10) keV [84] and 1619(10) keV [87] respective level energies for a 3^+_2 excited state in ^{24}Al. The mirror 3^+_2 analog state displays two γ-decay branches; a 38% branch to the ground state and a further 62% branch to the 2^+_1 excited state. Consequently, an additional transition from the 3^+_2 state, to the 2^+_1 level, is expected in the present ^{24}Al data. The coincidence data, displayed in Fig. 4.4, indicate that this is indeed the case and an 1117 keV decay transition to the 2^+_1 level is observed, with angular distribution measurements, $a_2 = -0.63(21)$ and $a_4 = 0.09(26)$, indicating a $\Delta I{=}\pm1$ transition. Thus, an 1117 keV transition from the 3^+_2 1617.0(8) keV excited state in ^{24}Al was assigned. The level energy obtained is in good agreement with the previous results [84][86][87] and the branching ratios of the two observed γ-ray transitions are consistent with those expected from the mirror system.

Shell model calculations [91] and mirror nucleus comparisons predict the existence of a 2^+_3 state below the proton threshold. Such a 2^+ level was not observed in the previous studies by Kubono *et al.* [84], Visser *et al.* [86] and Zegers *et al.*, respectively. However, in an earlier study in 1991 by Greenfield *et al.* [85] a 2^+_3 excited state in ^{24}Al was tentatively proposed at 1563(7) keV. In the present data, a γ-ray transition at 1048 keV was observed to decay to the

2_1^+ excited state, as seen in Fig. 4.4, indicating an excited state at 1548 keV in ^{24}Al. The analog 2_3^+ excited state in ^{24}Na exhibits a 25% γ-decay branch to the 2_1^+ state with a stronger 44% branch to the 1_2^+ excited state, which is known to be coincident with a subsequent 100% γ-decay branch transition from the 1_2^+ state to the 1_1^+ excited state. Consequently, a similar cascade of decay transitions is expected in ^{24}Al. In the present ^{24}Al data, a coincident pair of γ ray transitions are observed at 460 keV and 662 keV, respectively, as shown in Figs. 4.5 and 4.6. No further coincidence relationships were observed

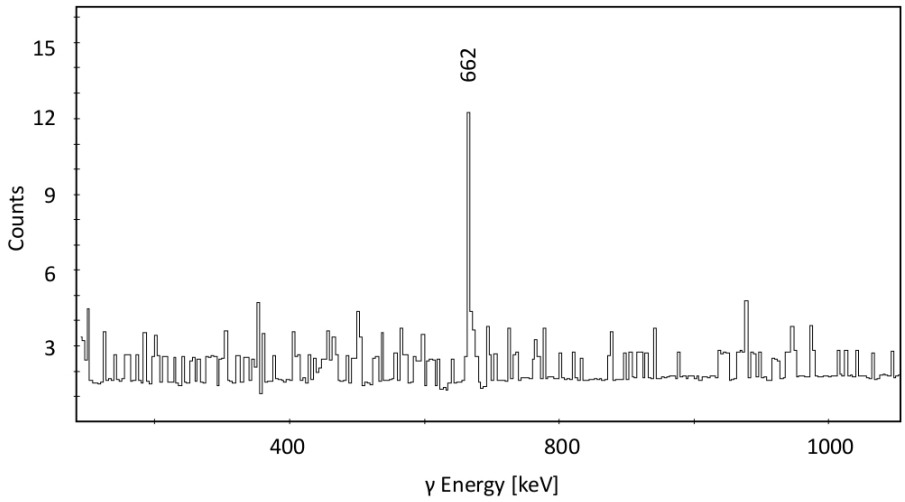

Figure 4.5: Gamma coincidence spectrum with a gate placed on the 460 keV γ-ray transition in ^{24}Al.

with either transition and the sum of the transition energies was found to be consistent with the associated energy gap between the current 2_3^+ 1548 keV level and the previously established 1_1^+ excited state [89]. The 1_2^+ excited state in ^{24}Al was previously observed by Kubono *et al.* [84] at 1101(10) keV and was predicted by shell model calculations in the same energy region. The 460 keV transition was found to be consistent with the associated energy gap between the current 2_3^+ level and the previously observed 1_2^+ excited state [84], with a decay branch, 61%, consistent with that expected from the mirror nucleus. A similar evaluation found the 662 keV transition to be consistent with the associated energy gap between the 1_2^+ [84] and 1_1^+ [89] excited states in ^{24}Al, again with a decay branch, 39%, consistent with the corresponding transition in the mirror

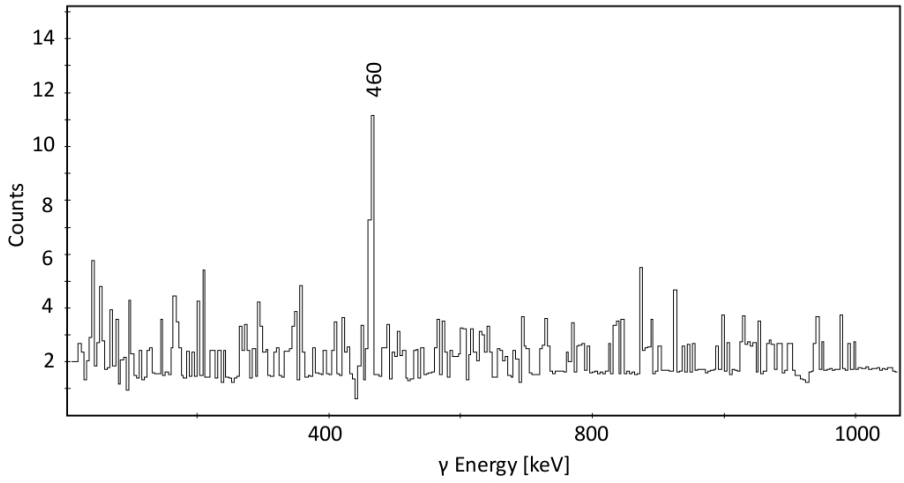

Figure 4.6: Gamma coincidence spectrum with a gate placed on the 662 keV γ-ray transition in ^{24}Al.

nucleus. Consequently, 460 keV and 662 keV transitions from 2_3^+ 1548.4(5) keV and 1_2^+ 1088.2(2) keV excited states, respectively, were assigned in ^{24}Al.

A final remaining 2_2^+ excited state below the proton threshold is predicted by shell model calculations and is expected from a comparison with the mirror nucleus. This state has not been firmly identified previously [84][85][86][87]. In the present data, a γ-ray transition with no coincidences was observed at 682 keV, as shown in Fig. 4.1. No excited states with direct decays to the ground state are expected in this energy region, and angular distribution measurements, $a_2 = -0.14(20)$ and $a_4 = 0.17(25)$, imply a $\Delta I{=}\pm 1$ transition. Consequently, a γ decay to the 1_1^+ excited state from a level at 1107.9(1) keV with a 2_2^+ assignment is proposed. This is in good agreement with the previously observed tentative 2_2^+ 1111(3) keV state by Greenfield *et al.* [85] and is also consistent with the observed 100% γ-decay branch from the 2_2^+ to the 1_1^+ state in the mirror system. The analysis thus far completes the level structure of states in ^{24}Al below the proton-emission threshold (1872(3) keV) [19].

4.2 Proton-unbound States and Implications for the Astrophysical ^{23}Mg$(p,\gamma)^{24}$Al Reaction Rate in ONe Novae

Previous studies of the ^{23}Mg$(p,\gamma)^{24}$Al stellar reaction rate [62; 84; 86; 92; 93] indicate that, over the temperature range 0.2–0.4 GK, the rate is dominated by resonant capture to excited states in ^{24}Al above the proton-emission threshold (1872(3) keV) [19]. The study by Kubono *et al.* [84] improved upon the initial theoretical estimates of the rate [92; 93] by using experimental constraints on the spins and excitation energies of resonant states in ^{24}Al. A level energy of 2328(10) keV was obtained for the lowest-lying excited state above the proton threshold with a tentative spin-parity assignment of 3^+ and was found to dominate the reaction rate over the temperature range of interest. The previous study by Greenfield *et al.* [85], however, reported a level energy of 2369(4) keV for the most influential astrophysical state with a contradictory possible spin-parity assignment of 4^+ or 5^+. The large discrepancies between these results [84; 85] led to a re-evaluation of the stellar reaction rate by Herndl *et al.* [62]. This study used both previous experimental results [84; 85] with the isobaric multiplet mass equation (IMME) to generate an average level energy of 2349(20) keV and 3^+ spin assignment for the dominant resonant state. The newly derived resonance strengths from this study further indicated that the rate is indeed dominated by the lowest-lying excited state above the proton threshold. However, the adopted uncertainty in the level energy, arising from differences in the experimental results [84; 85], leads to up to a factor 5 variation in the rate over the temperature range 0.2–0.4 GK. Consequently, the most recent evaluation of the reaction rate by Visser *et al.* [86] attempted to resolve the inconsistencies in experimental results. A level energy of 2346(6) keV was obtained for what is thought to be the most influential state, in disagreement with both prior reaction studies [84; 85], but in excellent agreement with the average value adopted by Herndl *et al.* [62]. The improved precision of the level energy reduced the relative uncertainty in the reaction rate [62] by a factor of 3 but no new information was obtained on the spin assignment of the state and the 3^+ assignment of Ref. [62] was simply adopted.

In the present work, if we again consider Fig. 4.4, a low intensity γ ray was observed at 1845 keV, indicating an excited state in ^{24}Al above the proton

threshold at 2345 keV with a γ-decay branch to the 2^+_1 excited state. No further transitions from this state or other excited states above the proton threshold, in this energy region, were observed in the present data. Consequently, it was concluded that this 2345 keV level corresponds to the lowest-lying excited state above the proton-emission threshold, in excellent agreement with the recent level energy obtained by Visser *et al.* [86].

Previous studies [84; 85], along with nuclear shell model calculations, indicate that two strong possibilities exist for the spin assignment of this state; a 3^+_3 or 4^+_2 assignment. In comparison with the mirror nucleus, the 3^+_3 state in ^{24}Na displays an 89% γ-decay branch to the 2^+_1 excited state with no further decay branches >6% to other lower-lying states, which is consistent with the γ-decay branches observed for the present ^{24}Al 2345 keV level. The analog 4^+_2 excited state in ^{24}Na, however, displays three significant γ-decay branches; a 15% branch to the 5^+_1 excited state, a 52% branch to the 3^+_1 excited state and a 33% branch to the ground state, none of which are observed in the present data. Thus, a 3^+_3 2345.1(14) keV excited state was assigned in ^{24}Al, confirming the tentative 3^+ assignment of Kubono *et al.* [84] and the IMME predictions [62]. Figure 4.7 shows a comparison between the presently obtained level energies of the mirror nuclei ^{24}Al and ^{24}Na, IMME calculations [62] and shell model calculations [67].

The observed relative intensity of the 1845 keV transition from the 3^+_3 state is markedly lower than the relative intensities observed for other transitions from either the 3^+_2 or 3^+_1 excited states in ^{24}Al. The ratio of relative intensities $3^+_3/[3^+_1+3^+_2+3^+_3]$ in ^{24}Al was found to be 0.02(1), while the ratio of relative intensities for the corresponding analog 3^+ states in the mirror nucleus ^{24}Na was found to be 0.160(1). It can be seen that the ratio between 3^+ states in ^{24}Al is a factor of 8 smaller than the corresponding ratio in the mirror nucleus and implies that the 3^+_3 state in ^{24}Al exhibits a dominant proton-decay branch in competition with the associated γ decay. In Ref. [62] the γ- and proton-decay widths for the 3^+_3 excited state were estimated to be 25 meV and 185 meV, respectively. This is consistent with what is seen in the present data, indicating a dominant proton-decay branch. Shell model calculations indicate that the next state to appear above the threshold is most likely a 4^+_2 excited state and the proton-decay width of this state is estimated to be $\sim$100 times bigger than the associated γ-decay width [62]. Consequently, this state and

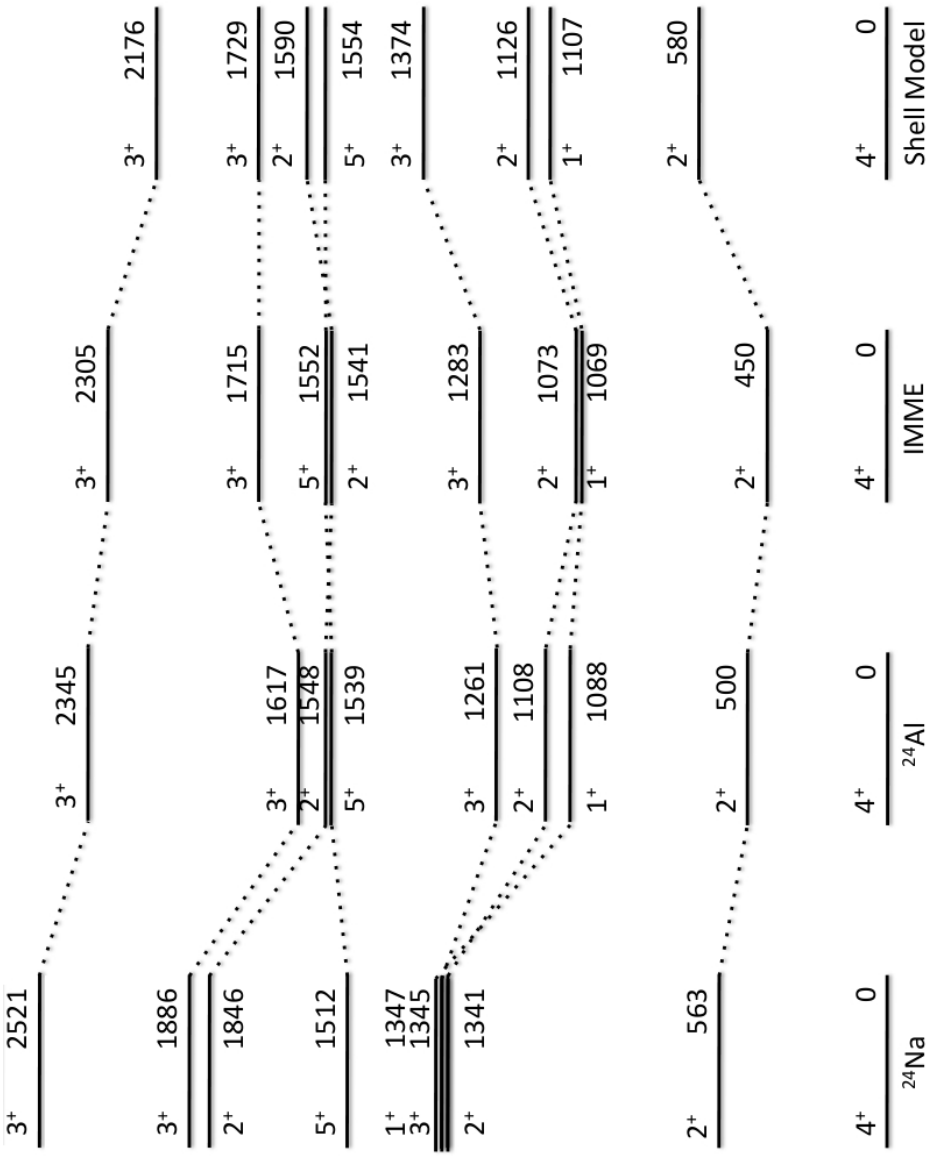

Figure 4.7: Comparison between the ^{24}Al levels, the states in ^{24}Na, IMME calculations and shell model calculations.

higher energy excited states, with generally stronger proton-decay branches, are extremely unlikely to be observed in the present data.

However, one further excited state above the threshold was observed and a γ-ray transition above the proton threshold at 2337 keV, shown in Fig. 4.1, was found to be coincident with a 1538 keV decay transition from the 5^+_1 excited state, indicating a level above the threshold at 3875 keV. The observation of a γ decay from a state so far above the threshold implies that such a state has a large angular momentum in order to survive long enough for the resulting γ ray to be detected within the GAMMASPHERE array. Nuclear shell model calculations [91] predict a 6^+ state at 3883 keV and as such the observed 3875 keV state was tentatively assigned a (6^+) quantum number. This state will have little effect on the rate over the temperature range of interest and as such, will not be considered in the following discussion of the stellar reaction rate.

As discussed in Chapter 2, the stellar reaction rate may be determined from the contributions of isolated resonances corresponding to unbound compound nuclear states and from the nonresonant direct capture process. The nonresonant component of the ^{23}Mg$(p,\gamma)^{24}$Al reaction has been well described in the previous study by Herndl *et al.* [62], in which the form of the astrophysical S-factor was determined. Consequently, this prescription was adopted in the present work for the direct capture contribution to the stellar reaction rate.

The lowest-lying excited state above the threshold has been identified as a 3^+_3 state with a level energy of 2345.1(14) keV, corresponding to a resonance energy (E_r) of 473(3) keV, and the results imply a predominant unobserved proton decay branch. Theoretical calculations by Herndl *et al.* [62] estimate the resonance strength for the 3^+_3 state in ^{24}Al to be 25 meV and calculations by Kubono *et al.* [84] obtain a similar estimate of 27 meV. Thus, a resonance strength of 26 meV was adopted for the determination of the resonant reaction rate in the present work. Furthermore, although no further excited states were observed in the present data, previous studies have indicated that the next lowest-lying resonant state above the proton threshold, after the observed 473 keV resonance, appears at ~650 keV [62; 84; 85; 86]. In fact, a very recent paper by Visser *et al.* [94] has used the excitation energy value obtained for the lowest-lying excited state above the threshold in this thesis work to make an energy calibration correction for the higher energy excited states observed in the (^{3}He, t) experiment of Ref. [86]. The work of Visser *et al.* [86] quote that

the 2345.1(14) keV measurement of this thesis work represents the most precise measurement of this excited state to date and report an excitation energy of 2523(3) keV for the next lowest-lying state above the threshold, corresponding to a resonance energy of E_r=651(4) keV.

From the present work, it is likely that this state has a 4_2^+ spin-parity assignment, an assignment also adopted in Refs. [62] and [86], and as such, the theoretically calculated resonance strength of Herndl *et al.* [62] of 58 meV, for such a state, was adopted in this work. This unobserved resonance has been included in the present determination of the stellar reaction rate as a test of the dominance of the 473 keV resonance over novae peak temperatures.

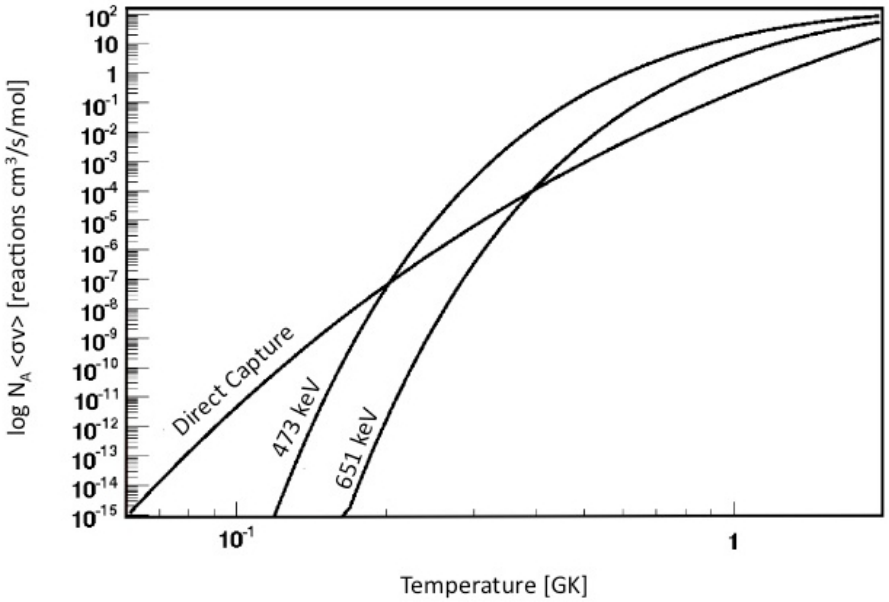

Figure 4.8: Direct capture and resonant contributions to the ^{23}Mg(p,γ)^{24}Al reaction rate.

Figure 4.8 shows the contributions of the direct capture, 473 keV and 651 keV resonant components to the stellar reaction rate. It is clear that the 473 keV resonance dominates the reaction rate for the temperature range of interest in novae environments, T=0.2–0.4 GK, and the 651 keV resonance is of minor importance until much higher temperatures. As stated in Chapter 1, the ^{23}Mg(p, γ)^{24}Al reaction rate, itself, becomes of minor importance at higher temperatures and consequently, the 473 keV state is indeed the dominant resonant

influence on the ^{23}Mg(p, γ)^{24}Al reaction rate of importance for stellar nucleosynthesis. The improved precision of the resonance energy on the previous values of Ref. [86] and Ref. [62] has reduced the relative uncertainties in the reaction rate by factors of 2 and 7, respectively. The uncertainty in the proton threshold, however, limits the precision of the resonance energy and as such further constraints on the presently observed level energy will not reduce the relative uncertainties in the reaction rate. The current 3^+_3 spin-parity assignment confirms the tentative assignment of Ref. [84] and disagrees with the possible assignments proposed in Ref. [85]. Resonance strength values of $\sim$25 meV are predicted for a 3^+_3 resonance, whereas for a 4^+_2 state values as high as 130 meV have been quoted. Thus, the current spin-parity assignment has also significantly reduced the uncertainties in the reaction rate.

Further constraints on the reaction rate uncertainty would now require a direct measurement of the 3^+_3 resonance strength using the ^{23}Mg(p, γ)^{24}Al reaction. The precise measurement of the resonance energy reported here was used in a recent experimental attempt to measure this resonance strength at the DRAGON facility at TRIUMF [95] and, although the required beam intensity was not achieved in this experiment, a follow-up experiment has been re-scheduled for some time in 2009.

Chapter 5

Level Structure of ^{27}Si and the ^{26}Al$(p,\gamma)^{27}$Si Reaction Rate

The rate of the astrophysical ^{26}Al$(p,\gamma)^{27}$Si reaction, in novae, is expected to be dominated by resonant capture to excited states above the proton-emission threshold (7463.0(2) keV) [19] in the nucleus ^{27}Si. It has been suggested that significant uncertainty remains in the ^{26}Al$(p,\gamma)^{27}$Si stellar reaction rate at low stellar temperatures, which could significantly affect the expected contribution of novae to the observed galactic abundance of ^{26}Al. Consequently, the principal objective of the present work was to determine the nuclear properties of excited states in the nucleus ^{27}Si, above the proton threshold, which are of astrophysical importance for the thermonuclear ^{26}Al$(p,\gamma)^{27}$Si destruction reaction in classical novae environments. It should be noted at this point that the nucleosynthesis of ^{26}Al is complicated by the presence of a short-lived ($\tau_{1/2}$=6.3 s) spin isomer. However, at temperatures below $T = 0.5$ GK, such as those found in novae environments, the ^{26}Al ground and isomeric states do not reach thermal equilibrium and consequently the ^{26}Al$^g(p,\gamma)^{27}$Si and ^{26}Al$^m(p,\gamma)^{27}$Si reactions must be treated separately. In a previous study by José *et al.* [36], it was found that the ^{26}Al$^m(p,\gamma)^{27}$Si reaction rate had no noticeable affect on the nucleosynthesis of ^{26}Al in novae environments, even when arbitrarily multiplied by a factor of 100. Hence, in this work I have only focused on proton-unbound states in ^{27}Si important for reactions on the 5^+ ^{26}Al ground state, omitting any higher-energy (E_x>7832 keV) low-spin states that were observed in this work from the analysis, which may be of importance for the ^{26}Al$^m(p,\gamma)^{27}$Si reaction rate.

In contrast to ^{24}Al, the proton-rich nucleus ^{27}Si is a relatively stable nucleus, containing only one less neutron than the stable ^{28}Si and lying relatively far

away from the proton drip line. This increase in stability, in comparison to ^{24}Al, means that the proton-emission threshold in ^{27}Si is located at a much higher energy. Such a high-energy threshold results in a much higher density of states and consequently, the analysis of the γ-ray transitions between excited states is increasingly more complex.

In this work a 6 pnA 26 MeV beam of ^{16}O ions was used to bombard a 143 μg/cm^2 thick ^{12}C target, producing ^{28}Si compound nuclei with an excitation energy of $\sim$27.9 MeV. Such a low-energy ^{16}O + ^{12}C heavy-ion collision reaction was chosen so that only three dominant fusion-evaporation channels were open; $1p$, $1n$ and 1α, leading to ^{27}Al, ^{27}Si and ^{24}Mg nuclei, respectively. As ^{27}Si nuclei were produced in a strongly produced reaction channel, prompt γ rays were detected using the GAMMASPHERE detector array in stand-alone mode, without the FMA or other recoil selection equipment. In choosing this method for the current study, the overall γ-ray detection efficiency was not compromised by the use of the FMA selection device and both γ-γ and γ-γ-γ coincidence techniques could be used to select γ rays from the nucleus ^{27}Si. Such measurements were essential for the determination of the nuclear properties of proton-unbound states, due to the complex level structure of ^{27}Si. However, it should also be noted that the high density of states in ^{27}Si meant that all but the most intense γ-ray transitions directly to the ground state of ^{27}Si could not be resolved in a γ-ray singles spectrum. A previous study by Jenkins *et al.* [73] also produced the relatively stable proton-rich ^{23}Mg nuclei using a 1n heavy-ion fusion-evaporation reaction and detected the resulting γ-ray transitions using the GAMMASPHERE array in stand-alone mode with great success.

Prior to the present work, γ-ray spectroscopy studies of the nucleus ^{27}Si have reported γ-ray transitions from excited states in ^{27}Si up to 5316 keV [63]. However, although this low-lying level structure of ^{27}Si is fairly well established, the spin-parity assignments of several of the excited states in this energy region remain ambiguous. With the thesis objective in mind, it is important to first focus on firmly establishing a low-lying level structure of ^{27}Si from 0–5547 keV, to which states above the proton threshold in ^{27}Si decay to, before discussing proton-unbound states of astrophysical importance. Furthermore, it is also important to mention that an attempt to construct a complete level structure of ^{27}Si from 0–7832 keV, or indeed above, is outside the scope of this thesis, although a tentative scheme is presented in Appendix C. Instead, partial schemes

have been determined, through which proton-unbound states of importance for the astrophysical $^{26}\mathrm{Al}^{g}(p,\gamma)^{27}\mathrm{Si}$ reaction have been identified.

5.1 Low-lying Level Structure of ^{27}Si

In the present work an ungated γ-ray singles spectrum, shown in Fig. 5.1, was obtained, displaying transitions in ^{27}Si, ^{27}Al and ^{24}Mg.

Since many of the excited states in ^{27}Si in the energy region between the $5/2^{+}$ ground state and 5316 keV level have been firmly established, I shall not enter into a detailed discussion of these states here. Instead, in this section I shall focus on excited states located at 2866 keV, 4135 keV, 4474 keV, 5260 keV and 5282 keV, for which the spin-parity assignments remain ambiguous. Furthermore I shall discuss the assignment of three additional excited states, outside the previously studied γ-ray region, at 5390 keV, 5500 keV and 5547 keV.

Table 5.1 presents a summary of the level energies, spins and γ-ray energies for observed low-lying excited states in ^{27}Si, together with a comparison with previous results. In addition, a level scheme for excited states up to 5547 keV in ^{27}Si is displayed in Fig. 5.2.

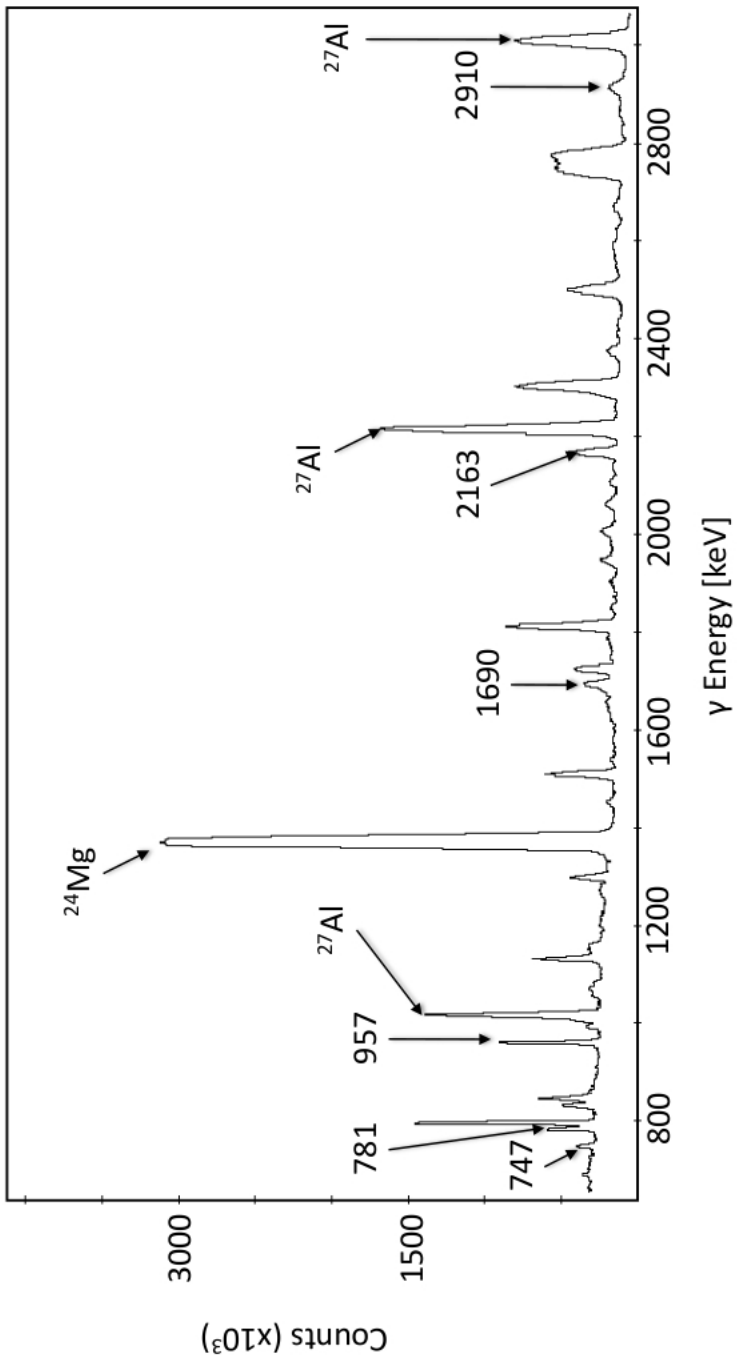

Figure 5.1: Presently observed ungated γ-ray singles spectrum. Known transitions in ^{27}Si have been annotated and the four most intense transitions in ^{24}Mg and ^{27}Al observed in the present data have also been labeled. It will be seen later that these intense transitions, from nuclei other than ^{27}Si, can potentially leak into ^{27}Si coincident spectra and consequently, it is important to note their locations within the present data.

Table 5.1: Summary of previous data combined with the present level energies and γ-ray energies obtained for low-lying excited states in ^{27}Si. A level energy correction has been included, which accounts for the energy taken away from the recoil by the associated γ ray. The current ^{27}Al mirror nucleus assignments have also been included.

E_x (keV) Endt [63]	J^π Endt [63]	E_x (keV) present	J^π present	E_γ	E_x (keV) ^{27}Al [63]
780.9(2)	$1/2^+$	780.8(1)	$1/2_1^+$	780.8(1)	844
957.4(2)	$3/2^+$	957.1(1)	$3/2_1^+$	176.3(1)	1014
				957.1(1)	
2163.6(2)	$7/2^+$	2163.2(1)	$7/2_1^+$	2163.1(1)	2212
2647.6(3)	$5/2^+$	2647.2(1)	$5/2_2^+$	1690.1(1)	2735
2866.3(3)	$(3/2, 5/2)^+$		$3/2_2^+$		2982
2909.9(2)	$9/2^+$	2910.1(1)	$9/2_1^+$	746.9(1)	3004
				2909.9(1)	
3540.2(11)	$1/2^+$	3539.8(1)	$1/2_2^+$	2582.5(1)	3680
				2758.9(1)	
3803.6(11)	$3/2^+$	3803.1(2)	$3/2_3^+$	1155.5(2)	3957
				3022.8(2)	
4138.1(14)	$(1/2, 3/2)^-$	4135.3(1)	$1/2_1^-$	3354.3(1)	4055
4289.2(9)	$5/2^+$	4284.9(1)	$5/2_3^+$	3327.6(1)	4410
4447.3(5)	$11/2^+$	4447.2(1)	$11/2_1^+$	1536.9(1)	4510
				2283.9(1)	
4474.8(7)	$(7/2, 9/2)^+$	4473.6(3)	$7/2_2^+$	1826.1(1)	4580
				2310.4(1)	
4703.8(11)	$5/2^+$	4705.2(2)	$5/2_4^+$	2541.9(2)	4812
				3747.6(1)	
5062(2)	$5/2^+$	5059.3(3)	$5/2_5^+$	2410.0(30)	5248
				2896.6(2)	
				4101.9(2)	
5208	$3/2^-$	5208.2(15)	$3/2_1^-$	4427.0(15)	5156
5262.0(5)	$(5/2^+, 7/2, 9/2^+)$	5260.4(10)	$7/2_3^+$	2350.7(1)	5433
				3096.0(30)	
5282.8(4)	$(7/2, 11/2)^+$	5282.4(2)	$11/2_2^+$	835.6(6)	5500
				2372.1(1)	
				3118.8(2)	
5316.7(5)		5318.0(1)	$9/2_2^+$	2670.3(2)	5420
				3154.7(1)	
5391.7(16)	$(3/2, 5/2)^+$	5389.7(7)	$5/2_6^+$	3227.2(11)	5551
				4431.7(4)	
5497(2)		5500.4(2)	$5/2_1^-$	2853.0(1)	5438
5547(4)		5547.3(1)	$9/2_3^+$	1099.9(1)	5667
				2637.1(1)	

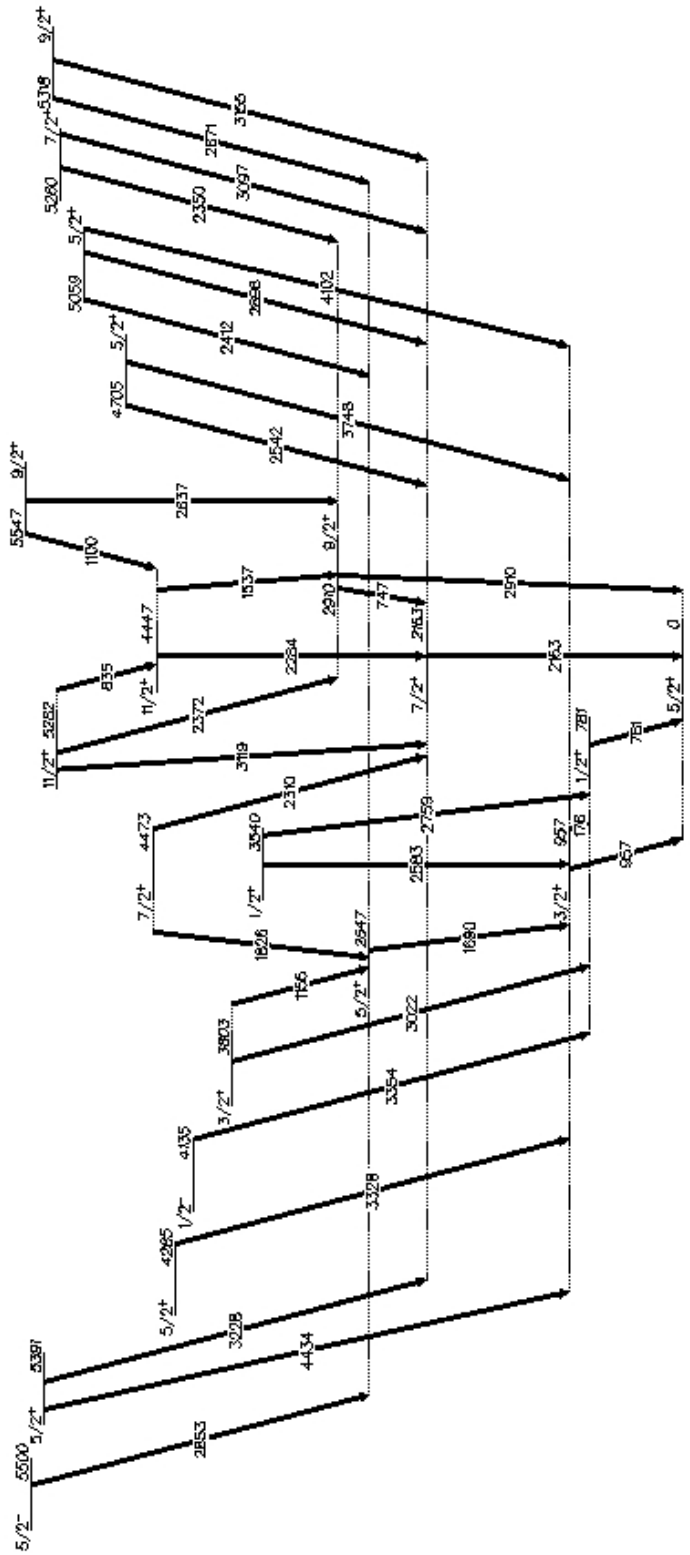

Figure 5.2: Low-lying level structure of ^{27}Si.

The $1/2^-_1$ 4135 keV Level

In previous work and in the present data the lowest energy excited state observed in ^{27}Si is a $1/2^+_1$ 781 keV state, which exhibits a single γ-ray transition to the ground state. A subsequent γ-γ coincidence analysis, with a gate set upon the 781 keV transition in ^{27}Si, was performed in order to identify coincidence relationships with the $1/2^+_1$ state. In this gate a strong γ-ray transition was observed at 3354.3(1) keV, as shown in Fig. 5.3, indicating an excited state in

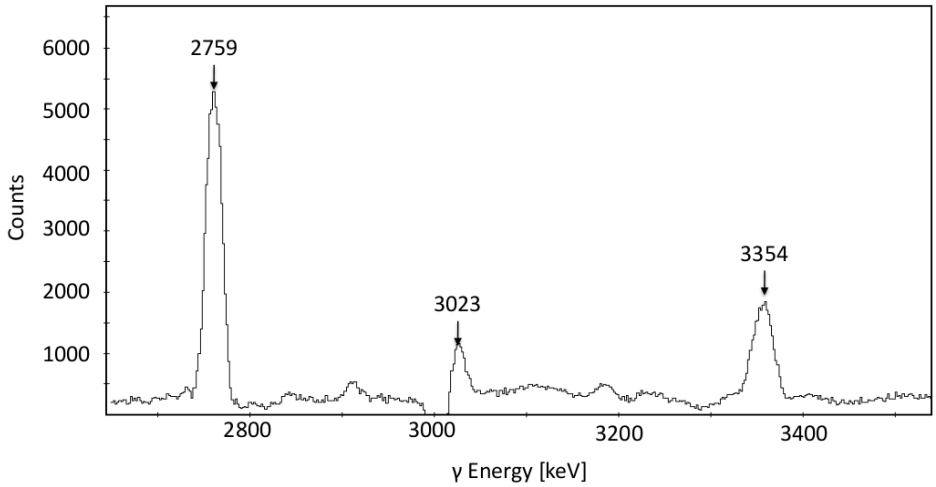

Figure 5.3: γ-γ coincidence spectrum with a gate placed on the 781 keV transition in ^{27}Si. A gap appears in this spectrum around 3000 keV, due to the over-subtraction of background counts at this point.

^{27}Si at 4135.3(1) keV. No further γ-ray transitions were observed to decay from this state, implying a large γ-decay branch to the $1/2^+_1$ state. The level energy obtained is in good agreement with a previously observed $(1/2, 3/2)^-$ level at 4138.1(14) [63], which is known to exhibit a 91% branch to the $1/2^+_1$ state, with a weaker 9% branch to the $3/2^+_1$. These observations are consistent with what is observed in the present data. In comparison with the mirror nucleus, ^{27}Al, the only negative-parity state in an energy region of 4135±1000 keV is the $1/2^-_1$ 4055 keV state [63]. This state is also known to exhibit an 86% γ-decay branch to the $1/2^+_1$ state and a 14% branch to the $3/2^+_1$ state. Therefore, a $1/2^-_1$ 4135 keV excited state was assigned in ^{27}Si.

The $7/2_2^+$ 4474 keV Level

The most intense transition in the present ^{27}Si data is observed at 2163 keV, which corresponds to a γ decay to the ground state from the $7/2_1^+$ 2163 keV state. A gate was placed on the 2163 keV transition and a further γ-γ coincidence analysis was performed. Coincidence relationships were observed at 2310.4(1) keV, 3096.0(30) keV, 3118.8(2) keV, 3154.7(1) keV and 3227.2(11) keV, as shown in Figs. 5.4 and 5.5, indicating excited states in ^{27}Si at 4473.6(3) keV, 5260.4(10) keV, 5282.4(2) keV, 5318.0(1) keV and 5389.7(7) keV, respectively.

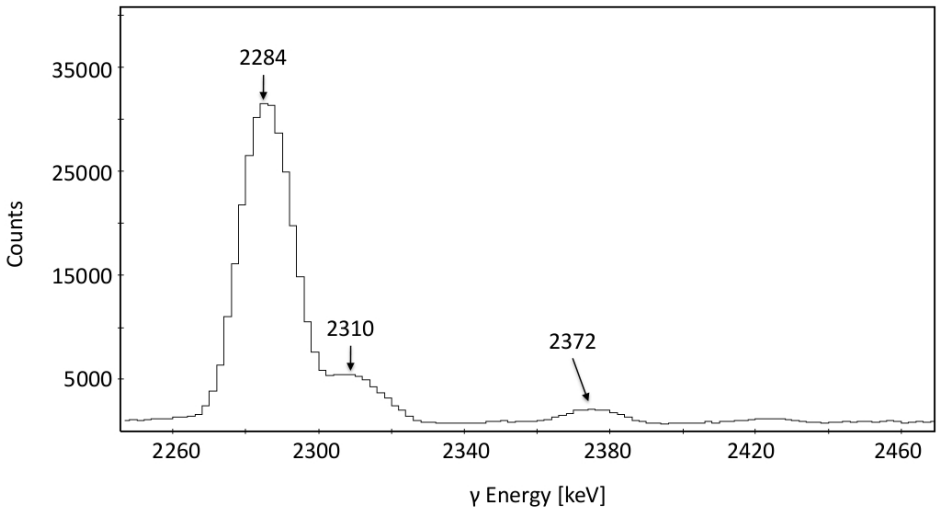

Figure 5.4: γ-γ coincidence spectrum with a gate placed on the 2163 keV transition in ^{27}Si showing the energy range 2260–2460 keV.

From the good agreement of level energy it is deduced that the presently observed 4474 keV excited state corresponds to the previously observed $(7/2, 9/2)^+$ 4474.8(7) keV [63] state in ^{27}Si. The previous study [63] only reports a single γ-ray transition to the ground state from the 4474 keV state and therefore, although a further γ-ray transition to the $7/2_1^+$ state was observed in the present data, this state should still be expected to exhibit a large γ-decay branch to the ground state. In considering the mirror nucleus system, the only high-spin state in an energy range of 4474±500 keV, exhibiting a large γ-decay branch to the ground with a further decay branch to the $7/2_1^+$ state, is the $7/2_2^+$ 4580 keV state in ^{27}Al. The 4580 keV state is also known to exhibit a γ-decay branch

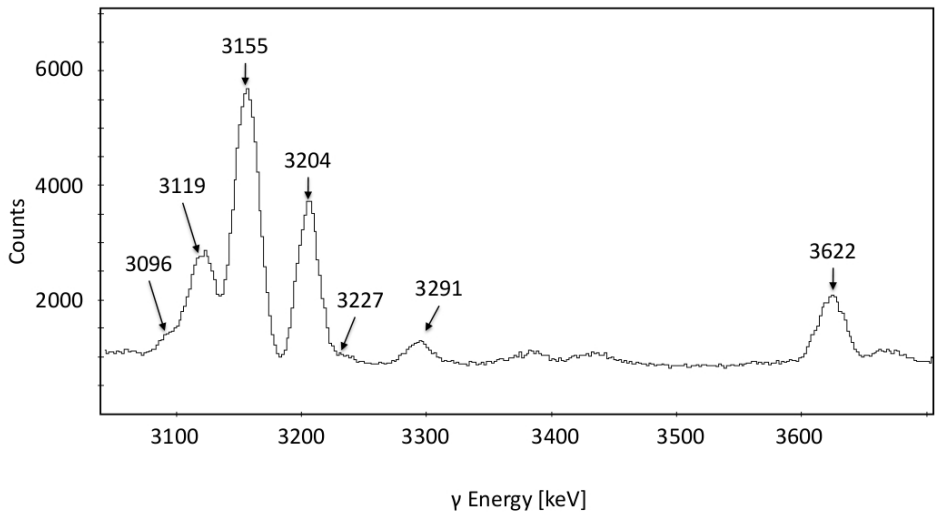

Figure 5.5: γ-γ coincidence spectrum with a gate placed on the 2163 keV transition in ^{27}Si showing the energy range 3000–3700 keV.

to the $5/2_2^+$ excited state and consequently, if the presently observed 4474 keV state in ^{27}Si is indeed its mirror analog then it should also exhibit a γ-decay branch to the corresponding $5/2_2^+$ excited state. A γ-γ-γ coincidence analysis with gates placed upon the 957 keV and 1690 keV transitions, shown in Fig. 5.6, was performed to identify coincidence relationships with the $5/2_2^+$ excited state in ^{27}Si.

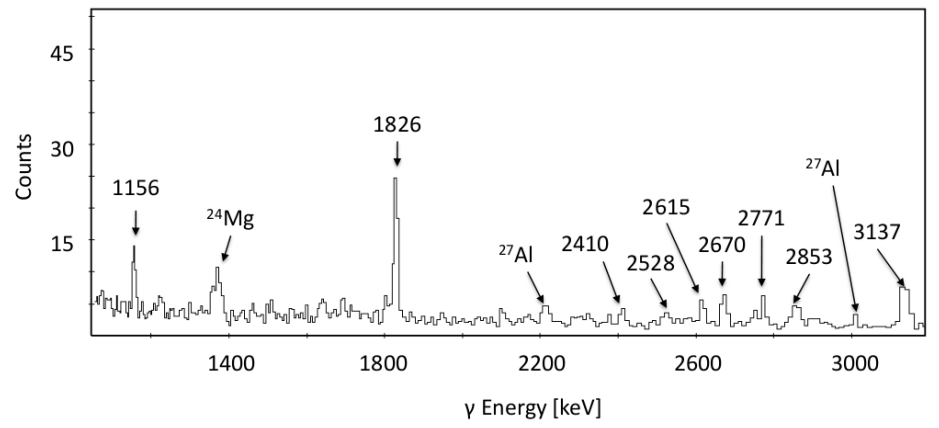

Figure 5.6: γ-γ-γ coincidence spectrum with gates placed on the 957 keV and 1690 keV transitions in ^{27}Si, showing the energy range 1000–3200 keV.

As can be seen in Fig. 5.6, a coincidence relationship with the $5/2_2^+$ excited state is observed at 1826 keV, indicating that the 4474 keV excited state in ^{27}Si does indeed exhibit a γ-decay branch to the $5/2_2^+$ level. Thus, 2310 keV and 1826 keV γ-ray transitions from a $7/2_2^+$ 4474 keV excited state in ^{27}Si were assigned.

The $7/2_3^+$ 5260 keV Level

Prior to the present work an excited state in ^{27}Si was observed at 5262.0(5) keV with possible spin-parity assignments of ($5/2^+$, 7/2, $9/2^+$) [63]. However, no information regarding the γ-ray transitions from this state was obtained. In the present work an excited state is observed at 5260.4(10) keV, in good agreement with the previously observed level energy, with a 3096(3) keV γ-decay branch to the $7/2_1^+$ state, as shown in Fig. 5.5. In addition, a γ-γ-γ coincidence analysis with gates placed upon the 2163 keV and 747 keV transitions was performed to identify coincidences with the $9/2_1^+$ state in ^{27}Si and a further 2350.7(1) keV γ-decay branch from the 5260 keV state to the $9/2_1^+$ state was observed, as shown in Fig. 5.7. The intensity of the 3096 keV and 2351 keV transitions were too

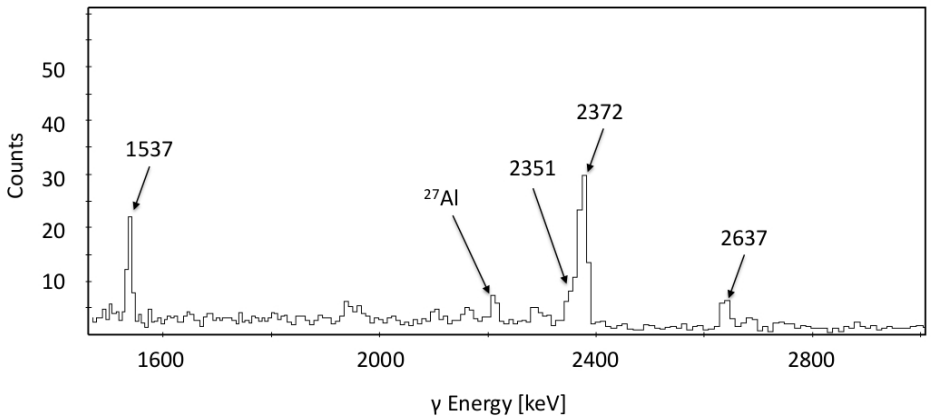

Figure 5.7: γ-γ-γ coincidence spectrum with gates placed on the 2163 keV and 747 keV transitions in ^{27}Si, showing the energy range 1500–3000 keV.

low to obtain a reliable angular distribution information and consequently, the analysis of this state relied upon mirror nucleus comparisons.

Within the spin-parity assignment restrictions and in an energy region of ±300 keV of 5260 keV, in ^{27}Al, only the $7/2^+_3$ 5433 keV state exhibits strong decays to the $7/2^+_1$ and $9/2^+_1$ states. Furthermore shell model calculations [91] predict the existence of a $7/2^+$ state in this energy region yet to be assigned in ^{27}Si. Therefore, I assign the 3096 keV and 2351 keV γ-ray transitions to a $7/2^+_3$ 5260 keV level in ^{27}Si.

The $11/2^+_2$ 5282 keV Level

In considering Fig. 5.7 a high intensity coincidence with the $9/2^+_1$ state is observed at 2372.1(1) keV, indicating an excited state in ^{27}Si at 5282.4(2) keV. This observation is in excellent agreement with the previous work, in which a 78% γ-decay branch to the $9/2^+_1$ state from a $(7/2, 11/2)^+$ 5282.8(4) keV state in ^{27}Si was reported [63]. In the present work a further 3118.8(2) keV γ-decay branch to the $7/2^+_1$ state from the 5282 keV state was observed, as shown in Fig. 5.5. This transition was measured to have an angular distribution of a_2 = 0.26(5) and a_4 = -0.04(13), indicating an angular momentum change of ΔI=±2 and thus, a spin assignment of 3/2 or 11/2 for the 5282 keV state. From the previously obtained spin-assignment information for the 5282 keV state, a 3/2 assignment is ruled out and an $11/2^+$ assignment is indicated. Furthermore, a γ-γ-γ coincidence analysis with gates placed upon the 2163 keV and 2284 keV transitions was performed to identify coincidences with the $11/2^+_1$ state in ^{27}Si and an additional 835.6(6) keV γ-decay branch from the 5282 keV state to the $11/2^+_1$ state was observed, as shown in Fig. 5.8. The observation of a decay to the $11/2^+_1$ state reinforces the ruling out of a possible $3/2^+$ assignment for the 5282 keV state. In comparison with the mirror nucleus, the $11/2^+_2$ 5500 keV state is known to exhibit γ-ray transitions to the $7/2^+_1$, $9/2^+_1$ and $11/2^+_1$ states. Thus, with the collective agreement of information, 836 keV, 2372 keV and 3119 keV γ-ray transitions from an $11/2^+_2$ 5282 keV state in ^{27}Si were assigned.

The $9/2^+_2$ 5318 keV Level

Returning to Fig. 5.5, a very strong coincidence relationship with the $7/2^+_1$ state is observed at 3154.7(1), indicating an excited state in ^{27}Si at 5318.0(1).

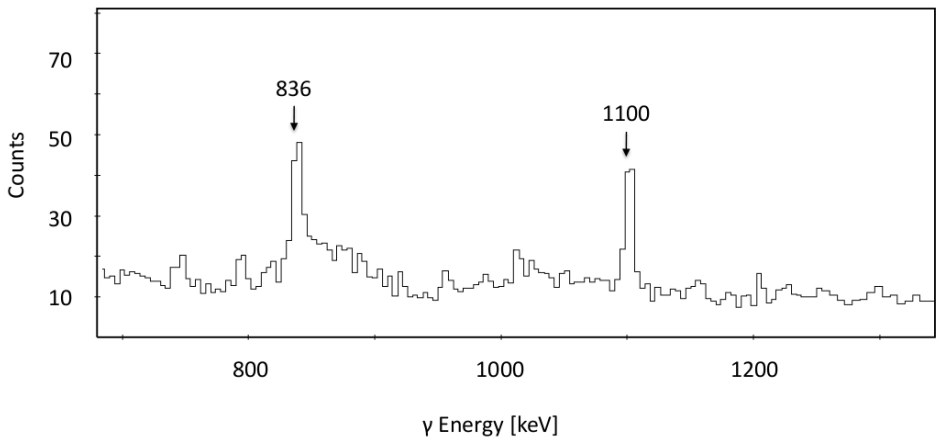

Figure 5.8: γ-γ-γ coincidence spectrum with gates placed on the 2163 keV and 2284 keV transitions in ^{27}Si, showing the energy range 700–1300 keV.

This observation is in good agreement with the previously reported 100% γ-decay branch to the $7/2^+_1$ state from a 5316.7(1) keV excited state in ^{27}Si. No spin-parity assignment has previously been obtained for this state and as such an angular distribution of the 3155 keV γ ray was performed. This analysis yielded a_k coefficients of a_2 = -0.78(3) and a_4 = 0.19(5), consistent with a ΔI=$\pm$1 transition, indicating a 5/2 or 9/2 spin assignment for the 5318 keV state. By comparison with the mirror nucleus system, the $9/2^+_2$ 5420 keV excited state is the only unassigned mirror state within the spin assignment restrictions, in an energy region of 5318$\pm$500 keV, which is known to exhibit a 91% γ-decay branch to the $7/2^+_1$ state. The 5420 keV state in ^{27}Al is also known to exhibit a weaker branch to the $5/2^+_2$ excited state and as can be seen in Fig. 5.6, a 2670.3(2) keV γ-ray transition is observed, indicating that the 5318 keV state also exhibits a decay to the $5/2^+_2$ state in ^{27}Si. Consequently, 2670 and 3155 keV γ-ray transitions from a $9/2^+_2$ 5318 keV excited state in ^{27}Si were assigned.

The $5/2^+_6$ 5390 keV Level

The lowest-lying excited state in the present data above 5318 keV, and thus outside the previously studied γ-ray energy region, is observed at 5389.7(7) keV. This is in good agreement with the $(3/2, 5/2)^+$ 5391.7(16) keV level reported in previous work [63] for the first excited state to appear above 5318 keV in ^{27}Si.

In this work, only low-intensity γ-ray transitions from the 5390 keV state to the $3/2_1^+$ and $7/2_1^+$ states were observed, as shown in Figs. 5.5 and 5.9, respectively. However, by considering the mirror nucleus system in an energy region ±500

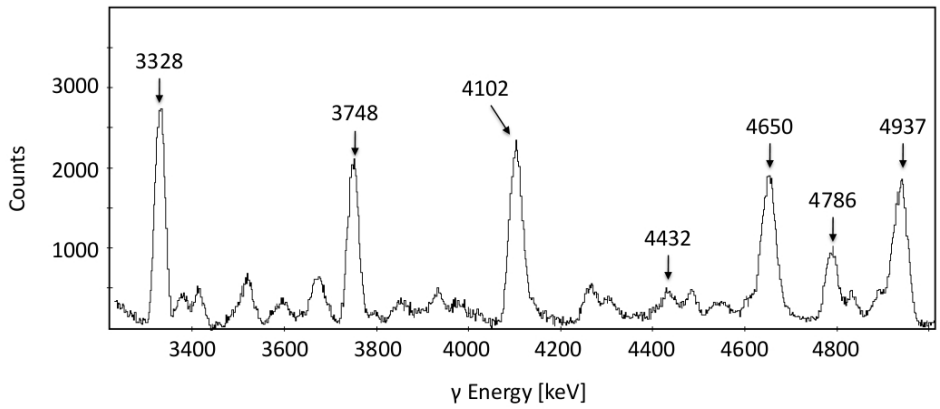

Figure 5.9: γ-γ coincidence spectrum with a gate placed on the 957 keV transition in ^{27}Si showing the energy range 3200–5000 keV.

keV of 5390 keV, only the 5/2 5551 state in ^{27}Al remains as a possible mirror candidate, due to the previously reported spin-parity assignment restrictions and present mirror assignments. The 5551 keV state in ^{27}Al is known to have a dominant decay branch to the ground state with weaker transitions to the $3/2_1^+$ and $7/2_1^+$ excited states. This is consistent with what is observed in the current work and consequently, with the previous spin-parity restrictions for this state [63], 3227 and 4432 keV γ-ray transitions from a $5/2_6^+$ 5390 keV excited state were assigned.

The $5/2_1^-$ 5500 keV Level

A mirror analog of the $5/2_1^-$ 5438 keV excited state in the nucleus ^{27}Al has yet to be identified by any previous study of ^{27}Si. The 5438 keV state in ^{27}Al is known to exhibit an 83% γ-decay branch to the ground with only one further notable 13% γ-decay branch to the $5/2_2^+$ state. In the present work, only the most intense transitions, up to 3 MeV, direct to the ground state are observed. Consequently, a γ-decay transition ∼5 MeV from a $5/2_1^-$ state direct to the ground, will not be observed. However, it is possible to observe decays to the $5/2_2^+$ state in the present data, as shown in Fig. 5.6. In considering Fig. 5.6,

a coincidence relationship with the $5/2_2^+$ state in ^{27}Si is observed at 2853.0(1) keV, indicating an excited state in ^{27}Si at 5500.4(2) keV, which agrees well with a previously observed 5497(2) keV excited state in ^{27}Si [63]. No further coincidence relationships were observed from the 5500 keV state in ^{27}Si. In fact, the 5500 keV state is the only remaining excited state in ^{27}Si with a coincidence relationship with the $5/2_2^+$ excited state and within an energy range of ±300 keV of 5438 keV, that is yet to be assigned to a corresponding mirror state in ^{27}Al. Consequently, a 2853 keV γ-ray transition from a $5/2_1^-$ 5500 keV excited state was assigned in ^{27}Si.

The $9/2_3^+$ 5547 keV Level

In the compilation data of Ref. [63], an excited state in ^{27}Si was observed at 5547(4) keV. In the present data an excited state was observed at 5547.3(1) keV, with γ-decay branches to the $11/2_1^+$ and $9/2_1^+$ states, shown in Figs. 5.8 and 5.7, respectively, in good agreement with the level energy obtained in the previous work [63]. The observed coincidence relationships indicate a minimum 7/2 spin-assignment for the 5547 keV level. In comparison with the mirror nucleus, ^{27}Al, the $9/2_3^+$ 5667 keV state is the only high-spin state, in an energy region 5547±300 keV, yet to be assigned to an analog state in ^{27}Si and is known to only exhibit γ-decay branches to the ground, $9/2_1^+$ and $11/2_1^+$ levels [63]. Therefore, from the good agreement of level energy and mirror nucleus comparisons, 1100 keV and 2637 keV γ-ray transitions from a $9/2_3^+$ 5547 keV level in ^{27}Si to the $11/2_1^+$ and $9/2_1^+$ states, respectively, were assigned.

Unobserved Low-lying Excited States

An excited state previously observed at 2866 keV, with a spin-parity assignment of $(3/2, 5/2)^+$ [63], was the only low-lying excited state in ^{27}Si not to be observed in the present data. This state is known to exhibit γ-ray transitions to the $7/2_1^+$, $3/2_1^+$, $1/2_1^+$ and ground states with branches of <0.5%, <1%, 4% and 95%, respectively. By comparison with the mirror nucleus, ^{27}Al, the $3/2_2^+$ excited state at 2982 keV is also known to decay to the $7/2_1^+$, $3/2_1^+$, $1/2_1^+$ and ground states with similar branches of <0.2%, 2%, 1% and 97%, respectively, to those listed above [63]. This is the only ^{27}Al mirror state, in the energy region of

0–5667 keV, presently not assigned to an analog state in ^{27}Si and, in fact, is also the only mirror state not observed in the present data. Thus, indicating that the dominant γ-ray transition to the ground state from the $3/2_2^+$ level cannot be observed in the present experimental setup and a 3_2^+ assignment was adopted for the unobserved 2866 keV in ^{27}Si.

The analysis thus far completes the discussion on the low-lying level structure of ^{27}Si.

5.2 Proton-unbound States in ^{27}Si

Previous studies of the ^{26}Al$(p,\gamma)^{27}$Si reaction [37; 38; 39; 40; 41; 42; 43] indicate that over typical novae temperatures (T=0.06–0.4 GK) the rate is dominated by resonant capture to excited states in ^{27}Si above the proton threshold energy (7463.0(2) keV) [19]. The first experimental evaluation of the ^{26}Al$(p,\gamma)^{27}$Si reaction rate was performed by Buchmann *et al.* [38], in which a proton capture reaction was used to investigate resonant states in ^{27}Si over the energy range E_p=0.17–1.58 MeV. In this study two strong resonances in the ^{26}Al + p system were identified at E_p=286.6(3) and 376(3) keV respectively. A later ^{26}Al$(^3\mathrm{He},d)^{27}$Si transfer reaction study, performed by Vogelaar *et al.* [41; 42], observed an excited state in ^{27}Si above the proton threshold at 7652(3) keV with an implied high spectroscopic factor. This indicated a possible previously unobserved resonance at E_p=195 keV and prompted a following direct (p,γ) study [41]. In Ref. [41] a resonance at E_p=195.6(11) keV was indeed observed and a resonance strength of 55(9) μeV was obtained, which has been more recently measured at 35(7) μeV in a study by Ruiz *et al.* using radioactive ion beams in inverse kinematics [43]. The resonance strength measurements obtained in the direct (p,γ) studies, covering the energy range 0.17–1.58 MeV, are expected to constrain the ^{26}Al$(p,\gamma)^{27}$Si stellar reaction rate for $T > 0.2$ GK [38; 41; 43]. However, it should be noted that prior to Refs. [41; 42; 43], ^{27}Al$(^3\mathrm{He},t)^{27}$Si and ^{28}Si(^{3}He, α)^{27}Si reaction studies, performed by Schmalbrock *et al.* [39] and Wang *et al.* [40] respectively, firmly identified excited states above the threshold in ^{27}Si at 7468(3) keV, 7532(3) keV and 7592(3) keV. These observed excited states correspond to possible resonant states in the ^{26}Al + p system with E_p<170 keV and thus, fall outside the presently covered energy range by direct (p,γ)

Table 5.2: γ-ray energies, angular distribution coefficients and level energies of excited states above the proton-emission threshold in ^{27}Si. Resonance strength measurements from direct (p, γ) studies have also been included.

E_x (keV) Endt [63]	E_x (keV) Present	E_r (keV)	E_γ (keV)	a2/a4	Assignment	Measured $\omega\gamma$ (meV)
7468(3)	7469.0(6)	6.0(6)	6511.1(6)	-0.64(25)/0.39(34)	$5/2^+ \rightarrow 3/2^+_1$	
7532(3)	7531.3(7)	68.3(7)	4883.5(5)		$5/2^+ \rightarrow 5/2^+_2$	
			6573.5(9)	-0.88(18)/0.34(22)	$5/2^+ \rightarrow 3/2^+_1$	
7557(3)						
7592(3)	7589.7(8)	126.7(8)	3115.6(14)		$9/2^+ \rightarrow 7/2^+_2$	
			3142.6(27)		$9/2^+ \rightarrow 11/2^+_1$	
			5425.9(1)	-0.52(2)/0.01(3)	$9/2^+ \rightarrow 7/2^+_1$	
7652(3)	7651.6(3)	188.6(4)	2371.0(40)		$11/2^+ \rightarrow 11/2^+_2$	
			3204.1(1)	0.40(3)/-0.01(4)	$11/2^+ \rightarrow 11/2^+_1$	0.055(9) [41], 0.035(7) [43]
7690(3)	7693.8(9)	230.8(9)	5530.1(9)	0.50(7)/0.24(9)	$5/2^+ \rightarrow 7/2^+_2$	$\leq$0.010 [41]
7702(2)	7704.3(2)	241.3(3)	5056.7(1)	-0.21(7)/0.09(9)	$7/2^- \rightarrow 5/2^+_2$	0.010(5) [41]
7740.8(9)	7739.3(4)	276.3(4)	2421.6(4)		$9/2^+ \rightarrow 9/2^+_2$	3.8(10) [38], 2.9(3) [41]
			2455.9(4)		$9/2^+ \rightarrow 11/2^+_2$	
			3291.3(1)		$9/2^+ \rightarrow 11/2^+_1$	
			4828.7(5)	0.25(12)/-0.25(17)	$9/2^+ \rightarrow 9/2^+_1$	
			5575.7(2)	-0.10(4)/0.11(5)	$9/2^+ \rightarrow 7/2^+_1$	
7792(3)	7794.8(19)	331.8(19)	5631.0(19)		$7/2^+ \rightarrow 7/2^+_1$	
7831(3)	7831.5(4)	368.5(4)	2329.8(8)		$9/2^- \rightarrow 5/2^-_1$	65(18) [38], 69(7) [41]
			3383.8(2)		$9/2^- \rightarrow 11/2^+_1$	
			4921.0(4)	0.18(7)/0.05(9)	$9/2^- \rightarrow 9/2^+_1$	
			5668.0(3)		$9/2^- \rightarrow 7/2^+_1$	

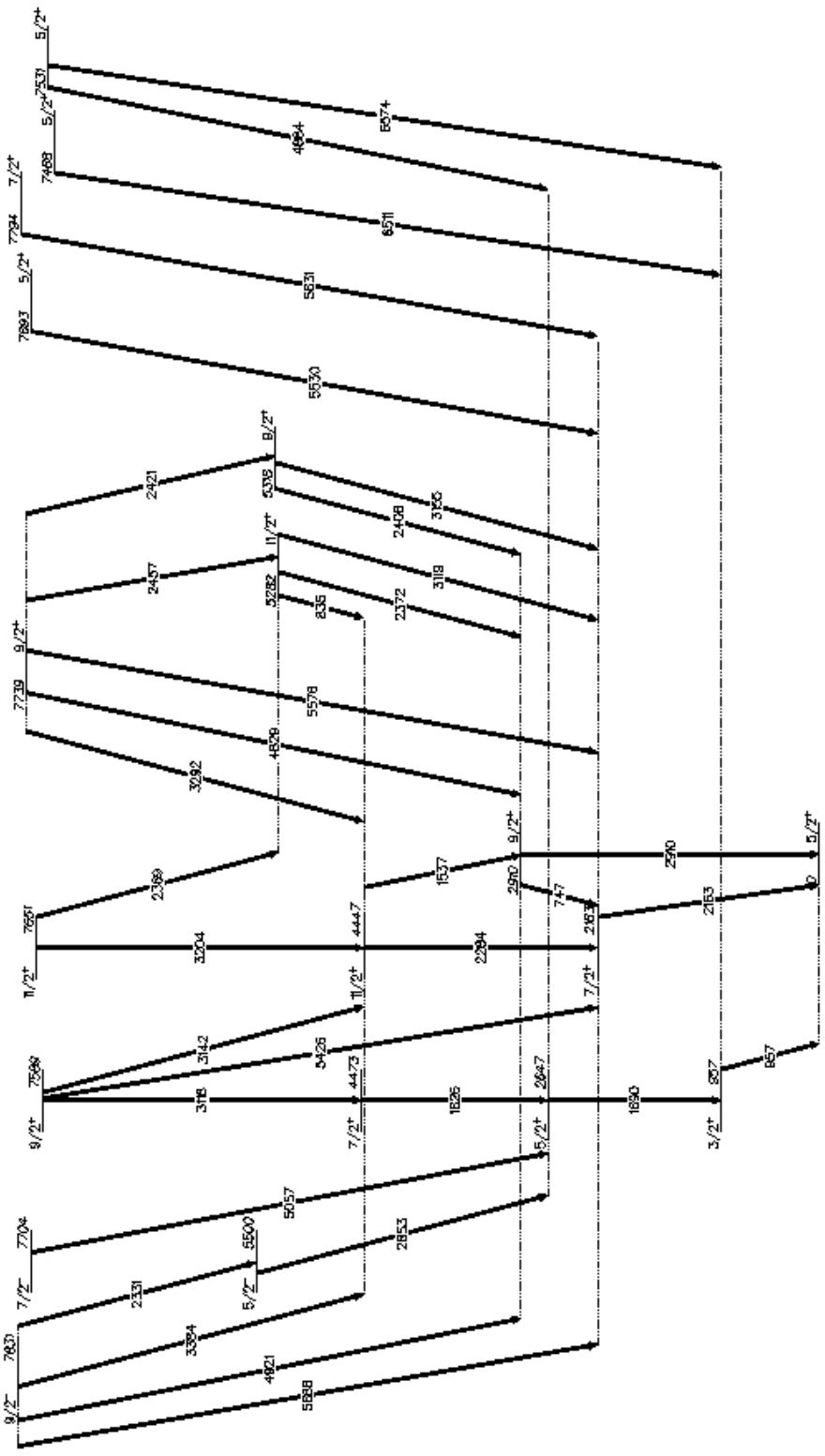

Figure 5.10: Partial level scheme showing relative positions and γ-decay branches of proton-unbound states in ^{27}Si.

studies. In fact, Vogelaar *et al.* comment that because they were not able to observe states below 7652 keV, significant uncertainty remains in the astrophysical reaction rate and conclude that the 7592(3) keV excited state in ^{27}Si [39; 40], corresponding to a resonance energy of 129(3) keV in the ^{26}Al + p system, could be astrophysically important [42].

In this thesis work proton-unbound states in ^{27}Si were populated in a heavy-ion fusion evaporation reaction, which strongly favours the population of high-spin states above the threshold. No firm spin-parity assignments have been previously made for any excited state above the proton threshold in ^{27}Si and, given that the 5^+ spin-parity of the ^{26}Al ground state also favours the population of high-spin states in ^{27}Si, determinations of this type are essential in identifying possible astrophysically important low-energy resonant states, for which direct (p, γ) resonance strength measurements are presently unavailable.

Table 5.2 presents a summary of the level energies, spins and γ-ray energies for observed proton-unbound excited states in ^{27}Si, together with a comparison with previous results. In addition, a partial level scheme for proton-unbound excited states in ^{27}Si is displayed in Fig. 5.10.

The $5/2^+$ 7469 keV Level (E_r=6 keV)

Previous studies of the nucleus ^{27}Si have reported the lowest-lying excited state above the proton threshold at 7468(3) keV [39; 40]. In the present work a 6511.1(6) keV γ-ray transition to the $3/2^+_1$ state from a level at 7469.0(6) keV in ^{27}Si was observed, as shown in Fig. 5.11. The current observed level energy is in excellent agreement with Ref. [63] and as no lower energy excited states above the threshold were observed it is accepted that the 7469 keV state is the lowest-lying excited state above the proton threshold in ^{27}Si. The 6511 keV transition to the $3/2^+_1$ state is measured to have an angular distribution consistent with a ΔI=$\pm$1 transition, indicating a spin assignment of 1/2 or 5/2 for the 7469 keV level. In comparison with the mirror nucleus, ^{27}Al, in an energy region 7469$\pm$300 keV, there are no known 1/2 states that exhibit a γ-decay branch to the $3/2^+_1$ level [63] ruling out a 1/2 assignment. In fact, in this energy region only two possible $5/2^+$ states are known to exhibit γ-decay branches to the $3/2^+_1$ level and only the $(3/2, 5/2)^+$ 7677 keV is known to exhibit a single γ-ray transition, other than to the ground, to the $3/2^+_1$ state. Consequently, as

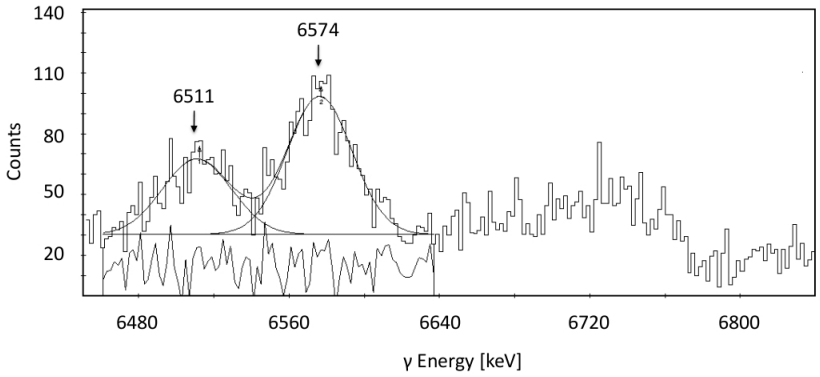

Figure 5.11: γ-γ coincidence spectrum with a gate placed on the 957 keV transition in ^{27}Si, showing the energy range 6440–6840 keV. Base line subtraction for the peak fits shown has been performed using the RadWare program gf3.

no further transitions from the 7469 keV were observed in the present data, a 6511 keV transition from a $5/2^+$ 7469 keV level in ^{27}Si was assigned.

The $5/2^+$ 7531 keV Level (E_r=68 keV)

In considering Fig. 5.11, an additional 6573.5(9) keV coincidence relationship with the $3/2^+_1$ state was observed, indicating an excited state in ^{27}Si at 7531.3(7) keV in good agreement with the previously observed level energies for this state [39; 40]. Furthermore, a 4883.5(5) keV γ-ray transition from the 7531 keV level to the $5/2^+_1$ state was also observed, as shown in Fig. 5.12. The 6574 keV transition to the $3/2^+_1$ state is measured to have an angular distribution consistent with a ΔI=$\pm$1 transition, indicating a spin assignment of 1/2 or 5/2 for the 7531 keV level. As with the 7469 keV level, mirror nucleus comparisons rule out a 1/2 assignment for the 7531 keV state as no known 1/2 states in ^{27}Al, in an energy region 7531$\pm$300 keV, exhibit a γ-decay branch to the $3/2^+_1$ state [63]. A $5/2^-$ assignment is also ruled out from a similar mirror nucleus comparison [63] and in fact, only a single remaining unassigned $5/2^+$ state, in the energy region 7531$\pm$300 keV in ^{27}Al, is known to exhibit a γ-decay branch to the $3/2^+_1$ state. Thus, 6574 keV and 4884 keV γ-ray transitions from a $5/2^+$ 7531 keV level to the $3/2^+_1$ and $5/2^+_2$ states, respectively, were assigned in ^{27}Si.

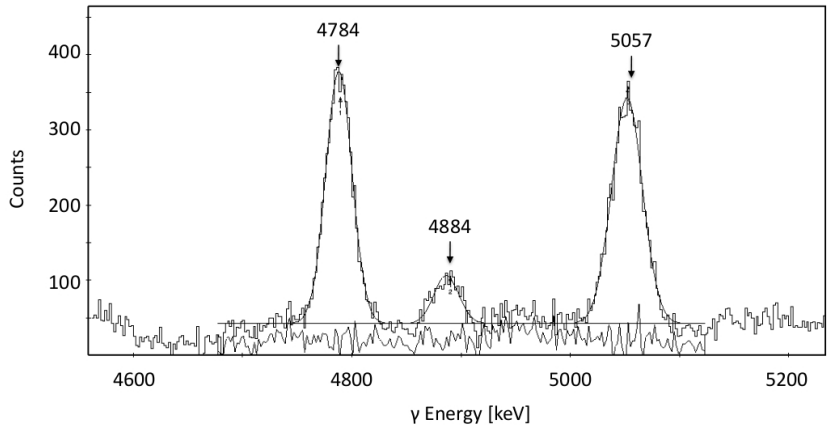

Figure 5.12: γ-γ coincidence spectrum with a gate placed on the 1690 keV transition in ^{27}Si, showing the energy range 4600–5200 keV.

The $9/2^+$ 7590 keV Level (E_r=127 keV)

An excited state previously observed at 7589(3) keV in ^{27}Si [40] has been suggested to correspond to a resonance at E_r = 126 keV, with a possible l_p = 0 component [39; 40; 41; 42]. In the present data an excited state is observed at 7589.7(8) keV, which shows excellent agreement with the previously reported level energies for this state [39; 40] and consequently, is also expected to correspond to a resonance at E_r = 126.7(8) keV. The 7590 keV state is observed to exhibit a high-intensity 5425.9(1) keV γ-ray transition to the known $7/2^+_1$ excited state in ^{27}Si, as shown in Fig. 5.13, and is measured to have an angular distribution consistent with a ΔI=$\pm$1 transition. Further 3115.6(14) keV and 3142.6(27) keV γ-decay branches to the known $7/2^+_2$ state and $11/2^+_1$ state in ^{27}Si, shown in Fig. 5.14, and in Fig. 5.15, respectively, were also observed. The angular distribution measurement indicates a spin assignment of 5/2 or 9/2 for this state. The high-intensity coincidence-relationship with the $7/2^+_1$ state and the further 3143 keV coincidence-relationship with the $11/2^+_1$ excited state in ^{27}Si rules out a 5/2 assignment and consequently, a 9/2 spin assignment is determined for the 7590 keV state. In fact, it should be noted at this point that all coincidences observed with the $11/2^+_1$ gate represent high-spin states. In previous work by Champagne *et al.* [37], excited states above the proton

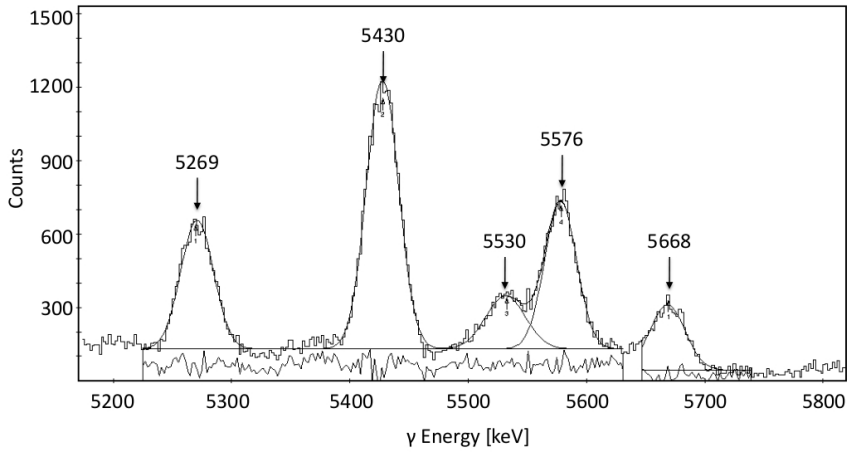

Figure 5.13: γ-γ coincidence spectrum with a gate placed on the 2164 keV transition in ^{27}Si, showing the energy range 5200–5800 keV.

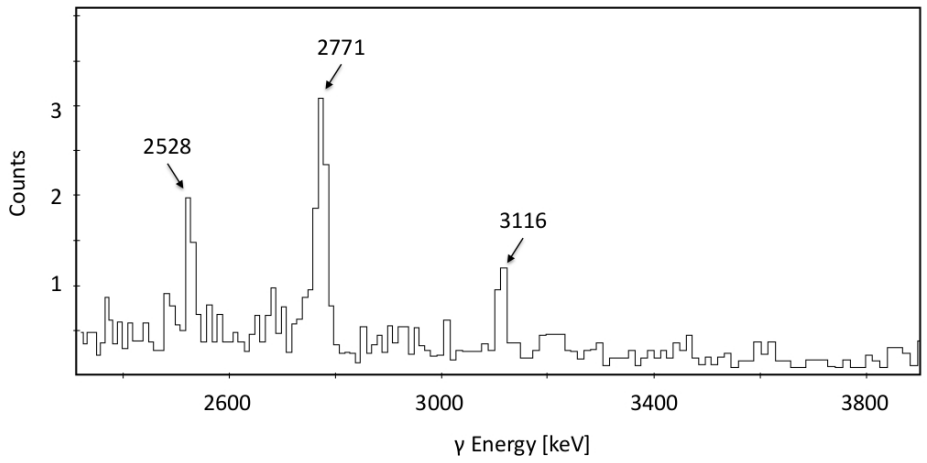

Figure 5.14: γ-γ-γ coincidence spectrum with gates placed on the 2163 keV and 2310 keV transitions in ^{27}Si, showing the energy range 2400–3800 keV.

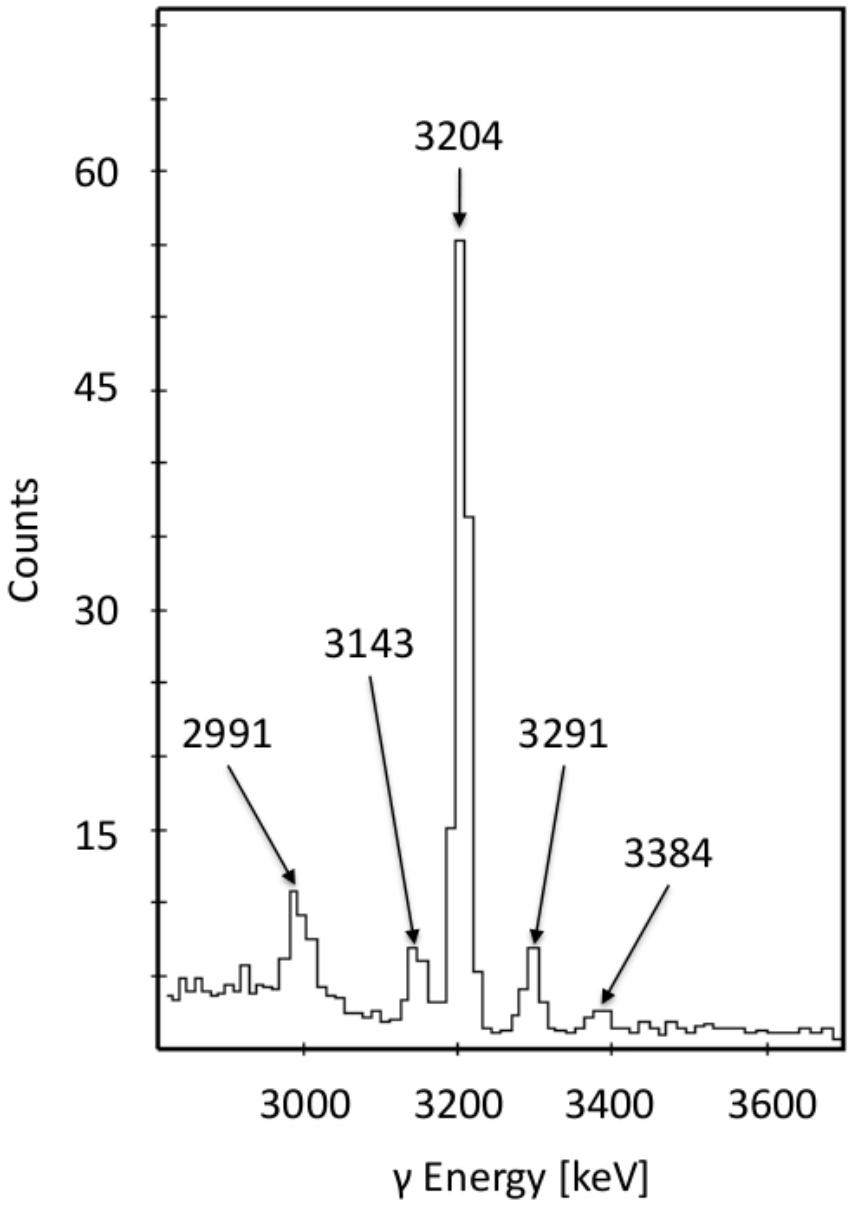

Figure 5.15: γ-γ-γ coincidence spectrum with gates placed on the 2163 keV and 2284 keV transitions in ^{27}Si, showing the energy range 2800–3600 keV.

threshold in ^{27}Si were matched to possible mirror states in ^{27}Al, together with possible sd-shell model configurations. In this study an approximate 200 keV shift was found between positive parity states in the mirror nuclei and the 7590 keV excited state in ^{27}Si was determined to be a possible analog to known $3/2^+$ and $9/2^+$ excited states in ^{27}Al. The presently determined spin assignment rules out the possible $3/2^+$ analog assignment and indicates that the known $9/2^+$ 7806 keV excited state in ^{27}Al represents a possible mirror analog to the presently observed 7590 keV state in ^{27}Si. As stated above, the 7590 keV state is observed to exhibit γ-decay branches to the known $7/2^+_1$, $11/2^+_1$ and $7/2^+_2$ excited states. In comparison with the mirror, the $9/2^+$ 7806 keV state is also known to exhibit similar γ-decay branches to the corresponding $7/2^+_1$, $11/2^+_1$ and $7/2^+_2$ excited states in ^{27}Al [63]. Consequently, a $9/2^+$ 7590 keV excited state was assigned in ^{27}Si. The newly determined spin-parity assignment for this state has indicated that if a resonance at 127 keV in the ^{26}Al + p system does indeed exist, it could have an $l_p = 0$ component in the reaction process. This in itself may be extremely important and will be discussed in section 5.3.

The $11/2^+$ 7652 keV Level (E_r=189 keV)

Vogelaar *et al.* [41] reported γ decays from a resonant state at 195 keV in the ^{26}Al + p system and observed a 90% decay branch to the known $11/2^+_1$ excited state. In the work by Vogelaar *et al.* [41; 42] it was indicated that this resonance corresponds to an excited state in ^{27}Si at 7652(3) keV, which was also previously observed in Refs. [39; 40]. Here, an excited state in ^{27}Si at 7651.5(2) keV is identified and a strong 3204.1(1) keV γ-decay transition to the known $11/2^+_1$ state in ^{27}Si is observed, as shown in Fig. 5.15. From the strong agreement of excitation energy with previous studies and the high-intensity coincidence-relationship with the $11/2^+_1$ excited state, it is expected that the presently observed 7652 keV state corresponds to the 195 keV resonant state observed by Vogelaar [41]. Angular distribution coefficients for the 3204 keV γ-ray transition are measured to be consistent with a ΔI=0 transition, indicating an 11/2 spin assignment for the 7652 keV excited state. In the previous study by Champagne *et al.* [37] a generic positive energy shift of ∼200 keV is expected between analog states in the mirror nuclei ^{27}Si and ^{27}Al. Taking this into account two possible mirror 11/2 states to the 7652 keV state exist in the

nucleus ^{27}Al. Both states are known to exhibit strong decays to the $11/2^+_1$ level [63], which are also observed in the present ^{27}Al data. However, the $(9/2, 11/2)^+$ 7948 keV excited state in ^{27}Al is also known to exhibit a low-intensity γ-decay branch to the $11/2^+_2$ level, a decay transition not known to exist in the other possible 11/2 state, which should also be observed from the 7652 keV state if these two states are mirror pairs. This is indeed the case and a 2371.0(40) keV coincidence relationship with the $11/2^+_2$ excited state from a level at 7652 keV was observed, as shown in Figs. 5.16 and 5.17.

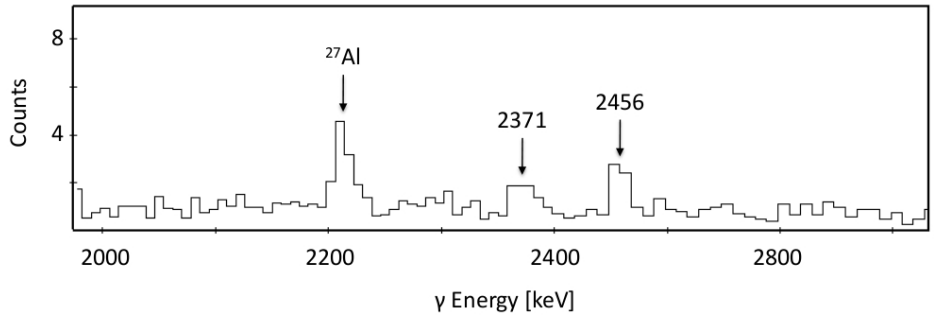

Figure 5.16: γ-γ-γ coincidence spectrum with gates placed on the 2910 keV and 2372 keV transitions in ^{27}Si, showing the energy range 2000–3000 keV. Coincidence relationships are observed at 2371 keV and 2456 keV.

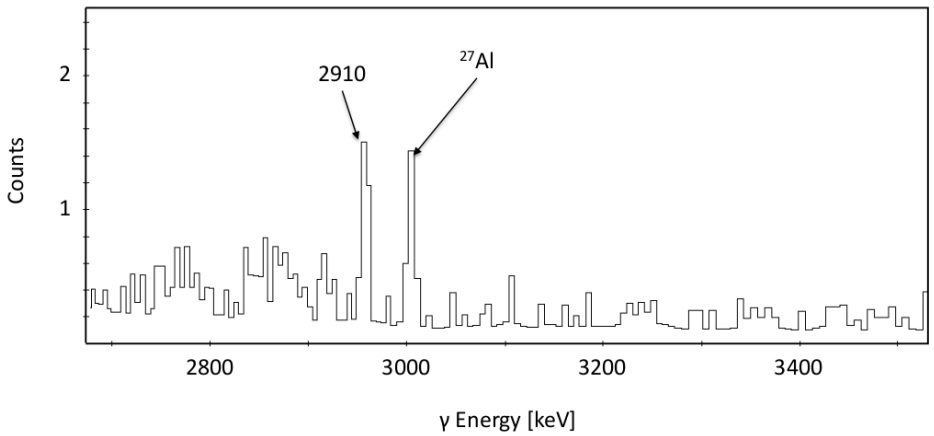

Figure 5.17: γ-γ-γ coincidence spectrum with gates placed on the 2371 keV and 2372 keV transitions in ^{27}Si, showing the energy range 2400–3800 keV. A coincidence relationship is observed at 2910 keV.

Consequently, 2371 keV and 3204 keV γ-ray transitions were assigned from an $11/2^+$ 7652 keV excited state in ^{27}Si. The presently observed excited state at 7652 keV in ^{27}Si, shows excellent agreement with the previously reported level energies for this state [39; 40; 41; 42] and indicates a resonance energy of 188.5(3) keV in the ^{26}Al + p system, in slight disagreement with a recently observed resonance energy of 184(1) keV by Ruiz *et al.* [43]. In the $(^3\mathrm{He}, d)$ experiment performed by Vogelaar *et al.* [42], single-particle resonance strength determinations were made for l_p=0–3 transitions from the 7652 keV state using a DWBA analysis. However, in the work of Vogelaar *et al.*, it is noted that they were unable to discriminate between the angular distributions obtained for l_p=0–3 transitions, shown in Fig. 2.7(b), and as such no definite l_p assignment for the 189 keV resonance was made [42]. Furthermore in Ref. [42], only single-particle states were considered and the possibility of mixed transitions was not explored. In considering Fig. 2.7(b), the angular distribution appears to rule out dominant l_p=0 and l_p=1 components, even though previous work by Ruiz *et al.* [43] assumes l_p=1 for the 189 keV resonant state, and suggests to some degree that the 189 keV resonance contains a dominant l_p=2 component. Therefore, from the newly determined spin-parity assignment of the 189 keV resonant state and the previously measured values of the resonance strength of 0.055(9) meV [41] and 0.035(7) meV [43], it is currently thought that the 189 keV resonance contains a mainly l_p=2 character with a small l_p=0 contribution.

The $5/2^+$ 7694 keV Level (E_r=231 keV)

In the $(^3\mathrm{He}, t)$ experiment performed by Wang *et al.* [40], an excited state in ^{27}Si was observed at 7690(3) keV. In the present ^{27}Si data a single 5530.1(9) keV γ-ray transition from an excited state at 7693.8(9) keV to the $7/2^+_1$ level was observed, as shown in Fig. 5.13, in good agreement with the previously obtained level energy of Ref. [40]. The 5530 keV transition was measured to have angular distribution coefficients consistent with a ΔI=$\pm$1, indicating a 5/2 or 9/2 spin assignment for the presently observed 7694 keV level. In comparison with the mirror nucleus, ^{27}Al, in an energy range 7694$\pm$200 keV, only a single excited state, within the current spin assignment restrictions, exists in which one would only expect to see a single γ-ray transition to the $7/2^+_1$ level; the 5/2 7721 keV state in ^{27}Al [63]. The 7721 keV state is known to exhibit γ-decay

branches to the $3/2^+_2$ and $7/2^+_1$ states [63]. As discussed in the previous section, the $3/2^+_2$ excited state was not observed in either the present ^{27}Si or ^{27}Al data, and consequently, one would only expect to see the decay from the 7721 keV state to the $7/2^+_1$ level. Thus, the 5530 keV γ-ray transition from a 5/2 7694 keV state was assigned in ^{27}Si.

In the direct (p,γ) study by Vogelaar [41] a resonance was observed at E_p=234 keV, corresponding to an excited state in ^{27}Si at 7690 keV, currently observed at 7694 keV. The 234 keV resonance was measured to have a resonance strength of $\leq$0.010 meV [41], which, together with the present 5/2 spin assignment for this state, suggests at least a notable l_p=2 transfer component rather than l_p=3 or higher components for this resonance and consequently, I deduce a $5/2^+$ assignment for the 7694 keV level. It should also be noted that the measured resonance strength of Ref. [41] for this state rules out strong l_p=0 or 1 resonant components and thus, further supports a 5/2 rather than 9/2 spin assignment for this state.

The $7/2^-$ 7704 keV Level (E_r=241 keV)

Previous work by Schmalbrock *et al.* [39] and Wang *et al.* [40] observed an excited state above the proton threshold in ^{27}Si at 7703(3) keV and 7702(3) keV, respectively. The later direct (p,γ) study by Vogelaar identified the 7702 keV state as a resonant state in the $^{26}\mathrm{Al}+p$ system, corresponding to an E_p=241 keV resonance with a resonance strength of 0.010(5) meV. In the present work an excited state above the proton threshold in ^{27}Si was observed at 7704.3(2) keV in agreement with the previously obtained level energies of this state [39; 40; 41] and consequently, it is deduced that the 7704 keV state corresponds to a 241.3(2) keV resonance in the $^{26}\mathrm{Al}+p$ system. In considering Fig. 5.12, a single 5056.7(1) keV coincidence relationship is observed with the $5/2^+_2$ level. No further decays were observed from the 7704 keV state, and the 5057 keV transition was measured to have an angular distribution consistent with a ΔI=$\pm$1 transition, indicating a spin assignment of 3/2 or 7/2 for the 7704 keV level in ^{27}Si. The fact that the 7704 keV state was observed as a resonance in Ref. [41] strongly suggests a 7/2 assignment rather than a 3/2 assignment, due to the fact that the ^{26}Al ground state has a spin-parity assignment of 5^+. In comparison with the mirror nucleus, ^{27}Al, in an energy region 7704$\pm$300 keV, only the $(5/2,\ 7/2)^-$

7900 keV exhibits a single γ-decay branch, other than to the ground state, to the $5/2^+_2$ level. Thus, a 5057 keV transition to the $5/2^+_2$ level from a $7/2^-$ 7704 keV excited state in ^{27}Si was assigned. This assignment is consistent with a possible l_p=1 component for the previously observed 0.010 meV resonance at 241 keV [41].

The $9/2^+$ 7739 keV Level (E_r=276 keV)

Buchmann *et al.* [38] reported γ decays from a resonant state at 287 keV in the ^{26}Al + p system and observed decay branches to the known $9/2^+_2$, $11/2^+_2$, $11/2^+_1$, $9/2^+_1$ and $7/2^+_1$ excited states. The strongest branches observed were to the $9/2^+_1$ and $7/2^+_1$ levels. Similar γ-decay branches from a resonant state at 287 keV in the ^{26}Al + p system were also observed in a study by Vogelaar [41]. In both the study by Buchmann *et al.* [38] and Vogelaar [41] it was indicated that this resonance corresponds to a (9/2, $11/2^+$) excited state in ^{27}Si at 7740.8(9) keV, which was also previously observed in Refs. [39] and [40]. In the present work γ-decay transitions from an excited state at 7739.3(4) keV in ^{27}Si to the $9/2^+_2$ state, shown in Fig. 5.18, the $11/2^+_2$ state, shown in Fig. 5.16, the $11/2^+_1$ state, shown in Fig. 5.15, the $9/2^+_1$, shown in Fig. 5.19 and the $7/2^+_1$ state, shown in Fig. 5.13, were observed. The excellent agreement of observed γ-ray transitions with Refs. [38] and [41] suggests that the presently observed 7739 keV excited state corresponds to a resonance in the ^{26}Al + p system at 276.3(4) keV. The resonance strength of the 276 keV resonance has been measured twice at 3.8(10) [38] and 2.9(3) keV [41], respectively, and as such is well defined.

The 5575.7(2) keV transition to the $7/2^+_1$ level is measured to have an angular distribution consistent with a ΔI=$\pm$1 transition, indicating a 9/2 assignment for the 7739 keV level in ^{27}Si. Furthermore, the 4828.7(5) keV transition to the $9/2^+_1$ level is measured to have an angular distribution consistent with a ΔI=0 transition, which also indicates a 9/2 assignment for the 7739 keV level in ^{27}Si. In the study by Champagne *et al.* [37], the 7739 keV excited state in ^{27}Si was determined to be a possible analog to the known $9/2^+$ 7997 keV and $(9/2, 11/2)^+$ 7948 keV excited states in ^{27}Al [63]. Although both represent possible 9/2 mirrors, exhibiting strong γ-decay branches to the $9/2^+_1$ level, only the $9/2^+$ 7997 keV state in ^{27}Al is known to exhibit a γ-decay branch to the $7/2^+_1$ level. In fact, the 7997 keV excited state in ^{27}Al is the only unassigned

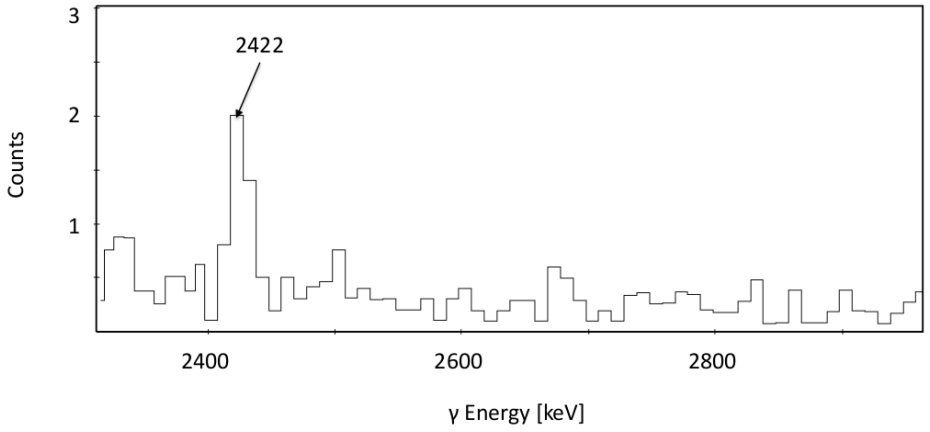

Figure 5.18: γ-γ-γ coincidence spectrum with gates placed on the 2163 keV and 3155 keV transitions in ^{27}Si, showing the energy range 2300–3000 keV.

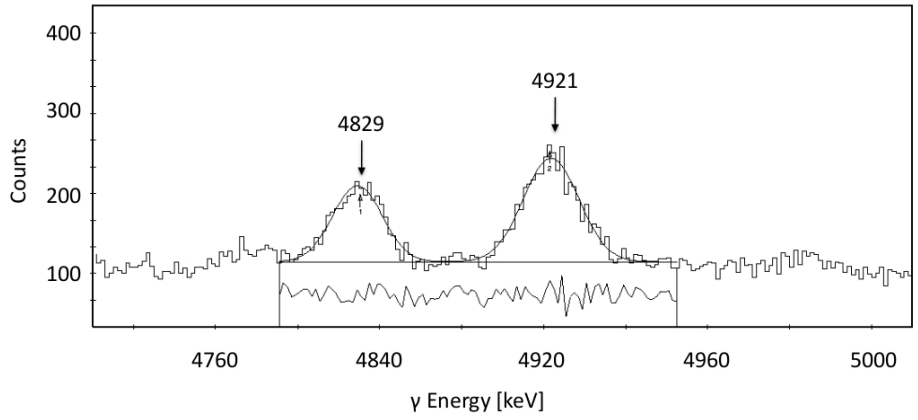

Figure 5.19: γ-γ coincidence spectrum with a gate placed on the 2910 keV transition in ^{27}Si, showing the energy range 4720–5000 keV.

9/2 state in an energy region of 7739±500 keV that exhibits a γ-decay branch to the $7/2^+_1$ level. Consequently, from the collective agreement of information, 2421.6(4) keV, 2455.9(4) keV, 3291.3(1) keV, 4828.7(5) keV and 5575.7(2) keV γ-ray transitions from a $9/2^+$ 7739 keV level to the $9/2^+_2$, $11/2^+_2$, $11/2^+_1$, $9/2^+_1$ and $7/2^+_1$ excited states, respectively, were assigned in ^{27}Si.

The $7/2^+$ 7795 keV Level (E_r=332 keV)

An excited state in ^{27}Si at 7792(3) keV has been previously observed in the separate work of Schmalbrock *et al.* [39] and Wang *et al.* [40]. At detector angles; 17°, 32°, 37° 70° and 90°, a 5631.0(19) keV γ-ray transition from an excited state at 7794.8(19) keV to the $7/2^+_1$ level is observed in the present ^{27}Si data, as shown in Fig. 5.20. The good agreement of the present level energy

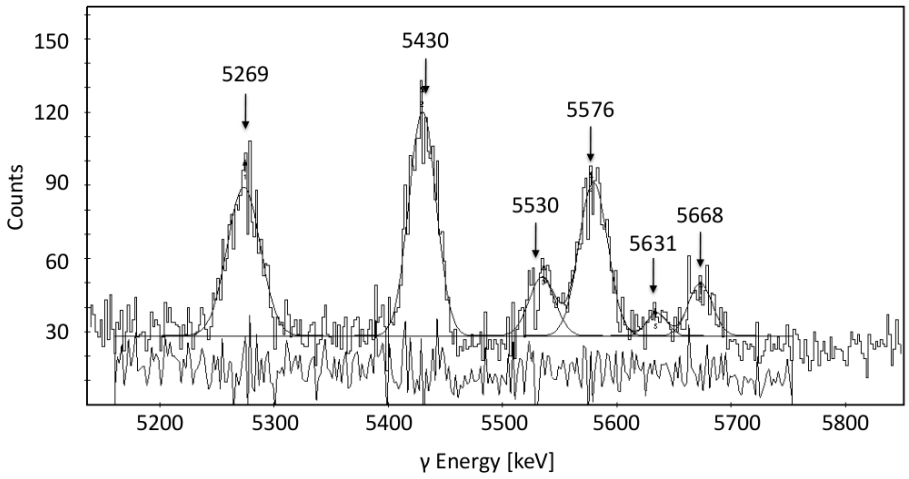

Figure 5.20: γ-γ coincidence spectrum with a gate placed on the 2163 keV transition in ^{27}Si for detectors placed at 37.38 degrees in the GAMMASPHERE detector array, showing the energy range 5200–5800 keV.

with those obtained in Refs. [39] and [40] indicates that the presently observed 7795 keV state corresponds to the previously observed state at 7792 keV. In the study by Champagne *et al.* [37] the 7792 keV excited state in ^{27}Si was determined to be a possible analog to the known $7/2^+$ 8037 keV and $(5/2–9/2)^+$ 8043 keV excited states in ^{27}Al. Although the intensity of the 5631 keV transition

was too low to obtain a reliable angular distribution for this transition, the 8043 keV state in ^{27}Al does not exhibit a known γ-decay branch to the $7/2^+_1$ level. Thus, a 5631 keV transition from a $7/2^+$ 7795 keV level was assigned in ^{27}Si. It should be noted at this point that the 7795 keV state would correspond to a resonance energy that lies well within the covered direct (p,γ) measurement studies of Refs. [38] and [41] and no such resonance was observed. Therefore, it is expected that the presently observed 7795 keV level does not correspond to an astrophysically important resonant state in the ^{26}Al + p system.

The $9/2^-$ 7832 keV Level (E_r=367 keV)

Buchmann *et al.* [38] reported γ decays from a resonant state at 376 keV in the ^{26}Al + p system and observed decay branches to the known $7/2^+_3$, $11/2^+_2$, $7/2^+_2$, $11/2^+_1$, $9/2^+_1$ and $7/2^+_1$ excited states. As with the 287 keV resonance, the strongest branches observed were to the $9/2^+_1$ and $7/2^+_1$ levels. Similar γ-decay branches from a resonant state at 361 keV in the ^{26}Al + p system were also observed in a study by Vogelaar [41]. In both the study by Buchmann *et al.* [38] and Vogelaar [41] it was indicated that this resonance corresponds to a (9/2, $11/2^+$) excited state in ^{27}Si at 7827(3) keV, which was also previously observed in Refs. [39] and [40] at 7832(3) keV and 7837(3) keV, respectively. In the present work γ-decay transitions from an excited state at 7831.5(4) keV in ^{27}Si to the $11/2^+_1$ state, shown in Fig. 5.15, the $9/2^+_1$ state, shown in Fig. 5.19 and the $7/2^+_1$ state, shown in Fig. 5.13, were observed. The excellent agreement of presently observed level energy with previous measurements and the similarity of observed γ-ray transitions with Refs. [38] and [41] suggests that the presently observed 7832 keV excited state in ^{27}Si corresponds to a resonance in the ^{26}Al + p system at 368.5(4) keV. The resonance strength of this resonance has been measured twice at 65(18) [38] and 69(7) keV [41], respectively, and as such is also well defined.

The 4921.0(4) keV transition to the $9/2^+_1$ level is measured to have an angular distribution consistent with a ΔI=0 transition, indicating a 9/2 assignment for the 7832 keV level in ^{27}Si. In the present data, a further 2329.8(8) keV low-intensity γ-decay branch from the 7832 keV level to the $5/2^-_1$ state, as shown in Fig. 5.21, was observed. Closer inspection of this 2330 keV transition was performed and gates were placed on the 2330 keV and 2853 keV transitions in

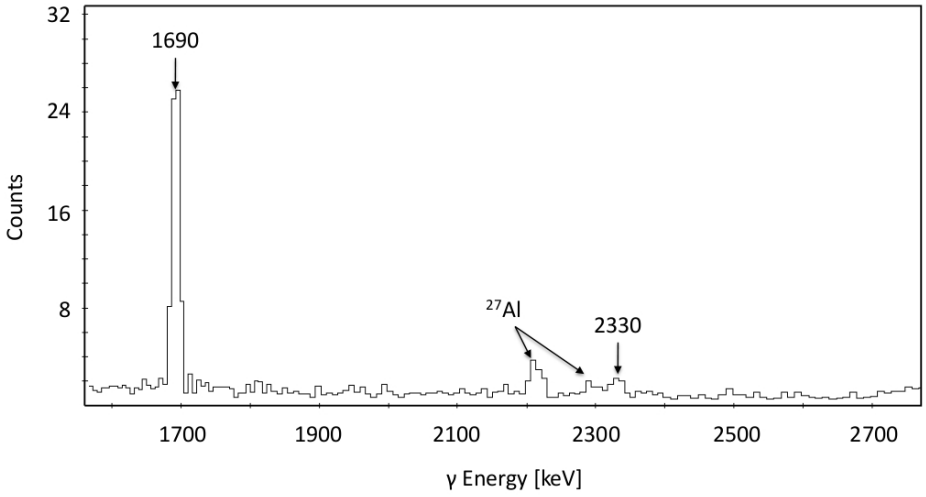

Figure 5.21: γ-γ-γ coincidence spectrum with gates placed on the 957 keV and 2853 keV transitions in ^{27}Si, showing the energy range 1600–2700 keV.

^{27}Si, as shown in Fig. 5.22. Figure 5.22 shows clear coincidence relationships with the 2330 keV and 2853 keV transitions in ^{27}Si at 1690 keV and 957 keV, confirming the presence of a γ-ray transition from the 7832 keV level to the $5/2^-_1$ state. A decay branch to the $5/2^-_1$ level indicates a $9/2^-$ assignment for the 7832

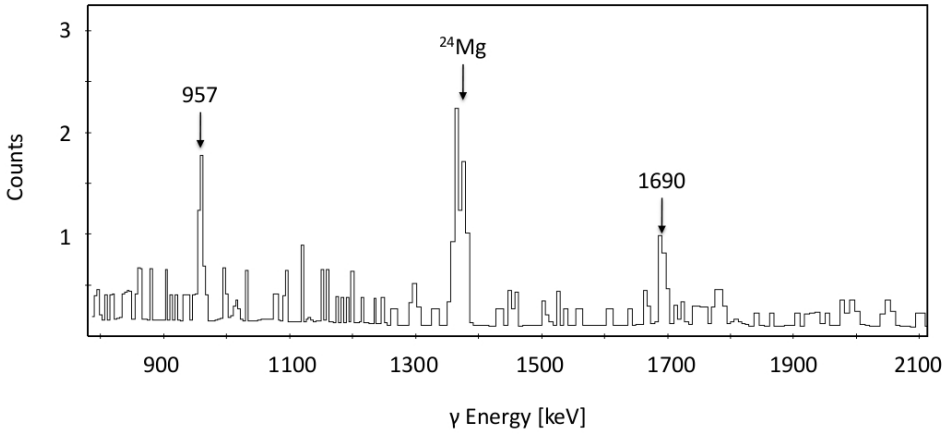

Figure 5.22: γ-γ-γ coincidence spectrum with gates placed on the 2330 keV and 2853 keV transitions in ^{27}Si, showing the energy range 800–2100 keV.

keV level and in comparison with the mirror nucleus, the $9/2^-$ 8287 keV excited state in ^{27}Al is the only $9/2^-$ state in an energy region 7400–8300 keV, known

to exhibit γ-decay branches to the $5/2^-_1$, $9/2^+_1$ and $7/2^+_1$ levels. Thus, 2329.8(8) keV, 3383.8(2) keV, 4921.0(4) keV and 5668.0(3) keV γ-ray transitions from a $9/2^-$ 7832 keV level to the $5/2^-_1$, $11/2^+_1$, $9/2^+_1$ and $7/2^+_1$ states, in ^{27}Si, were assigned.

Unobserved Proton-unbound State in ^{27}Si at 7557 keV

A weakly populated excited state at 7557(3) keV was observed in the previous ^{27}Al(^{3}He, t)^{27}Si and ^{28}Si(^{3}He, α)^{27}Si studies of Wang *et al.* [40]. This state was the only previously observed excited state in ^{27}Si, above the proton-emission threshold in the energy range E_x=7463–7832 keV, that was not observed in the present data set. In considering the present analysis of the low-lying level structure of ^{27}Si in the energy range 0–5547 keV, only one previously observed excited state was not observed in the present data and in fact, the mirror analog of this single unobserved excited state in the low-lying region of ^{27}Si was also not observed in the present strongly produced ^{27}Al data. Therefore, it is expected that the unobserved 7557 keV proton-unbound state in ^{27}Si may correspond to an unobserved mirror analog in the present ^{27}Al data.

In the previous study by Champagne *et al.* [37] a global energy shift of ∼200 keV was predicted between mirror analog states and in adopting this prescription for the current data, a comparison with the mirror nucleus system reveals that two unassigned excited states in ^{27}Al remain as possible mirrors to the 7557 keV level; the (3/2–7/2) 7798 keV state and T=3/2 $3/2^+$ 7858 keV level [63]. From an examination of the current ^{27}Al data in the energy range 7679–8037 keV, it is found that only the T=3/2 $3/2^+$ 7858 keV level is not observed in ^{27}Al, whereas a γ-ray transition to the $5/2^-_1$ state from the 7798 keV level was relatively strongly observed in ^{27}Al. The present reaction mechanism used to populate excited states in ^{27}Si and ^{27}Al only contains T=0 ^{12}C and ^{16}O nuclei in its entrance channel and single T=1/2 neutrons or protons and T=1/2 ^{27}Si or ^{27}Al nuclei in its exit channel. Presumably, as states near the proton threshold are populated directly by single neutron or single proton evaporation of the compound nucleus, ^{28}Si, only T=1/2 residual excited states in either ^{27}Si or ^{27}Al are isospin allowed in the present reaction mechanism. The T=3/2 7858 keV state in ^{27}Al, therefore, is isospin forbidden, is of low-spin nature and is known to exhibit a dominant γ-decay branch to the ground state. The combination of these three properties

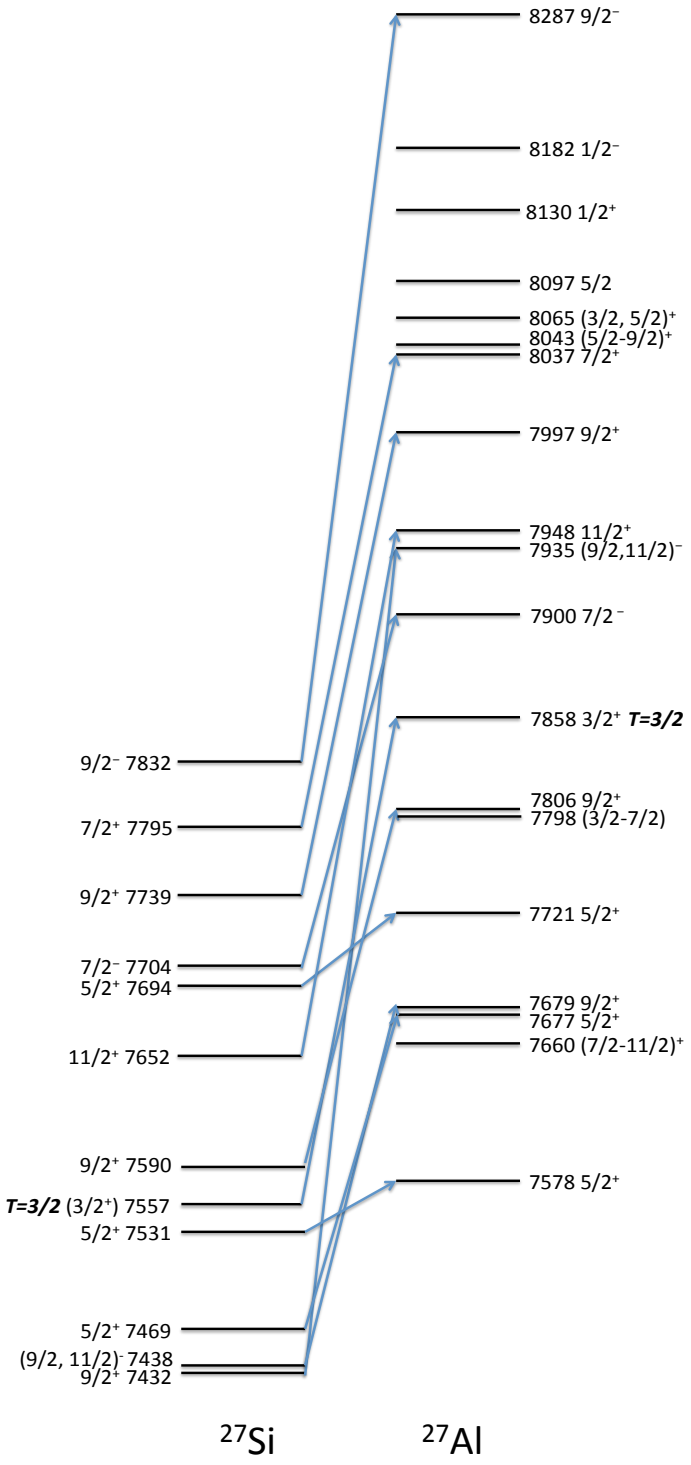

Figure 5.23: Mirror nucleus assignments in ^{27}Si and ^{27}Al.

indicate strong reasons why such a state would not be observed in the present data. In fact, a further known T=3/2 state in ^{27}Al at 6814 keV, whose mirror in ^{27}Si is located with an energy shift of -188 keV at 6626 keV, was also not observed in the present data, which could indeed support the non-observation of isospin forbidden states in this work. In contrast, experiments in which T=3/2 states are isospin allowed, such as the ^{26}Mg(p,γ) reaction [96], the T=3/2 states are heavily populated. Consequently, it is assumed that because the 7557 keV state is the only proton-unbound state not observed in ^{27}Si, it corresponds to a $3/2^+$ T=3/2 state and thus, is of little astrophysical importance. Furthermore, as T=3/2 states were also isospin forbidden in the work by Wang *et al.* [40], it would offer some explanation as to why the 7557 keV level was so weakly populated in that particular work. As a result, the T=3/2 7858 keV excited state in ^{27}Al is favoured as the mirror to the unobserved 7557 keV level in ^{27}Si and the 7557 keV level is given a tentative spin-parity assignment of $3/2^+$.

For completeness near-threshold states at 7432 keV and 7438 keV in ^{27}Si were also considered in the present analysis of proton-unbound states. However, the justification of these states, which is presented in Appendix C, will not be discussed here and the analysis of proton-unbound state assignments is concluded. Figure 5.23 shows the presently predicted mirror assignments of proton-unbound states in ^{27}Si.

5.3 Implications for the Astrophysical ^{26}Al(p, γ)^{27}Si Reaction Rate

In the previous work of Champagne *et al.* [37], the direct capture contribution to the overall ^{26}Al$(p,\gamma)^{27}$Si reaction rate was determined to be negligible for temperatures greater than 0.02 GK. Therefore, such contributions will be ignored in the following discussion of the ^{26}Al(p, γ)^{27}Si stellar reaction rate in classical novae environments.

Direct (p,γ) studies of the ^{26}Al$(p,\gamma)^{27}$Si reaction have obtained resonance strength measurements for resonances as low as E_r=189 keV [38; 41; 43]. Such measurements are expected to constrain uncertainties in the reaction rate in the temperature range T=0.2–0.4 GK. However, it has been suggested that previously unobserved low-energy resonances, below E_r=189 keV, may dramatically affect the rate over low stellar temperatures [37; 39; 40; 42]. In the present data

the first spin-parity assignments and most precise excitation energies to date have been determined for excited states above the proton threshold. Consequently, from this work, relative contributions to the reaction rate from low-lying excited states above the threshold were estimated.

The 7469 keV excited state is instantly ruled out as corresponding to a possible astrophysically important resonance as its resonance energy is simply too small to allow any significant penetration of the Coulomb barrier. The 7531 keV excited state in ^{27}Si is also ruled out as corresponding to a possible astrophysically important resonance as the presently deduced $5/2^+$ spin-parity assignment indicates a minimum of an l_p=2 contribution to the reaction process. This coupled with the relatively low resonance energy, E_r = 68 keV, indicates a negligible contribution to the rate from a possible resonant state at 68 keV, over novae temperatures. In addition, the present $3/2^+$ spin-parity assignment of the 7557 keV excited state indicates a minimum of an l_p=4 component to the reaction rate from this state and thus, rules out the possibility that the 7557 keV state corresponds to an astrophysically important resonance in the ^{26}Al + p system. However, it should be noted that the (3/2–7/2) 7798 keV state in ^{27}Al still remains unassigned to a mirror analog in ^{27}Si and could indeed be the mirror of the 7557 keV state. The (3/2–7/2) 7798 keV state in ^{27}Al is known to exhibit a 78% γ-decay branch to the $5/2^-_1$ level with a further 22% branch to the ground state [63]. The γ-decay branch to the $5/2^-_1$ level from the 7798 keV state was strongly observed in the present ^{27}Al and as such, although the 7798 keV level is a possible mirror to the 7557 keV level in ^{27}Si, it is unusual that a similar decay to the $5/2^-_1$ state from the 7557 keV is not observed in the present ^{27}Si data. Thus, $3/2^+$ assignment for the 7557 keV state is currently favoured. Nevertheless a 3/2–7/2 assignment remains open as a possibility for the 7557 keV level, which in an extreme case could allow for an l_p=1 contribution to the reaction process from a resonant state at 94 keV in the ^{26}Al + p system.

The presently observed excited state at 7590 keV, corresponding to a potential resonance at 127 keV, is expected to be the lowest energy resonance that will have a significant influence on the reaction rate. This state has been determined to have a $9/2^+$ spin-parity assignment and thus, has been identified as the only possible, previously unobserved, s-wave resonance below E_r=189 keV. In the previous transfer reaction study by Vogelaar *et al.* [42], an estimate of $<5.9\text{x}10^{-6}$ meV was obtained for the resonance strength of the possible 127 keV

resonant state. This estimate was made from a limit placed on the spectroscopic factor for the 127 keV resonant state but an earlier estimate of the resonance strength by Wang *et al.* [40] obtained a widely differing result of 5.7x10^{-3} meV. Therefore, if the presently observed excited state at 7590 keV does indeed correspond to a resonance at 127 keV, the newly determined possible l_p=0 component indicates that, with only a single experimental determination of the spectroscopic factor for this state and no direct measurement of the resonance strength, the rate remains significantly uncertain over stellar temperatures, in which the 127 keV resonance may dominate the rate.

For completeness, an excited state above the threshold, not observed in any of the direct (p, γ) studies [38; 41; 43], was observed in the present ^{27}Si data at 7795 keV, corresponding to a resonance energy (E_r) of 332 keV. The energy of this state lies well within the investigated energy range of Refs. [38; 41; 43]. Such a non-observation in the direct astrophysical studies, suggests that this state does not make a significant contribution to the overall ^{26}Al(p, γ)^{27}Si stellar reaction rate and consequently, this state shall not be considered as a potentially important astrophysical resonance.

A plot showing all resonant contributions to the reaction rate is shown in Fig. 5.24. This plot includes the previous estimate of the 127 keV resonance strength obtained by Vogelaar *et al.* [42] and a current estimate of the 127 keV resonance strength, assuming an l=0 single-particle state with a spectroscopic factor of 1. In Fig. 5.24 it can be clearly seen that the 127 keV resonance may indeed dominate the ^{26}Al(p, γ)^{27}Si reaction rate at low stellar temperatures and the uncertainty in its resonance strength represents the dominant remaining uncertainty in the overall reaction rate.

In the previous work of Champagne *et al.* [37] it was suggested that significant ^{26}Al production may occur at stellar temperatures as low as T=0.06 GK, and, furthermore, at a temperature of T=0.08 GK the net production of ^{26}Al would depend critically on the rate of the ^{26}Al(p, γ)^{27}Al reaction. In Ref. [37] it appeared that the ^{26}Al(p, γ)^{27}Al reaction rate was too slow to destroy a significant amount of ^{26}Al at these temperatures. However, as can be seen in Fig. 5.24, the 127 keV resonance may contribute significantly to the ^{26}Al(p, γ)^{27}Al reaction rate at low stellar temperatures and thus, significantly reduce the expected amount of ^{26}Al synthesized in novae environments.

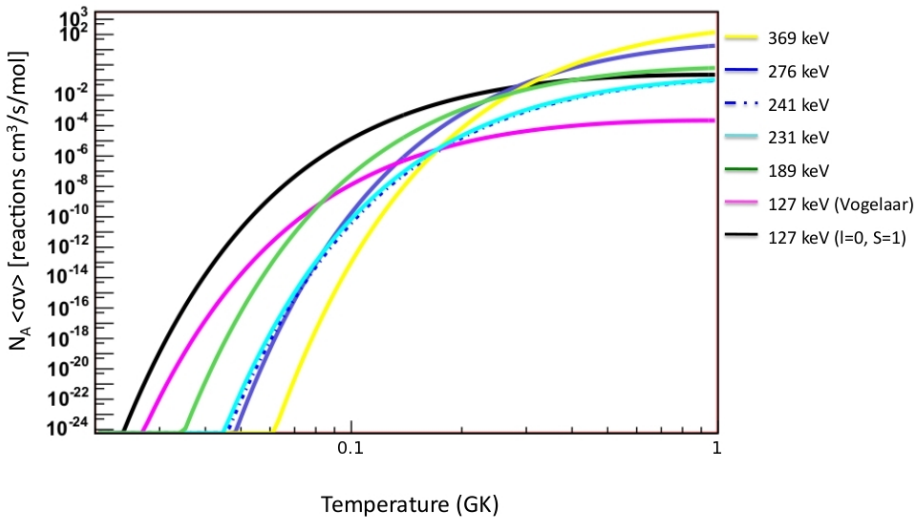

Figure 5.24: Reaction rate plot showing relative contributions to the ^{26}Al$(p,\gamma)^{27}$Si from individual resonances, over typical novae temperatures.

Consequently, further constraints on the reaction rate would now require an accurate determination of the 127 keV resonance strength. Ideally, this would be achieved by a direct (p,γ) measurement using radioactive ion beams in inverse kinematics. With reference to the previous work of Ruiz *et al.* [43], present calculations for such a measurement, using the DRAGON facility at TRIUMF, indicate that, if a spectroscopic factor of 1 is assumed and the resonance strength is indeed as large as 5.7x10^{-3} meV, approximately 10 detected recoils are expected per week. This current estimate suggests that, for a 127 keV resonance with a spectroscopic factor approaching 1, a direct measurement of the resonance strength could well be feasible. However, the only previous measurement of the spectroscopic factor of this state by Vogelaar *et al.* [42] indicates a value notably less than 1 and as such, it is presently expected that the resonance strength of the potential 127 keV resonant state is too small to be measured directly. Therefore, in order to reduce uncertainties in the resonance strength of the potential 127 keV resonance, a further indirect measurement of its relative spectroscopic factor is needed. Such a measurement may achieved from a ^{26}Al$(^3\mathrm{He},d)^{27}$Si transfer reaction study, in analogy with the previous work of Vogelaar *et al.* [42]. A transfer reaction study of this nature would require the fabrication of a radioactive ^{26}Al target and, in fact, a proposal for the fabrication

of such a target has recently been accepted [97]. However, in light of the present thesis work, a measurement of the spectroscopic factor of the now known corresponding mirror state in ^{27}Al is also a possibility. An ^{26}Al$(d, p)^{27}$Al transfer reaction study performed in inverse kinematics would allow such a measurement to be carried out and would both utilize the intense ^{26}Al radioactive beam available at TRIUMF and bypass the need to fabricate a radioactive ^{26}Al target. Furthermore, such an experiment would allow the simultaneous determination of spectroscopic factors for other potentially important astrophysical states.

Chapter 6

Conclusions and Future Work

An experiment has been performed to study the astrophysical ^{23}Mg$(p,\gamma)^{24}$Al reaction in ONe novae. A complete level structure of the nucleus ^{24}Al has been determined below the proton-emission threshold (1872(3) keV) [19] with improved precision on all previous studies [84; 85; 86; 87]. The lowest-lying excited state above the threshold has been identified as a 3^+_3 state with a level energy of 2345.1(14) keV, corresponding to a resonance energy (E_r) of 473(3) keV. The 2345 keV level energy obtained is in disagreement with the 2328(10) keV [84] and 2369(4) keV [85] excitation energies previously observed for this state, but shows good agreement with both the adopted 2349(20) keV level [62] and recently observed 2346(6) keV [86] level energy. This resonance dominates the ^{23}Mg$(p,\gamma)^{24}$Al stellar reaction rate and consequently, the improved precision of the resonance energy on the previous values of Ref. [86] and Ref. [62] has reduced the relative uncertainties in the reaction rate by factors of 2 and 7, respectively. In order to reduce the uncertainty in the rate, with regards to the resonance energy, further, the proton threshold needs to be measured with greater precision. The current 3^+_3 spin-parity assignment confirms the tentative assignment of Ref. [84] and disagrees with the possible assignments proposed in Ref. [85]. Theoretical calculations by Herndl *et al.* [62] estimate the resonance strength for the 3^+_3 state in ^{24}Al to be 25 meV and calculations by Kubono *et al.* [84] obtain a similar estimate of 27 meV. By comparison, the study by Kubono *et al.* quoted values as high as 130 meV for the 4^+_2 resonance. Consequently, this work has established that further constraints on the reaction rate uncertainty would now require a direct measurement of the 3^+_3 resonance strength using the ^{23}Mg$(p,\gamma)^{24}$Al reaction. An attempt to perform such an experiment has been

proposed and approved at the DRAGON facility at TRIUMF and is scheduled to run later this year.

In addition, a further experiment has been performed to investigate the astrophysical ^{26}Al$(p,\gamma)^{27}$Si reaction in classical novae environments. An unambiguous low-lying level structure, from 0–5547 keV, has been determined for the nucleus ^{27}Si. Proton-unbound states, important for the ^{26}Al$^g(p,\gamma)^{27}$Si reaction, were observed at 7469.0(6) keV, 7531.3(7) keV, 7589.7(8) keV, 7651.6(3) keV, 7693.8(9) keV, 7704.3(2) keV, 7739.3(4) keV, 7794.8(19) keV and 7831.5(4) keV with spin-parity assignments of $5/2^+$, $5/2^+$, $9/2^+$, $11/2^+$, $5/2^+$, $7/2^-$, $9/2^+$, $7/2^+$ and $9/2^-$, respectively. The present more precise excitation energies of proton-unbound states, over previous studies [39; 40], have constrained uncertainties in the ^{26}Al$(p,\gamma)^{27}$Si reaction rate by a factor of 8, over the temperature range 0.2–0.4 GK. In addition to this, the first spin-parity determinations of proton-unbound states in ^{27}Si have allowed a reevaluation of possible astrophysically important low-energy resonances, for which no previous direct resonance strength measurements exist. The 7590 keV excited state in ^{27}Si, corresponding to a potential resonance at 127 keV, has been identified as the only possible s-wave resonance below E_r=189 keV and it is suggested that such a low-energy resonance with an l_p=0 component could dominate the ^{26}Al$(p,\gamma)^{27}$Si reaction rate for T<0.2 GK. The previous work of Champagne *et al.* [37] indicated that at temperatures as low as 0.08 GK, the ^{26}Al$(p,\gamma)^{27}$Si reaction rate is critical for the overall production rate of ^{26}Al in stellar environments. Consequently, an accurate determination of the ^{26}Al$(p,\gamma)^{27}$Si reaction rate in the temperature region T<0.2 GK is of great importance in ascertaining the expected contribution of novae environments to the observed galactic abundance of ^{26}Al.

From the present work, it is clear that the resonance strength of the 127 keV state represents the key remaining uncertainty in the reaction rate for T<0.2 GK. The previous work of Vogelaar *et al.* [42] assigned a limit on the spectroscopic factor of this state and obtained the only experimental estimate of the resonance strength to date. However, earlier estimates [39; 40] and a present calculation of the resonance strength, assuming a pure l=0, S=1, single-particle state, indicate that the resonance strength of the 127 keV state could be significantly higher than the estimation of Ref. [42]. Therefore, in order to reduce uncertainties in the ^{26}Al$(p,\gamma)^{27}$Si reaction rate further, for T<0.2 GK, an additional experimental determination of the resonance strength is needed.

Present calculations suggest that, although a direct measurement of the resonance strength may be feasible if the resonance strength is assumed to be as large as the upper limit, a transfer reaction study, by which the spectroscopic factor of the resonant state is determined, would be a possible next step in determining the resonance strength. Furthermore, it should be noted that in light of this thesis work, two distinct possibilities exist for the determination of the spectroscopic factor of the 127 keV resonant state from transfer reaction studies. The first, slightly more obvious method, would be to perform a similar ^{26}Al(^{3}He, d)^{27}Al experiment to that of Vogelaar *et al.* [42]. Such a study would require the fabrication of a radioactive ^{26}Al target and, in fact, a proposal for the manufacture of a radioactive ^{26}Al target at the TRIUMF national laboratory has recently been accepted [97]. The second, would be to measure the spectroscopic factor of the mirror analog of the 127 keV resonant state, which, from the current work, has now been firmly established. This measurement could be made using an ^{26}Al$(d, p)^{27}$Al transfer reaction in inverse kinematics, utilizing the intense ^{26}Al radioactive beam available at TRIUMF and bypassing the need to fabricate a radioactive ^{26}Al target. In addition to this, such a study would allow the simultaneous determination of spectroscopic factors for other potentially important mirror states. In particular, a spectroscopic factor may be deduced for the (3/2–7/2) 7798 keV possible mirror state of the potential ^{26}Al + p resonance at 94 keV, which would further constrain the uncertainties in the ^{26}Al$(p, \gamma)^{27}$Si reaction rate at low stellar temperatures.

As a final note, low-spin excited states were observed well above the proton threshold in ^{27}Si, which may be of importance in reducing uncertainties in the ^{26}Al$^m(p, \gamma)^{27}$Si reaction rate. An analysis of these states was outside the scope of the present thesis work as it is expected that the contribution of ^{26}Al$^m(p, \gamma)^{27}$Si reaction to the overall ^{26}Al$(p, \gamma)^{27}$Si reaction rate over typical novae temperatures is negligible [36]. However, a tentative level scheme of ^{27}Si is presented in Appendix C, in which four states with E_x>7832 keV, including a newly observed excited state, are displayed. Any one of these four states may make a significant contribution to the ^{26}Al$^m(p, \gamma)^{27}$Si reaction rate and consequently, an analysis of these observed proton-unbound low-spin states will be the subject of future work on the ^{26}Al$^m(p, \gamma)^{27}$Si reaction.

In summary, the work carried out in this thesis has reduced the relative uncertainties of both the ^{23}Mg$(p, \gamma)^{24}$Al and ^{26}Al$(p, \gamma)^{27}$Si stellar reaction rates,

constraining the production of $A \geq 20$ nuclei in classical novae. Future work, in which these reactions may be investigated further, has been outlined and it is clear that the present thesis work makes a significant contribution to such efforts.

Appendix A

Gamma-ray Detectors

The detectors used in this thesis work can be divided into two types: scintillators and solid state detectors. Both can be made from relatively high-Z material, which results in high interaction probabilities for the photoelectric effect to occur within the detector volume, and the energy deposited is measured by conversion to an electrical signal.

A.1 Scintillation Detectors

In the case of scintillators, the deposition of some or all of the energy of incident photons results in the ionisation of atoms, and electrons are excited across the band structure of the detector, as shown in Fig. A.1. The atomic excited states then rapidly emit visible light, as the promoted electrons return to the valence band, and the material is said to "fluoresce". The light produced in this process strikes a photosensitive surface, releasing at most one photo-electron per photon and the secondary electrons are then multiplied, accelerated and formed into an output pulse using photomultiplier tubes (PMTs). To increase the probability for photon emission and to reduce self-absorption of the emitted light, small amounts of impurities called "activators" are added to the crystal. These activators create "luminescence" or "recombination" centres within the band gap of the detector, enabling the emission of light between activator states, as shown in Fig. A.1.

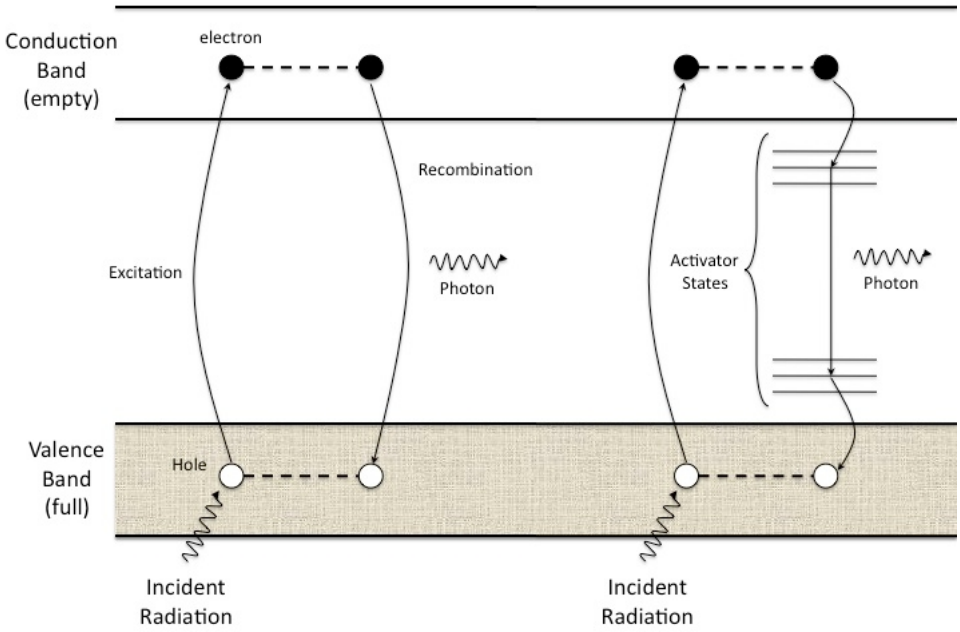

Figure A.1: Energy bands in a detector crystal. (Left) processes characteristic of a pure crystal such as NaI. (Right) processes characteristic of a detector containing an activator, such as NaI(TI).

Many different types of scintillators are available. However, for the detection of γ rays, inorganic scintillators are favoured, such as sodium iodide (NaI(TI)), barium fluoride (BaF_2) and bismuth germanate ($Bi_4Ge_3O_{12}$), commonly referred to as BGO. It should be noted at this stage that due to the low efficiency of the fluorescence and multiplication process, radiation detection using scintillators is limited by a relatively poor energy resolution $\geq$6%. For the construction of level schemes, which have many transitions of similar energy, such as those of the nuclei under investigation in the current study, an energy resolution of $\sim$ 1% is required. This problem may be resolved through the use of semiconductor diode detectors, which produce a far greater number of information carriers for each interaction.

A.2 Semiconductor Diode Detectors

As in scintillators, the deposition of energy by incident radiation will cause an electron to be excited to the conduction band, leaving a "hole" in the valence band. However, rather than extracting an electrical signal from the re-emission of radiation when the electron falls back to the valence band, the electron-hole pairs are made to drift under the influence of an electric field applied to the semiconductor crystal. This motion results in an electric current, which provides the basis for the measurement of the radiation.

To control the electrical conduction in semiconductors, small amounts of materials called "dopants" are added, which increase the concentration of electrons in the conduction band or the holes in the valence band, forming what are known as n-type and p-type semiconductors, respectively. This process of doping is of particular importance in the detection of γ-ray radiation as a junction between these two types of semiconductor, known as a p-n junction, provides a good contact for extracting the electrical signal from the crystal.

When p-type and n-type materials are brought into contact, the electrons from the n-type material can diffuse across the junction and recombine with the holes in the p-type material, creating a region depleted of charge carriers called the "depletion region". The diffusion of electrons from the n-type region leaves behind positively charged ionized fixed donor sites, while the similar diffusion of holes from the p-type region leaves behind negatively charged fixed acceptor

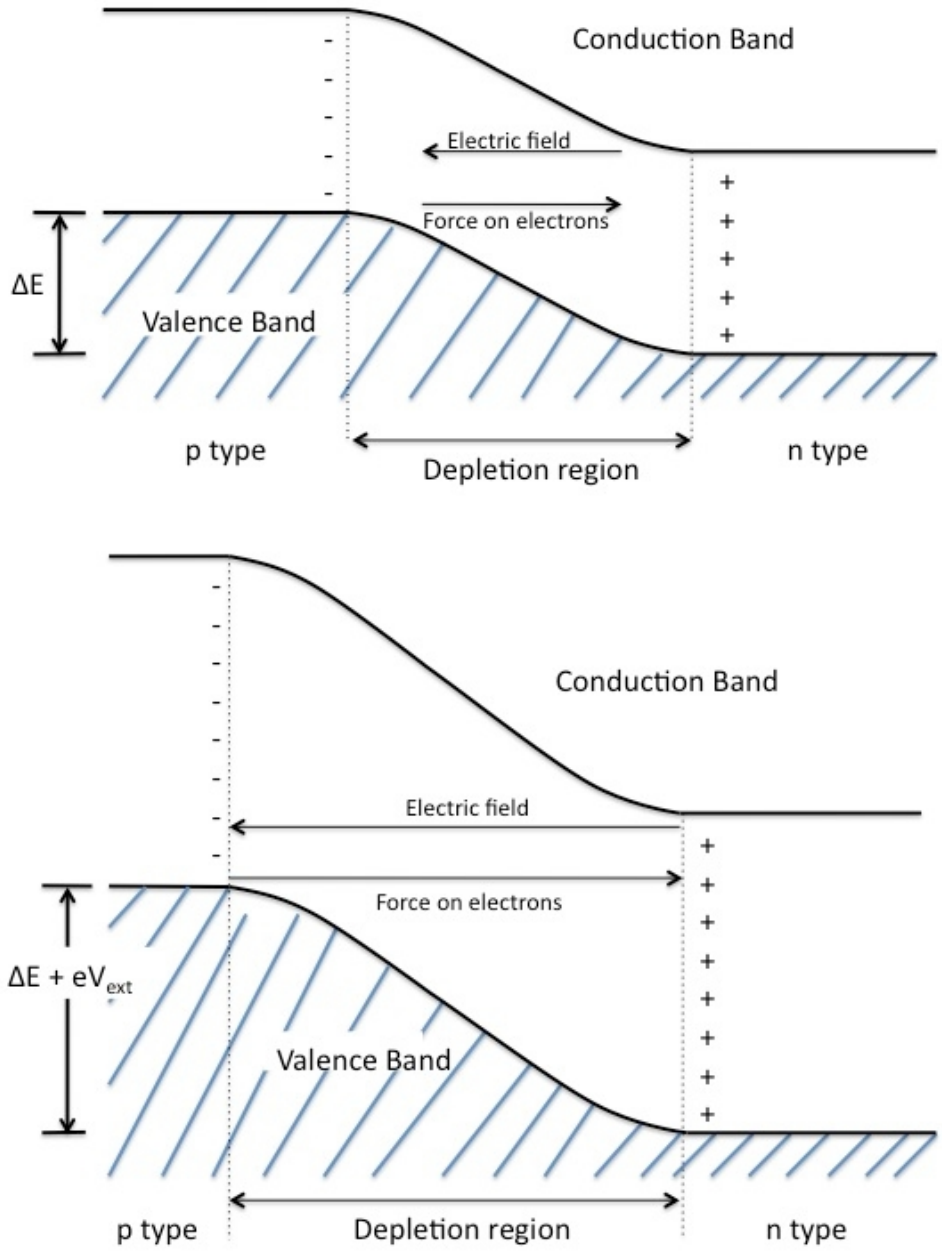

Figure A.2: (Top) When n-type and p-type materials are brought into contact, electrons and holes near the junction can recombine to create a region that is depleted of charge carriers. (Bottom) Under reverse bias, the depleted region becomes larger and the magnitude of the electric field increases.

sites. The space charge from the fixed sites creates an electric field, which eventually halts further migration and results in a "junction diode", shown in Fig. A.2 [98].

If radiation enters the depletion region and creates electron-hole pairs, the electrons flow in one direction and holes in the other. The total number of electrons collected may then be used to form an electronic pulse whose amplitude is proportional to the energy of the incident radiation. In practice, these detectors are operated with large reverse bias voltages (1000-3000 V), which has two effects; (1) it increases the magnitude of the electric field in the depletion region, making charge collection more efficient, and (2) it increases the dimensions of the depletion region by forcing more carriers to drift across from one type of material to the other.

A.3 HPGe Detectors

In the current study, germanium crystals with impurity levels as low as 10^9 atoms/cm^3 (HPGe), were chosen as the semiconductor detector material. The advantage in using such high-purity material is that the size of the depletion layer can be much larger (up to several cm in depth) than that for ordinary semiconductors. This can be easily seen from the expression for the depletion depth,

$$d = \left(\frac{2\epsilon V}{eN}\right), \tag{A.1}$$

where ϵ is the dielectric constant, V is the reverse bias voltage, e is the electronic charge and N is the net impurity concentration of the entire semiconductor. Germanium detectors may also be produced in coaxial geometries, which provide a large active volume, allowing high γ-ray detection efficiencies to be achieved. The electrical contacts in such a geometry are very thin, heavily doped layers of material, denoted as n^+ and p^+. These contact regions contain a very low concentration of charge carriers and thus, make excellent candidates for the electrical readout of a p-n junction system. A schematic diagram of an n-type coaxial HPGe detector (the detector used in the current study) is shown in Fig. A.3.

A minor disadvantage in the use of Ge detectors, however, is that thermal excitation at room temperature is enough to promote electrons to the conduction

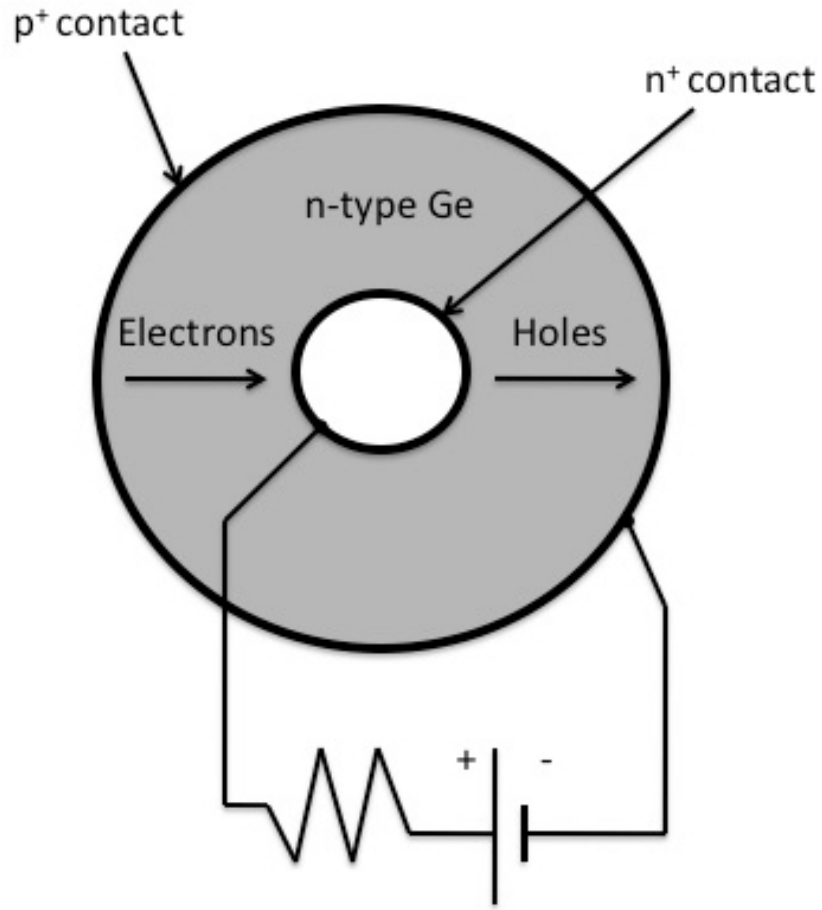

Figure A.3: Schematic diagram of an n-type coaxial HPGe detector, taken as a cross section perpendicular to the cylindrical axes.

band. Hence, it is necessary to frequently cool the semiconductor crystal to a low temperature, most commonly 77 K, using liquid nitrogen (LN_2).

A.4 Detector Arrays

The field of γ-ray spectroscopy has evolved significantly with the development of large γ-ray detector arrays to surround a reaction target. These systems, containing a number of γ-ray detectors, allow coincidence measurements to be performed, as γ rays can be measured in several different detectors simultaneously. Such measurements are essential for the construction of complicated level schemes, which in turn lead to much more refined studies of nuclear structure. In addition to this, a detector array consisting of a large number of detectors allows a large-solid angle coverage of a γ-ray source, while maintaining granularity, and thus, provides a powerful means to extract angular distribution information for a given transition.

However, a problem common to all detector arrays is that of Compton suppression and consequently, suppression shielding is needed around each detector used in the array.

A.5 Compton Suppression

When a photon is Compton scattered by an electron in a detector crystal, its resulting energy E_γ' can be described by,

$$E'_\gamma = \frac{E_\gamma}{1 + \frac{E_\gamma}{m_e c^2}(1 - cos\theta)}, \tag{A.2}$$

where E_γ is the energy of the unscattered photon, $m_e c^2$ is the rest mass of the electron and θ is the scattering angle.

In some cases it is possible that the incident photon is Compton scattered out of the detector completely. In such situations, which may occur after a frequent number of scatters, a fraction of the original γ-ray energy is lost, thus generating a background in the γ-ray spectrum below the energy of the photopeak. The minimisation of this Compton background is referred to as "Compton suppression".

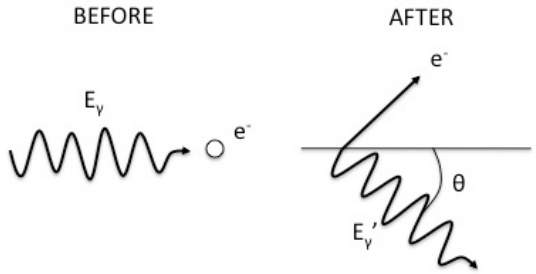

Figure A.4: Diagrammatical representation of Compton scattering.

The most common method in performing Compton suppression is to surround the initial γ-ray detector (HPGe) by a second detector (BGO). Consequently, photons detected in the second detector within a certain time of a detection in the first will be processed as Compton scattering events, vetoing signals from the first detector. An example of such a Compton suppression for a ^{60}Co γ-ray source is displayed in Fig. A.5. It is clear from Fig. A.5 that in using

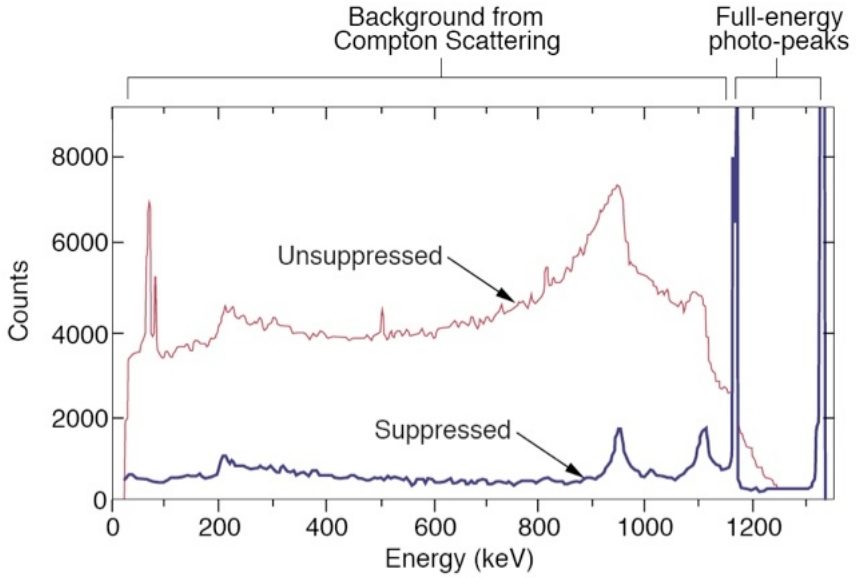

Figure A.5: The effect of a BGO Compton-suppression shield on γ-ray spectra.

.

this method, the full-energy peaks remain relatively unaffected whilst Compton background is significantly reduced.

Appendix B

Energy and Efficiency Calibrations

The γ-ray peaks shown in Figs. B.1 and B.2 were fitted using the "gf3" program [70], which determined the centroids and areas of the peaks and their associated errors. The recorded centroid channel numbers were related to the known source γ-ray energies (E_γ) through the polynomial expression,

$$E_\gamma = a_0 + a_1 x + a_2 x^2 + ... \tag{B.1}$$

In most cases the first- or second-order approximation is sufficient for GAMMASPHERE data. In this thesis the second-order relation was employed for the ^{24}Al experiment and the first-order relation was employed for the ^{27}Si experiment. The coefficients a_0, a_1 and a_2 for the GAMMASPHERE detector array were determined by using the "ENCAL" codes from the RadWare software package [70].

The γ-ray sources were also used to generate a relative efficiency curve of the detector array for each of the experiments. This was accomplished by comparing the areas of the fitted photopeaks to the known relative intensities of the γ-ray sources [70]. The relative intensities were re-normalised such that they could be combined to produce an efficiency curve of the form,

$$\epsilon = exp[(A + Bx + Cx^2)^{-G} + (D + Ey + Fy^2)^{-G}]^{-1/G}, \tag{B.2}$$

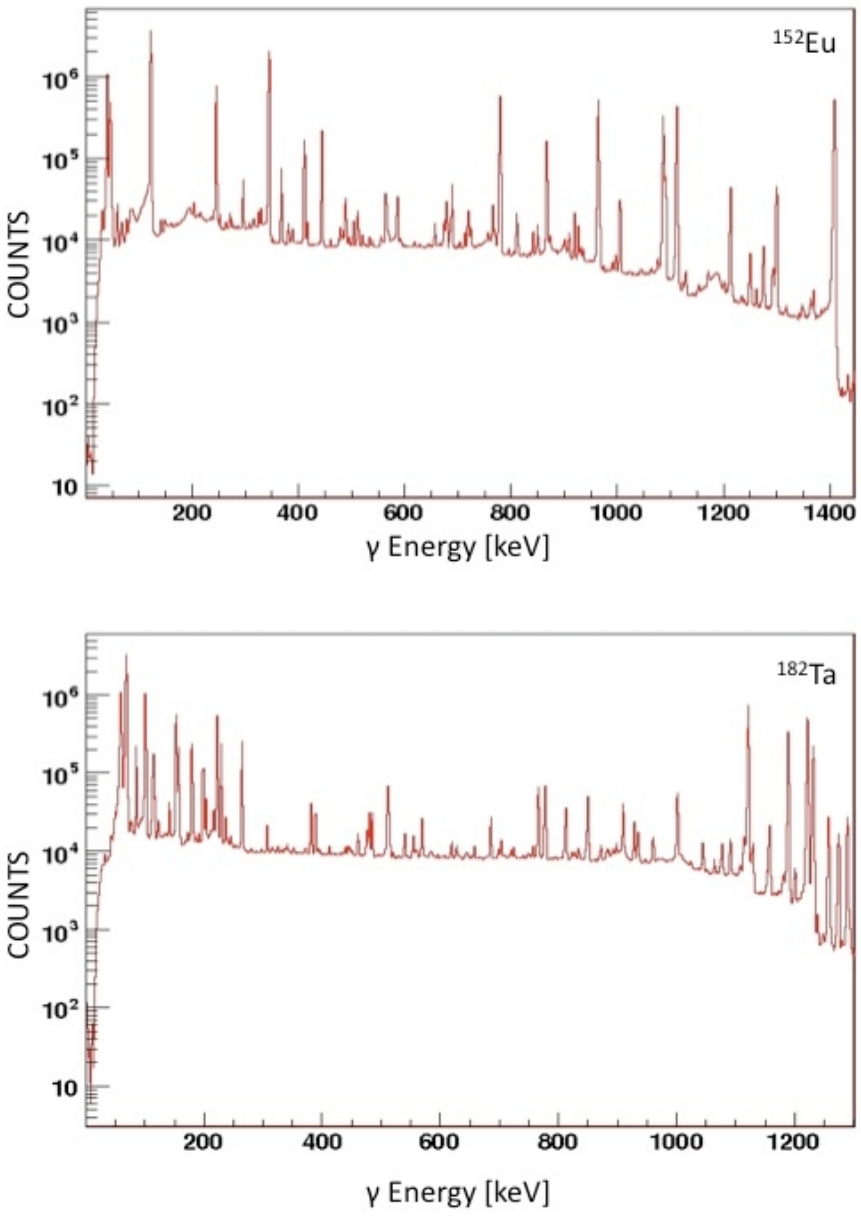

Figure B.1: γ-ray calibration spectra obtained for the ^{24}Al experiment.

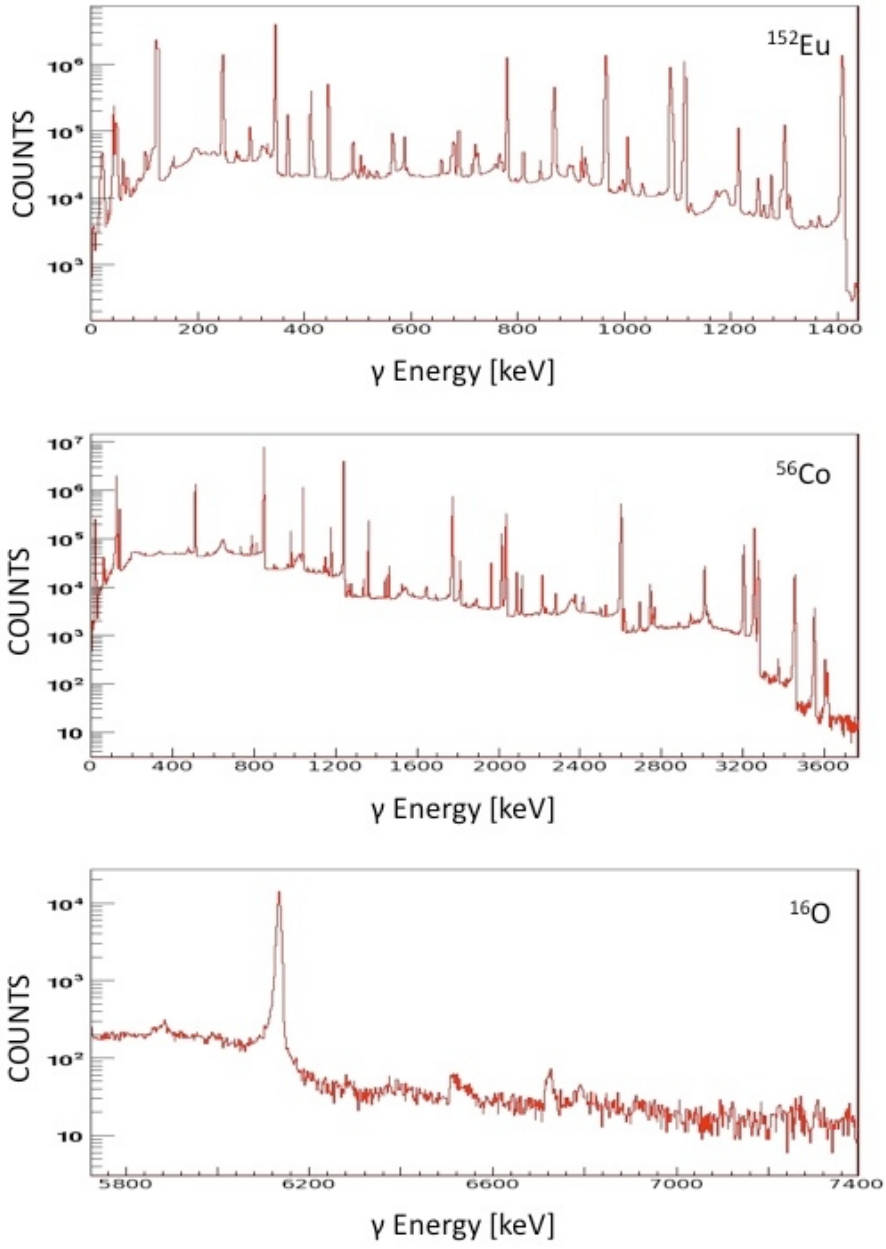

Figure B.2: γ-ray calibration spectra obtained for the ^{27}Si experiment.

where ϵ is the relative efficiency, x and y are given by,

$$x = ln(E_\gamma/100keV) \tag{B.3}$$

$$y = ln(E_\gamma/1000keV), \tag{B.4}$$

and E_γ is in keV. The seven parameters A, B, C, D, E, F and G are constants, which are determined by the efficiency curve fit using the "EFFIT" codes in RadWare [70]. A, B and C describe the efficiency at low energies ($\sim$200 keV) and D, E and F have the same role for higher energies. The last parameter G is an interaction parameter between the two regions and determines the efficiency at the turnover point. Relative efficiency curves of the detector array for the ^{24}Al and ^{27}Si experiments are shown in Figs. B.3 and B.4, respectively.

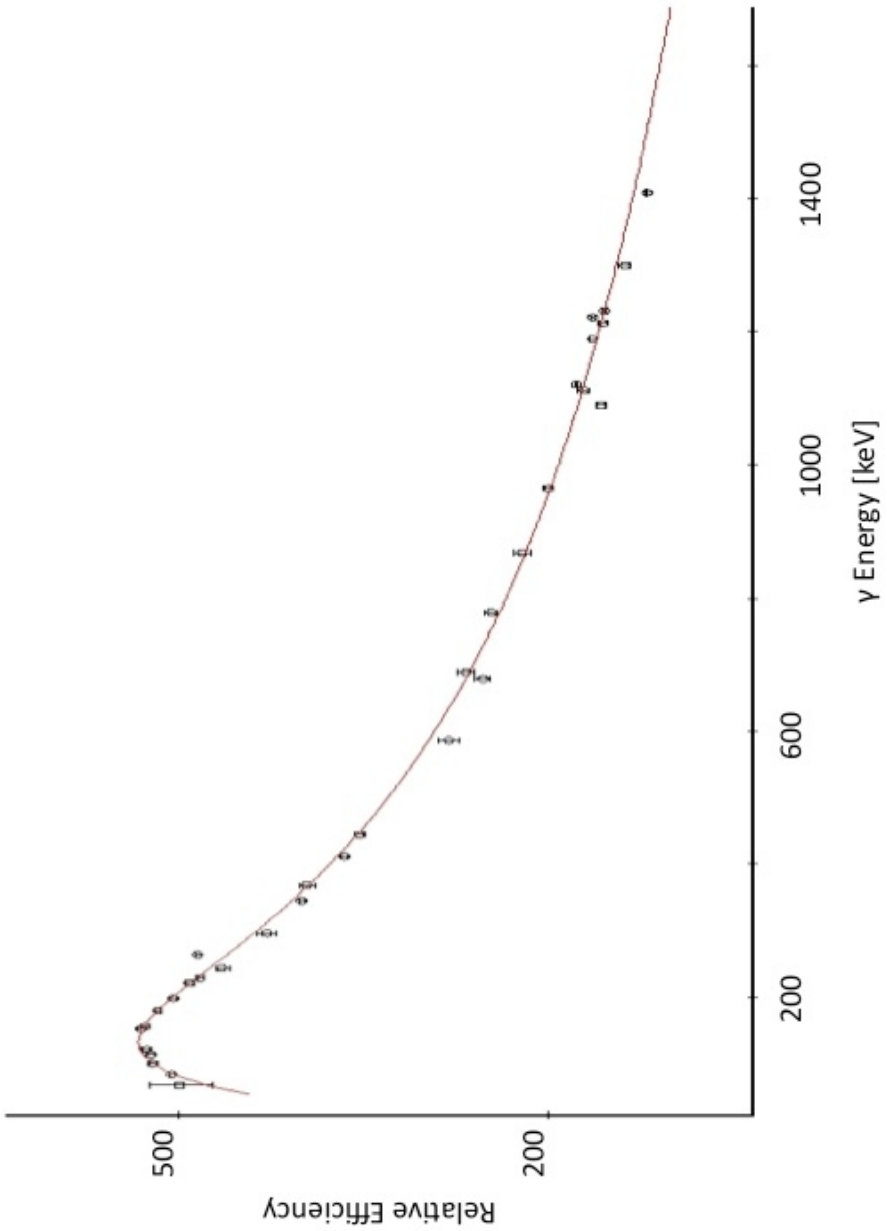

Figure B.3: Relative efficiency curve for the GAMMASPHERE detector array as a function of energy for the ^{24}Al experiment.

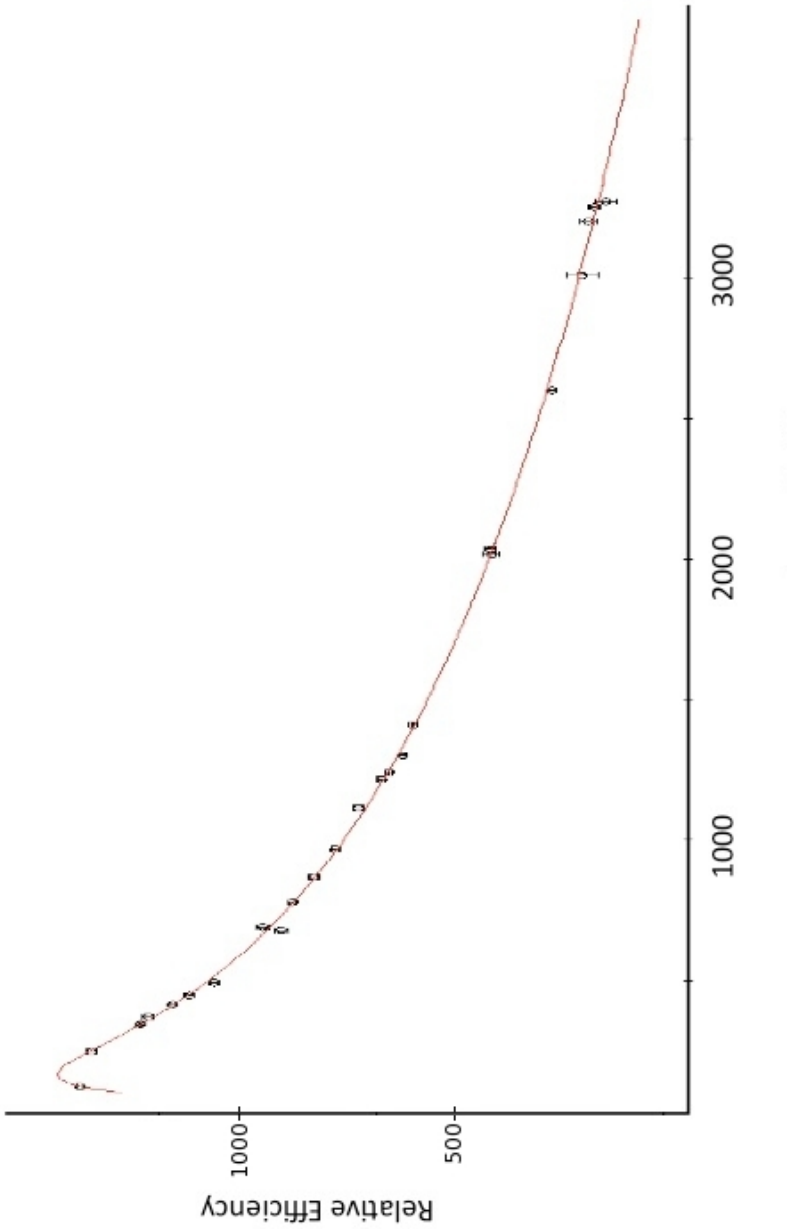

Figure B.4: Relative efficiency curve for the GAMMASPHERE detector array as a function of energy for the ^{27}Si experiment.

Appendix C

Excited States of ^{27}Si

C.1 Near-threshold States in ^{27}Si

Gamma-ray transitions were observed from two levels just below the proton threshold at 7432.3(4) keV and 7438.2(23) keV, in good agreement with the two previously reported highest energy excited states below the threshold at 7428(4) keV and 7436(3) keV, respectively, in ^{27}Si [63]. The presently observed 7432 keV state exhibits a 5269.0(3) keV γ-decay branch to the $7/2^+_1$ level, as shown in Fig. 5.13. Angular distribution coefficients of a_2=0.58(7) and a_4=0.12(8) were obtained for this transition, indicating the 7432 keV level to have a 5/2 or 9/2 spin assignment. A 4784.3(2) keV decay transition to the $5/2^+_2$ level was also observed from the 7432 state, as shown in Fig. 5.12, as well as a 4521.1(8) keV decay branch to the $9/2^+_1$ level. These additional transitions rule out a negative-parity assignment for the 7432 state.

In the previous work by Champagne *et al.* [37], the 7428 keV and 7436 keV states were both suggested to be possible mirror analogs of the ($7/2^+$, 9/2, $11/2^+$) 7660 keV or (7/2, $9/2^+$) 7679 keV states in ^{27}Al. The 7679 keV state in ^{27}Al satisfies the present spin-parity restrictions for the possible 7432 keV mirror state in ^{27}Si and is known to exhibit γ-decay branches to the $9/2^+_1$, $5/2^+_2$ and $7/2^+_1$ levels [63]. The 7660 keV state in ^{27}Al is not known to exhibit a γ-decay branch to the $5/2^+_2$ level and as such, it is expected that the 7660 keV state is not the mirror analog of the 7432 keV state in ^{27}Si. From the presently obtained

information for the 7432 keV level and mirror nucleus comparisons; 4521 keV, 4784 keV and 5269 keV γ-ray transitions from a $9/2^+$ 7432 keV level to the $9/2^+_1$, $5/2^+_2$ and $7/2^+_1$ states, respectively, were assigned in ^{27}Si.

In the current work, a 2990.8(23) keV γ-ray transition from a 7438 keV level in ^{27}Si to the $11/2^+_1$ state was observed, as shown in Fig. 5.15. No further γ-ray transitions were observed to decay from this state and as γ-ray transitions carrying greater than two units of angular momentum are too weak to be observed in this study, the spin assignment of the 7438 keV state can initially be limited to 7/2–15/2. The ($7/2^+$, 9/2, $11/2^+$) 7660 keV state in ^{27}Al has previously been suggested to be a possible mirror [37] of the presently observed 7438 keV state, and is also known to exhibit a γ-decay branch to the $11/2^+_1$ level [63]. However, the 7660 keV state is also known to exhibit stronger γ-decay branches to the $9/2^+_1$ and $7/2^+_1$ levels, which were not observed from the 7438 keV state. At this point, I decided to investigate the presently obtained ^{27}Al data for the 7660 keV state. Interestingly, no γ-ray transitions from an excited state at 7660 keV in ^{27}Al to the $11/2^+_1$ or $9/2^+_1$ states were observed in the present data and only a single weak γ-ray transition from the 7660 keV state to the $7/2^+_1$ level was observed. One would expect that if a γ-ray transition from a particular state in ^{27}Si was observed, its corresponding mirror transition would be seen with greater intensity due to the fact that ^{27}Al is more strongly populated in the current experimental mechanism. Therefore, the non-observation of a corresponding transition to the $11/2^+_1$ state from the 7660 keV state in ^{27}Al is an unusual result if it is indeed the mirror analog of the 7438 keV state in ^{27}Si. A hypothesis arises here, that the 7438 keV state could be a possible negative-parity state and as such its mirror would not have been predicted in the earlier work of Champagne *et al.* [37]. In the present data, an excited state at 7935 keV in ^{27}Al, which has been previously assigned $(9/2, 11/2)^-$ and reported to have a dominant γ-decay branch to the $11/2^+_1$ level [63], was also observed to exhibit a single γ-decay branch to the $11/2^+_1$ level. The 7935 keV state was the only excited state in ^{27}Al observed to exhibit a single decay branch to the $11/2^+_1$ level and consequently, we favour the assignment of a 2991 keV transition from a $(9/2, 11/2)^-$ 7438 keV state in ^{27}Si.

C.2 Tentative Level Scheme of ^{27}Si

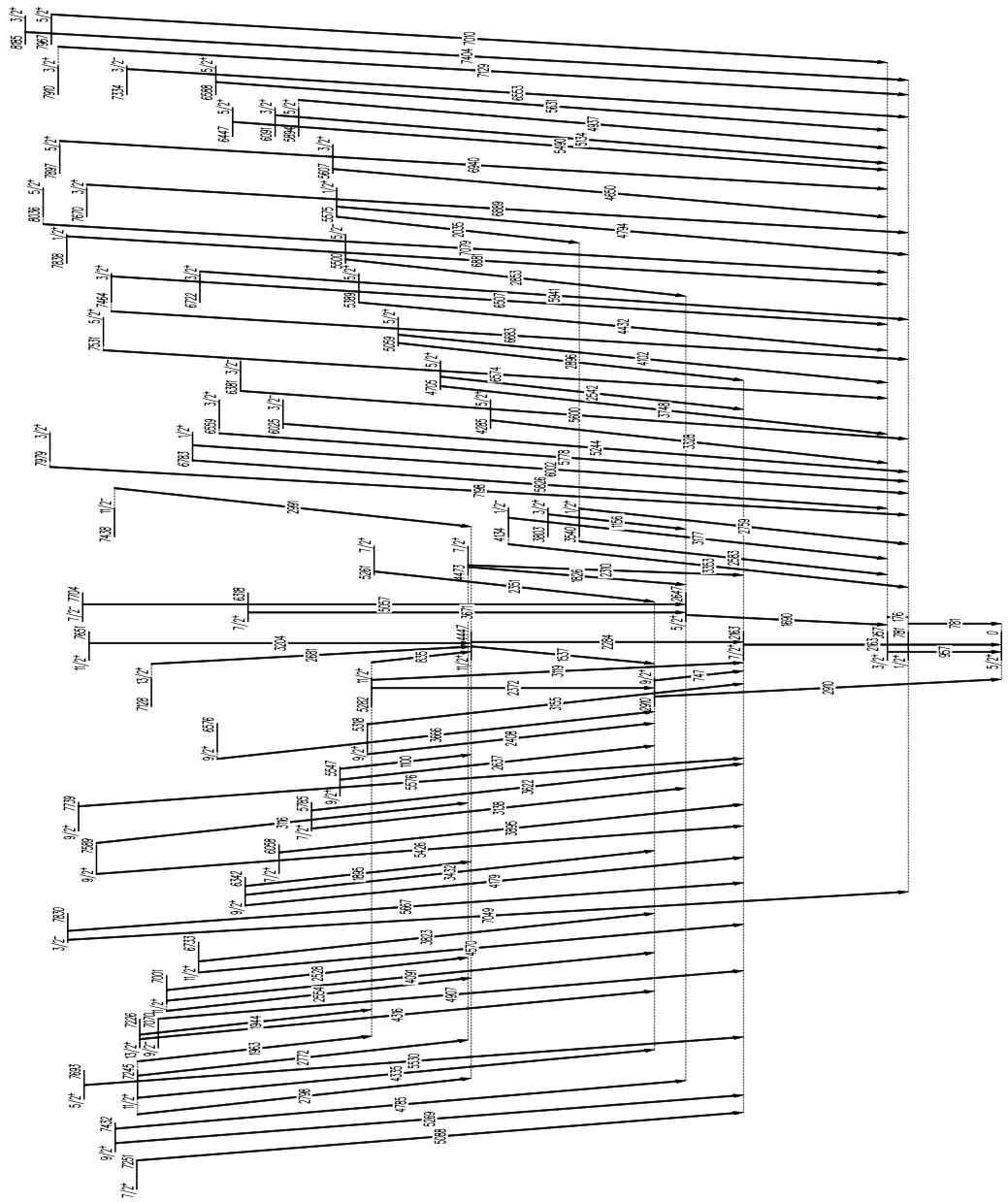

Figure C.1: Tentative level scheme of ^{27}Si

Bibliography

[1] R.d'E. Atkinson. *The Astrophysical Jounal*, **73**:250, 1931. 1.1, 1.2.2

[2] C.L. Critchfield H.A. Bethe. *Physical Review*, **54**:248, 1938. 1.1, 1.2.2

[3] H.A. Bethe *et al.* *Physical Review*, **55**:434, 1939. 1.1, 1.2.2

[4] F. Hoyle. *Monthly Notices of the Royal Astronomical Society*, **106**:343, 1946. 1.1

[5] F. Hoyle. *The Astrophysical Journal Supplement Series*, **1**:121, 1946. 1.1, 1.2.3.1

[6] E.M. Burbidge *et al.* *Reviews of Modern Physics*, **29**:547, 1957. 1.1, 1.2.3.3, 1.2.3.3

[7] H.C. Urey H.E. Suess. *Reviews of Modern Physics*, **28**:53, 1956. 1.1.1

[8] K. Lodders. *The Astrophysical Journal*, **591**:1220, 2003. 1.1.1

[9] P.W. Merrill. *The Astrophysical Journal*, **116**:21, 1952. 1.1.2

[10] W.A. Mahoney *et al.* *The Astrophysical Journal*, **262**:742, 1982. 1.1.2

[11] J.N. Bahcall. *Neutrino Astrophyics*. Cambridge University Press, 1989. 1.1.2

[12] K. Hirata *et al.* *Physical Review Letters*, **58**:1490, 1987. 1.1.2

[13] H.N. Russell. *Popular Astronomy*, **22**:275, 1914. 1.1.3

[14] F.H. Shu. *The Astrophysical Journal*, **214**:488, 1977. 1.2.1

[15] C. Hayashi. *PASJ*, **13**:450, 1961. 1.2.1

[16] A. Maeder T. de Jong. Star formation. IAU Symposium No. 75. Dordrecht:Reidel, 1977. 1.2.1

[17] C. Iliadis. *Nuclear Physics of Stars*. Wiley VCH, 2007. 1.2.2.2, 1.2.2.3, 1.3, 1.3, 2

[18] E.E. Salpeter. *The Astrophysical Journal*, **115**:326, 1952. 1.2.3.1

[19] G. Audi and A.H. Wapstra. *Nuclear Physics*, **A729**:337, 2003. 1.2.3.1, 2.1, 2.3.3.5, 2.3.3.5, 4, 4.1, 4.2, 5, 5.2, 6

[20] S. McMillan E. Chaisson. *Astronomy Today*. Benjamin Cummings, 2007. 1.2.3.3

[21] Y. Grosdidier. False colour image obtained with the Wide Field Planetary Camera 2 of the Hubble Space Telescope. 1.2.3.3

[22] F. Hoyke and W.A. Fowler. *Quasi-Stellar Sources and Gravitational Collapse*. University of Chicago Press, 1965. 1.3

[23] J.S. Gallagher and S. Starrfield. *Annual Reviews of Astronomy and Astrophysics*, **16**:171, 1978. 1.4.1

[24] www.jsc.nasa.gov. 1.4.1

[25] J. Jose *et al.* *Nuclear Physics*, **A777**:550, 2006. 1.4.1, 1.4.1, 1.5.1

[26] D. Prialnak. *The Astrophysical Journal*, **310**:222, 1986. 1.4.2

[27] A.E. Champagne et al. C. Iliadis. *The Astrophyical Journal Supplement Series*, **142**:105, 2002. 1.5.1, 4

[28] T. Lee *et al.* *Geophysical Research Letters*, **3**:109, 1976. 1.5.2

[29] W.A. Mahoney *et al.* *The Astrophysical Journal*, **286**:578, 1984. 1.5.2

[30] D.D. Clayton *et al.* *The Astrophysical Journal*, **262**:742, 1982. 1.5.2

[31] R. Diehl *et al.* *Astronomy and Astrophysics*, **298**:445, 1995. 1.5.2

[32] F.X. Timmes *et al.* *The Astrophysical Journal*, **449**:204, 1995. 1.5.2

[33] N. Prantzos. *Astronomy and Astrophysics*, **420**:1033, 2004. 1.5.2

[34] R. Diehl *et al.* *Nature Letters*, **439**:45, 2006. 1.5.2

[35] J. José *et al.* *The Astrophysical Journal*, **479**:L55, 1997. 1.5.2

[36] J. José *et al.* *The Astrophysical Journal*, **520**:347, 1999. 1.5.2, 2.3.3.5, 2.3.3.5, 5, 6

[37] A.E. Champagne *et al.* *Nuclear Physics*, **A556**:123, 1994. 1.5.2, 2.3.3.4, 5.2, 5.2, 5.2, 5.2, 5.2, 5.3, 5.3, 6, C.1

[38] L. Buchmann *et al.* *Nuclear Physics*, **A415**:93, 1984. 1.5.2, 2.3.3.1, 2.3.3.2, 5.2, 5.2, 5.2, 5.2, 5.3

[39] P. Schmalbrock *et al.* *Nuclear Physics*, **A457**:182, 1986. 1.5.2, 2.3.3.1, 2.3.3.1, 5.2, 5.2, 5.2, 5.2, 5.2, 5.2, 5.2, 5.3, 6

[40] T.F. Wang *et al.* *Nuclear Physics*, **A499**:546, 1989. 1.5.2, 2.3.3.1, 2.3.3.1, 5.2, 5.2, 5.2, 5.2, 5.2, 5.2, 5.2, 5.2, 5.2, 5.3, 6

[41] R.B. Vogelaar. Ph.d. thesis. California Institute of Technology, 1989. 1.5.2, 2.3.3.2, 2.3.3.2, 5.2, 5.2, 5.2, 5.2, 5.2, 5.2, 5.3

[42] R.B. Vogelaar *et al.* *Physical Review C*, **53**:1945, 1996. 1.5.2, 2.3.3.1, 5.2, 5.2, 5.2, 5.2, 5.3, 5.3, 6

[43] C. Ruiz *et al.* *Physical Review Letters*, **96**:252501, 2006. 1.5.2, 2.3.3.2, 2.3.3.2, 5.2, 5.2, 5.2, 5.3, 5.3

[44] C. Rolfs. *Cauldrons in the Cosmos*. The University of Chicago Press, 1988. 2

[45] B.A. Zimmerman W.A. Fowler, G.R. Caughlan. *Annual Reviews of Astronomy and Astrophysics*, **5**:525, 1967. 2.3

[46] B.A. Zimmerman W.A. Fowler, G.R. Caughlan. *Annual Reviews of Astronomy and Astrophysics*, **13**:69, 1975. 2.3

[47] G.R. Caughlan M.J. Harris, W.A. Fowler and B.A. Zimmerman. *Annual Reviews of Astronomy and Astrophysics*, **21**:165, 1983. 2.3

[48] G. Gamow. *Zeitschrift fur Physik*, **51**:204, 1928. 2.3.1

[49] K.E. Rehm M.S. Smith. *Annual Review of Nuclear and Particle Science*, **51**:91, 2001. 2.3.3.2

[50] A. Schotter J.C. Blackmon, C. Angulo. *Nuclear Physics*, **A777**:531, 2006. 2.3.3.2

[51] P. Decrock *et al.* *Physical Review Letters*, **67**:7, 1991. 2.3.3.2

[52] S. Bishop *et al.* *Physical Review Letters*, **90**:162501, 2003. 2.3.3.2

[53] L. Gialanella *et al.* *Nuclear Instruments and Methods in Physics Research*, **A376**:174, 1996. 2.3.3.2

[54] T. Motobayashi *et al.* *Physics Letters*, **B264**:259, 1991. 2.3.3.2

[55] www.dragon.triumf.ca/home.html. 2.3.3.2

[56] S. Engel *et al.* *Nuclear Instruments and Methods in Physics Research A*, **553**:491, 2005. 2.3.3.2

[57] C. Iliadis. *Nuclear Physics*, **A618**:166, 1997. 2.3.3.3

[58] W. Heisenburg. Structure of atomic nuclei. *Z. Physics*, **77**:1, 1932. 2.3.3.4

[59] E. Wigner. *Physical Review*, **51**:106, 1937. 2.3.3.4

[60] E.P. Wigner. Proceedings of the Robert A Welch Conference on Chemical Research, vol. 1, Robert A Welch Foundation, Houston, Texas, 1957, p. 67. 2.3.3.4

[61] B.A. Brown W.E. Ormand. *Nuclear Physics*, **A491**:1, 1989. 2.3.3.4

[62] H. Herndl *et al.* *Physical Review C*, **58**:1798, 1998. 2.3.3.4, 4.2, 4.2, 4.2, 6

[63] P.M. Endt. *Nuclear Physics*, **A521**:1, 1990. 2.3.3.4, 5, 5.1, 5.1, 5.1, 5.1, 5.1, 5.1, 5.1, 5.2, 5.2, 5.2, 5.2, 5.2, 5.2, 5.2, 5.3, C.1

[64] D. Seweryniak *et al.* *Physics Letters B*, **590**:170, 2004. 2.3.3.5, 2.3.3.5, 2.4, 3.1, 4

[65] J. Ekman *et al.* *Physical Review Letters*, **92**:13, 2004. 1

[66] D. Seweryniak *et al.* *Physical Review C*, **75**:062801, 2007. 2.3.3.5, 2.3.3.5, 2.4, 3.1, 4

[67] B.A. Brown. www.nscl.msu.edu/brown/resources/SDE.HTM. 2.3.3.5, 4.2

[68] Y. Parpottas *et al.* *Physical Review C*, **70**:065805, 2004. 2.3.3.5

[69] D. Schwalm D. Pelte. *Heavy Ion Collisions*. North Holland Publishing Company, 1982. 2.4.3

[70] www.radware.phy.ornl.gov. 2.4.3, 3.7.1, 3.7.3, 3.7.4, 4.1, B, B, B, B

[71] www.nucalf.physics.fsu.edu/ riley/gamma. 3.1

[72] D. Seweryniak and P.J. Woods. *Physical Review Letters*, **94**:032501, 2005. 3.1, 4

[73] D.G. Jenkins *et al.* *Physical Review Letters*, **92**:031101, 2004. 3.1, 5

[74] I.Y. Lee. *Nuclear Physics*, **A520**:641c, 1990. 3.4

[75] http://imglib.lbl.gov. 3.4

[76] J. Simpson C.W. Beausang. *Journal of Physics G*, **22**:527, 1996. 3.4

[77] C.N. Davids *et al.* *Nuclear Instruments and Methods in Physics Research*, **B70**:358, 1992. 3.5.1

[78] J.P. Greene *et al.* *Nuclear Instruments and Methods in Physics Research*, **A459**:334, 2001. 3.5.2

[79] H. Bethe. *Annalen de Physik*, **397**:325, 1930. 3.5.3

[80] A.N. Deacon. *Shape Changes in Neutron-Rich fp-Shell Nuclei*. PhD thesis, University of Manchester, School of Physics and Astronomy, 2006. 3.6.2

[81] www.root.cern.ch. 3.7

[82] www.phy.anl.gov/gammasphere/doc/GSSort/GSSort.htm. 3.7

[83] J.H. Kelley *et al.* *Nuclear Physics*, **564**:1, 1993. 3.7.1

[84] K. Kubono *et al.* *Nuclear Physics*, **A588**:521, 1995. 4, 4, 4.2, 4.1, 4.1, 4.1, 4.2, 4.2, 4.2, 6

[85] M.B. Greenfield *et al.* *Nuclear Physics*, **A524**:228, 1991. 4, 4, 4.2, 4.1, 4.1, 4.2, 4.2, 4.2, 6

[86] D.W. Visser *et al.* *Physical Review C*, **76**:065803, 2007. 4, 4, 4.2, 4.1, 4.1, 4.2, 4.2, 4.2, 6

[87] R.G.T. Zegers *et al.* *Physical Review C*, **78**:014314, 2008. 4, 4, 4.2, 4.1, 4.1, 4.1, 6

[88] G. Lotay *et al.* *Physical Review C*, **77**:042802(R), 2008. 4

[89] J. Honkanen *et al.* *Physica Scripta*, **19**:239, 1979. 4, 4.1, 4.1

[90] R.B. Firestone. *Nuclear Data Sheets*, **108**:2319, 2007. 4.1

[91] www.nscl.msu.edu/brown/resources/SDE.html. 4.1, 4.2, 5.1

[92] R.K. Wallace and S.E. Woosley. *The Astrophyical Journal Supplement Series*, **45**:389, 1981. 4.2

[93] M. Weischer *et al.* *Astronomy and Astrophysics*, **160**:56, 1986. 4.2

[94] W. Visser *et al.* *Physical Review C*, **78**:028802, 2008. 4.2

[95] T. Davinson. Private Communication. 4.2

[96] J.J.A. Smit *et al.* *Nuclear Physics*, **A377**:15, 1982. 5.2

[97] A. Parikh. Private Communication. 5.3, 6

[98] K. Krane. *Introductory Nuclear Physics*. John Wiley and Sons Inc., 1988. A.2